Author:
Wasik, Patryk

Title:
Unusual “coffee rings”: Hierarchical surface patterns from evaporation of a reactive ZnO nanofluid sessile drop

Unusual “coffee rings”: Hierarchical surface patterns from evaporation of a reactive ZnO nanofluid sessile drop

By

Patryk Wąsik

School of Chemistry

University of Bristol

A dissertation submitted to the University of Bristol in accordance with the requirements for award of the degree of Doctor of Philosophy in the Faculty of Science.

JULY 2019

Word count: 72 773

Abstract

Drying of a particle laden droplet is widespread in everyday life and industrial processes, and can lead to a plethora of residual patterns, most notably the coffee ring. Its formation mechanism was first elucidated around two decades ago. The vast academic interest it stimulated continues to thrive today, and it is also directly relevant to producing functional devices and nanomaterials. However, the dispersed particles are inert in most studies. In this work, I present studies on formation of complicated surface structures under conditions far from equilibrium *via* rapid evaporation of a sessile drop containing reactive ZnO nanoparticles in a mechanism that is very different from that observed in the coffee ring effect.

Dedication and Acknowledgement

To all my dear friends.

Author’s Declaration

I declare that the work in this dissertation was carried out in accordance with the requirements of the University's Regulations and Code of Practice for Research Degree Programmes and that it has not been submitted for any other academic award. Except where indicated by specific reference in the text, the work is the candidate's own work. Work done in collaboration with, or with the assistance of, others, is indicated as such. Any views expressed in the dissertation are those of the author.

SIGNED: ..... DATE:.....

Table of Contents

List of Figures:

Chapter 1:

Chapter 2:

Chapter 2: Supplementary Information

Chapter 3:

Chapter 3: Supplementary Information

Chapter 4:

Chapter 4: Supplementary Information

Chapter 5: Supplementary Information

Chapter 6:

List of Tables

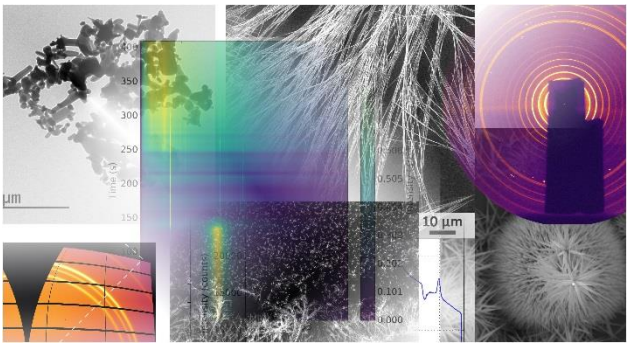

Chapter 1

INTRODUCTION

A wide range of nanostructures with tuneable sizes and shapes are readily available thanks to the significant progress in nanomaterials synthesis. Assembling these nanomaterials in desired locations can produce complex functional structures that could be used as building blocks for device fabrication or for further processing. Assembly is central in nanoscience and important to application of nanomaterials, and substantial effort has been devoted to creating patterned surfaces with tailored structures and enhanced functionalities [1]. A simple and versatile "bottom-up" approach to create sophisticated, hierarchical surface patterns from a wide range of different materials (nanoparticles, polymers, biomaterials, *etc*.) is evaporation induced self-assembly (EISA) [2-4]. In this technique, particles inside a drying droplet are arranged into a variety of structures as the result of the delicate, temporally and spatially fluctuating balance between the inter-particle forces and evaporation-induced solvent flows. This balance may be tuned by manipulating parameters such particle size, shape, concentration, solvent composition, evaporation rate, and surface chemistry of the substrate. EISA from drying of a particle-laden droplet enables efficient coverage over large areas with small functional features. This idea has been successfully applied to inkjet printing of carbon nanotubes [5], production of conductive graphene networks [6], transparent films [7], DNA microarrays [8], ultraviolet photodetectors [9], mesoporous carbons [10], photoluminescent films [11], and bacterial deposits [12].

The most commonly observed deposition patterns resulting from the EISA process are so called "coffee-rings", in which particles are deposited at the perimeter of a drying droplet, forming ring-like residues. The explanation of the mechanism for the coffee ring formation was initially proposed by Deegan and co-workers [13-15]. When a droplet of coffee dries on a solid substrate, the contact line between the droplet and the substrate can be pinned due to some irregularities of the substrate surface. If that is the case, as the liquid evaporates, the contact line cannot recede inwards because of the pinning effect. To compensate for the loss of the liquid removed by the evaporation from the edge of the droplet, an outward flow of liquid from the interior is induced. This outward flow carries the dispersed solutes, which are deposited at the perimeter of the droplet, enhancing the pinning effect by increasing the surface irregularities. This is often referred to as "self-pinning". Consequently, the solutes are transported to the edge of the droplet with the outward capillary flow and form a characteristic ring-like residual pattern upon evaporation.

The formation of coffee rings can be suppressed by the flow driven by thermal Marangoni stresses (Bénard-Marangoni convection) that carries particles from the edge inward, towards the centre of the droplet. During droplet evaporation, evaporative cooling reduces the temperature of the droplet surface in a nonuniform way while the substrate acts as a heat source for the liquid within the droplet. Due to the difference in the thermal conduction path between the substrate and the liquid-air interface (the distance across which heat is transferred from the substrate to the surface of the droplet), the temperature at the top centre of the droplet is lower compared to the surface temperature at the edge. This temperature difference generates surface tension gradient along the droplet free surface, *i.e.* the lower the temperature, the higher the surface tension, inducing the inward Marangoni flow, which transports solutes back towards the centre of the droplet. Solutes can either adsorb to the substrate at the centre or further recirculate to the edge of the droplet. By manipulating the temperature profiles on the substrate it is possible to reduce the Marangoni flow, suppressing the coffee ring effect [16].

The coffee ring effect could also be restrained by affecting capillary interactions in a drying droplet by carefully selecting the shape of dispersed particles. When anisotropic particles inside a drying droplet reach the air-water interface, they are formed into loosely packed quasi-static or arrested structures due to strong long-ranged attractions between particles. These interactions are strong enough to keep the

particles bonded to each other and to the interface. The energetic cost of alteration of these structures is very large, therefore the mobility of the anisotropic particles is significantly reduced. This in turn allows particles to oppose the radially outward flow and produce uniform deposits eliminating the coffee ring effect [17].

Amongst other non-uniform deposition patterns resulting from far from equilibrium processes are spatially periodic, hexagonally shaped manifestations of Rayleigh-Bénard and Bénard-Marangoni (BM) convective instabilities [18-22]. The instabilities, discussed in detail in the following sections, reveal themselves as vortices within the film, where liquid flows upward in the central part of the hexagons and subsequently outward to their edges. As mentioned earlier, the Bénard-Marangoni convection results from a surface tension gradient on the free surface [23-24]. This gradient may arise either from a temperature difference between the hot substrate and the cooled surface, or from a concentration gradient between the bottom surface rich in solvent and the top, rich in solutes. Rayleigh-Bénard convection, on the other hand, is generated as a result of a change in fluid density due to a temperature gradient between the top and bottom surfaces [25]. Because of small fluctuations in the droplet surface temperature, many adjacent Bénard cells can be induced, in contrast to a situation when a whole droplet acts as a single Bénard cell. Therefore, suspended particles are dragged with the flow and deposited on the substrate, forming corrugated pattern of connected polygons [21-22, 25-31].

Another interesting type of EISA deposits include the fingering structures. The formation of these patterns is provoked by fingering instabilities, originating from fluctuations at the interface between two fluids of different viscosities, where the low-viscosity fluid pushes towards the more viscous one [32-34]. Finger-like stripes perpendicular to the contact line are often produced in vertical deposition techniques (*i.e*. plate withdrawal), and radial spoke patters are commonly observed in horizontal deposition techniques (*i.e.* drop-casting) [35]. Symmetric and asymmetric shapes of the fingering structures are formed due to nonuniform distribution of the evaporation rate along the surface of the droplet or the dynamic motion of the contact line [36].

MOTIVATION AND RESEARCH QUESTIONS

As discussed above, drying of a particle laden droplet is a widespread phenomenon amongst processes related to everyday life and industry, which in turn can be harnessed to produce multifarious residual patterns across many length scales. The detailed explanation of the coffee ring formation, one of the most renown residual pattern, has been thriving in the scientific community for about two decades, stimulating advances in functional devices and nanomaterials fabrication methods. However, in most of these studies the dispersed particles are inert, therefore the formation of the residual patterns is governed by the by inter-particle forces and evaporation-induced solvent flows.

In contrast, a very recent paper by Wu *et al*. [37] in the Briscoe group reported a novel method of producing complex fibrous residual network structures upon evaporation of a reactive ZnO nanofluid sessile drop in a mechanism very different from that associated with the coffee ring effect. This, and related Master's thesis by Redeker [38] were the only works published and the current state of knowledge at the time I started working on my research project in February 2015. The paper reported that when a ZnO nanofluid drop, produced by dispersing ZnO nanorods in a mixture of cyclohexane and isobutylamine, dries on a solid substrate, the reactive ZnO nanorods undergo spontaneous chemical and morphological transformation, from ZnO to $Zn(OH)_2$ and from nanorods to centimetre-long fibres, leading to the formation of fibrous and dendric networks on the surface [37]. (The mechanism is described in detail in subsequent sections of Chapter 1). The thesis reported the effect of different solvents, ZnO nanorod concentration, and aging of nanofluid on the residual pattern formation [38]. In addition, some initial work on evaporation of binary mixtures composed of ZnO nanorods and SiO_2 nano/microparticles was performed by Slastanova *et al*. (unpublished work).

My first research question driven by the scientific curiosity was related to the effect of ZnO particles on the residual pattern formation itself, as the previous studies focused solely on ZnO nanorods [37-38]. Therefore, I experimented with different ZnO particles varying in size, shape, morphology, and crystallinity, which included in-house synthesised ZnO nanoparticles (*ca* 9 nm in diameter) and commercially acquired ZnO nanopowder and ZnO powder. These different ZnO particle systems and resulting residual surface patterns produced upon evaporation were studied with various techniques such scanning and transmission electron microscopy (SEM and TEM, respectively), optical

microscopy, energy-dispersive X-ray spectroscopy (EDX), powder X-ray diffraction (XRD), grazing incident XRD, and dynamic light scattering (DLS). As a result, we have shown that by varying the size, morphology, and crystallinity of the ZnO particles, we were able to control the dissolution of the ZnO nanocrystals inside of the drying droplet. This affected solvent flows and instabilities and, in turn, the morphology of the residual surface structures. Our findings were published in *Langmuir* as a research article [39], which serves as a base for Chapter 2.

By the end of my PhD, another work by Wu and Briscoe [40] was published, where a system consisting of ZnO pellet-like particles in a mixture of chloroform/methanol/isobutylamine was investigated. The work reported the formation of dendritic patterns attributed to the Bénard-Marangoni convection triggered by the fluctuations in the local fluid viscosity induced by the variation in the local particle concentration during the evaporation [40]. This was consistent with my observations, where similar structures that resembled solidified manifestations of BM convective cells were formed from the in-house ZnO nanoparticles and commercially acquired ZnO nanopowder and ZnO powder nano/microfluids. However, Wu and Briscoe based their comparison of the residual pattern structures on a rather superficial descriptive characteristic of the dendritic patterns, comparing their morphology with the foliage of red algae, Spanish dagger, and spider plant [40]. To go beyond such descriptive characterisation, I performed a fractal dimension analysis of these quasi 2-dimensional structures to quantify differences correlated with the morphological details of the BM cells produced in different experimental conditions. We found that the different degree of interpenetration and structural complexity between BM cells produced from different ZnO nano/microfluids were reflected in the calculated box counting fractal dimensions. Our observations as well as a detailed step by step approach to such fractal dimension analysis of solidified manifestation of BM cells were published as a communication letter in the *Journal of Colloid and Interface Science* [41], manuscript for which is included in Chapter 3. To my best knowledge at the point of writing this paragraph, it would be the first reported attempt to use fractal dimension analysis to quantify differences in the formation of BM cells manifestations in the residual patterns from the EISA process.

With the recently developed methodology used as a feasible tool for providing quantitative information on structures constituting the residual surface patterns produced from different ZnO

nano/microfluid, my next work focused on reporting findings on the influence of the surface chemistry of the material used as a substrate for ZnO nano/microfluid evaporation. We found that the dimensions of the BM cells and their size distribution were affected by the substrate used. This is discussed in detail in Chapter 4, which was published as a research article in *Langmuir* [42].

To this point, my approach to the investigation of the system consisting different ZnO nano/microfluids dried on different substrates acknowledged mainly the initial experimental conditions such as the type of ZnO particles, solvent composition, temperature, relative humidity, substrate used, *etc.*, with the conclusions that were based on the form of arrested residual surface patterns after the drying process stopped. However, this approach lacked in insights when the things were in motion, that is as the drying process was happening. At that time, we were already able to predict the outcome of the EISA process based on the initial conditions, *i.e.* if the ambient humidity in which a drop of ZnO nanofluid was dried was too low, the initial moisture assisted dissolution of ZnO nanocrystals was inhibited, resulting in undissolved ZnO crystal residues and the lack of $Zn(OH)_2$ fibrous structures in the dried residues. By lowering the evaporation flux, for example by performing the experiment inside of a beaker covered with a punctured parafilm or by saturating the experimental system with the vapour of the solvent mixture used for nanofluid preparation, no Bénard-Marangoni instabilities were triggered, and the residual patterns were composed of long $Zn(OH)_2$ fibres, which thickness increased with the increasing evaporation time. If larger ZnO particles with a high degree of crystallinity were used for ZnO nano/microfluid preparation, the evaporation left the surface covered with dense, fibrous structures intercalated with ZnO nano/microcrystal residues that did not fully undergo the moisture assisted dissolution. The above was concluded based on the morphology and structure assessment of the dried residual surface patterns using electron microscopy techniques. Therefore, to take the research further, we aimed to capture what was exactly happening as the drop of ZnO nanofluid was drying.

To catch a drying nanofluid droplet in the act, we performed *in situ* grazing incident X-ray diffraction experiments to track the crystal structure changes inside a drying drop as the evaporation progressed. Using the high flux focused X-ray beam from synchrotron radiation sources at Diamond Light Source and the European Synchrotron Radiation Facility, we were able to obtain high temporal and spatial resolutions to map the local structures both under *in situ* evaporation and on the resulting

dried films. This work is currently under preparation for publication as a research article and the initial results are partially presented in Chapter 5. In short, we were able to observe the initial ZnO dissolution and recrystallisation process by identifying the diffraction signals from different constituents such as layered zinc hydroxide and zinc oxide structures inside a drying drop at different times, which provided mechanistic insights into the dissolution mechanism itself. What is more, we investigated various materials as solid substrates as we previously found the substrate affected the micromorphology of the residual surface patterns. However, this was not reflected in the crystal structure transformations inside of a drying ZnO nanofluid drop as it was manifested in the diameters of the solidified manifestation of Bénard-Marangoni cells. In addition, we also observed a phase transition in the residual surface pattern from $Zn(OH)_2$ to ZnO upon annealing at 50 - 100 °C.

Another research question I found worth exploring was connected again to the ZnO crystals used as a starting point in this EISA process. I wondered whether it would be possible to produce fibrous zinc hydroxide networks from ZnO nanostructures that were immobile, *i.e.* were fixed to the surface of the substrate. Therefore, I synthesised various ZnO nanostructures including nanorods, nanourchins and nanopellets on different substrates with the idea to deposit a drop of a pure mixture (without the addition of ZnO particles) of cyclohexane and isobutylamine onto such substrate and allow it to evaporate. I found that it was possible to produce fibrous residual patterns from ZnO nanostructured substrates, but the grown ZnO nanostructures remained largely undissolved and became braided or intercalated with the zinc hydroxide fibres left upon evaporation. The findings are planned to be published as a research article, and some of the preliminary results and suggestions for future work are included in Chapter 6. It is worth to mention that a part of this work contributed to developing a facile fabrication method of multifunctional ZnO urchins under collaboration with Tripathy *et al.*, published in *Colloids Interfaces* [43].

A naturally following question that intrigued me during my research work was whether ZnO was the only one and unique component that could be used in formation of fibrous residual structures from reactive nanofluids. Based on the literature, where people reported similarly looking zinc hydroxide nanostrands [44-45] to the fibres formed from ZnO nano/microfluids, I identified a series of potential oxides as suitable candidates for the EISA experiments, including CdO [46-47], CuO [48-50], and MnO

[51], which was later extended to Cu_2O, HgO, NbO, NbO_2, Nb_2O_5, SrO, and TiO_2. My initial observations revealed that CdO, CuO, HgO, SrO, and MnO could produce fibrous residual deposits after the evaporation of respective nanofluids, however with a large amount of undissolved crystals still present in the residues, similarly to the ZnO nano/microfluids produced from the commercially acquired nanopowder and powder [39]. These findings are intended to be published after the optimal conditions for these systems are established. Some initial results and suggested future work on cadmium, copper, and mercury oxides are included in Chapter 6. In addition, the evaporation of CuO and CdO nano/microfluids have also been investigated in the *in situ* grazing incident XRD experiments.

In the course of my research, I devoted some attention to a few other things that could be explored in the future, providing the time and resources would be available. Building on the work by Redeker [38] on the effect of different solvents on the residual patterns formation from ZnO nanofluids, I investigated mixtures of cyclohexane and different amines such as benzylamine, butylamine, dodecylamine, hexylamine, isobutylamine, isopentylamine, octylamine, propylamine, sec-butylamine, and tert-butylamine. Some success in producing fibrous residues from ZnO and CdO nano/microfluids was achieved using benzylamine, octylamine, propylamine, and sec-butylamine, all mixed with cyclohexane, however this research avenue still requires more dedicated studies. In addition, different nano/microfluid drop deposition techniques and droplet drying configurations were considered. I performed initial experiments using a spin coater to investigate how the centrifugal force would affect the orientation of the zinc hydroxide fibres in the residual network. However, this would require reconfiguration or rebuilding of the spin coater to control the moisture level inside of the spin coating chamber. With respect to different drying geometries, I suggested a potential Master's thesis project involving the evaporation of ZnO nanofluids in a confined geometry based on Ref. [2], which was undertaken by Ollie Hughes, a student at the Briscoe group at that time.

THESIS SUMMARY

Summarising, I have devoted my research to producing complex hierarchical structures from evaporative drying of reactive ZnO nanofluids that form in a mechanism that is very different from that observed in the coffee ring effect. As a drop of ZnO nanofluid dries on a solid substrate, ZnO

nanocrystals undergo chemical and morphological transformation to produce fibrous residual patterns upon evaporation. I have studied various experimental systems, which include the effect of the ZnO particles and the solid substrate on the residual surface pattern formation, developed a methodology to quantify differences in the solidified manifestations of Bénard-Marangoni cells formed within the residual patterns by employing fractal dimension analysis, and investigated drying nanofluid droplet in act using the *in situ* grazing incident X-ray diffraction experiments to track the crystal structure changes inside of a drying drop, providing mechanistic insights into the dissolution-crystallisation mechanism. In addition, I established a method to produce hierarchical zinc hydroxide fibrous structures from ZnO nanostructured surfaces, contributed to developing of a facile fabrication method of multifunctional ZnO urchins, and extended this novel evaporation induced self-assembly process to reactive nanofluid systems of other than ZnO oxides, *i.e.* CdO, CuO, and HgO. The majority of my PhD research work is described in detail in the following chapters.

BÉNARD-MARANGONI INSTABILITIES

Henri Claude Bénard, a French physicist widely known for his studies on convection in liquids, initially observed ordered hexagonal cells formation in a melted paraffin with graphite dusts in 1900 [30-31]. Subsequently, he conducted extensive studies of cellular vortices induced in a horizontal layer of different volatile liquids heated on a metallic plate [52-53]. The first theoretical explanation of Bénard's results was published by Lord Rayleigh in 1916 and was based on the stability analysis, implicating buoyancy as the driving force for the convective motion [54]. However, a few decades later it was demonstrated both experimentally by Block in 1956 [23] and theoretically by Pearson in 1958 [24] that the cellular vortices, also known as the Bénard-Marangoni (BM) convection cells, were induced by variations in the surface tension caused by temperature fluctuations at the free fluid surface.

Rayleigh number

The main difference between the Bénard experiment and the model experiment of Rayleigh is that Bénard allowed the upper surface of the liquid to be open to the air, while Rayleigh considered the liquid layer confined between two rigid boundaries. Even though Rayleigh's theory does not apply to

the system studied by Bénard, it is worth outlining it for completeness, as it is often the starting point for modern theories on convection.

In Rayleigh's model, there is no free surface as a thin layer of fluid completely fills the space under confinement between two horizontal plates. Heating the fluid from below creates temperature and density gradients across the thin layer. In these conditions, an imbalance of forces is required to induce a convective flow. If a portion of warm liquid emerges slightly from the bottom to a region of greater average density, it becomes subject to an upward buoyant force. Equally, when a portion of cool liquid from the top is displaced downwards, it enters a region of lower average density and sinks to the bottom. The two opposing factors to the buoyancy force are viscous drag and heat diffusion. The drag force acts opposite to the relative motion of the fluid and is determined by the kinematic viscosity of the fluid. The heat diffusion leads to the temperature equilibrium between a displaced portion of liquid and its surroundings, and depends on the thermal diffusivity of the liquid [30].

Lord Rayleigh demonstrated that it is necessary for the buoyancy arising from a temperature gradient to exceed the dissipative effects of viscous drag and heat diffusion to induce convective flow. The dimensionless ratio of these effects is called the Rayleigh number, *R,* which is expressed in equation 1 below:

$$R = \frac{g\alpha\Delta T h^3}{\nu\kappa}, \tag{1}$$

where g is acceleration due to the gravity, α is the coefficient of thermal volume expansion, ΔT is the vertical temperature gradient, h is the thickness of the liquid layer, ν is the kinematic viscosity, and κ is the thermal diffusivity of the liquid [54].

Convection is initiated when R exceeds a critical value, R_c, and the motionless equilibrium becomes unstable. This leads to the liquid layer being spontaneously divided into a pattern of convection polygonal cells with the fluid circulating in closed orbits. The warm fluid flows upward in the centre of a convection cell, spreads out over the upper surface, and flows downward at the perimeter, adjacent to another cell. The distance between the centres of neighbouring cells is defined as the wavelength of the system [30]. The critical Rayleigh number depends on the boundary conditions of the liquid layer and is related to the critical wavelength of the system. It is possible to calculate R_c based on the linear

stability theory, which takes values of 1708, 1101, and 658 for the rigid-rigid, rigid-free, and free-free boundaries, respectively [55].

Marangoni number

In the Bénard experiment, the upper surface of the liquid was open to the air, therefore the flow was affected predominantly by the surface tension rather than the buoyant force. The Bénard convection, also referred to as Bénard-Marangoni (BM) convection, results from a surface tension gradient on the free surface, which is a consequence of a temperature gradient (thermal BM), a concentration gradient (concentrational BM), or a convolution of both [25]. The concentrational BM convection will be described in later paragraphs.

The surface tension of a liquid is reduced as the temperature increases, thus the warmer regions will exhibit weaker tension when compared to the colder ones. Small fluctuations in the surface temperature create gradients in the surface tension, which leads to an imbalance of forces. As the warm liquid is pulled towards the high tension regions, the convection is induced and reinforced by a temperature driven Marangoni flow [19-20]. In his analysis, Pearson introduced a new dimensionless ratio called the Marangoni number, M, shown in equation 2 below:

$$M = \frac{\frac{d\gamma}{dT}\Delta T h}{\rho \nu \kappa}, \tag{2}$$

where $\frac{d\gamma}{dT}$ is the temperature derivative of the surface tension and ρ is the density at a reference temperature. It describes the ratio between forces resulting from the surface tension gradient and the viscous drag and the rate of heat diffusion. In the context of this theory, convection is induced when the Marangoni number exceeds a critical value of $M_c \approx 80$ [24, 30].

A surface tension gradient can be also induced by a concentration gradient, leading to Bénard-Marangoni convection [25, 56]. The solvent loss due to evaporation could generate a gradient of solute concentration between the solvent rich bottom and the solute rich top of the liquid layer. The fluid rich in solvent flows upward to the surface in the centre of the convection cell, reducing the solute concentration in this region and generating a surface tension gradient on the surface. This in turn results

in the transport of fluid to the regions of higher solute concentration, initiating convective instabilities. This type of instability is described by the concentrational (solutal) Marangoni number, M_{conc}, defined as

$$M_{\text{conc}} = \frac{\frac{d\gamma}{dc}\Delta C^{u-s} h}{\rho \nu D_{\text{coop}}}, \tag{3}$$

where $\frac{d\gamma}{dc}$ is the concentration derivative of the surface tension, ΔC^{u-s} is the solvent concentration difference between the free surface and the substrate, and D_{coop} is the cooperative diffusion coefficient of the fluid in a solute / fluid mixture [25]. It is often challenging to estimate ΔC^{u-s}, but can be done by assuming its linear vertical profile and applying Fick's law for the rate of diffusion, J,

$$J = D_{\text{coop}} \frac{\Delta C^{u-s}}{h}, \tag{4}$$

while assuming a constant D_{coop} through the layer. Combining equations 3 and 4 gives the expression for the concentrational Marangoni number:

$$M_{\text{conc}} = \frac{\frac{d\gamma}{dc} J h^2}{\rho \nu D_{\text{coop}}}. \tag{5}$$

Relation between Rayleigh and Marangoni numbers

By combining equations 1 and 2, an interesting relation between the Rayleigh and Marangoni numbers can be obtained

$$\frac{R}{M} = \left(\frac{\rho \alpha g}{\frac{d\gamma}{dT}} \right) h^2, \tag{6}$$

which shows that the relative importance of the two effects contributing to the convection instabilities depends on the thickness of the liquid layer. In a typical experiment, the parameters inside the brackets are defined by the liquid, thus take constant values. The convection is controlled by surface tension forces for small thickness of the liquid layer (high Marangoni number) and by buoyant forces in the thick liquid layers (high Rayleigh number) [30].

Bernard-Marangoni cell diameters

Bernard-Marangoni convection cells appear in the form of the periodic flow patterns described by a characteristic wavelength, λ_{BM}, which is defined as the distance between the centres of neighbouring BM cells. This wavelength can also be related to the diameters of solute residues left by the flow upon evaporation [19]. For a flat liquid layer, the height of the BM cell coincides with the layer thickness, h. In his original considerations, Pearson showed a relation between the Marangoni number, M, and a dimensionless constant, ξ, arising from the separation of variables during the stability analysis, that

$$M \simeq 8\xi^2 \tag{7}$$

for large values of ξ [24]. If the Marangoni number exceeds the critical value, then the characteristic wavelength can be expressed as [57]

$$\lambda_{\mathrm{BM}} = \frac{2\pi h}{\xi} \ . \tag{8}$$

Combining equations 7 and 8 relates the Marangoni number to the characteristic wavelength of the BM instabilities:

$$M = 32\left(\frac{\pi h}{\lambda_{\mathrm{BM}}}\right)^2 , \tag{9}$$

based on the previously mentioned assumptions ($M > M_c$). Wu and Briscoe used this relation to calculate a range of Marangoni numbers in the investigated ZnO nanofluid systems ($M \sim 300$ - 2000) based on the diameters of the dendritic cellular patterns left upon nanofluid droplet evaporation ($\lambda_{BM} \sim 200$ - 500 μm) and a droplet thickness ($h \sim 500$ μm) estimated from the droplet volume and footprint [40].

Comments on the data presented in the thesis

In this work, the residual surface patterns in the form of circular patches produced upon evaporation of ZnO nano/microfluids, identified as solidified Bénard–Marangoni convection cells consists the main scope of Chapters 3 and 4. These cells resembled spoke-like radial structures and exhibited a range of diameters corresponding to the BM characteristic wavelength λ_{BM} = 200 - 800 μm. Their appearance was also similar to the BM flow pattern observed during the evaporation of toluene from polystyrene/toluene solution [21].

The Marangoni numbers for the results presented in the thesis were calculated accordingly to equation 9, which relates the Marangoni number to the cell diameter and the liquid film thickness, estimated from the droplet volume and footprint, similarly to Wu and Briscoe [40]. This approach allowed for the calculations to be performed based on the data already collected, without the need of repeating the experiments. However, it would be valuable to further estimate the Marangoni numbers for the systems and conditions investigated here using equation 2 derived by Pearson, which requires the knowledge of a set of different parameters, including the coefficient of thermal volume expansion, the vertical temperature gradient, the thickness of the liquid layer, the kinematic viscosity, the thermal diffusivity, temperature derivative of the surface tension, and the density of the nano/microfluid at a reference temperature. Most of the values could be assumed to lie between these quantities for corresponding solvents of the mixture of cyclohexane and isobutylamine in 5:1 volume ratio. The temperature gradient between the substrate and the free surface layer could be measured using a thin thermocouple as in the work by Bassou and Rharbi [25].

Further analysis would require specifying the solutal component of the BM flow using equation 5, especially that Wu and Briscoe showed that there existed a critical ZnO nanoparticle concentration (0.1 mg/mL) below which the cellular residual pattern was observed [40]. On the other hand, they also emphasised that the exact composition and structure of the surface crust composed of the surface-active isobutylamine-ZnOH molecular complexes are not known, which would have to be examined before making any assumptions on the solute concentration profile and estimation of the concentrational Marangoni number.

One could also discuss the relative boiling points for cyclohexane (80.7 °C) and isobutylamine (68.8 °C) [58]. As the isobutylamine has the lower boiling point than cyclohexane, it evaporates faster than cyclohexane, which creates a solvent concentration gradient between the free surface and the bulk of the droplet. Isobutylamine has also lower surface tension (21.75 mN/m [59]) when compared to cyclohexane (25.1 mN/m [60]) therefore, the solvent concentration gradient results in the surface tension gradient, contributing to the Marangoni flow. In principle, different compositional (related to both solvents and solutes) and thermal gradients could reinforce or supress Bénard–Marangoni convection inside of a drying ZnO nano/microfluid droplet. However, having the unknown composition

and structure of the surface crust together with the rapid timescale of the process in mind, it is challenging to definitely specify the solutal and thermal components in the BM flow without performing further experiments.

THE MECHANISM

Fibrous network formation

The first attempt to explain the mechanism behind the formation of hierarchical residual surface patterns from evaporation of a ZnO nanofluid sessile drop was proposed by Wu *et al.* in a paper published in 2014 [37]. It has been shown that the nanostructure and micromorphology in the residual surface patters depends on ambient moisture, nanofluid solvent composition, and substrate surface chemistry. In addition, it has been demonstrated that the structure of as produced zinc hydroxide fibres could be transformed to porous ZnO by thermal annealing, with the pore size depending on the temperature of the process.

When a droplet containing ZnO nanorods dispersed in a mixture of isobutylamine and cyclohexane is placed on a substrate, water molecules are rapidly taken up from air and incorporated onto the surface of isobutylamine-coated ZnO nanorods, where reaction 10 is initiated:

$$\text{i-}C_4H_{11}N + H_2O \leftrightarrow \text{i-}C_4H_{12}N^+ + OH^- \quad (10)$$

The hydration-dissolution of ZnO nanorods proceeds afterwards, likely starting from the (0001) facets located at the tips of the nanorods due to their exposed OH- groups:

$$ZnO_{(s)} + \text{i-}C_4H_{12}N^+ + OH^- + H_2O \leftrightarrow Zn(OH)_3^{-}\cdot^{+}\text{Ni-}C_4H_{12(aq)} \quad (11)$$

Convective flows shuttle liquid $Zn(OH)_3^{-}\cdot^{+}\text{Ni-}C_4H_{12(aq)}$ away from the nanorods, allowing their further dissolution. As the evaporation progresses, the solution reaches its saturation point at the liquid-air interference towards the edge of the droplet, where crystallisation of $Zn(OH)_2$ is initiated according to reaction 12:

$$Zn(OH)_3^{-}\cdot^{+}\text{Ni-}C_4H_{12(aq)} \leftrightarrow Zn(OH)_{2(s)} + \text{i-}C_4H_{11}N + H_2O \quad (12)$$

The authors suggested that the driving force leading to the assembly of $Zn(OH)_2$ nanocrystals into long fibres was a combination of the solvent evaporation, crystallisation-mediated fingering instabilities at dewetting front of the drying droplet, and hydrogen bonding between nanocrystals. As isobutylamine is surface active and evaporates rapidly, the solutes, which include undissolved ZnO nanorods and liquid $Zn(OH)_3^{-}\cdot^{+}Ni\text{-}C_4H_{12}$, tend to localise and concentrate close to the liquid-air interface.

Crystallisation of $Zn(OH)_2$ is thus initiated at the vicinity of the liquid-air interface due to the increased solute concentration. The three-phase contact line between the solvent, wet $Zn(OH)_2$ nanocrystals, and air subsequently arises and recedes in the direction of fibre growth as evaporation dewetting proceeds. Surface tension gradient induced by fast solvent evaporation and concentration gradient in the proximity of nonequilibrium crystallisation growth provoke fingering instabilities at the receding dewetting front. The instabilities originate from numerous crystallisation sites at the droplet surface and its perimeter propagating inwards.

The freshly formed $Zn(OH)_2$ nanoplatelets covered with isobutylamine and water interplay with each other and bond through hydrogen bonding. $Zn(OH)_3^{-}\cdot^{+}Ni\text{-}C_4H_{12}$ in its supersaturated isobutylamine solution is transported towards and into the growth front of the fingering instabilities, congesting $Zn(OH)_2$ nanoplatelets at the finger front *via* sustained crystallisation and promoting the growth fingers into fibrous networks. This process would propagate from the liquid-air interface towards the substrate surface and from the perimeter to the centre of the droplet, giving rise to the fibrous hierarchical structure.

Revised mechanism for Bénard-Marangoni (BM) dendrite formation

In 2018, Wu and Briscoe proposed a revised mechanism of hierarchal residual patterns formation from evaporation of reactive ZnO nanofluid sessile drops [40]. The suggested mechanism is expanded to account for the cellular patters with dendritic morphologies, formed within the central region of the residue that is surrounded by a coffee-ring band. The considerations of the structural hierarchy on nano-/micro-/macroscopic levels are based on time-resolved transmission electron microscopy (TEM) and cryo-TEM observations of the constituent nanostructures inside the droplet at different stages of the evaporation process and video microscopy studies of the capillary waves at the droplet surface. For the

completeness of the description, the schematics for the pattern formation mechanism are reproduced from Ref. [40] below. The authors used droplets containing 1 mg/mL ZnO nanoparticles (~5-10 nm) dispersed in a mixture of chloroform/methanol/isobutylamine (at ratios of 3.85:1.15:1).

At the initial stage of evaporation, the outward flow transports ZnO nanoparticles to the edge of the droplet where they undergo moisture assisted dissolution into amphiphilic isobutylamine-ZnOH complexes (iZMCs) with a core size *ca.* 0.24 nm (**Figure 1**a-c), which then form solvated aggregates around 100 nm in size (**Figure 1**d and f). At the same time, the iZMC aggregates are being distributed along the drop surface by the Marangoni flow (**Figure 1**f). In this rapid process, most ZnO nanoparticles are dissolved and transformed into iZMC aggregates within a few minutes of evaporation (**Figure 1**a, b, d, and e). As the process progresses, iZMCs assemble into primary clusters with 2 - 5 nm in size within the initially formed aggregates (**Figure 1**e and i). The primary clusters are suggested to be micelle- or vesicle-like, consisting of a polar core of isobutylamine, methanol, and water shielded from the adjacent nonpolar solvent. However, the authors emphasised that the exact composition and structure of the primary clusters was not known and would require further investigation. These primary clusters further assemble into a network of secondary clusters with ~30 nm in size (**Figure 1**j-l). The coalescence of secondary clusters leads to the formation of linear or branched aggregates, shown in red frames in (**Figure 1**j). It is suggested that the self-assembly of clusters is prominent at the droplet surface due to their surface activity and is also driven by evaporation.

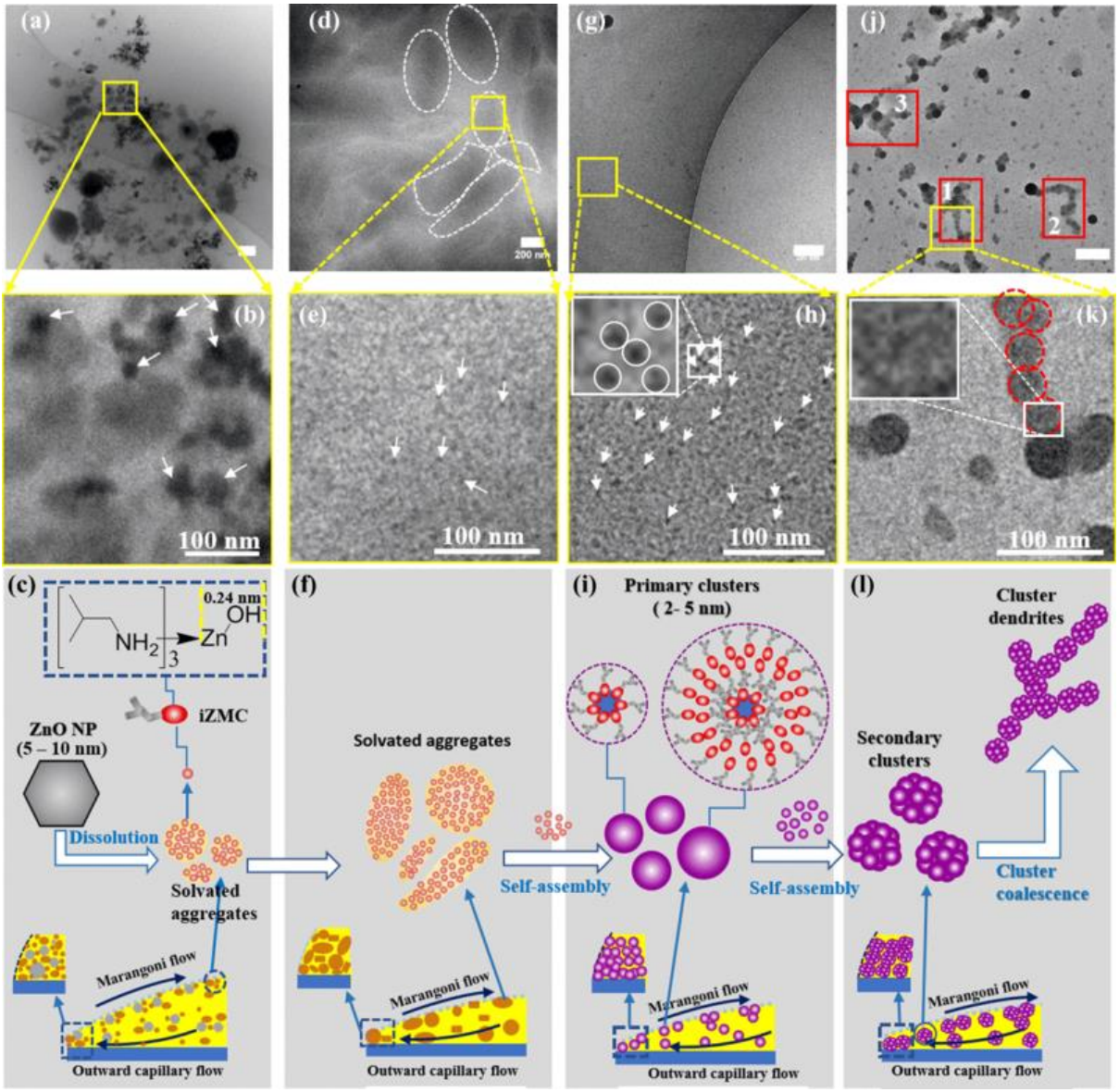

Figure 1. Cryo-TEM images of nanoconstituents in an evaporating droplet at different time intervals: 2 min (a), (b), 4 min (d), (e), 6 min (g), (h), and 8 min (j), (k); and corresponding schematic of flows and cluster formation (c), (f), (i) and (l). Images (b), (e), (h), (k) are enlarged views of the white frames in (a), (d), (g), (j), respectively. The insets in (h), (k) show enlarged views of the white frames in (h), (k), respectively. The scale bars in (a), (d), (g), (j) are 200 nm. The red frames (numbered 1–3) in (k) highlight branched or linear aggregates of coalesced secondary clusters (red dashed circles in (l)). Reprinted with permission from Ref. [40], Copyright (2019) by the American Physical Society.

Cellular patters with dendritic morphologies

With the droplet thinning due to the loss of the solvent during evaporation, the drying condition can become satisfactory to trigger Bénard-Marangoni (BM) instabilities that coincide with the dendrite growth in the droplet. The induced Bénard-Marangoni flows cause concentration inhomogeneities in a crust composed of the surface active iZMC clusters spread along the drop surface, which in turn results in stress initiating capillary ripples (**Figure 2**a). The solidification of a BM cell is initiated at the centre of the ripple, where the coalesce of the secondary clusters along radial BM flows leads to the branched growth of fibres (**Figure 2**b). These arrested secondary clusters form gel-like residual patterns that compose a three-dimensional swollen fibrillar network. The coalescence of the secondary clusters is believed to be facilitated by inter-cluster solvophobic interactions while the resulting dendritic morphology is attributed to diffusion limited aggregation (DLA) [61]. The difference in the Bénard-Marangoni cell diameters, λ_{BM}, is connected to the local inhomogeneities in the local viscosity and cluster concentration. In a similar manner, cluster coalescence happens upon rapid recession of the contact line, which leads to dendritic growth of swollen fibres forming the peripheral coffee ring (**Figure 2**a(i) and b(i)).

Thanks to the enhanced surface elasticity caused by the surface crust made of clusters, Wu and Briscoe were able to observe the capillary ripples using video microscopy. The extracted video frames are shown in **Figure 2**c-h and present the cluster pattern formation at sites 1 - 10 and capillary ripples with a constant wavelength $\lambda_{cp} \approx 50$ μm, characteristic for capillary waves in polymer films [62] and soft gels [63]. The authors also estimated the viscosity of the fluid layer mediating the ripples, $\eta_s \approx 8.4$ - 13.0 mPa·s, to be ~20 times larger than the viscosities of the solvents (~0.55 mPa·s for chloroform). The estimations were based on equation 13:

$$\mu \approx \left(\rho\gamma\lambda_{cp}^3\right)^{\frac{1}{2}}/\eta_s, \tag{13}$$

where μ is the characteristic attenuation length (distance intervals between the ripple initiation and diminishment), ρ is the density, γ is the interfacial tension at the drop-air interface, and η_s is the viscosity of the fluid layer mediating the ripples [56]. $\mu \approx 1$ was determined from video microscopy, $\gamma \approx 22.25$ (isobutylamine) - 26.67 (chloroform) mN/m, and $\rho \approx 0.735$ (isobutylamine) - 1.49 (chloroform) g/cm^3

as lower and upper limits of these quantities [40]. A similar growth rate of 92 ± 15 μm/s for all the Bénard-Marangoni cells was observed (**Figure 2**i), which is much higher than the capillary flow rate of *ca.* 0.1 μm/s, exhibited by the coffee ring formation [15]. The growth of a single BM cell at site 1 is shown in a set of magnified video microscopy frames in **Figure 2**j-m. Using the relation between the Marangoni number, B, and the droplet thickens, h, expressed in equation 9 [24, 57], the authors calculated B values in order of 300 - 2000, exceeding the critical Marangoni number of $B_c = 80$, above which BM instabilities are induced, *i.e.* the surface tension gradient force is much greater the viscous drag and the rate of heat diffusion [30].

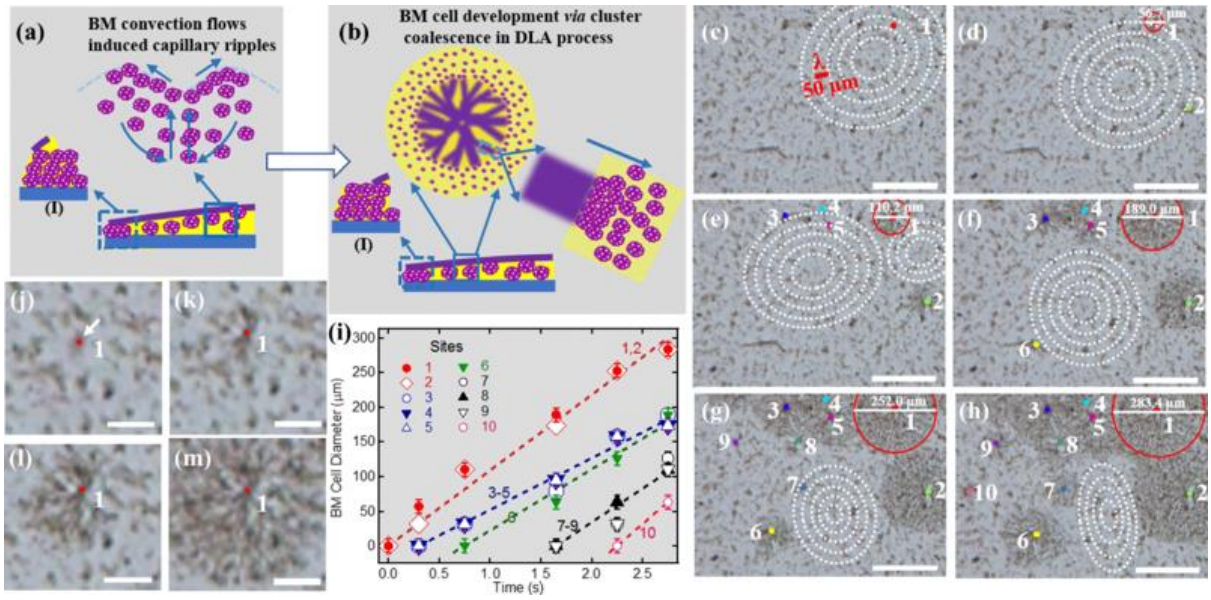

Figure 2. Schematic images of capillary ripples and following BM cell development via cluster coalescence (a), (b), and a series of images (c)–(h) extracted from a video at time sequence of 0, 0.3, 0.75, 1.65, 2.25, and 2.7 s respectively: (a) BM convection flows induced capillary ripples (schematically); (b) BM cell formation *via* cluster coalescence in DLA process; (i) the diameter of BM cells at ten site as a function of time, with the growth of the BM cell at site 1 highlighted with red circles from (b) to (f) as an example; and (j)–(m) the magnified images of site 1 in (c), (d), (e), (f), respectively. For the video microscopy experiment, a 100-μL droplet containing 1 mg/mL ZnO nanoparticles was dropped on the glass coverslip (1 mm × 1 mm). The scale bars are 200 μm in (c)–(h) and 50 μm in (j)–(m). Reprinted with permission from Ref. [40], Copyright (2019) by the American Physical Society.

Further evaporation and crystallisation

As the evaporation proceeds, the dendritic morphologies of gel-like residual patterns are preserved, making the constituent fibres well defined. It is believed that the spatial alteration of iZMCs within the clusters is facilitated by solvent molecules, which leads to the formation of multi-layered crystallites with square packing. This self-assembly based, evaporation-driven nucleation in transient aggregates considerably reduces the nucleation barrier, and crystallite formation happens in a near spinodal regime [64], with many crystals forming at once, leading to the polycrystalline structure in the solvated filaments. The ultimate reorganisation of the iZMCs to a lower energy configuration exhibited by multi-layered crystallites with hexagonal packing is subject to the final solvent removal [40].

There is a very interesting hypothesis about the role of water molecules in the dissolution of ZnO nanocrystals and subsequent formation of hierarchical residual surface patterns. The moisture assisted dissolution of ZnO has been identified as a key step. Water is characterised by its high permittivity of ~80 at room temperature [65], which means that water molecules reduce the electric field between charges by the factor of ~80 when compared to the vacuum. Therefore, the presence of water molecules absorbed from air during evaporation of ZnO nanofluid may reduce the energy required for the dissolution to happen. Especially, as it has been shown that relative humidity greater than 45 - 60 % is needed to produce residual surface patterns from ZnO nanofluid without undissolved ZnO crystals [37, 39]. It is emphasised that this hypothesis would be very interesting to validate with further experimental and theoretical efforts, should resources for these to be found.

Thermal conversion to porous fibres

In the previous work, Wu *et al.* also observed that the zinc hydroxide fibres composing the residual pattern formed from evaporation of ZnO nanofluid undergo further chemical and morphological transformation upon thermal annealing into nanoporous ZnO fibres (**Figure 3**) [37]. The fibres in the residual surface patterns annealed at 100 and 250 °C were made of ZnO nanocrystals of 4 - 7 nm in size, while for the residues annealed at 550 °C ZnO nanocrystals composing the fibres were 20 - 70 nm (**Figure 3**c-d). Thermogravimetry analysis of the residual patterns performed in a flowing air atmosphere (**Figure 3**e) showed a 30 % weight loss in the temperature range 25 - 93 °C due to

evaporation of isobutylamine. A further 32.8 % weight loss in the temperature between 93 - 250 °C was attributed to the removal of the physiosorbed water intercalated between zinc hydroxide nanocrystal layers and the final weight loss of 3.7 % to the elimination of chemically bound water.

The authors suggested that the rearrangement and realignment of the nanocrystals, together with smaller ZnO nanocrystals sintering into larger ones, were promoted by the elevated annealing temperature. As a result, the fibrous structure become increasingly porous due to the pore size increasing with the heat treatment temperature. The three-dimensional network of the residual surface patterns is preserved after the annealing process and its structural integrity can be attributed to multiple contact points between nanoparticles within the network, stabilising the structure.

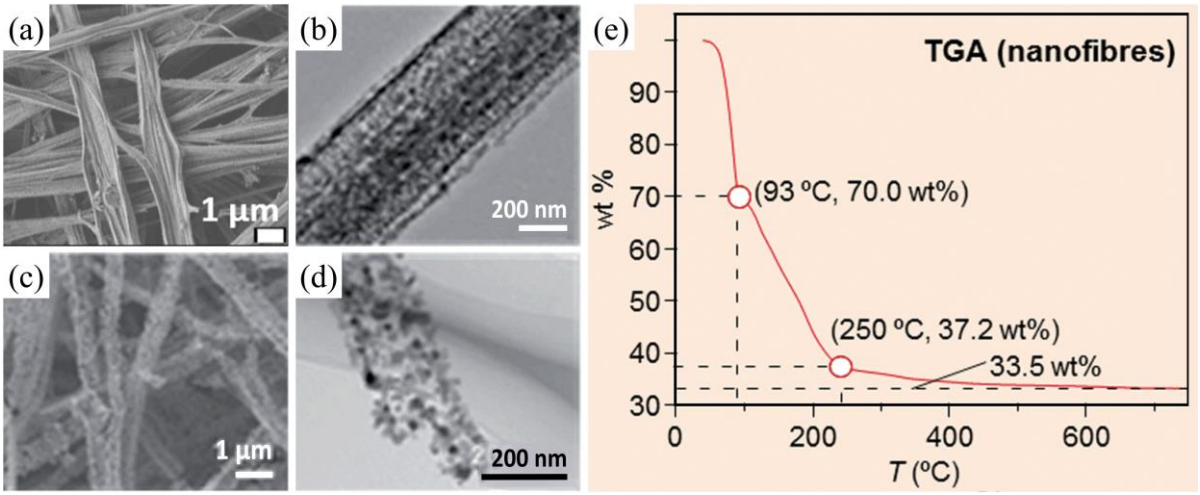

Figure 3. (a) SEM image of the residual pattern formed after drying of 1 mg/mL ZnO suspension in a mixture of cyclohexane and isobutylamine in a ratio 5 : 1 on a glass coverslip, (b) TEM image of a fibre composing the residue, (c) SEM image of the residual pattern calcinated at 550 °C, (d) TEM image of an individual fibre after calcination, (e) thermogravimetry analysis (TGA) curve for the fibres. Adapted from Ref. [37] and its Supplementary Information with permission from the Royal Society of Chemistry.

EXAMPLES OF REACTIVE DEPOSITION OF NANOPARTICLES

Even though the field of evaporation induced self-assembly has been under extensive development since the first elucidation of the coffee ring around two decades ago [14-15, 66], the process of creating hierarchical fibrous surface structures from evaporation of reactive nanofluids has not received much

attention outside of my research group [37, 39-42]. Some researches produced similarly looking zinc hydroxide nanostrands, however thorough a 30 min synthesis of aqueous solution of aminoethanol and zinc nitrate rather than evaporation [44-45]. Similar syntheses of different nanostrands have also been demonstrated for cadmium [47, 67-68], copper [48, 69], and manganese [51] hydroxides.

A study by Elbahri *et al.* demonstrated an interesting approach to the fabrication of hierarchical nanostructures from droplets using the Leidenfrost effect [70]. When a liquid droplet comes in contact with a substrate at a temperate much higher than the boiling point of the liquid, the bottom region of the droplet will immediately evaporate, and the droplet will levitate above its own vapour, which reduces friction between the droplet and the substrate. This levitating droplet is called a Leidenfrost drop. The researchers used the reduced friction of the Leidenfrost droplet to deliver materials while the droplet moved over the surface, schematically presented in **Figure 4**a-c. A dispersion of the desired material powder in water was placed on a substrate at a temperature of 230 °C, left for 5 seconds, and then the substrate was tilted by 30° so the droplet could slide across the substrate, depositing wires or cluster chains of the material. **Figure 4**d-e shows such chains produced from a running droplet loaded with commercially available ZnO powder.

Elbahri *et al.* also realised that the high temperature, nonequilibrium zone underneath the droplet could be used as a chemical reactor to produce nanoparticles directly from solution [70]. In addition to silver wires produced by reacting a solution of $AgNO_3$ at 180 °C, nanocluster chains of zinc oxide (**Figure 4**f) were formed by the thermal decomposition of zinc acetate at 280 °C. (The thermal decomposition of zinc acetate is a common technique used to seed various substrates with ZnO nanostructures to promote a synthesis of ZnO nanorods *via* hydrothermal methods [71-75].) Nanoparticles can also be arranged into concentric rings with the Leidenfrost structuring under certain conditions. Upon impact of a droplet with a substrate at the Leidenfrost temperature, a droplet explosion takes place creating smaller droplets, resulting in a formation of rings (**Figure 4**g-i) [70].

However, the work by Elbahri *et al.* discussed the formation of hierarchal surface patterns by direct deposition of *inert* particles from Leidenfrost droplets or producing zinc oxide nanostructures in a reaction of zinc acetate solution rather than using *reactive* ZnO nanoparticles as precursors for fibrous zinc hydroxide structures as in the work presented in this thesis.

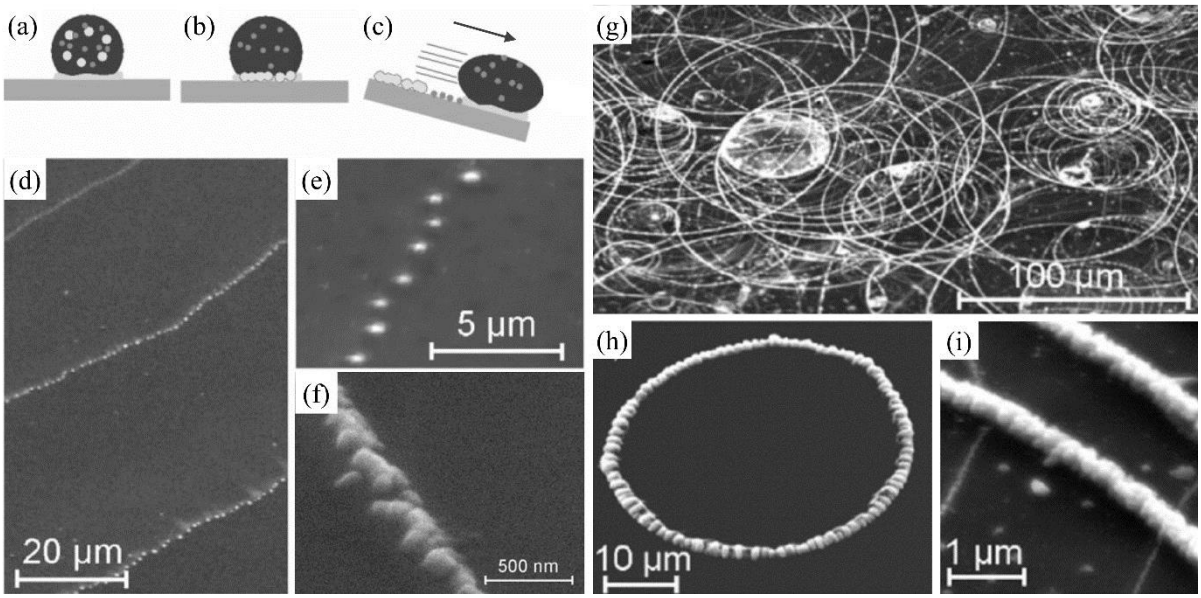

Figure 4. Deposition of nanoparticles. (a) Schematic of a nanofluid droplet levitating on its own vapour at the Leiden frost temperature. (b) Deposition form a Leidenfrost droplet. (c) Delivering particles in lines due to the anti-Lotus effect on a tilted substrate. (d-e) Deposited ZnO nano/microparticles from a suspension at the Leidenfrost temperature. (f) Nanocluster chain of ZnO formed by reacting a solution of zinc acetate at 280 °C. (g) Rings consisting of ZnO nanorods produced from a drop loaded with zinc acetate impacting with the substrate. (h-i) The resulting wires are composed of a dense assembly of rods. Adapted with permission from Ref. [70], Copyright (2019) by John Wiley and Sons.

TECHNIQUES

This section briefly describes the principles of the main techniques used in the thesis including the assumptions and limitations that are relevant to the work presented in the subsequent chapters. Some portion of the following text are reproduced from related Supporting Information sections of the published manuscripts.

X-ray diffraction

X-ray diffraction (XRD) is a powerful technique that allows for non-destructive study of crystalline materials. Due to its sensitivity to periodic arrangement of atoms, it is widely employed for determination of unknown structures or making measurements of structural parameters [76]. When a beam of X-rays impinges upon the sample, the photons are elastically scattered in all directions by

the electron shells of the atoms present in the sample. If the atoms within the sample are arranged in a periodic network, X-rays can be coherently scattered by the crystal lattice when the beam hits the structure at the angle specified by Braggs' law,

$$n\lambda = 2d \sin\theta, \tag{14}$$

where n is the order of reflection (positive integer), λ is the wavelength of incident X-ray radiation, d is the lattice spacing, and θ is the scattering angle [77]. In powder XRD, the material under investigation is in a form of powder consisted of an abundant number of crystallites. This implies a uniform representation of every possible crystalline orientation in the sample. Therefore, if the sample is scanned through a range of angles on a typical diffractometer with the Bragg-Brentano geometry, the coherent scattering can be observed as a series of peaks on a diffractogram. Careful analysis of an XRD profiles allows for phase identification, determination of lattice parameters, assessment of crystallinity, and microstructure analysis.

Each profile in the diffraction pattern is a result of the complex combination of instrumental and specimen-related effects. An instrumental profile component contribution, $g(\epsilon)$ includes instrumental-related geometrical factors such as diffraction optics and sample transparency [78]. A sample profile component, $f(\epsilon)$, is derived from the microstructure of the sample, usually referred to as the size and strain broadening due to the finite size of coherently diffracting domains (crystallites) and lattice strains caused by the presence of lattice defects (point, line or plane defects). The size of coherently diffracting domains is generally not the same as the grain size. A grain can be composed of multiple domains disoriented with respect to each other, especially in a polycrystalline aggregate. However, the crystallite size can be the same as the grain size if one considers a proper nanosized powder [79-81].

What is observed as the experimental peak profile, $h(\epsilon)$, is in fact a product of the convolution of the profile components:

$$h(\epsilon) = \int g(\eta) f(\epsilon - \eta) d\eta, \tag{15}$$

where ϵ is the angular deviation from the theoretical peak position given by Braggs' law [82]. Deconvolution of the instrumental profile, $g(\epsilon)$, from the experimentally measured profile, $h(\epsilon)$, is one of the most common procedures in the diffraction profile line analysis.

The instrumental profile can be established experimentally using an appropriate standard sample which allows for numerical or analytical deconvolution in order to find $f(\epsilon)$ [78, 82-84], or be calculated on the basis of the known instrumental and/or geometrical specification of the experiment [85]. A material must meet several requirements to qualify for the standard, namely exhibiting the absence of size-strain effects, non-toxicity, easy of availability in appropriate quantities, and the presence of strong, well separated XRD peaks [82]. It was proposed by Warren and Averbach [86-87] that the instrumental profile could be obtained using a perfectly crystalline sample of the material under investigation as a standard. In fact, it has become a common method to apply an annealing treatment to the studied material in order to reduce the density of defects and increase the crystallite size, making it suitable for the Warren and Averbach approach of obtaining the instrumental component [88-90]. On the other hand, this is usually suitable only for semi-qualitative analysis. Amongst the most popular standards for obtaining the instrumental profile or for equipment calibration are commercially available reference materials such as LaB_6 (SRM 660c), silicon powder (SRM 640e), or alumina discs (SRM 1976b), provided by the National Institute of Standards and Technology (Gaithersburg, Maryland, United States) [91].

Several key elements providing information about the crystals in the material can be distinguished in the XRD profile: maximum peak intensity, peak position, and the width of the peak. The peak position is determined by the dimensions of the unit cell of the crystal. This in turn imposes conditions for constructive interference from crystal lattice planes at particular angles (Braggs' law, equation 14). With this information, interplanar spacing and atoms positions can be calculated. The peak intensity depends on the abundance of the reflecting phase in the sample. Therefore, it can be used to establish the absolute or relative amount of individual phases in an analysed mixture. If no phase is present, the disruption of the long-range order due to amorphisation will result in reducing in maximum intensity of the peak [92]. The broadening of the peak is often described as the full width at the half maximum (FWHM) of the peak or as the integral breath (IB), with the latter defined as the ratio between peak area and peak intensity [80].

The field of diffraction profile analysis methods has evolved shortly after the first X-ray crystal diffraction experiment by Walter Friedrich, Paul Knipping and Max von Laue in 1912 [93]. The first

methods were based on the profile line broadening and are therefore often referred to as traditional integral breath methods. The formula proposed by Scherrer (equation 16) assumes that the line broadening is only due to the size effect, and that the apparent size of crystallites $\langle L \rangle_V$ is inversely proportional to the integral breath β:

$$\langle L \rangle_V = \frac{K\lambda}{\beta cos\theta} \,, \tag{16}$$

where θ is the Bragg angle, λ is the wavelength of the radiation, β is the width of the peak (FWHM or IB), and K is the shape factor [94]. Even though the line broadening could be entirely caused by the size effects in some rare occasions, the apparent size parameter, $\langle L \rangle_V$, scarcely relates to the actual dimensions of the crystallites and is valid only if the assumptions that the formula was derived on are met [81]. One way to correlate the apparent size parameter is to use the appropriate Scherrer constant that takes into account the size-induced anisotropic line broadening [95]. However, in real polydisperse systems, crystals often have different size and shape, which is reflected in the shapes and widths of all diffraction profiles. This gives rise to the difficulties in evaluating $\langle L \rangle_V$.

The William-Hall analysis is a simplified IB method which accounts for the contribution of strain in addition to the size broadening effect. This is achieved by combing the Scherrer formula with the apparent strain equation, derived from differentiating Braggs' law [96]. The premise of this method is that the contributions to size and strain broadening (β_L and β_e, respectively) vary differently with the Bragg angle θ. With the further assumptions that the size and strain profiles are Voigtian functions, expressions involving the Gaussian (G) and Lorentzian (L) components can be further derived. The most common expressions are:

$$\beta(d^*) = \beta_L + \beta_e = \frac{1}{\langle L \rangle_V} + 2ed^* \,, \tag{17}$$

$$\beta^2(d^*) = \beta_L^2 + \beta_e^2 = \frac{1}{\langle L \rangle_V^2} + 4e^2 d^{*2} \,, \tag{18}$$

where $\beta(d^*)$ is the total integral breath in the reciprocal space, $d^* = (2\sin\theta)/\lambda$ is the reciprocal space variable (inverse of the interplanar distance), and e is an upper limit for the lattice strain. Equations 17 and 18) can be regarded as L-L and G-G, respectively. By constructing a plot of β *versus* d^* (or

β^2 *versus* d^{*2}) and determining the intercept and slope, estimated values of $\langle L \rangle_V$ and e can be obtained respectively.

The Warren-Averbach (WA) method [86-87] is based on the evaluation of the Fourier coefficients of the peak profiles. If the profiles are symmetrical, the peak intensity can be expressed as a Fourier sum, where the cosine components $A_L$are the product of the size and strain (lattice distortion) broadening components, A_L^S and A_L^D, respectively, yielding $A_L = A_L^S A_L^D$. Warren has demonstrated that the Fourier coefficients can be written as:

$$\ln A_L(\boldsymbol{q}) \simeq \ln A_L^S - 2\pi L^2 \boldsymbol{q}^2 \langle \varepsilon_{\boldsymbol{g}}^2 \rangle \ , \tag{19}$$

where L is the Fourier length, $\boldsymbol{q}$ is the diffraction vector and $\langle \varepsilon_{\boldsymbol{q}}^2 \rangle$ is the mean square strain in the direction of the diffraction vector. The measurement of the structural broadening of two or more reflections from the same crystallographic planes allows for the separation of strain and size effects under the assumption that the size effects are independent of the order of reflection, whereas the strain effects vary with that order. Finding the root mean square strain component and surface averaged crystallite size (average column length) requires appropriate substitution for $\boldsymbol{q}$ depending on the crystal unit cell type in equation 19, and constructing relevant plots to read coefficients analogously to the William-Hall method [97].

The limiting factor in the WA analysis lies in evaluating the Fourier coefficients resulting from profile overlapping especially in broad diffraction peaks produced by nanocrystalline materials. This issue can be addressed by fitting the XRD profile by analytical functions such as Voigt, pseudo-Voigt or Pearson VII functions [98]. Modelling a diffraction profile by an analytical function allows also for the inclusion of the instrumental broadening component and a background function. This method is often adopted for quick and efficient extraction of information from a diffractogram as it is easily conducted by software programs. However, it should be bore in mind that even though analytical functions can reproduce the experimental data reasonably well, this arbitrary choice can be fraught with possible artefacts caused by the limitation of possible profile shapes. In fact, experimental profiles can have any shape [80].

An introduction of the whole powder pattern fitting (WPPF) method significantly reduced the arbitrariness in the choice of the analytical peak profile function, which was a major step in the line profile analysis [78-79, 99-100]. In this method, a large portion of the diffractogram is still fitted by analytical functions, but the least square minimisation algorithm based on appropriate models of the grain shape, size distribution, and lattice defects is used to optimise the fitting procedure.

Traditional line profile analysis methods are still the most commonly used for preliminary assessment of the microstructure, as the information in terms of "average crystallite size" and "microstrain" can be easily obtained from the width of individual diffraction peaks. However, due to their limitations deriving from the elementary models of shape and size distribution of crystalline domains and crystal defects together with the arbitrariness in the separation of line-broadening effects, these methods provide only semi-qualitative information on the microstructure of the investigated material. On the other hand, the Rietveld method and the WPPM interpret the whole diffraction pattern in terms of physical models. WPPM is considered the most completed method for the line profile analysis as it combines the advantages of the Fourier approach with a parameter refinement procedure performed directly on the experimental data [101].

In Chapter 2, the crystallinity of the ZnO samples was evaluated on the basis of the coherence length L_a, which provides an indication of the lower limit of the crystal domain size [102-103]:

$$L_a = \frac{2\pi K}{\Delta q} \tag{20}$$

where K is the shape factor from the Scherrer formula [95], and Δq is the width at the half maximum of the diffraction peak expressed in the unites of the wave vector q, where $q = 4\pi \sin\theta / \lambda$. Δq was obtained by fitting peak profiles with a Gaussian function, which was an arbitrary choice. The obtained L_a values give an indication of the broadening effects caused by the finite domain size and lattice distortion, which are referred to as the sample crystallinity in Chapter 2.

Electron microscopy

One can say that "seeing is believing" or "a picture is worth a thousand words", therefore images are often invaluable when it comes to conveying information accessibly, especially in an easy to relate and understand manner. Some objects can be seen with a naked eye; however, this becomes inadequate

when one wishes to inspect matter at the microscopic scale. This can be done using optical microscopy, one of the oldest scientific techniques that has been widely used since 16th - 17th century, when first compound light microscopes were constructed [104].

An optical microscope possesses the ability of revealing the detailed features of a sample using visible light and a system of lenses. The process in which a magnified image of an object is produced can be explained using ray optics. However, when dimensions of the object under investigation get smaller and are in the range of the wavelength of visible light, *i.e.* 380 - 740 nm, one has to take into consideration the wave properties of light such as diffraction and interreference, which impose limitations on the resolving power of a microscope [105]. Ernst Abbe pioneered quantitative numerical calculations for the resolution limit of an optical microscope and derived a fundamental resolution limit based on the diffraction theory of light in 1873. The smallest distance between two adjacent points that can be resolved, d_{res}, assuming a periodic structure consisted of lines, an immersion microscope objective, and a circular aperture with direct illumination, can be expressed as

$$d_{\text{res}} = \frac{\lambda}{n \sin\alpha}, \tag{21}$$

where λ is the wavelength of the illumination light in vacuum, α is one-half of the angular aperture of the microscope objective, and n is the refraction index of the medium between the object and the microscope objective [105-106]. Based on equation 21, one can deduce that the resolution can be enhanced using an immersion fluid with a high refractive index, or by reducing the wavelength of light towards ultraviolet. For a comprehensive discussion on the resolution limit and resolution enhancing techniques in microscopy, which is beyond the scope of this work, please refer to the paper by Cremer and Masters, Ref. [105].

Electrons are charged particles that display the wave properties of an electromagnetic radiation. Therefore, it is possible to further reduce the wavelength of the radiation, λ, used to illuminate the specimen by using a beam of electrons instead of an electromagnetic radiation (visible light spectrum), which is the foundation of the electron microscopy techniques. In 1924, Louis de Broglie hypothesised that matter behaved like a wave [107]. The de Broglie wavelength associated with a massive particle can be expressed as

$$\lambda = \frac{h}{p}, \tag{22}$$

where p is the momentum of a particle and h is the Planck constant. The momentum is the product of the mass and the velocity of a particle: $p = mv$. The velocity of electrons, v, emitted by a cathode is directly related to the potential applied by the anode to the electron beam, and can be expressed as

$$v = \left(\frac{2eU}{m_0}\right)^{\frac{1}{2}}, \tag{23}$$

where m_0 is the rest mass of an electron, e is the elementary charge of an electron, and U is the accelerating voltage. Combining equations 22 - 23 gives the non-relativistic de Broglie wavelength of an electron as

$$\lambda = \frac{h}{(2m_0eU)^{\frac{1}{2}}}. \tag{24}$$

However, when the velocity of an electron becomes comparable with the velocity of light due to the high accelerating voltage applied, the expression in equation 24 has to be corrected to account for the relativistic effects and can be expressed as

$$\lambda = \frac{h}{\left[2m_0eU\left(1 + \frac{eU}{2m_0c^2}\right)\right]^{\frac{1}{2}}}, \tag{25}$$

where c is the velocity of light in vacuum [108].

As discussed above, an electron microscope profits from the much shorter wavelength of an electron, *i.e.* λ in the range of 0.004 - 0.017 nm for the accelerating voltage, U, in the range of 5 - 100 kV (calculated using equation 25), when compared to the wavelength of the visible light, *i.e.* λ in the range of 380 - 740 nm. With the increasing accelerating voltage, the wavelength of the electron decreases, which in turn increases the theoretical resolving power of an electron imaging system. The beam of electrons used for imaging is controlled through a set of electromagnetic lenses inside a vertical column. The column and the sample stage are operated under vacuum to reduce the mean free path of electrons, so there are fewer scattering events with air molecules. This imposes additional limitations on the nature of samples that can be imagined, *e.g.* they must be vacuum stable, which will be discussed in detail in later paragraphs.

When an accelerated electron hits a specimen, a plethora of different outcomes can be generated. As the beam of electrons interacts strongly with electrostatic potentials of positively charged nuclei screened by negatively charged electrons, it produces signals that can be employed to reveal topographic features, composition, crystal structure, and local electrical and magnetic fields within the specimen. These signals originate from a variety of physical processes called scattering events, and include the backscattered electrons (BSE), secondary electrons (SE), and X-rays. The scattering events can be broadly classified as inelastic and elastic scattering [109].

Inelastic scattering is a process in which the kinetic energy of an incident electron is transferred to the atoms of the specimen. As a result, the following can occur: a weakly bound outer-shell atomic electron can be ejected as a secondary electron; a tightly bounded inner shell atomic electron can be ejected, which generates emission of characteristic X-rays; a beam electron can deaccelerate in the electrical field of the atoms emitting continuous X-ray radiation called *bremsstrahlung* or breaking radiation; waves in the free electron gas that spread throughout conductive metals can be generated in the form of plasmons; phonons can be generated, which is manifested in heating of the specimen. The energy loss due to inelastic scattering dictates how far inside the specimen a beam electron can travel before it gets absorbed due to the loss of all its energy. Even though the energy is lost, beam electrons do not deviate significantly from their previous path [109].

In elastic scattering processes, where the kinetic energy of a particle is conserved, a beam electron is deflected by atomic nuclei and continues its motions along a new trajectory, deviating from its previous path. It is possible for the beam electron to undergo enough scattering events to return to the surface and exit the specimen. These electrons are denoted as backscattered electrons (BSE) and provide information on the specimen composition, topography, mass thickness, and crystallography. A backscattered electron loses a part of its initial energy, which depends on the distance travelled within the specimen [110].

The most common signals originating from the electron - specimen interactions and the electron interaction volume are schematically shown in **Figure 5**. The interaction volume in thick samples is usually pear-shaped. The volume is defined by an envelope satisfies a specific condition, *e.g.* the

electron energy has been reduced by a specific factor, or that the volume contains 95% of all incident electros [111].

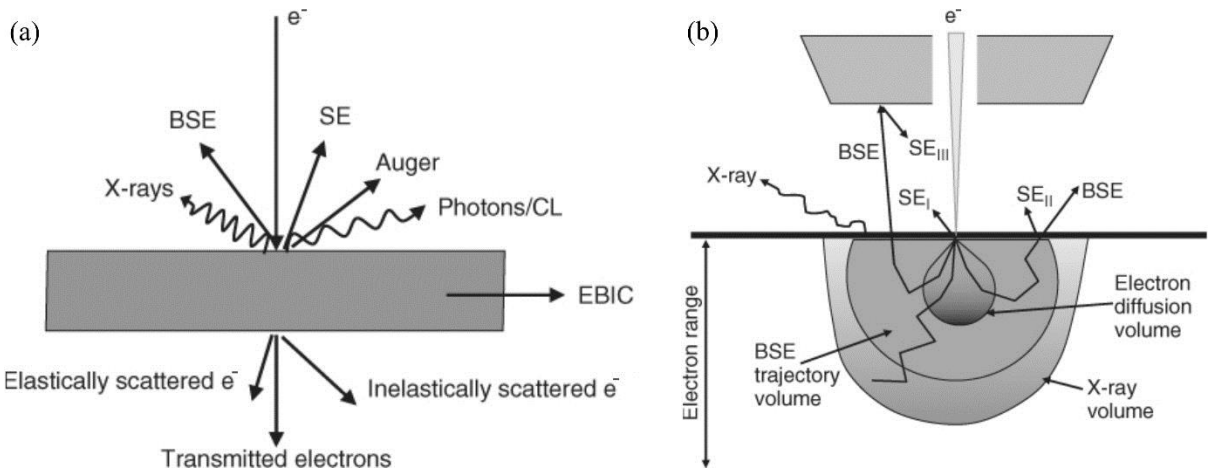

Figure 5. (a) Signals generated when an electron beam interacts with a relatively thin specimen: secondary (SE), backscatter (BSE), Auger, and transmitted electrons, X-ray emission, cathodoluminescence (CL), and electron beam induced current (EBIC). (b) A schematic diagram of the interaction volume of the primary electron beam with a specimen as well as the signal range. Adapted with permission from Ref. [112], Copyright (2019) by John Wiley and Sons.

There are two main classes of electron microscopes which differ in the type of signal used for imaging and the mode of operation. In principle, the scanning electron microscope (SEM) uses the low energy SE and elastically scattered BSE to create an image of the specimen surface with the three-dimensional appearance, while the transmission electron microscope (TEM) produces a two-dimensional projection image from electrons that passed through a thin slice of the specimen. There is also a third class of electron microscope, which combines raster scanning of SEM with imaging based on transmitted electrons as in TEM, called a scanning transmission electron microscope. The two main electron microscopy techniques that have been used in this thesis, SEM and TEM, are described in the following paragraphs.

Scanning electron microscopy

Scanning electron microscopy is a powerful method to study surface topography of different materials. In this technique, the electron beam is focused on the specimen surface, which is then scanned

across in a raster pattern. The intensity of the low energy secondary electrons (or backscattered electrons) from each point is used to produce an image, sometimes called an electron micrograph. The contrast generation mechanism is based on the topography of the surface as the SE emission from the surface is highly sensitive to the sample curvature. Due to the low energy of secondary electrons (the most probable energy of 2 - 5 eV, with the conventional limit between SE and BSE at 50 eV [113]) they are only able to escape the specimen if they are within ~10 nm away from the surface. These two factors are responsible for the high resolution of topographic information provided by the SE signal. Contrary to secondary electrons, backscattered electrons escape the surface with much higher energies and are produced within a greater interaction volume, therefore do not provide as good topographic resolution as SE. However, they are more likely to be scattered by atoms of higher atomic weight, hence can be employed to provide qualitative compositional information in heterogenous specimens [114].

Differing from the TEM that requires the specimen to be relatively small and as thin as possible (less than 1μm), the SEM can accommodate much larger specimens limited only by the size of the sample chamber without any additional sample thickness restriction. In addition to the general electron beam and vacuum stability criteria of the specimens, non-conductive samples should be coated in a thin conductive film (C, Au, Pt/Pd) to prevent charge accumulation on the specimen. Sample charging causes image distortion as the electrons trapped on the sample will repel electrons from the incoming beam [114].

While working with the scanning electron microscope, it is possible to adjust several operating conditions such as the accelerating voltage, scan speed, spot size, aperture diameter, working distance, and tilt. The accelerating voltage is usually selected between 1 - 30 kV depending on the nature of the specimen, magnification range, and image resolution required. The magnification is given by the ratio of the size of the micrograph to the size of the area scanned on the sample. The performance of the SEM in terms of magnification and resolution is limited by the beam diameter as it impacts the sample surface. To achieve a small beam diameter for high resolution work, it is necessary to use high acceleration voltages. However, this increases the penetration depth of the specimen, which subsequently leads to the loss of the surface detail and higher chances of the sample damage [114].

One of the advantages of SEM compared to the light microscopy is the increased depth of field, *i.e.* sample features above and below the actual plane of focus can be resolved clearly without losing much sharpness of the image. This is most noticeable when tilted specimens are imaged. The depth of field can be increased by using a small aperture in the objective lens or increasing the working distance. However, increasing the working distance reduces the resolution [115]. Larger beam diameters and apertures are used to increase the beam current in order to improve the signal strength in BSE imaging and X-ray analysis [114].

Another great advantage of the scanning electron microscope is the possibility to perform qualitative elemental analysis of the specimen based on the characteristic X-rays emitted due to inelastic scattering of beam electrons with the sample atoms, called energy dispersive X-ray spectroscopy (EDX). When an inner shell atomic electron is ejected creating an electron hole, the electron from an outer, higher-energy shell fills the hole, and the difference in energy between the higher and lower energetic states may be released in the form of an X-ray. These differences are dependent on the atomic number, hence allowing for the elemental analysis. However, due to the larger electron interaction volume that the X-rays are emitted from within the specimen, as produced elemental maps have lower resolutions than the corresponding SEM micrographs [109, 114].

Transmission electron microscopy

The transmission electron microscope is regarded as an essential and powerful tool for biological and material science as it can produce images of materials under investigation with a magnification in the range of 10^3 - 10^6 in addition to electron diffraction patterns for crystal structure analysis. In principle, the TEM system is composed of an electron gun and a set of electromagnetic lenses, which are stacked in a column. In the conventional TEM mode operation, an electron beam emerging from the electron gun at the top of the microscope column is condensed into a parallel beam at the sample level by the condenser lens system. Then, the electrons that passed through the specimen are collected and focused by the objective lens. A magnified real image of the sample is projected onto an imaging device, *i.e.* a fluorescent screen, a photographic film, or a scintillator coupled to a charge-coupled device camera, at the bottom of the column [116].

The image in the TEM is produced from the electrons that passed through a specimen. This imposes additional conditions on the specimen electron transparency, which can be tuned by changing the energy of the incident electrons and the thickness of the specimen. In general, a TEM specimen should be very thin, usually in the range of 10 nm to 1 μm. Therefore, the sample preparation step for bulk materials can be challenging and time consuming, though nanosized materials are typically electron-transparent and do not require additional sample preparation [117].

The two main factors limiting the resolution in the TEM are chromatic and achromatic (spherical) aberrations, as it is difficult to compensate for them in electron optical systems. These aberrations are responsible for the electron beam being focused on different positions along the optical axis. This is due to the differences in the energy of the electrons for chromatic aberration, and the differences in the distance that electrons travelled in the case of achromatic aberration. Monochromatic sources can be used to negate chromatic aberration; however, the electrons transmitted through the specimen will have a spread of energy as a result of inelastic scattering interactions. The number of inelastic scattering events can be reduced by using thinner samples and higher accelerating voltages. Achromatic aberration can be diminished by selecting electrons close to the optical axis, which is regulated by the objective aperture. Using a smaller objective aperture also increases the contrast of the image by preventing electrons scattered at large angles from contributing to the image. On the other hand, this reduces the theoretical resolution of the TEM [114].

In the standard TEM operation mode, an objective aperture is centred around the optical axis. The diameter of the aperture controls the number of the electrons that contribute to the image formation. If the electrons pass through a region with no specimen, they remain unscattered so the corresponding image appears bright in relation to the specimen. This is referred as a brightfield imaging. The three main mechanisms responsible for contrast in TEM images are mass/thickness, diffraction, and phase contrast. Thicker areas of the specimen scatter a higher fraction of the incident electron, therefore corresponding areas in the image appear dark. Due to the increased number of elastic scattering events within the higher atomic number regions, these also appear darker than their surroundings. These two effects are often taken together and described as mass-thickness contrast [114, 116].

If the specimen contains crystalline regions, then the electrons can be diffracted according to Braggs' law (equation 14) based on the crystal orientation. As a result, strongly diffracting areas will appear dark on the image. Instead of showing the spatial variation in the intensity of the transmitted electrons, it is possible to record the angular variation in intensity, referred to as a diffraction pattern [117]. This is done by adjusting the magnetic lenses so that the back focal plane of the lens instead of the imaging plane is magnified and projected. A diffraction pattern for a single crystal contains sharp spots, which correspond to the satisfied diffraction condition for the crystal structure of the specimen. In case of a polycrystalline specimen, the diffraction pattern consists of a series of rings [118].

Phase contrast is a consequence of electrons of different phases going through the objective aperture and contributing to the image formation. Even though it is not possible to measure the phase directly, it causes observable interference between electron waves that have passed through different regions of the specimen. These electrons can be gathered when a TEM image is defocused. Because a large portion of scattering events causes a change in phase, it is likely to have some phase contrast in most of TEM images [114, 116].

The main operating conditions of the transmission electron microscope are the accelerating voltage and objective aperture size. Selecting a set of optimal conditions is often a compromise between contrast and resolution, depending highly on the nature of the specimen under investigation. By increasing the acceleration voltage, it is possible to achieve better resolution (shorter electron wavelength), increased specimen penetration, reduced image contrast, and reduced specimen damage. Increasing the objective aperture size is responsible for obtaining better theoretical resolution, reduced contrast, and increased spherical (achromatic) aberration [114].

The transmission electron microscopy is an indispensable tool for the investigation of nanomaterials. In addition to the internal structure and crystallographic information, it can also provide data on chemical composition of the specimen using X-ray energy dispersive spectroscopy or electron energy loss spectroscopy (EELS). One of the sought features of the TEM is the ability to perform various experiments *in situ* while recording microstructural changes, making it a versatile laboratory for the study on nucleation, growth, and behaviour of nanostructures. Even though there are other methods outperforming TEM with respect to the spatial and energy resolutions for imaging and

spectroscopy, the main advantage of the TEM is being able to execute imaging, diffraction, and spectroscopy on the same small region of the sample [117].

Contact angle

The chemical composition of a substrate's surface governs the chemical reactions and processes that happen on the surface layer, playing a fundamental role in various phenomena occurring in nature and many industrial technologies [119]. Wettability, and directly related to it, the surface free energy, of a solid, can be investigated by measuring the angle that is created by a given liquid drop resting on a flat, horizontal solid surface [120]. The Young equation [121] describes the balance at the three-phase contact line, which is the intersection of the solid-liquid, solid-vapor, and liquid-vapor interfaces (**Figure 6**), based on the assumptions that the surface is chemically homogenous and topographically smooth. The Young equation can be expressed as follows

$$\gamma_{SV} = \gamma_{SL} + \gamma_{LV} \cos \Theta, \tag{26}$$

where γ_{SL}, γ_{SV}, and γ_{LV} are the interfacial free energies at the solid-liquid, solid-vapor, and liquid-vapor interfaces, respectively, and Θ is the contact angle, which is often called the Young contact angle.

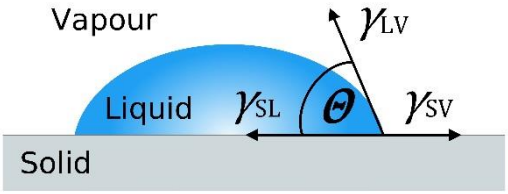

Figure 6. Illustration of the contact angle, Θ, formed by a sessile liquid drop on a solid surface and the interfacial free energies (tensions) at the three-phase boundary: γ_{SL}, γ_{SV}, and γ_{LV} for solid-liquid, solid-vapour, and liquid-vapour interfaces, respectively.

The contact angle, Θ, and the interfacial free energy at the liquid-vapor interface (liquid surface tension), γ_{LV}, can be easily measured experimentally in contrast to the SFE of a solid, γ_{SV}, which cannot be measured directly. Therefore, further assumptions about the relation between γ_{SL}, γ_{SV}, and γ_{LV} must

be made to solve the Young equation (eq 26). The physical interpretation of these assumptions forms a base for derivation of different methods for calculating the SFE [122].

Before proceeding to the SFE theories, several concepts have to be introduced first. Thermodynamic adhesion can be defined as the reversible work required to separate two phases initially in contact to a distance at which they no longer interact. The equation for the work of adhesion, W_{A}, can be expressed as

$$W_A = \gamma_A + \gamma_B - \gamma_{AB}, \tag{27}$$

where γ_{A} and γ_{B} are surface free energies of phases A and B, respectively, and γ_{AB} is the interfacial energy between these two phases. Thus, if one considers the solid and liquid phases, the solid-liquid work of adhesion [123] can be written as

$$W_{SL} = \gamma_{SV} + \gamma_{LV} - \gamma_{SL}. \tag{28}$$

This is derived under the assumption that the excess vapor adsorbed on the surface is negligible due to the low enough vapor pressure of the liquid, and that the plastic deformation of the surface upon separating solid and liquid phases is negligible due to the high enough stiffens of the solid [124]. The work of adhesion (eq 27) can be rewritten to determine the work of cohesion W_{C}, when the two phases are identical and no interface is present [125], expressed as

$$W_C = \gamma_A + \gamma_A - 0 = 2\gamma_A. \tag{29}$$

Thus, the work of cohesion when the respective phases are both solids, W_{SS}, and liquids, W_{LL}, can be written as

$$W_{SS} = 2\gamma_{SV}, \text{ and} \tag{30}$$

$$W_{LL} = 2\gamma_{LV}. \tag{31}$$

According to Żenkiewicz [122], Berthelot conceived the idea at the end of the 19$^{\mathrm{th}}$ century that the work of adhesion between the solid and liquid phases (interfacial adhesion work), W_{SL}, could be assumed to be equal to the geometric mean of the cohesion work of a solid, W_{SS}, and the cohesion work of a measuring liquid, W_{LL}, expressed as

$$W_{SL} = \sqrt{W_{SS} W_{LL}}. \tag{32}$$

By combining equations 28 and 30 - 32, Berthelot formulated a hypothesis, which was later named after him, in the form of the following equation

$$\gamma_{SL} = \gamma_{SV} + \gamma_{LV} - 2\sqrt{\gamma_{SV}\gamma_{LV}}. \quad (33)$$

The Berthelot hypothesis (eq 33) has been successfully used as the principle for deriving further semi-empirical analytical models dedicated to calculating the SFE of a solid, γ_{SV}, from contact angle measurements. The list includes models such as Neumann [126], Fowkes [127-129], Owens-Wendt [130] (or Owens-Wendt-Rabel-Kaelble [130-132]), van Oss-Chaudhury-Good [133], and Zisman [134] among others. At this point, it is worth mentioning that the calculated SFE value of a solid depends on the liquids chosen for contact angle measurements and which model is used for the data analysis [135].

Based on the further assumption that the SFE corresponding to the solid-liquid interface, γ_{SL}, depends on different interfacial interactions governed by the properties of both, the surface layer of the studied solid and the measuring liquid, Fowkes [127-129] proposed that the SFE of a solid, γ_{SV}, (and of

a liquid, γ_{LV}) is a sum of independent components related to these specific interactions

$$\gamma_{SV} = \gamma_{SV}^{D} + \gamma_{SV}^{P} + \gamma_{SV}^{H} + \gamma_{SV}^{I} + \gamma_{SV}^{AB} + \gamma_{SV}^{O}, \quad (34)$$

where $\gamma_{\mathrm{SV}}^{\mathrm{D}}$, $\gamma_{\mathrm{SV}}^{\mathrm{P}}$, $\gamma_{\mathrm{SV}}^{\mathrm{H}}$, $\gamma_{\mathrm{SV}}^{\mathrm{I}}$, and $\gamma_{\mathrm{SV}}^{\mathrm{AB}}$ are the dispersion, polar, hydrogen bonding, induction, and acid-base components, while $\gamma_{\mathrm{SV}}^{\mathrm{O}}$ refers to the all remaining interactions. By analogy, the same equation can be written for the SFE of a liquid, γ_{LV}. In his considerations, Fowkes related the dispersion component of the SFE, $\gamma_{\mathrm{SV}}^{\mathrm{D}}$, to the London interactions, arising from the correlated fluctuations of the electrons in interacting molecules. Remaining van der Waals interactions (Keesom and Debey) were considered as a part of induction interactions [122]. Fowkes focused his studies on systems exhibiting the dispersion interactions only, thus determined the SFE corresponding to the solid-liquid interface as

$$\gamma_{SL} = \gamma_{SV} + \gamma_{LV} - 2\sqrt{\gamma_{SV}^{D}\,\gamma_{LV}^{D}}\,. \quad (35)$$

Owens and Wendt [130] derived from the Fowkes idea and assumed that the sum of all of the SFE components related to different interactions except $\gamma_{\mathrm{SV}}^{\mathrm{D}}$ in eq 34 can be attributed to the polar interaction, $\gamma_{\mathrm{SV}}^{\mathrm{P}}$, developing a two component model of the SFE expressed as

$$\gamma_{SL} = \gamma_{SV} + \gamma_{LV} - 2\left(\sqrt{\gamma_{SV}^{D}\,\gamma_{LV}^{D}} + \sqrt{\gamma_{SV}^{P}\,\gamma_{LV}^{P}}\right). \quad (36)$$

In the Owens-Wendt model, the dispersive component is related to the van der Waals and other non-site specific interactions, while the polar component accounts for dipole-dipole, dipole-induced dipole, hydrogen bonding, and other site-specific interactions that a solid is capable of heaving with a measuring liquid [135]. The polar interaction definition by Owens and Wendt is different from the one by Fowkes, thus the meanings of $\gamma_{\mathrm{SV}}^{\mathrm{P}}$ and $\gamma_{\mathrm{LV}}^{\mathrm{P}}$ in equations 34 and 36 are different [122].

A computationally convenient form of the Owens-Wendt model can be derived by combining equations 26 (the Young equation) and 36, and then bringing the result into a linear form of $y = mx + b$, where m is the gradient and b is the intercept, which leads to the following relationship

$$\frac{\gamma_{LV}(1 + cos\,\Theta)}{2\sqrt{\gamma_{LV}^{D}}} = \sqrt{\gamma_{SV}^{P}}\sqrt{\frac{\gamma_{LV}^{P}}{\gamma_{LV}^{D}}} + \sqrt{\gamma_{SV}^{D}}\,, \quad (37)$$

where the linear components of the line, $y = mx + b$, are expressed as

$$y = \frac{\gamma_{LV}(1 + cos\,\Theta)}{2\sqrt{\gamma_{LV}^{D}}}, \quad (38)$$

$$m = \sqrt{\gamma_{SV}^{P}}\,, \quad (39)$$

$$x = \sqrt{\frac{\gamma_{LV}^{P}}{\gamma_{LV}^{D}}}, \quad \text{and} \quad (40)$$

$$b = \sqrt{\gamma_{SV}^{D}}\,. \quad (41)$$

There are two unknown variables in eq 37, $\gamma_{\mathrm{SV}}^{\mathrm{P}}$ and $\gamma_{\mathrm{SV}}^{\mathrm{D}}$, therefore the contact angle has to be measured using at least two measurement liquids, preferably one with a dominant polar component and the other one with a dominant dispersive component, *e.g.* water and diiodomethane, to determine the SFE of a solid [122]. By plotting the contact angle data for a series of measurement liquids with known values of dispersive and polar components of the SFE on a solid, and then fitting the data with a best line fit, it is possible to determine both, polar ($\gamma_{\mathrm{SV}}^{\mathrm{P}}$) and dispersive ($\gamma_{\mathrm{SV}}^{\mathrm{D}}$) components of the SFE of the

solid using the equations given above. The polar component, γ_{SV}^{P}, is calculated from the slope, m, using eq 39 and the dispersive component, γ_{SV}^{D}, from the intercept, b, using eq 41.

In this work, the wettability of the substrates was characterized using sessile droplet static contact angle measurements of various probing liquids such as *Milli-Q* water, diiodomethane, ethylene glycol, n-hexadecane, n-dodecane, cyclohexane, and a mixture of cyclohexane and isobutylamine in a 5:1 volume ratio, in addition to ZnO nano/microfluids prepared from the in-house synthesized ZnO nanoparticles and commercially acquired ZnO nanopowder and ZnO powder dispersed in the cyclohexane and isobutylamine mixture. The measurements were performed using the state-of-the-art Drop Shape Analyzer – DSA100 (KRÜSS) operated with the KRÜSS ADVANCE 1.9.0.8 software.

One could argue that performing dynamic contact angle measurements, *i.e.* recording advancing and receding contact angles of different liquids on the tested substrates, would be a better experimental approach as it provides a more meaningful characteristic of the surface properties [136-137]. On the other hand, static contact angles can provide a significant insight into the wettability of a given substrate on the assumption that the contact angle hysteresis is low. In general, further contact angle hysteresis would offer different understandings on *e.g.* surface roughness and inhomogeneity [138].

The surface free energies (SFEs) of the substrates were calculated according to the previously described Owens-Wendt method [130], which separates the SFE into two components, polar and dispersive. The results are thoroughly discussed in Chapter 4, but the key point is that a subtle difference in the polar components of the surface energies of the different substrates (glass, silicon, and hydrophilised silicon), were identified. One could further decompose the polar components of the surface free energy into the acid and base contributions using the van Oss-Good-Chaudhury method [133]. However, taking under consideration the uncertainties associated with the contact angle measurements even with the state-of-the-art instrumentation and the fact that the surface chemistry of these substrates is not immensely different, further decomposition of the surface free energy components was not performed.

REFERENCES

1. Whitesides, G. M.; Grzybowski, B., Self-Assembly at All Scales. *Science* **2002,** *295* (5564), 2418-2421.

2. Han, W.; Lin, Z., Learning from "Coffee Rings": Ordered Structures Enabled by Controlled Evaporative Self-Assembly. *Angew. Chem. Int. Ed.* **2012,** *51* (7), 1534-1546.

3. Zhong, X.; Crivoi, A.; Duan, F., Sessile nanofluid droplet drying. *Adv. Colloid Interface Sci.* **2015,** *217*, 13-30.

4. Xu, Z.; Wang, L.; Fang, F.; Fu, Y.; Yin, Z., A Review on Colloidal Self-Assembly and their Applications. *Current Nanoscience* **2016,** *12* (6), 725-746.

5. Dinh, N. T.; Sowade, E.; Blaudeck, T.; Hermann, S.; Rodriguez, R. D.; Zahn, D. R. T.; Schulz, S. E.; Baumann, R. R.; Kanoun, O., High-resolution inkjet printing of conductive carbon nanotube twin lines utilizing evaporation-driven self-assembly. *Carbon* **2016,** *96*, 382-393.

6. Janowska, I., Evaporation-induced self-assembling of few-layer graphene into a fractal-like conductive macro-network with a reduction of percolation threshold. *Phys. Chem. Chem. Phys.* **2015,** *17* (12), 7634-7638.

7. Shim, J.; Yun, J. M.; Yun, T.; Kim, P.; Lee, K. E.; Lee, W. J.; Ryoo, R.; Pine, D. J.; Yi, G.-R.; Kim, S. O., Two-Minute Assembly of Pristine Large-Area Graphene Based Films. *Nano Lett.* **2014,** *14* (3), 1388-1393.

8. Dugas, V.; Broutin, J.; Souteyrand, E., Droplet Evaporation Study Applied to DNA Chip Manufacturing. *Langmuir* **2005,** *21* (20), 9130-9136.

9. Cheng, W.; Niederberger, M., Evaporation-Induced Self-Assembly of Ultrathin Tungsten Oxide Nanowires over a Large Scale for Ultraviolet Photodetector. *Langmuir* **2016,** *32* (10), 2474-2481.

10. Mitome, T.; Hirota, Y.; Uchida, Y.; Nishiyama, N., Porous structure and pore size control of mesoporous carbons using a combination of a soft-templating method and a solvent evaporation technique. *Colloids Surf., A* **2016,** *494*, 180-185.

11. Uchiyama, H.; Sasaki, R.; Kozuka, H., Evaporation-driven self-organization of photoluminescent organic dye-doped silica-poly(vinylpyrrolidone) hybrid films prepared by low-speed dip-coating. *Colloids Surf., A* **2014,** *453*, 1-6.

12. Thokchom, A. K.; Swaminathan, R.; Singh, A., Fluid Flow and Particle Dynamics Inside an Evaporating Droplet Containing Live Bacteria Displaying Chemotaxis. *Langmuir* **2014,** *30* (41), 12144-12153.

13. Deegan, R. D., Pattern formation in drying drops. *Phys. Rev. E* **2000,** *61* (1), 475-485.

14. Deegan, R. D.; Bakajin, O.; Dupont, T. F.; Huber, G.; Nagel, S. R.; Witten, T. A., Capillary flow as the cause of ring stains from dried liquid drops. *Nature* **1997,** *389* (6653), 827-829.

15. Deegan, R. D.; Bakajin, O.; Dupont, T. F.; Huber, G.; Nagel, S. R.; Witten, T. A., Contact line deposits in an evaporating drop. *Phys. Rev. E* **2000,** *62* (1), 756-765.

16. Hu, H.; Larson, R. G., Marangoni Effect Reverses Coffee-Ring Depositions. *J. Phys. Chem. B* **2006,** *110* (14), 7090-7094.

17. Yunker, P. J.; Still, T.; Lohr, M. A.; Yodh, A. G., Suppression of the coffee-ring effect by shape-dependent capillary interactions. *Nature* **2011,** *476* (7360), 308-311.

18. Getling, A. V.; Brausch, O., Cellular flow patterns and their evolutionary scenarios in three-dimensional Rayleigh-Bénard convection. *Phys. Rev. E* **2003,** *67* (4), 046313.

19. Nguyen, V. X.; Stebe, K. J., Patterning of Small Particles by a Surfactant-Enhanced Marangoni-Bénard Instability. *Phys. Rev. Lett.* **2002,** *88* (16), 164501.

20. Truskett, V. N.; Stebe, K. J., Influence of Surfactants on an Evaporating Drop: Fluorescence Images and Particle Deposition Patterns. *Langmuir* **2003,** *19* (20), 8271-8279.

21. Maillard, M.; Motte, L.; Pileni, M. P., Rings and Hexagons Made of Nanocrystals. *Adv. Mater.* **2001,** *13* (3), 200-204.

22. Maillard, M.; Motte, L.; Ngo, A. T.; Pileni, M. P., Rings and Hexagons Made of Nanocrystals: A Marangoni Effect. *J. Phys. Chem. B* **2000,** *104* (50), 11871-11877.

23. Block, M. J., Surface Tension as the Cause of Bénard Cells and Surface Deformation in a Liquid Film. *Nature* **1956,** *178*, 650.

24. Pearson, J. R. A., On convection cells induced by surface tension. *J. Fluid Mech.* **1958,** *4* (5), 489-500.

25. Bassou, N.; Rharbi, Y., Role of Bénard−Marangoni Instabilities during Solvent Evaporation in Polymer Surface Corrugations. *Langmuir* **2009,** *25* (1), 624-632.

26. Uchiyama, H.; Matsui, T.; Kozuka, H., Spontaneous Pattern Formation Induced by Bénard–Marangoni Convection for Sol–Gel-Derived Titania Dip-Coating Films: Effect of Co-solvents with a High Surface Tension and Low Volatility. *Langmuir* **2015,** *31* (45), 12497-12504.

27. Sakurai, S.; Furukawa, C.; Okutsu, A.; Miyoshi, A.; Nomura, S., Control of mesh pattern of surface corrugation via rate of solvent evaporation in solution casting of polymer film in the presence of convection. *Polymer* **2002,** *43* (11), 3359-3364.

28. Wang, H.; Wang, Z.; Huang, L.; Mitra, A.; Yan, Y., Surface Patterned Porous Films by Convection-Assisted Dynamic Self-Assembly of Zeolite Nanoparticles. *Langmuir* **2001,** *17* (9), 2572-2574.

29. Mutabazi, I.; Wesfreid, J. E.; Guyon, E., *Dynamics of Spatio-Temporal Cellular Structures: Henri Bénard Centenary Review*. Springer-Verlag New York: New York, 2006; Vol. 207.

30. Maroto, J. A.; Pérez-Muñuzuri, V.; Romero-Cano, M. S., Introductory analysis of Bénard–Marangoni convection. *European Journal of Physics* **2007,** *28* (2), 311.

31. Bénard, H., Étude expérimentale des courants de convection dans une nappe liquide. — Régime permanent : tourbillons cellulaires. *J. Phys. Theor. Appl.* **1900,** *9* (1), 513-524.

32. Pauliac-Vaujour, E.; Stannard, A.; Martin, C. P.; Blunt, M. O.; Notingher, I.; Moriarty, P. J.; Vancea, I.; Thiele, U., Fingering Instabilities in Dewetting Nanofluids. *Phys. Rev. Lett.* **2008,** *100* (17), 176102.

33. Homsy, G. M., Viscous Fingering in Porous Media. *Annu. Rev. Fluid Mech.* **1987,** *19*, 271-311.

34. Ajaev, V. S., Evolution of dry patches in evaporating liquid films. *Phys. Rev. E* **2005,** *72* (3), 031605.

35. Huang, J.; Kim, F.; Tao, A. R.; Connor, S.; Yang, P., Spontaneous formation of nanoparticle stripe patterns through dewetting. *Nat Mater* **2005,** *4* (12), 896-900.

36. Crivoi, A.; Duan, F., Evaporation-Induced Branched Structures from Sessile Nanofluid Droplets. *J. Phys. Chem. C* **2013,** *117* (15), 7835-7843.

37. Wu, H.; Chen, L. X.; Zeng, X. Q.; Ren, T. H.; Briscoe, W. H., Self-assembly in an evaporating nanofluid droplet: rapid transformation of nanorods into 3D fibre network structures. *Soft Matter* **2014,** *10* (29), 5243-5248.

38. Redeker, C.; Briscoe, W. H. Evaporative Self-Assembly of ZnO Nanorods. University of Bristol, 2013.

39. Wąsik, P.; Redeker, C.; Dane, T. G.; Seddon, A. M.; Wu, H.; Briscoe, W. H., Hierarchical Surface Patterns upon Evaporation of a ZnO Nanofluid Droplet: Effect of Particle Morphology. *Langmuir* **2018,** *34* (4), 1645-1654.

40. Wu, H.; Briscoe, W. H., Morphogenesis of polycrystalline dendritic patterns from evaporation of a reactive nanofluid sessile drop. *Physical Review Materials* **2018,** *2* (4), 045601.

41. Wąsik, P.; Seddon, A. M.; Wu, H.; Briscoe, W. H., Dendritic surface patterns from Bénard-Marangoni instabilities upon evaporation of a reactive ZnO nanofluid droplet: A fractal dimension analysis. *J. Colloid Interface Sci.* **2019,** *536*, 493-498.

42. Wąsik, P.; Seddon, A. M.; Wu, H.; Briscoe, W. H., Bénard-Marangoni dendrites upon evaporation of a reactive ZnO nanofluid droplet: Effect of substrate chemistry *Langmuir* **2019,** *35* (17), 5830-5840.

43. Tripathy, A.; Wąsik, P.; Sreedharan, S.; Nandi, D.; Bikondoa, O.; Su, B.; Sen, P.; Briscoe, W. H., Facile Fabrication of Multifunctional ZnO Urchins on Surfaces. *Colloids Interfaces* **2018,** *2* (4), 74.

44. Peng, X.; Jin, J.; Kobayashi, N.; Schmitt, W.; Ichinose, I., Time-dependent growth of zinc hydroxide nanostrands and their crystal structure. *Chem. Commun.* **2008,** (16), 1904-1906.

45. Li, J.; Cao, W.; Mao, Y.; Ying, Y.; Sun, L.; Peng, X., Zinc hydroxide nanostrands: unique precursors for synthesis of ZIF-8 thin membranes exhibiting high size-sieving ability for gas separation. *CrystEngComm* **2014,** *16* (42), 9788-9791.

46. Tang, Z.; Kotov, N. A.; Giersig, M., Spontaneous Organization of Single CdTe Nanoparticles into Luminescent Nanowires. *Science* **2002,** *297* (5579), 237-240.

47. Ichinose, I.; Huang, J.; Luo, Y.-H., Electrostatic Trapping of Double-Stranded DNA by Using Cadmium Hydroxide Nanostrands. *Nano Lett.* **2005,** *5* (1), 97-100.

48. Yu, Q.; Huang, H.; Chen, R.; Wang, P.; Yang, H.; Gao, M.; Peng, X.; Ye, Z., Synthesis of CuO nanowalnuts and nanoribbons from aqueous solution and their catalytic and electrochemical properties. *Nanoscale* **2012,** *4* (8), 2613-2620.

49. Wang, Z. L.; Kong, X. Y.; Wen, X.; Yang, S., In Situ Structure Evolution from Cu(OH)2 Nanobelts to Copper Nanowires. *J. Phys. Chem. B* **2003,** *107* (33), 8275-8280.

50. Lu, C.; Qi, L.; Yang, J.; Zhang, D.; Wu, N.; Ma, J., Simple Template-Free Solution Route for the Controlled Synthesis of Cu(OH)2 and CuO Nanostructures. *J. Phys. Chem. B* **2004,** *108* (46), 17825-17831.

51. Peng, X.; Ichinose, I., Green-Chemical Synthesis of Ultrathin β-MnOOH Nanofibers for Separation Membranes. *Adv. Funct. Mater.* **2011,** *21* (11), 2080-2087.

52. Wesfreid, J. E., Scientific Biography of Henri Bénard (1874–1939). In *Dynamics of Spatio-Temporal Cellular Structures: Henri Bénard Centenary Review*, Mutabazi, I.; Wesfreid, J. E.; Guyon, E., Eds. Springer New York: New York, NY, 2006; pp 9-37.

53. Fauve, S., Henri Bénard and pattern-forming instabilities. *Comptes Rendus Physique* **2017,** *18* (9), 531-543.

54. Rayleigh, L., LIX. On convection currents in a horizontal layer of fluid, when the higher temperature is on the under side. *The London, Edinburgh, and Dublin Philosophical Magazine and Journal of Science* **1916,** *32* (192), 529-546.

55. Norris, S. E. A Parallel Navier Stokes Solver for Natural convection and Free Surface Flow. University of Sydney, Sydney, 2000.

56. de Gennes, P.-G.; Brochard-Wyart, F.; Quere, D., *Capillarity and Wetting Phenomena*. Springer-Verlag: New York, 2004.

57. Barash, L. Y.; Bigioni, T. P.; Vinokur, V. M.; Shchur, L. N., Evaporation and fluid dynamics of a sessile drop of capillary size. *Phys. Rev. E* **2009,** *79* (4), 046301.

58. Rumble, J. R.; Rumble, J., *CRC Handbook of Chemistry and Physics, 99th Edition (Internet Version 2019)*. CRC Press LLC: 2019.

59. Jasper, J. J., The Surface Tension of Pure Liquid Compounds. *J. Phys. Chem. Ref. Data* **1972,** *1* (4), 841-1010.

60. Gómez-Díaz, D.; Mejuto, J. C.; Navaza, J. M., Physicochemical Properties of Liquid Mixtures. 1. Viscosity, Density, Surface Tension and Refractive Index of Cyclohexane + 2,2,4-Trimethylpentane

Binary Liquid Systems from 25 °C to 50 °C. *Journal of Chemical & Engineering Data* **2001,** *46* (3), 720-724.

61. Daccord, G.; Lenormand, R., Fractal patterns from chemical dissolution. *Nature* **1987,** *325*, 41.

62. Bandyopadhyay, D.; Singh, G.; Becker, M. L.; Karim, A., Capillary Wave Confinement-Induced Stabilization of Polymer Films. *ACS Applied Materials & Interfaces* **2013,** *5* (10), 4006-4010.

63. Kikuchi, H.; Sakai, K.; Takagi, K., Complex propagation of surface waves on soft gels. *Physical Review B* **1994,** *49* (5), 3061-3065.

64. Filobelo, L. F.; Galkin, O.; Vekilov, P. G., Spinodal for the solution-to-crystal phase transformation. **2005,** *123* (1), 014904.

65. Malmberg, C. G.; Maryott, A. A., Dielectric Constant of Water from 00 to 1000 C. *Journal of research of the National Bureau of Standards* **1956,** *56* (1), 1.

66. Lin, Z., *Evaporative Self-assembly of Ordered Complex Structures*. World Scientific: Singapore, 2012.

67. Ichinose, I.; Kurashima, K.; Kunitake, T., Spontaneous Formation of Cadmium Hydroxide Nanostrands in Water. *J. Am. Chem. Soc.* **2004,** *126* (23), 7162-7163.

68. Luo, Y.-H.; Huang, J.; Ichinose, I., Bundle-like Assemblies of Cadmium Hydroxide Nanostrands and Anionic Dyes. *J. Am. Chem. Soc.* **2005,** *127* (23), 8296-8297.

69. Luo, Y.-H.; Huang, J.; Jin, J.; Peng, X.; Schmitt, W.; Ichinose, I., Formation of Positively Charged Copper Hydroxide Nanostrands and Their Structural Characterization. *Chem. Mater.* **2006,** *18* (7), 1795-1802.

70. Elbahri, M.; Paretkar, D.; Hirmas, K.; Jebril, S.; Adelung, R., Anti-Lotus Effect for Nanostructuring at the Leidenfrost Temperature. **2007,** *19* (9), 1262-1266.

71. Greene, L. E.; Law, M.; Goldberger, J.; Kim, F.; Johnson, J. C.; Zhang, Y.; Saykally, R. J.; Yang, P., Low-Temperature Wafer-Scale Production of ZnO Nanowire Arrays. *Angew. Chem. Int. Ed.* **2003,** *42* (26), 3031-3034.

72. Greene, L. E.; Law, M.; Tan, D. H.; Montano, M.; Goldberger, J.; Somorjai, G.; Yang, P., General Route to Vertical ZnO Nanowire Arrays Using Textured ZnO Seeds. *Nano Lett.* **2005,** *5* (7), 1231-1236.

73. Greene, L. E.; Yuhas, B. D.; Law, M.; Zitoun, D.; Yang, P., Solution-Grown Zinc Oxide Nanowires. *Inorg. Chem.* **2006,** *45* (19), 7535-7543.

74. Law, M.; Greene, L. E.; Johnson, J. C.; Saykally, R.; Yang, P., Nanowire dye-sensitized solar cells. *Nat Mater* **2005,** *4* (6), 455-459.

75. Sugunan, A.; Warad, H.; Boman, M.; Dutta, J., Zinc oxide nanowires in chemical bath on seeded substrates: Role of hexamine. *J. Sol-Gel Sci. Technol.* **2006,** *39* (1), 49-56.

76. Ibach, H.; Lüth, H., Diffraction from Periodic Structures. In *Solid-State Physics: An Introduction to Principles of Materials Science*, Springer Berlin Heidelberg: Berlin, Heidelberg, 2009; pp 51-82.

77. Bragg, W. H.; Bragg, W. L., The Reflection of X-rays by Crystals. *Proc. R. Soc. London, Ser. A* **1913,** *88* (605), 428-438.

78. Scardi, P.; Leoni, M., Whole powder pattern modelling. *Acta Crystallographica Section A* **2002,** *58* (2), 190-200.

79. Scardi, P.; Leoni, M., Diffraction line profiles from polydisperse crystalline systems. *Acta Crystallographica Section A* **2001,** *57* (5), 604-613.

80. Leoni, M.; Di Maggio, R.; Polizzi, S.; Scardi, P., X-ray Diffraction Methodology for the Microstructural Analysis of Nanocrystalline Powders: Application to Cerium Oxide. *J. Am. Ceram. Soc.* **2004,** *87* (6), 1133-1140.

81. Scardi, P.; Leoni, M.; Delhez, R., Line broadening analysis using integral breadth methods: a critical review. *J. Appl. Crystallogr.* **2004,** *37* (3), 381-390.

82. Scardi, P.; Lutterotti, L.; Maistrelli, P., Experimental determination of the instrumental broadening in the Bragg–Brentano geometry. *Powder Diffr.* **1994,** *9* (03), 180-186.

83. Leoni, M.; Scardi, P.; Langford, J. I., Characterization of standard reference materials for obtaining instrumental line profiles. *Powder Diffr.* **1998,** *13* (04), 210-215.

84. Stokes, A. R., A Numerical Fourier-analysis Method for the Correction of Widths and Shapes of Lines on X-ray Powder Photographs. *Proceedings of the Physical Society* **1948,** *61* (4), 382.

85. Mittemeijer, E. J.; Welzel, U., The "state of the art" of the diffraction analysis of crystallite size and lattice strain. *Zeitschrift für Kristallographie International journal for structural, physical, and chemical aspects of crystalline materials* **2008,** *223* (9), 552-560.

86. Warren, B. E.; Averbach, B. L., The Effect of Cold-Work Distortion on X-Ray Patterns. *J. Appl. Phys.* **1950,** *21* (6), 595-599.

87. Warren, B. E.; Averbach, B. L., The Separation of Stacking Fault Broadening in Cold-Worked Metals. *J. Appl. Phys.* **1952,** *23* (9), 1059-1059.

88. Varin, R. A.; Bystrzycki, J.; Calka, A., Effect of annealing on the microstructure, ordering and microhardness of ball milled cubic (L12) titanium trialuminide intermetallic powder. *Intermetallics* **1999,** *7* (7), 785-796.

89. Dongol, M.; El-Denglawey, A.; Abd El Sadek, M. S.; Yahia, I. S., Thermal annealing effect on the structural and the optical properties of Nano CdTe films. *Optik - International Journal for Light and Electron Optics* **2015,** *126* (14), 1352-1357.

90. Shaaban, E. R.; Afify, N.; El-Taher, A., Effect of film thickness on microstructure parameters and optical constants of CdTe thin films. *J. Alloys Compd.* **2009,** *482* (1–2), 400-404.

91. Dinnebier, R. E., *Powder diffraction: theory and practice*. Royal Society of Chemistry: 2008.

92. Li, J.; Hitch, M., Characterization of the microstructure of mechanically-activated olivine using X-ray diffraction pattern analysis. *Miner. Eng.* **2016,** *86*, 24-33.

93. Eckert, M., Max von Laue and the discovery of X-ray diffraction in 1912. *Annalen der Physik* **2012,** *524* (5), A83-A85.

94. Scherrer, P., Estimation of the size and internal structure of colloidal particles by means of röntgen. *Nachr. Ges. Wiss. Göttingen* **1918,** *2*, 96-100.

95. Langford, J. I.; Wilson, A. J. C., Scherrer after sixty years: A survey and some new results in the determination of crystallite size. *J. Appl. Crystallogr.* **1978,** *11* (2), 102-113.

96. Williamson, G. K.; Hall, W. H., X-ray line broadening from filed aluminium and wolfram. *Acta Metall.* **1953,** *1* (1), 22-31.

97. Vives, S.; Gaffet, E.; Meunier, C., X-ray diffraction line profile analysis of iron ball milled powders. *Materials Science and Engineering: A* **2004,** *366* (2), 229-238.

98. Izumi, F.; Young, R., The Rietveld Method, International Union of Crystallography. *Young, RA, Ed* **1993**, 13.

99. Leoni, M.; Martinez-Garcia, J.; Scardi, P., Dislocation effects in powder diffraction. *J. Appl. Crystallogr.* **2007,** *40* (4), 719-724.

100. Scardi, P.; Leoni, M.; Dong, Y. H., Whole diffraction pattern-fitting of polycrystalline fcc materials based on microstructure. *Eur. Phys. J. B* **2000,** *18* (1), 23-30.

101. Balagurov, A. M.; Bobrikov, I. A.; Bokuchava, G. D.; Vasin, R. N.; Gusev, A. I.; Kurlov, A. S.; Leoni, M., High-resolution neutron diffraction study of microstructural changes in nanocrystalline ball-milled niobium carbide NbC0.93. *Mater. Charact.* **2015,** *109*, 173-180.

102. Dane, T. G.; Bartenstein, J. E.; Sironi, B.; Mills, B. M.; Alexander Bell, O.; Emyr Macdonald, J.; Arnold, T.; Faul, C. F. J.; Briscoe, W. H., Influence of solvent polarity on the structure of drop-cast electroactive tetra(aniline)-surfactant thin films. *Phys. Chem. Chem. Phys.* **2016,** *18* (35), 24498-24505.

103. Sironi, B.; Snow, T.; Redeker, C.; Slastanova, A.; Bikondoa, O.; Arnold, T.; Klein, J.; Briscoe, W. H., Structure of lipid multilayers via drop casting of aqueous liposome dispersions. *Soft Matter* **2016,** *12* (17), 3877-3887.

104. Weisenburger, S.; Sandoghdar, V., Light microscopy: an ongoing contemporary revolution. *Contemporary Physics* **2015,** *56* (2), 123-143.

105. Cremer, C.; Masters, B. R., Resolution enhancement techniques in microscopy. **2013,** *38* (3), 281-344.

106. Abbe, E., Beiträge zur Theorie des Mikroskops und der mikroskopischen Wahrnehmung. *Archiv für mikroskopische Anatomie* **1873,** *9* (1), 413-418.

107. De Broglie, L. Recherches sur la théorie des quanta. Migration-université en cours d'affectation, 1924.

108. Kohl, H.; Reimer, L., Transmission Electron Microscopy. Springer: New York, NY, 2008; Vol. 36, pp 43-74.

109. Goldstein, J. I.; Newbury, D. E.; Michael, J. R.; Ritchie, N. W. M.; Scott, J. H. J.; Joy, D. C., Scanning Electron Microscopy and X-Ray Microanalysis. Springer New York: 2017; pp 2 - 14.

110. Goldstein, J. I.; Newbury, D. E.; Michael, J. R.; Ritchie, N. W. M.; Scott, J. H. J.; Joy, D. C., Scanning Electron Microscopy and X-Ray Microanalysis. Springer New York: 2017; pp 15 - 28.

111. Dehm, G.; Howe, J. M.; Zweck, J., In-situ Electron Microscopy: Applications in Physics, Chemistry and Materials Science. Wiley: Weinheim, 2012; pp 3- 37.

112. Bell, D. C.; Erdman, N., Introduction to the Theory and Advantages of Low Voltage Electron Microscopy. In *Low Voltage Electron Microscopy: principles and applications*, Bell, D. C.; Erdman, N., Eds. John Wiley & Sons Ltd.: Chichester, 2013; pp 1-30.

113. Reimer, L.; MacAdam, D. L.; Hawkes, P. W.; Schawlow, A. L.; Shimoda, K.; Siegman, A. E.; Tamir, T.; Lotasch, H. K., Scanning Electron Microscopy: Physics of Image Formation and Microanalysis. Springer: New York, 1998; pp 1 - 12.

114. Cosgrove, T., Colloid Science: Principles, Methods and Applications. John Wiley & Sons: Bristol, 2010; pp 311 - 327.

115. Stokes, D., *Principles and Practice of Variable Pressure / Environmental Scanning Electron Microscopy (VP-ESEM)*. Wiley: Padstow, 2008.

116. Egerton, R. F., The Transmission Electron Microscope. In *Physical Principles of Electron Microscopy: An Introduction to TEM, SEM, and AEM*, Egerton, R. F., Ed. Springer International Publishing: Cham, 2016; pp 55-88.

117. Ravishankar, N., Seeing is Believing: Electron Microscopy for Investigating Nanostructures. *The Journal of Physical Chemistry Letters* **2010,** *1* (8), 1212-1220.

118. Williams, D. B.; Carter, C. B., Diffraction in TEM. In *Transmission Electron Microscopy: A Textbook for Materials Science*, Springer US: Boston, MA, 2009; pp 197-209.

119. Somorjai, G. A.; Li, Y., Impact of surface chemistry. *Proceedings of the National Academy of Sciences* **2011,** *108* (3), 917-924.

120. Yuan, Y.; Lee, T. R., Contact Angle and Wetting Properties. In *Surface Science Techniques*, Bracco, G.; Holst, B., Eds. Springer Berlin Heidelberg: Berlin, Heidelberg, 2013; pp 3-34.

121. Young, T., III. An essay on the cohesion of fluids. *Philosophical Transactions of the Royal Society of London* **1805,** *95*, 65-87.

122. Żenkiewicz, M., Methods for the calculation of surface free energy of solids. *Journal of Achievements in Materials and Manufacturing Engineering* **2007,** *24* (1), 137-145.

123. Leroy, F.; Müller-Plathe, F., Dry-Surface Simulation Method for the Determination of the Work of Adhesion of Solid–Liquid Interfaces. *Langmuir* **2015,** *31* (30), 8335-8345.

124. Leroy, F.; Muller-Plathe, F. In *Calculation of the Work of Adhesion of Solid-Liquid Interfaces by Molecular Dynamics Simulations*, John von Neumann-Institut für Computing (NIC) Symposium, 2016.

125. Ebnesajjad, S., 2 - Surface Tension and Its Measurement. In *Surface Treatment of Materials for Adhesion Bonding*, Ebnesajjad, S., Ed. William Andrew Publishing: Norwich, NY, 2006; pp 9-28.

126. Neumann, A. W.; Good, R. J.; Hope, C. J.; Sejpal, M., An equation-of-state approach to determine surface tensions of low-energy solids from contact angles. *J. Colloid Interface Sci.* **1974,** *49* (2), 291-304.

127. Fowkes, F. M., Calculation of work of adhesion by pair potential suummation. *J. Colloid Interface Sci.* **1968,** *28* (3), 493-505.

128. Fowkes, F. M., Attractive Forces at Iinterfaces. *Industrial & Engineering Chemistry* **1964,** *56* (12), 40-52.

129. Fowkes, F. M., Donor-Acceptor Interactions at Interfaces. *The Journal of Adhesion* **1972,** *4* (2), 155-159.

130. Owens, D. K.; Wendt, R. C., Estimation of the surface free energy of polymers. *J. Appl. Polym. Sci.* **1969,** *13* (8), 1741-1747.

131. Rabel, W., Einige Aspekte der Benetzungstheorie und ihre Anwendung auf die Untersuchung und Veränderung der Oberflächeneigenschaften von Polymeren. *Farbe und Lacke* **1971,** *77* (10), 997-1005.

132. Kaelble, D. H., Dispersion-Polar Surface Tension Properties of Organic Solids. *The Journal of Adhesion* **1970,** *2* (2), 66-81.

133. Van Oss, C. J.; Chaudhury, M. K.; Good, R. J., Interfacial Lifshitz-van der Waals and polar interactions in macroscopic systems. *Chem. Rev.* **1988,** *88* (6), 927-941.

134. Fox, H. W.; Zisman, W. A., The spreading of liquids on low-energy surfaces. II. Modified tetrafluoroethylene polymers. *J. Colloid Sci.* **1952,** *7* (2), 109-121.

135. Rulison, C., So you want to measure surface energy? In *A tutorial designed to provide basic understanding of the concept solid surface energy, and its many complications, TN306/CR*, 1999; pp 1-16.

136. Polster, D.; Graaf, H., Advancing and receding angles – Dynamic contact angle measurements on mixed alkyl monolayers. *Appl. Surf. Sci.* **2013,** *265*, 88-93.

137. Law, K.-Y., Definitions for Hydrophilicity, Hydrophobicity, and Superhydrophobicity: Getting the Basics Right. *The Journal of Physical Chemistry Letters* **2014,** *5* (4), 686-688.

138. Eral, H. B.; 't Mannetje, D. J. C. M.; Oh, J. M. J. C.; Science, P., Contact angle hysteresis: a review of fundamentals and applications. **2013,** *291* (2), 247-260.

Hierarchical surface patterns upon evaporation of a ZnO nanofluid droplet: Effect of particle morphology

Patryk Wąsik[a,b], Christian Redeker[b], Thomas G. Dane[c], Annela M. Seddon[a,d], Hua Wu[b], and Wuge H. Briscoe[b,]*

[a] Bristol Centre for Functional Nanomaterials (BCFN), HH Wills Physics Laboratory, University of Bristol, Tyndall Avenue, Bristol, BS8 1TL, UK

[b] School of Chemistry, University of Bristol, Cantock's Close, Bristol, BS8 1TS, UK

[c] The European Synchrotron (ESRF) 71, Avenue des Martyrs, Grenoble, France

[d] School of Physics, HH Wills Physics Laboratory, Tyndall Avenue, University of Bristol, Bristol, BS8 1TL, UK

Information

This chapter has been published as a research article: **Wąsik, P.**; Redeker, C.; Dane, T. G.; Seddon, A. M.; Wu, H.; Briscoe, W. H., Hierarchical Surface Patterns upon Evaporation of a ZnO Nanofluid Droplet: Effect of Particle Morphology. *Langmuir* **2018,** *34* (4), 1645-1654. DOI: 10.1021/acs.langmuir.7b03854. This chapter has been authored by the candidate with no more input from co-authors and supervisors that would have been provided in a conventional thesis chapter. PW conducted the research and wrote the manuscript, PW and CR synthesised ZnO nanoparticles, PW and TGD performed μGIXRD, HW and WHB corroborated the project, WHB co-wrote the manuscript, AMS and WHB supervised the project, and all co-authors commented on the manuscript.

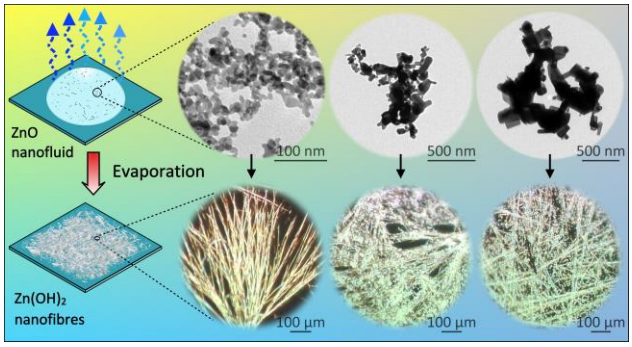

Abstract

Surface structures with tailored morphologies can be readily delivered by the evaporation induced self-assembly process. It has been recently demonstrated that ZnO nanorods could undergo rapid chemical and morphological transformation into 3D complex structures of $Zn(OH)_2$ nanofibers as a droplet of ZnO nanofluid dries on the substrate, *via* a mechanism very different from that observed in the coffee ring effect. Here, we have investigated how the crystallinity and morphology of ZnO nanoparticles would affect the ultimate pattern formation. Three ZnO particles differing in size and shape were used, and their crystal structures were characterized by powder X-ray diffraction (XRD) and Transmission Electron Microscopy (TEM). Their dispersions were prepared by sonication in a mixture of isobutylamine and cyclohexane. Residual surface patterns were created by drop casting a droplet of the nanofluid on a silicon substrate. The residual surface patterns were analyzed by Scanning Electron Microscopy (SEM) and micro-focus Grazing Incidence X-ray Diffraction (µGIXRD). Nanofluid droplets of the in-house synthesized ZnO nanoparticles resulted in residual surface patterns consisting of $Zn(OH)_2$ nanofibers. However, when commercially acquired ZnO powders composed of crystals with various shapes and sizes were used as the starting material, $Zn(OH)_2$ fibers were found covered by ZnO crystal residues that did not fully undergo the dissolution and recrystallization process during evaporation. The difference in the solubility of ZnO nanoparticles was linked to the difference in their crystallinity, as assessed using the Scherrer equation analysis of their XRD Bragg peaks. Our results show that the morphology of the ultimate residual pattern from evaporation of ZnO nanofluids can be controlled by varying the crystallinity of the starting ZnO nanoparticles which affects the nanoparticle dissolution process during evaporation.

Keywords Evaporation Induced Self-Assembly (EISA), residual surface patterns, zinc oxide, zinc hydroxide, dissolution, crystallinity.

Introduction

Controlled assembly at interfaces on a nanoscale is central in nanoscience and important to application of nanomaterials [1-2], and considerable effort has been devoted to creating patterned surfaces with tailored structures and enhanced functionalities. A simple and versatile bottom-up approach for generating surface patterns is evaporation induced self-assembly (EISA) [3]. In this process, particles (nanoparticles, polymers, biomaterials, *etc*.) dispersed in a drying droplet are arranged into a variety of structures as the result of the delicate, temporally and spatially fluctuating balance between inter-particle forces [4-5] and evaporation-induced solvent flows. This balance may be tuned by manipulating parameters such particle size, shape, concentration, solvent composition, evaporation rate and surface chemistry of the substrate. EISA has been successfully applied to applications such as inkjet printing of carbon nanotubes [6], production of conductive graphene networks [7], transparent films [8], DNA microarrays [9], ultraviolet photodetectors [10], mesoporous carbons [11], photoluminescent films [12], bacterial deposits [13], and evaporative cooling [14].

The most commonly observed deposition patterns resulting from the EISA process are so called “coffee-rings” [15-17]. When the contact line between the droplet and the substrate is pinned upon evaporation, an outward capillary flow of liquid is induced to compensate faster liquid loss at the droplet edge. This carries the dispersed solutes to the droplet perimeter, where they are deposited and form the ring-like residual pattern.

The formation of coffee rings can be suppressed by the inward Marangoni flow that carries particles towards the droplet center [18], or by the shape anisotropy of dispersed particles [19]. The residual EISA pattern may also be affected by convective instabilities in the drop [20], which manifest as multiple vortices with liquid flowing upward in the center and subsequently outward to the edge of the convection cell, such as the Bénard-Marangoni and the Rayleigh-Bénard convection [21], which could lead to residual patterns of connected polygons templating the convective cells.

Fingering structures may also form from EISA due to fluctuations at the interface between two fluids of different viscosities [22-24]. Finger-like stripes perpendicular to the contact line are often produced in vertical deposition techniques (*i.e*. plate withdrawal), and radial spoke patters are commonly observed in horizontal deposition techniques (*i.e.* drop-casting) [25].

Very recently, we have made an unexpected observation of residual surface patterns from an EISA process [26]. When a tiny droplet of a nanofluid containing ZnO nanorods dries on a glass slide at room temperature, a uniform thin film with a 3D porous network structure comprising centimeter-long $Zn(OH)_2$ nanofibers and dendrites can spontaneously form. The observation of this rapid chemical (ZnO to $Zn(OH)_2$) and morphological (nanorods to centimeter-long fibers) transformation of a drying nanofluid is surprising and reveals a new mechanism, which is very different from that associated with the coffee rings, as outlined below. Once a droplet containing ZnO nanorods in an isobutylamine and cyclohexane mixture is placed on the substrate surface, water molecules present in air are taken up by the solvent due to the high miscibility of isobutylamine with water. These water molecules are then incorporated to the surface of isobutylamine-coated ZnO nanorods, where isobutylamine undergoes hydrolysis with entrained water molecules, raising pH within the proximity of ZnO nanorods. When pH reaches a value above 9, ZnO nanorods transform into soluble hydroxyl complexes with ZnOH- coordinated with isobutylamine. Those complexes may further assemble in clusters that serve as building blocks in the formation of zinc hydroxide nanocrystals, whose self-organization is driven by the thermal and solutal Marangoni flows and instabilities during the evaporation. This ultimately leads to the residual surface pattern comprised of a uniform film with the structure of 3D fiber networks forming on a substrate.

A key step involved in this mechanism is initial moisture-assisted rapid dissolution of isobutylamine-coated ZnO nanorods that differs from previous studies where the dispersed particles are typically inert. However, a question concerning this novel EISA process remains: is it necessary to use the ZnO nanoparticles of size and morphology (*i.e.* nanorods) [26] to produce the hierarchical residual surface patterns? To address this question, in this work we have used three different ZnO particles varying in shape, size and crystal structure in the nanofluid dispersion used for the EISA process and investigated

how the initial structure and morphology of ZnO nanocrystals would affect the ultimate residual pattern formation. ZnO particles were dispersed in a mixture of cyclohexane and isobutylamine and dried on a silicon substrate. The starting particles were characterized by X-ray powder diffraction (XRD), transmission electron microscopy (TEM) and energy-dispersive X-ray spectroscopy (EDX), ZnO nano/microfluids by dynamic light scattering (DLS), and the obtained residual surface patterns by scanning electron microscopy (SEM) and micro-focus grazing incidence X-ray diffraction (μGIXRD). It was demonstrated that the morphology of the final residual surface pattern from a drying ZnO-nano(micro)fluid droplet could be controlled by varying the crystallinity of the starting ZnO particles, which affected the initial ZnO dissolution mechanism.

Materials and Methods

ZnO particles

Three types of zinc oxide (ZnO) particles were used: in-house synthesized ZnO nanoparticles, and commercially acquired ZnO nanopowder (Sigma-Aldrich, <100 nm particle size, ~80% Zn basis) and ZnO powder (Sigma-Aldrich, ACS reagent, ≥99.0% (KT)). The in-house ZnO nanoparticles synthesis was carried out according to a modified method described by Sun *et al.* [27] as described in detail in the Supporting Information section SI1.

Particle characterization

Particles morphology was analyzed by TEM (see SI2 for details). The sizing of the in-house synthesized ZnO nanoparticles and commercially acquired ZnO nanopowder and ZnO powder was performed using ImageJ software (see SI3 for details). The structure of ZnO particles was analyzed by XRD (see SI4 for details), and their chemical composition by EDX (see SI5).

Substrates

Silicon wafers (ID 452, UniversityWafer, Inc.) were cut into ~1×1 cm^2 squares using a pen diamond cutter. The substrates were then sonicated in acetone and ethanol for 10 minutes each, then rinsed three times with Milli-Q water, before being sonicated in Milli-Q water for 10 minutes and dried with a stream of nitrogen.

Evaporative drying of ZnO nano/microfluid droplets

ZnO particles were dispersed in a mixture of cyclohexane and isobutylamine (5:1 volume:volume ratio), the same solvent composition as in Ref. [26]. (The effect of the solvent composition on the residual pattern will be reported elsewhere.) Suspensions of the final ZnO concentration of 1 mg/mL were sonicated for 2 hours to form homogenous dispersions. As prepared ZnO nano/microfluids were studied with DLS (see SI6). 30 µL droplets of ZnO nanofluids were drop-cast by a pipette onto the surface of the substrates placed inside compartments of a polystyrene petri-dish (25 compartment sterile 100 mm box; Sterilin) and left to evaporate. The process took place at room temperature (~23°C) and relative humidity (RH) ~45%, measured with a humidity/temperature pen (Tracable®). Within several minutes all droplets evaporated leaving the substrates covered with white deposits.

Characterization of the residual surface patterns resulted from evaporative drying

Residual surface patterns formed by the evaporative drying of ZnO nano/microfluids were investigated using SEM (JSM-IT300 SEM, JEOL), optical microscopy (see SI7), and micro-focus Grazing Incidence X-ray Diffraction (µGIXRD). µGIXRD analysis of the residual surface patterns was performed at Beamline ID13 at the European Synchrotron Radiation Facility (France) (See SI8 for details).

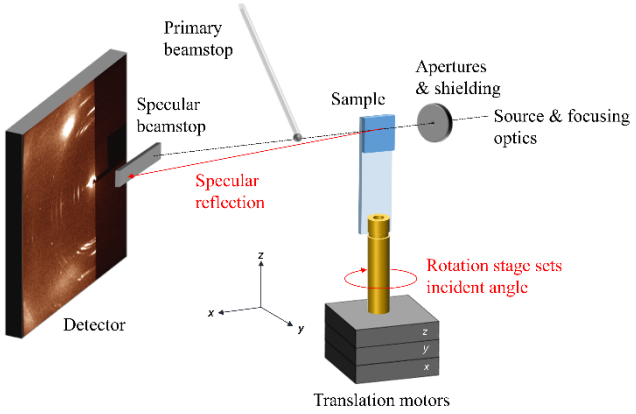

Figure 1. Experimental set-up for µGIXRD analysis. A sample with residual surface patterns was glued to a glass slide and mounted on the top of translation/rotation stage. Sample's surface was scanned with X-rays by moving the sample position along z-axis and recording a µGIXD pattern every 2 µm. The 'Position' parameter in **Figure 7** and **8** refers to the position of the X-ray beam between the edges of the sample along the *z*-axis.

Crystallinity assessment of ZnO (nano)particles

The crystallinity of the ZnO samples was evaluated using the Scherrer formula [28] to yield the coherence length L_a, which gives an indication of the lower limit of the crystal domain size [29-30] (see SI4 for details).

Results and discussion

Characterization of ZnO nano-/micro-particles

TEM micrographs and corresponding size distributions of ZnO particles are shown in **Figure 2**. The in-house synthesized ZnO sample was largely composed of spherically shaped nanocrystals (**Figure 2a**). Their size distribution (**Figure 2d**) was fitted with the lognormal distribution function (see SI3) with the geometric mean particle size M = 9.2 nm and the geometric standard deviation σ_g = 1.3.

In contrast, the commercially acquired ZnO particles (**Figure 2b-c**) exhibited diverse morphologies, including spherical, faceted, elongated rod-like, and irregular parallelepiped structures, with a wide size distribution. Therefore, a maximum dimension parameter, which is the greatest distance between any two surface points of the particle and can be directly measured in case of aspherical particles [31], was used as a variable of a size distribution instead of a diameter for commercially acquired ZnO nanopowder and ZnO powder.

The ZnO nanopowder sample (**Figure 2b**) had particle sizes varying from 10 nm for the smallest spherical particles to up to 530 nm elongated parallelepiped crystals. The size distribution of the ZnO nanopowder sample is shown in **Figure 2e**, with calculated lognormal fit parameters of M = 71.7 nm (the mean maximum dimension) and σ_g = 2.0. This means that 68.3% of all particles in ZnO nanopowder sample had the maximum dimension between 36.2 nm and 141.8 nm (between M/σ_g and $M \cdot \sigma_g$). The ZnO powder (**Figure 2c**) contained particles with sizes ranging from 15 nm for the smallest spheres to more than 1 μm for elongated crystals, with lognormal fit parameters M = 133.4 nm and σ_g = 2.2. Based on its size distribution analysis (**Figure 2f**), it is concluded that 68.3% of all particles in ZnO powder sample exhibited the maximum diameter between 61.2 nm and 290.9 nm.

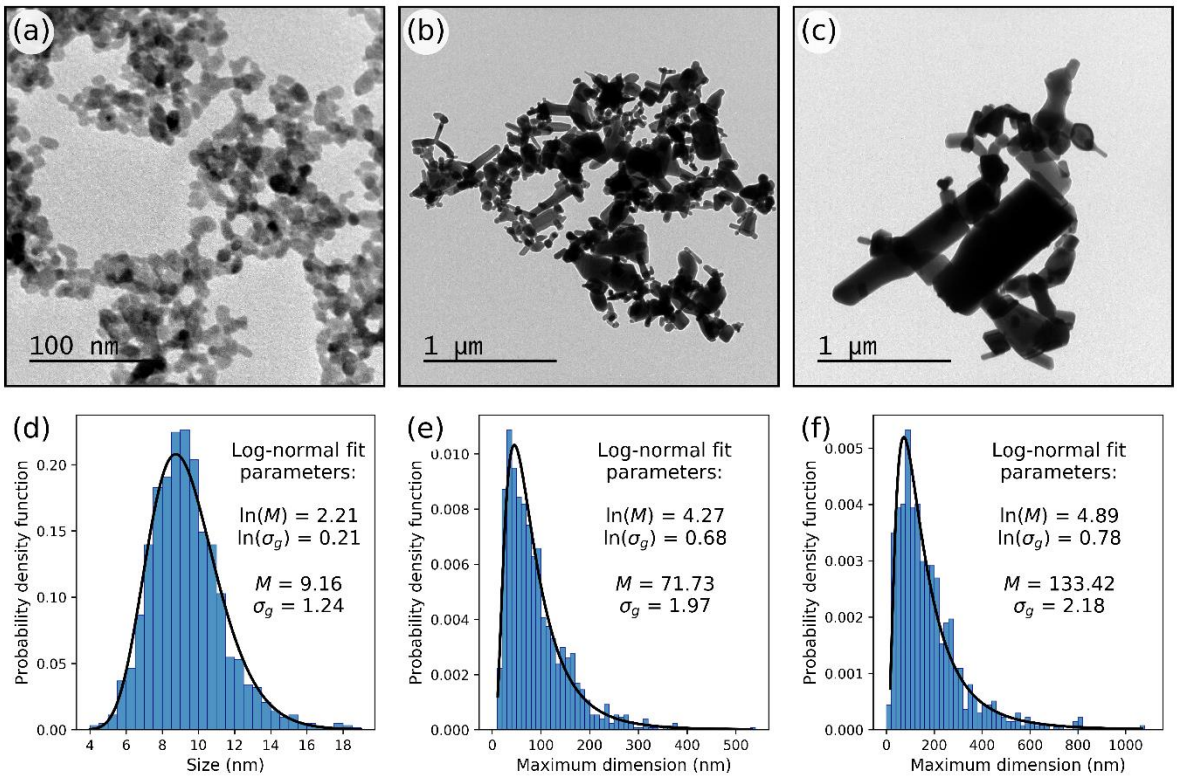

Figure 2. TEM micrographs of the ZnO particles: (a) the in-house synthesized ZnO nanoparticles, and commercially acquired (b) ZnO nanopowder and (c) ZnO powder. Below the micrographs, the corresponding size distributions for particles (d) diameter and (e-f) maximum dimension are shown for (a), (b) and (c), respectively.

Figure 3 presents XRD diffraction profiles of the three types of ZnO particles. All the peaks were characteristic for a Wurtzite structure of ZnO (PDF 01-075-0576). The XRD line profile of the in-house synthesized ZnO sample (*cf.* **Figure 2a**) exhibits large peak broadening. The line profiles of commercially acquired ZnO particles, nanopowder and powder (*cf.* **Figure 3b-c**) show sharp peaks. The XRD results indicate that the commercial ZnO nanopowder and powder samples possessed higher crystallinity (larger size of coherently scattering domains and less strain caused by crystal defects) compared to the in-house prepared ZnO nanoparticles.

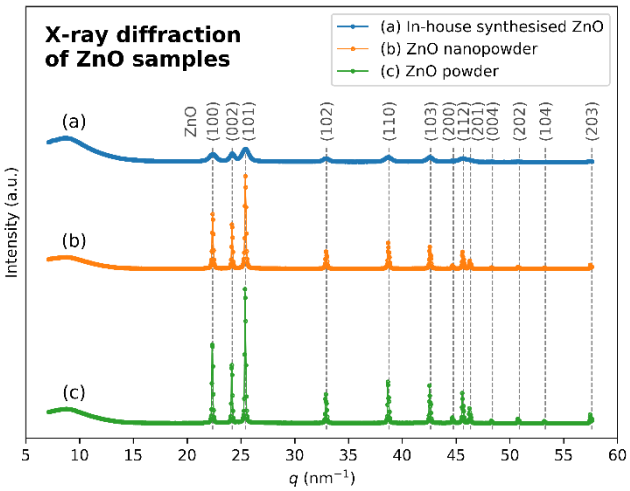

Figure 3. Powder XRD profiles of ZnO particles used for the preparation of nanofluids: (a) in-house synthesized ZnO nanoparticles, (b) ZnO nanopowder (Sigma-Aldrich), and (c) ZnO powder (Sigma-Aldrich). The numbers in brackets are the Miller indices of the crystallographic planes of ZnO (PDF 01-075-0576).

Table 1 lists the calculated coherence lengths according to eq S3, where the value for the shape constant $K = 1$ was used, and their corresponding errors calculated by the partial derivative method [29-30] for the six peaks in the XRD line profiles of the in-house synthesized ZnO nanoparticles, ZnO nanopowder, and ZnO powder. Amongst the three most pronounced peaks, (100), (002) and (101), the coherence length L_a corresponding to the (002) plane diffraction for all samples is the largest, indicating that the crystallites were elongated in the (002) direction (*c* axis), which is the preferential ZnO crystal growth direction during synthesis [32-33]. The shortest average coherence length, L_a = 8.9 nm, was exhibited by the in-house synthesized ZnO nanoparticles, which is comparable to its geometric median diameter for lognormal distribution, M = 9.2 nm (68.3% of all particles between M/σ_g = 7.4 nm and $M \cdot \sigma_g$ = 11.4 nm, *cf.* SI3). The intermediate value, L_a = 40.9 nm, was shown by ZnO nanopowder, and the largest, L_a = 44.6 nm, by ZnO powder. These values are indicative of the lower limit of the apparent crystallite size, with the shape constant, K, in eq S3 accounting for a distribution of shapes as well as for a distribution of sizes to some degree. Even though the value of 8.9 nm correlates with the geometric median particles diameter in lognormal size distribution obtained from TEM analysis of the in-house prepared ZnO sample (**Figure 2a-b**), TEM micrographs of the other two samples, nanopowder and

powder show that the crystals present in these sample had dimensions much larger than 100-150 nm, and that is the upper limit of the grain size for which the XRD analysis remains valid [34]. Overall, the TEM analysis shows that the in-house ZnO nanoparticles were smaller, with a narrower size distribution, as compared with the commercially acquired ZnO particles, which appeared polycrystalline with larger particles comprising multiple crystal domains.

Table 1. Calculated correlation lengths (L_a) and errors (δL_a) for the six most pronounced peaks based on a Gaussian fit to the experimental X-ray diffraction line profiles of the in-house prepared ZnO nanoparticles, and commercially acquired ZnO nanopowder and ZnO powder.

	In-house synthesized ZnO NP		ZnO nanopowder		ZnO powder	
Peak (hkl)	L_a (nm)	$\pm$ δL_a (nm)	L_a (nm)	$\pm$ δL_a (nm)	L_a (nm)	$\pm$ δL_a (nm)
(100)	7.6	0.1	44.6	0.6	50.4	0.8
(002)	10.4	0.1	49.8	0.9	51.5	1.1
(101)	8.0	0.1	42.5	0.3	47.6	0.4
(102)	9.3	0.2	38.3	1.6	42.6	1.8
(110)	8.2	0.1	35.9	1.0	38.7	1.1
(103)	10.1	0.2	34.1	1.2	36.8	1.3
Average:	8.9		40.9		44.6	

In addition, ZnO particles were characterized with EDX (*cf*. SI5). The results shown in **Figure S1** and **Table S2** indicate that small amounts of carbon, likely due to airborne contaminants, were present within all samples (3 - 6 atomic %). However, as they were dispersed in a mixture of organic solvents and sonicated for 2 hours before drop casting, it is conceivable that the trace carbon dissolved and did not significantly influence the EISA process.

Residual surface patterns from ZnO nanofluid dispersion of different particle size and morphology

The DLS measurements of the ZnO nano/microfluids immediately after the sonication (see SI6) indicated cluster formation, with polydisperse clusters of size 1 - 2 μm in all ZnO nano/microfluids (**Table S2**), suggesting the suspensions were not inherently stable over time. Evaporation of the droplet occurred on a much shorter time scale, and clustering happened for all the samples to the same extent and thus could not account for the vastly different surface patterns observed.

SEM image of the residual surface patterns from the nanofluid of the in-house ZnO nanoparticles shows densely packed patches (**Figure 4a**), with a distinct peripheral coffee ring (**Figure 4b**). These patches, approximately circular in shape and 475 μm on average in diameter, resemble spoke-like radial patterns, with some of them exhibiting a bowtie projection. Most of them have a center from which the fibers radiate. These structures appear mostly as well-defined cells, overlapping or interpenetrating with each other (**Figure 4i**) at the edges. There are however some regions of high density with a large degree of overlapping (**Figure 4e**). The main difference between these regions is the presence of small, irregular residues covering the surface of the fibers located in the high-density regions (**Figure 4h**), which are not present in the low-density regions (**Figure 4d** and **l**).

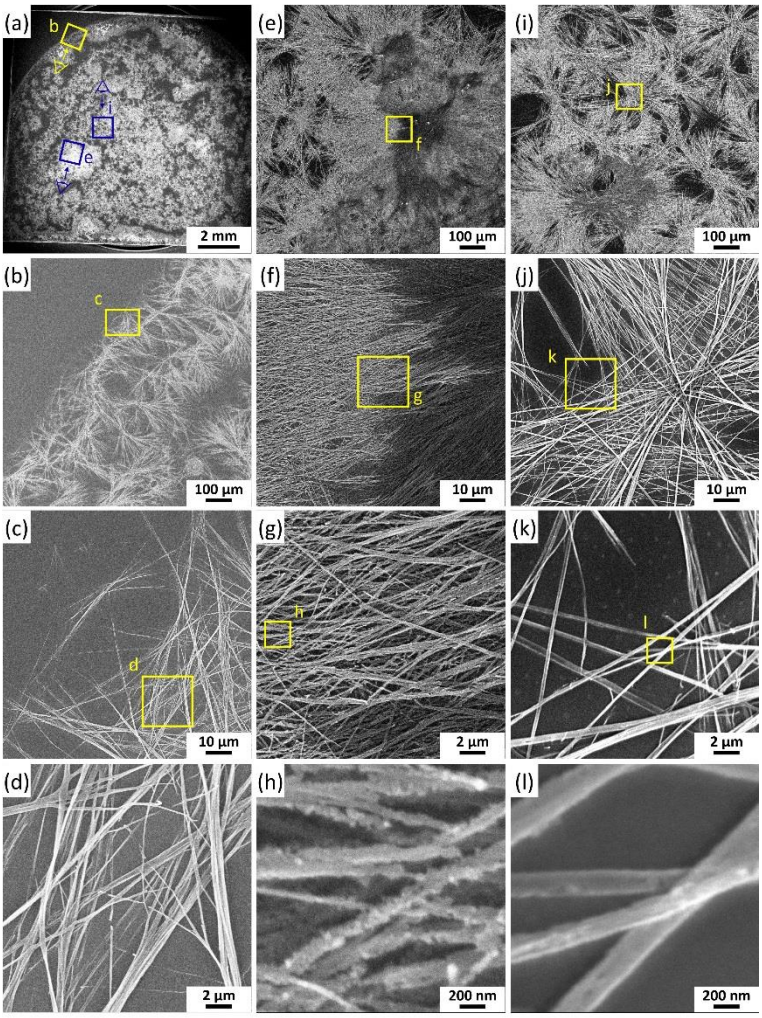

Figure 4. SEM images of the residual surface patterns from evaporative drying of a 30 µL ZnO nanofluid sessile droplet on a ~1×1 cm^2 silicon wafer at room temperature and relative humidity of ~45%. The nanofluid was prepared from the in-house synthesized ZnO nanoparticles, dispersed in a mixture of cyclohexane and isobutylamine (5:1 volume:volume ratio). The rectangular regions in the figures are enlarged, with their labels corresponding to those of the figures. The schematic drawings of the eye and arrow in (a) indicate the direction of viewing of the regions as shown in their corresponding magnified images.

Figure 5 shows an optical photograph and SEM images of the residual surface patterns from ZnO nanopowder (*cf*. **Figure 2c**) nanofluid on a silicon substrate. The entire surface is covered by a dense, fibrous network composed of structures resembling the spoke-like radial patterns of a bow-tie projection. The network has the highest density in the central region of the surface (**Figure 5**b), and is

less dense, with small particulate residues between fibrous 'bow-ties', closer to the perimeter (**Figure 5c**). The higher magnification images (**Figure 5d** and **g**) show that the fibers are covered with particulate residues and aggregates, especially where fibers intersect (**Figure 5e** and **h**). The structure of these aggregates (**Figure 5f** and **i**) is similar to that of the ZnO nanopowder crystals originally used (**Figure 2b**).

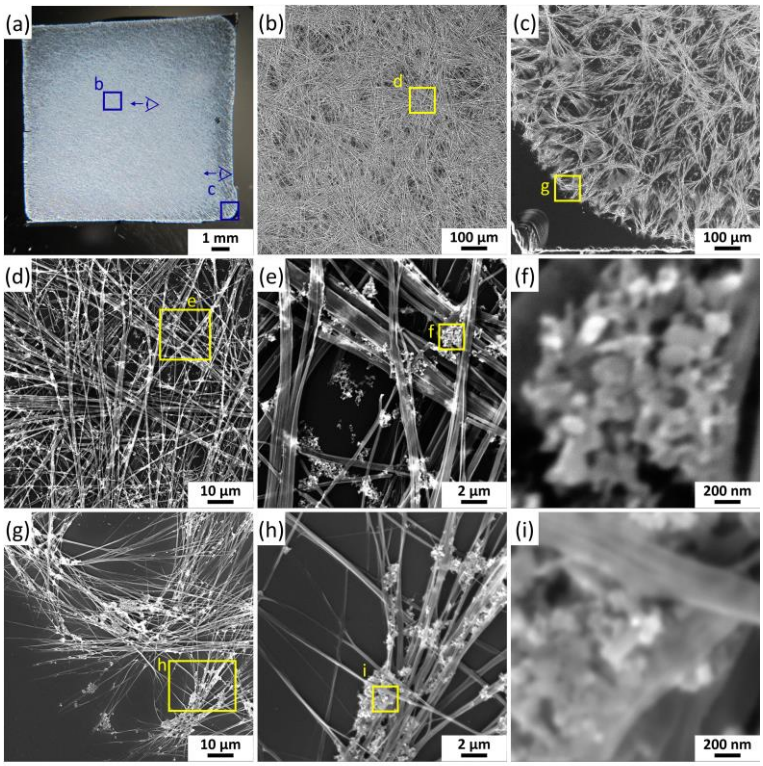

Figure 5. Optical (a) and SEM (b-i) images of the residual surface patterns from evaporative drying of 30 µL ZnO nanofluid sessile droplet on a ~1×1 cm^2 silicon wafer at room temperature and relative humidity (RH) ~45%. The nanofluid was prepared from the commercially acquired ZnO nanopowder, dispersed in a mixture of cyclohexane and isobutylamine (5:1 volume:volume ratio). The rectangular regions in the figures are enlarged, with their labels corresponding to those of the figures. The schematic drawings of the eye and arrow in (a) indicate the direction of viewing of the regions as shown in their corresponding magnified images.

In **Figure 6**, the optical and SEM images of the residual surface patterns from evaporative drying of ZnO nanofluid containing the commercially acquired ZnO powder (*cf*. **Figure 2c**) are presented. Similar to the patterns from the ZnO nanopowder nanofluid (**Figure 5**), the entire surface is covered by a dense,

fibrous structure. The structures in the central part of the surface (**Figure 6b**) have the appearance of the spoke-like radial patterns of a bow-tie projection, with the dendritic fibers radiating from the center. At the edge of the substrate (**Figure 6c**), elongated dendritic fibers extend in a direction perpendicular to the edge forming branched structures pointing inwards. Higher magnification images of both central and peripheral areas (**Figure 6d-i**) show that the constituent fibers are decorated with a large number of aggregates, distributed along the fibrous framework, also in areas where fibers do not cover the substrate. A magnified image of one of these aggregates (**Figure 6f**) indicates that it was formed from crystals exhibiting very similar structures and dimensions to those of the ZnO powder (*cf*. **Figure 2c**) used to prepare the ZnO dispersion.

All three types of dispersions produced residual surface patterns composed of fibrous 3D networks, and the main difference is the amount of the small aggregates incorporated into the fibrous matrix. All the surfaces were covered by similar structures of the spoke-like radial patterns, but the coverage and overlapping of these structures were the highest for the patterns produced from the commercially acquired ZnO nanopowder and powder. Additional optical microscopy images can be seen in **Figure S2**.

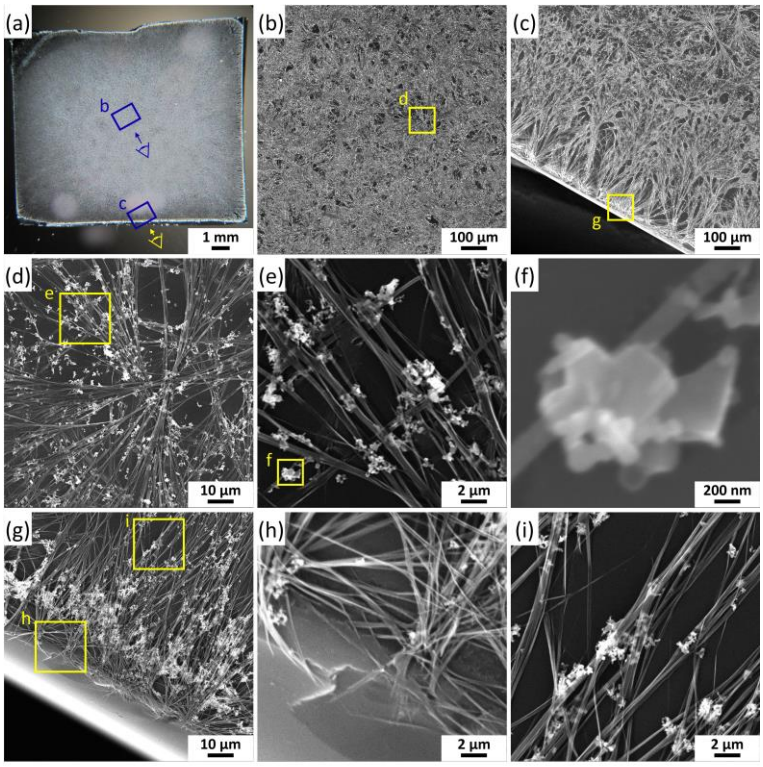

Figure 6. Optical (a) and SEM (b-i) images of the residual surface patterns from evaporative drying of a 30 µL ZnO nanofluid sessile droplet on a ~1x1 cm^2 silicon wafer at room temperature and relative humidity of ~45%. The nanofluid was prepared from the commercially acquired ZnO powder, dispersed in a mixture of cyclohexane and isobutylamine (5:1 volume:volume ratio). The rectangular regions in the figures are enlarged, with their labels corresponding to those of the figures. The schematic drawings of the eye and arrow in (a) indicate the direction of viewing of the regions as shown in their corresponding magnified images.

The crystal structure of the residual surface patterns formed upon evaporation of ZnO (nano)fluids on a silicon wafer was studied by µGIXRD. **Figure 7** and **Figure 8** present 2D heat-maps (intensity vs. momentum transfer vector q) from the µGIXRD data by recording an X-ray diffraction pattern at every 2 µm interval across the z-axis (**Figure 1**). To provide statistical information for each sample, diffraction profiles were averaged across the scan area of interest and are shown as line plots in **Figure 7b** and **Figure 8c**.

The µGIXRD profile of the residual surface patterns produced from the in-house synthesized ZnO nanoparticles (**Figure 7a**) exhibits strong diffraction peaks (arrows in **Figure 7a**) which accounts for

~5% of the total area. These diffraction peaks can be assigned to ZnO according to the ZnO reference standard (PDF 01-075-0576), with the corresponding line profile shown in **Figure 7b** (line (iii)). The line profile averaged over the remaining 95% of the scanned area is presented as line (ii) in **Figure 7b**, showing no ZnO diffractions. All the peaks attributed to the layered zinc hydroxide (LZH) structures are marked with '⋆' (star) on line profiles (i) and (ii) in **Figure 7b**. For instance, the two peaks in the low q range correspond to the interplanar spacing d = 1.37 nm (q = 4.60 nm^{-1}) and d = 0.68 nm (q = 9.20 nm^{-1}), and can be indexed as (001) and (002) LZH planes and interlayer anionic species complex structures [35-36]. The peaks at d = 0.27 nm (q = 23.17 nm^{-1}) and 0.52 nm (q = 39.99 nm^{-1}) are indexed as (100) and (110), respectively of the brucite-type zinc hydroxide structure [37-38].

The 2D intensity heat-maps (**Figure 8a-b**) from the μGIXRD profiles of ZnO nanopowder and ZnO powder samples exhibit intense ZnO diffraction patterns throughout the entire scanned area, also evident from the corresponding line profiles in **Figure 8c**. However, no LZH diffractions are observed. This suggests that the main crystalline phase present is zinc oxide, consistent the SEM images (**Figure 5** and **Figure 6**) that revealed the abundance of ZnO crystals covering the fibrous network in all the areas.

The distribution of the ZnO phase within the residual surface patterns differs among the three types of ZnO nano/microfluids investigated. Zinc oxide diffraction patterns are present only in about 5% of the scanned area in the case of in-house synthesized ZnO nanofluid, whilst they are manifested uniformly throughout μGIXRD profiles with much higher intensities for the other two nano/microfluids.

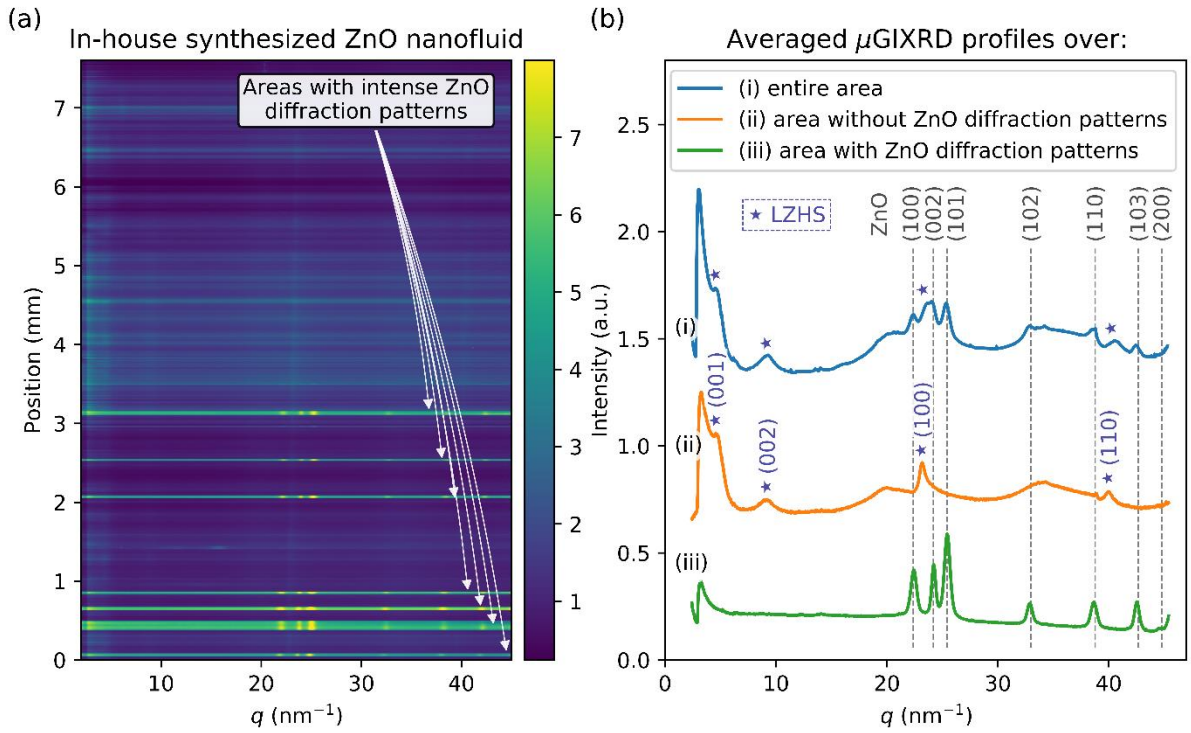

Figure 7. μGIXRD analysis of the residual surface patterns from evaporative drying of a 30 μL ZnO nanofluid sessile droplet on a ~1×1 cm^2 silicon wafer at room temperature and relative humidity of ~45%. The nanofluid was prepared from the in-house synthesized ZnO nanoparticles, dispersed in a mixture of cyclohexane and isobutylamine (5:1 volume:volume ratio). (a) shows a 2D intensity heat-map with respect to position of the scan point on the sample (along *z*-axis in **Figure 1**) and momentum transfer vector, *q*. Arrows show regions of the sample that produced intense ZnO diffraction patterns. Intensity (a.u.) shown in (a) was calculated as a percentile in the range 0.05-99.95% for better contrast. (b) presents μGIXRD line profile profiles averaged over: (i) the entire scan area, (ii) area that did not show ZnO diffraction patters, and (iii) are with intense ZnO diffraction patterns, marked with arrows in (a). ZnO peaks are indexed with accordance to the reference pattern (PDF 01-075-0576), and layered zinc hydroxide (LZH) structures are labelled with star markers, '⋆' and indexed according to [37-38].

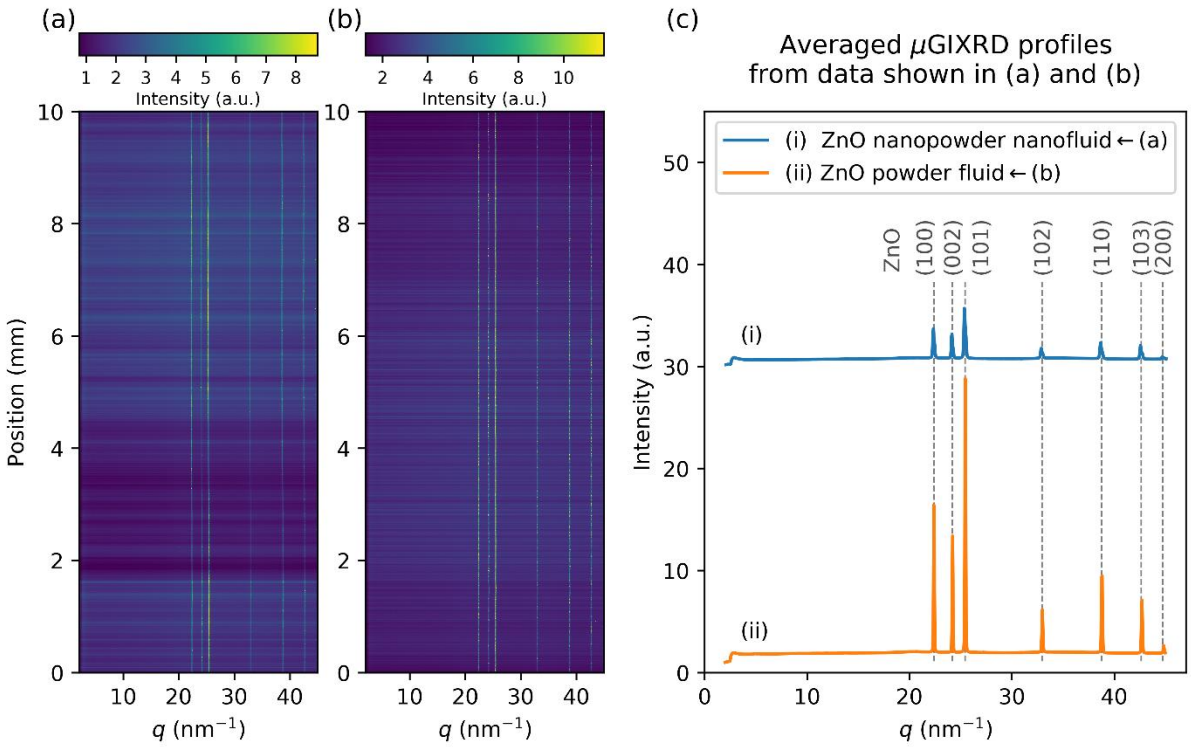

Figure 8. μGIXRD analysis of the residual surface patterns from evaporative drying of a 30 μL ZnO (nano)fluid sessile droplets on a ~1×1 cm^2 silicon wafer at room temperature and relative humidity of ~45%. The (nano)fluid were prepared from comercially acquired ZnO nanopowder and powder, dispersed in a mixture of cyclohexane and isobutylamine (5:1 volume:volume ratio). (a) and (b) show 2D intensity heat-maps for surface patterns from ZnO nanopowder and ZnO powder (nano)fluids, respectively. These heat-maps are plotted with respect to position of the scan point on the sample (along *z*-axis in **Figure 1**) and momentum transfer vector, q. Intensities (a.u.) in (a) and (b) were calculated as a percentile in the range 0.1 - 99.9% and 0.3 - 99.7%, respectively, to improve the contrast. (c) presents μGIXRD line profile profiles averaged over the entire scan areas for: (i) patterns from ZnO nanopowder nanofluid (data in (a)), and (ii) patterns from ZnO powder fluid (data in (b)).

The crystallinity of the residual ZnO (nano)crystal aggregates present within residual surface patterns was further evaluated from the peak broadening in the line profiles (**Figure 7b** and **Figure 8b**). The coherence lengths L_a values are listed in **Table S4** and discussed in some detail in the SI section (*cf.* SI9). In general, the L_a values for the ZnO residual nano(crystals) follow the same trend as the starting particles used for the preparation of ZnO nanofluids.

Further discussion on the effect of the particle morphology

The particles in the commercially acquired ZnO nanopowder and powder showed a wide range of morphologies and particle size distribution. These anisotropic particles could have affected capillary interactions in a drying droplet by forming loosely packed, quasi-static or arrested structures at the droplet surface [19]. As the mobility of these particles was reduced, they could have restrained the outward capillary flow in induced by evaporation Bénard cells, contrary to in-house synthesized sample with a more monodisperse shape and size distribution, which produced well specified spoke-like radial patterns of a bowtie projection on the surface.

It has been previously observed that when ZnO nanofluids were dried at relative humidity ~30%, ZnO nanorods and their large aggregates coexisted with short zinc hydroxide fibers, as the ambient H_2O molecules were crucial for the moisture assisted dissolution of ZnO nanorods [26]. Our experiments were performed at RH about 45%, which explains the presence of undissolved ZnO nanoparticles due to insufficient water molecule uptake from ambient air during droplet drying.

Residual surface patterns produced from the commercially acquired ZnO nanopowder and ZnO powder samples exhibited intense ZnO Wurtzite diffraction peaks across all the μGIXRD scanned regions (**Figure 8**) due to more prominent presence of undissolved ZnO residues. This is consistent with the SEM observations which confirmed that a network of residual fibers was covered by a large number of crystal agglomerates, accumulating especially at the fiber intersections (**Figure 5** and **Figure 6**). These agglomerates are attributed to ZnO crystals that did not undergo the complete dissolution-recrystallization process, which is a key step in the formation of hierarchical surface morphologies in the novel EISA process [26].

The coherence length, L_a, from the line profile analysis of μGIXRD peaks of the undissolved ZnO particles in the residual patterns was larger than that from the XRD peak analysis for the starting particles for all the three samples (*cf.* **Table 1** and **Table S4**) The relative change in the correlation length varies on the type of ZnO compound used, and amounts to 19.5%, 20.0% and 35.3 % for the in-house synthesized ZnO, and commercially acquired ZnO nanopowder and powder, respectively. This suggests that less crystalline particles underwent dissolution preferentially, whereas the more

crystallinity particles remained. Upon evaporation, these particles aggregated, forming agglomerates which were deposited across the fibrous network of the residual patterns.

Dissolution of the nanoparticles has been previously considered in terms of the Oswald-Freundlich (*i.e.* the modified Kelvin) equation, particularly within pharmaceutical nanotechnology (*cf.* section SI10) [39]. Accordingly, this equation predicts that the solubility will increase exponentially with decreasing particle size. David *et al.* [40] studied the solubility of ZnO nanoparticles of three different average particle diameters of 6, 20, and 71 nm respectively, and found that the particles larger than 20 nm had the same solubility as that of the bulk material, whereas the 6 nm particles exhibited the highest solubility, as predicted by the Oswald-Freundlich equation. Mudunkotuwa *et al.* [41] found that smaller ZnO nanoparticles (4-7 nm) showed a greater extent of dissolution compared to larger particles; however, the solubility of larger particles (15-130 nm) did not differ significantly.

Shape dependent surface enthalpy at the nanoscale level has also been discussed in terms of exposed surface structures. Crystal surfaces are complex and may exhibit a variety of planes, kinks, steps and defect sites, which lead to a different bonding environment compared to the bulk. The distribution of these structures can vary between particles and is often dependent on sample preparation. Meulenkamp [42] observed size dependent chemical reactivity in ZnO nanoparticles (of size 7.0 to 2.5 nm), which was attributed to the variations in the defect density and surface faceting of the nanocrystals. Gerischer and Sorg [43] showed that the dissolution rate of single crystal ZnO hexagonal needles was dependent on the crystal surface orientation. Michaelis *et al.* [44] showed that the dissolution behavior of polar and nonpolar crystal surfaces of single ZnO crystals in ultrapure water was controlled by the density of point defects and screw dislocations on the crystal surface.

Zhang *et al.* [45] examined surface enthalpies of ZnO crystals possessing different morphologies, and consequently demonstrated that nanoparticles and nanoporous composites had significantly lower surface enthalpies than nanorods and nanotetrapods. It was suggested that this arose from the difference in their morphologies, not their sizes. Similar observations were also made by Park *et al.* [46] in the study on nanocrystalline TiO_2 of different morphologies. In the study of Liu *et al.* [47], a correlation

between the differences in nanotopography and crystallographic facets present, as nanocrystals had a much larger fraction of atoms located at the preferred detachment/dissolution sites.

Mihranyan *et al.* [48] disputed the classical Oswald-Freundlich equation, stating that it was inadequate in describing the solubility of highly irregular nanoparticles in their study on dissolution of solid particles with rough surfaces. The surface roughness was modelled as fractal structures, and particles smaller than 100 nm with the same core diameter but various fractal dimensions exhibited a significant difference in the solubility. Schmidt *et al.* [49] studied the solubility of TiO_2 nanoparticles within aqueous solutions and observed that material samples containing the amorphous form showed higher solubility than their crystalline counterparts. Avramescu *et al.* [50] recently investigated the dissolution behavior of Zn, ZnO and TiO_2 nanomaterials within solutions mimicking body fluids. It was concluded that the crystalline form of TiO_2 was found to be an important factor, as the solubility of nano-anatase was significantly higher than that of nano-rutile. In addition, investigated nanomaterials exhibited higher solubility than their bulk counterparts.

Other studies have also supported possible correlations between solubility a material and its crystallinity. For example, natural glasses were found to dissolve at least 1.6 orders of magnitude faster compared to their mineral counterparts [51]. Dissolution of hydroxyapatite coatings, was associated with its crystallinity [52]. In addition, Li and co-workers [53] found that the solubility of the simultaneously nucleated $Zn(OH)_2$ and ZnO phases in aqueous solution was related to their crystalline nature.

The line profile analysis using the Scherrer equation and the TEM imaging show that the in-house synthesized ZnO nanoparticles were fairly monodisperse, single crystalline. As suggested by the Oswald-Freundlich equation, their relatively small size and large surface area make them more prone to dissolution, a key initial step in the proposed mechanism by Wu *et al.* [26]. For the larger, polydisperse nanopowder and powder samples, the larger particles consisted of multiple grains with size exceeding that of the in-house synthesized ZnO nanoparticles. The shape anisotropy [19] in the particles might contribute to particle clustering at the drop surface which would suppress the Bénard-Marangoni convections. This is evident from a less pronounced manifestation of the cellular pattern

with multiple spoke-like radial microstructures of a bow-tie projection, compared to the in-house synthesized ZnO nanoparticle sample.

Summary and concluding remarks

Residual patterns as a result of evaporation induced self-assembly (EISA) from a sessile drop of a reactive nanofluids have not been widely studied previously. As observed by Wu *et al.* [26], when a nanofluid droplet containing ZnO nanorods dispersion dries on a substrate, ZnO particles undergo morphological and chemical transformation to form organized structures composed of zinc hydroxide nanofibers. The key step in this process is the initial moisture-assisted dissolution of ZnO nanocrystals, crucial for the formation of soluble $Zn(OH)_2$ complexes. These complexes further assemble into clusters which then form the ultimate polycrystalline residual patterns, with the micromorphology controlled by convective and Marangoni flows and instabilities induced by evaporation of the solvent.

In this work, to shed light on how different morphologies and crystal structures might impact on proposed dissolution-recrystallization mechanism by Wu *et al.* [26], the residual patterns from three different ZnO particles, in-house synthesized ZnO nanoparticles, commercially acquired ZnO nanopowder and ZnO powder (Sigma-Aldrich) have been studied. The microscopic and nanoscopic structure of the residual pattern was correlated with that of the starting particles, *via* detailed TEM and XRD analyses. The average coherence length L_a value (from XRD peak broadening analysis) for the in-house prepared ZnO sample was 8.9 ± 0.2 nm, compared to those for the ZnO nanopowder and ZnO powder (40.9 ± 1.6 and 44.6 ± 1.8 nm, respectively).

The hierarchical surface patterns generated from evaporation of a 30 μL nanofluid sessile droplet on a silicon substrate showed different morphologies for the three types of ZnO particles used to prepare the nanofluid. For the in-house synthesized ZnO nanoparticles (**Figure 4**), the substrate was covered by 'spoke-like' radial structures, similar to those reported for gold nanoparticles on hydrophilic SiO_2/Si substrate [25]. These spoke-like radial structures were a solidified manifestation of Bénard-Marangoni cells (Wąsik *et al.,* in preparation) induced by evaporation, and they also resembled the shape of convective cells produced during the evaporation of toluene from polystyrene/toluene solution [21]. Furthermore, a small amount of undissolved ZnO nanoparticle aggregates was found on the constituent

fibers in only a few areas with a high fiber density (**Figure 4**h). The residual surface patterns from the nanofluids prepared from the commercially acquired ZnO nanopowder (**Figure 5**) and powder (**Figure 6**) appeared as dense layer of spoke-like radial patterns covering the entire surface of the silicon substrates. The width (~0.7 μm on average) of the constituent fibers in the residual pattern was similar to that in the in-house synthesized ZnO nanoparticle sample. However, ZnO crystal aggregates were found scattered across the fibrous structures.

Our analyses show that the residual hierarchical surface structures are linked to the morphology, size, and crystallinity of starting ZnO particles through its influence on the initial moisture-assisted rapid dissolution of isobutylamine-coated ZnO nanocrystals. The shape anisotropy of the particles might also play a role in modifying the Marangoni flows and the occurrence of the Bénard-Marangoni instability. Our finding is important to further understanding the novel mechanism underpinning the formation of the complex hierarchical surface patterns from evaporative drying of a reactive nanofluid sessile drop. It also points to the possibility to tailor the structure and morphology of the residual surface patterns for enhanced functionalities from the facile method of evaporative drying of ZnO (and other reactive) nanofluids in nanotechnological applications. A detailed microscopy analysis of the flow dynamics and *in situ* synchrotron X-ray surface scattering in the evaporating droplet would shed further light on the pattern formation mechanism, and will be the focus of our future work.

Associated content

Supporting Information

The Supporting Information (SI) is available free of charge on the ACS Publications website at DOI: 10.1021/acs.langmuir.7b03854. SI1. ZnO nanoparticle synthesis. SI2. ZnO particles TEM characterization. SI3. Size distribution of ZnO particles. SI4. ZnO particles XRD characterization. SI5. ZnO particles EDX characterization. SI6. DLS of ZnO nano/microfluids. SI7. Optical Microscopy of the residual surface patterns. SI8. μGIXRD analysis of the residual surface patterns. SI9.Coherence length analysis of the residual ZnO nanocrystals in the surface patterns. SI10. Ostwald–Freundlich (modified Kelvin) equation. SI11. Aging of ZnO nanofluids (photographs of vials with aged (nano)fluid solutions left to evaporate in very slow rate).

Corresponding Author

* E-mail: wuge.briscoe@bristol.ac.uk; Phone: +44 (0)117 3318256

Acknowledgements

Funding from the UK Engineering and Physical Sciences Research Council (EPSRC) through the Bristol Centre for Functional Nanomaterials (BCFN) (grant no. EP/G036780/1) is acknowledged. H.W. is supported by a Marie Skłodowska-Curie Individual Fellowship (Project Number 656830). W.H.B. would like to acknowledge funding from the EPSRC (EP/H034862/1 and Building Global Engagement in Research (BGER)), European Cooperation in Science and Technology (CMST COST) Action CM1101 "Colloidal Aspects of Nanoscience for Innovative Processes and Materials", and Marie Curie Initial Training Network (MCITN) on "Soft, Small, and Smart: Design, Assembly, and Dynamics of Novel Nanoparticles for Novel Industrial Applications" (NanoS3, Grant no. 290251). Dr Hazel Sparkes and Dr Natalie Pridmore are thanked for their help with XRD experiments, as Mr Jonathan Jones and Dr Sean Davis for their help with TEM and SEM imaging. We thank Dr Jean-Charles Eloi for the help with EDX analysis and Ms Anna Slastanova for the help with DLS measurements. We acknowledge the European Synchrotron Radiation Facility for provision of synchrotron radiation facilities (beamline ID13).

References

1. Whitesides, G. M.; Grzybowski, B., Self-Assembly at All Scales. *Science* **2002,** *295* (5564), 2418-2421.

2. Rodarte, A. L.; Cao, B. H.; Panesar, H.; Pandolfi, R. J.; Quint, M.; Edwards, L.; Ghosh, S.; Hein, J. E.; Hirst, L. S., Self-assembled nanoparticle micro-shells templated by liquid crystal sorting. *Soft Matter* **2015,** *11* (9), 1701-1707.

3. Han, W.; Lin, Z., Learning from "Coffee Rings": Ordered Structures Enabled by Controlled Evaporative Self-Assembly. *Angew. Chem. Int. Ed.* **2012,** *51* (7), 1534-1546.

4. Pilkington, G. A.; Briscoe, W. H., Nanofluids mediating surface forces. *Adv. Colloid Interface Sci.* **2012,** *179–182* (0), 68-84.

5. Briscoe, W. H., Depletion forces between particles immersed in nanofluids. *Curr. Opin. Colloid Interface Sci.* **2015,** *20* (1), 46-53.

6. Dinh, N. T.; Sowade, E.; Blaudeck, T.; Hermann, S.; Rodriguez, R. D.; Zahn, D. R. T.; Schulz, S. E.; Baumann, R. R.; Kanoun, O., High-resolution inkjet printing of conductive carbon nanotube twin lines utilizing evaporation-driven self-assembly. *Carbon* **2016,** *96*, 382-393.

7. Janowska, I., Evaporation-induced self-assembling of few-layer graphene into a fractal-like conductive macro-network with a reduction of percolation threshold. *Phys. Chem. Chem. Phys.* **2015,** *17* (12), 7634-7638.

8. Shim, J.; Yun, J. M.; Yun, T.; Kim, P.; Lee, K. E.; Lee, W. J.; Ryoo, R.; Pine, D. J.; Yi, G.-R.; Kim, S. O., Two-Minute Assembly of Pristine Large-Area Graphene Based Films. *Nano Lett.* **2014,** *14* (3), 1388-1393.

9. Dugas, V.; Broutin, J.; Souteyrand, E., Droplet Evaporation Study Applied to DNA Chip Manufacturing. *Langmuir* **2005,** *21* (20), 9130-9136.

10. Cheng, W.; Niederberger, M., Evaporation-Induced Self-Assembly of Ultrathin Tungsten Oxide Nanowires over a Large Scale for Ultraviolet Photodetector. *Langmuir* **2016,** *32* (10), 2474-2481.

11. Mitome, T.; Hirota, Y.; Uchida, Y.; Nishiyama, N., Porous structure and pore size control of mesoporous carbons using a combination of a soft-templating method and a solvent evaporation technique. *Colloids Surf., A* **2016,** *494*, 180-185.

12. Uchiyama, H.; Sasaki, R.; Kozuka, H., Evaporation-driven self-organization of photoluminescent organic dye-doped silica-poly(vinylpyrrolidone) hybrid films prepared by low-speed dip-coating. *Colloids Surf., A* **2014,** *453*, 1-6.

13. Thokchom, A. K.; Swaminathan, R.; Singh, A., Fluid Flow and Particle Dynamics Inside an Evaporating Droplet Containing Live Bacteria Displaying Chemotaxis. *Langmuir* **2014,** *30* (41), 12144-12153.

14. Mahmud, M. A.; MacDonald, B. D., Experimental investigation of interfacial energy transport in an evaporating sessile droplet for evaporative cooling applications. *Phys. Rev. E* **2017,** *95* (1).

15. Deegan, R. D., Pattern formation in drying drops. *Phys. Rev. E* **2000,** *61* (1), 475-485.

16. Deegan, R. D.; Bakajin, O.; Dupont, T. F.; Huber, G.; Nagel, S. R.; Witten, T. A., Capillary flow as the cause of ring stains from dried liquid drops. *Nature* **1997,** *389* (6653), 827-829.

17. Deegan, R. D.; Bakajin, O.; Dupont, T. F.; Huber, G.; Nagel, S. R.; Witten, T. A., Contact line deposits in an evaporating drop. *Phys. Rev. E* **2000,** *62* (1), 756-765.

18. Hu, H.; Larson, R. G., Marangoni Effect Reverses Coffee-Ring Depositions. *J. Phys. Chem. B* **2006,** *110* (14), 7090-7094.

19. Yunker, P. J.; Still, T.; Lohr, M. A.; Yodh, A. G., Suppression of the coffee-ring effect by shape-dependent capillary interactions. *Nature* **2011,** *476* (7360), 308-311.

20. Getling, A. V.; Brausch, O., Cellular flow patterns and their evolutionary scenarios in three-dimensional Rayleigh-Bénard convection. *Phys. Rev. E* **2003,** *67* (4), 046313.

21. Bassou, N.; Rharbi, Y., Role of Bénard−Marangoni Instabilities during Solvent Evaporation in Polymer Surface Corrugations. *Langmuir* **2009,** *25* (1), 624-632.

22. Pauliac-Vaujour, E.; Stannard, A.; Martin, C. P.; Blunt, M. O.; Notingher, I.; Moriarty, P. J.; Vancea, I.; Thiele, U., Fingering Instabilities in Dewetting Nanofluids. *Phys. Rev. Lett.* **2008,** *100* (17), 176102.

23. Homsy, G. M., Viscous Fingering in Porous Media. *Annu. Rev. Fluid Mech.* **1987,** *19*, 271-311.

24. Ajaev, V. S., Evolution of dry patches in evaporating liquid films. *Phys. Rev. E* **2005,** *72* (3), 031605.

25. Huang, J.; Kim, F.; Tao, A. R.; Connor, S.; Yang, P., Spontaneous formation of nanoparticle stripe patterns through dewetting. *Nat Mater* **2005,** *4* (12), 896-900.

26. Wu, H.; Chen, L. X.; Zeng, X. Q.; Ren, T. H.; Briscoe, W. H., Self-assembly in an evaporating nanofluid droplet: rapid transformation of nanorods into 3D fibre network structures. *Soft Matter* **2014,** *10* (29), 5243-5248.

27. Sun, B.; Sirringhaus, H., Solution-Processed Zinc Oxide Field-Effect Transistors Based on Self-Assembly of Colloidal Nanorods. *Nano Lett.* **2005,** *5* (12), 2408-2413.

28. Scherrer, P., Estimation of the size and internal structure of colloidal particles by means of röntgen. *Nachr. Ges. Wiss. Göttingen* **1918,** *2*, 96-100.

29. Dane, T. G.; Bartenstein, J. E.; Sironi, B.; Mills, B. M.; Alexander Bell, O.; Emyr Macdonald, J.; Arnold, T.; Faul, C. F. J.; Briscoe, W. H., Influence of solvent polarity on the structure of drop-cast electroactive tetra(aniline)-surfactant thin films. *Phys. Chem. Chem. Phys.* **2016,** *18* (35), 24498-24505.

30. Sironi, B.; Snow, T.; Redeker, C.; Slastanova, A.; Bikondoa, O.; Arnold, T.; Klein, J.; Briscoe, W. H., Structure of lipid multilayers via drop casting of aqueous liposome dispersions. *Soft Matter* **2016,** *12* (17), 3877-3887.

31. Zender, C., Particle size distributions: theory and application to aerosols, clouds, and soils. http://dust.ess.uci.edu/facts/psd/psd.pdf (accessed 12th Dec 2017).

32. Pacholski, C.; Kornowski, A.; Weller, H., Self-Assembly of ZnO: From Nanodots to Nanorods. *Angew. Chem. Int. Ed.* **2002,** *41* (7), 1188-1191.

33. Xu, S.; Wang, Z., One-dimensional ZnO nanostructures: Solution growth and functional properties. *Nano Res.* **2011,** *4* (11), 1013-1098.

34. Jiang, H. G.; Rühle, M.; Lavernia, E. J., On the applicability of the x-ray diffraction line profile analysis in extracting grain size and microstrain in nanocrystalline materials. *J. Mater. Res.* **1999,** *14* (02), 549-559.

35. Song, B.; Cui, X.; Wang, Y.; Si, L.; Kou, Z.; Tian, W.; Yi, C.; Sun, Y., Controllable Growth of Unique Three-Dimensional Layered Basic Zinc Salt/ZnO Binary Structure. *Cryst. Growth Des.* **2016,** *16* (9), 4877-4885.

36. Song, R. Q.; Xu, A. W.; Deng, B.; Li, Q.; Chen, G. Y., From Layered Basic Zinc Acetate Nanobelts to Hierarchical Zinc Oxide Nanostructures and Porous Zinc Oxide Nanobelts. *Adv. Funct. Mater.* **2007,** *17* (2), 296-306.

37. Poul, L.; Jouini, N.; Fiévet, F., Layered Hydroxide Metal Acetates (Metal = Zinc, Cobalt, and Nickel): Elaboration via Hydrolysis in Polyol Medium and Comparative Study. *Chem. Mater.* **2000,** *12* (10), 3123-3132.

38. Song, B.; Wang, Y.; Cui, X.; Kou, Z.; Si, L.; Tian, W.; Yi, C.; Wei, T.; Sun, Y., A Series of Unique Architecture Building of Layered Zinc Hydroxides: Self-Assembling Stepwise Growth of Layered Zinc Hydroxide Carbonate and Conversion into Three-Dimensional ZnO. *Cryst. Growth Des.* **2016,** *16* (2), 887-894.

39. Kaptay, G., On the size and shape dependence of the solubility of nano-particles in solutions. *Int. J. Pharm.* **2012,** *430* (1–2), 253-257.

40. David, C. A.; Galceran, J.; Rey-Castro, C.; Puy, J.; Companys, E.; Salvador, J.; Monné, J.; Wallace, R.; Vakourov, A., Dissolution Kinetics and Solubility of ZnO Nanoparticles Followed by AGNES. *J. Phys. Chem. C* **2012,** *116* (21), 11758-11767.

41. Mudunkotuwa, I. A.; Rupasinghe, T.; Wu, C.-M.; Grassian, V. H., Dissolution of ZnO Nanoparticles at Circumneutral pH: A Study of Size Effects in the Presence and Absence of Citric Acid. *Langmuir* **2012,** *28* (1), 396-403.

42. Meulenkamp, E. A., Size Dependence of the Dissolution of ZnO Nanoparticles. *J. Phys. Chem. B* **1998,** *102* (40), 7764-7769.

43. Gerischer, H.; Sorg, N., Chemical dissolution of zinc oxide crystals in aqueous electrolytes—An analysis of the kinetics. *Electrochim. Acta* **1992,** *37* (5), 827-835.

44. Michaelis, M.; Fischer, C.; Colombi Ciacchi, L.; Luttge, A., Variability of Zinc Oxide Dissolution Rates. *Environ. Sci. Technol.* **2017,** *51* (8), 4297-4305.

45. Zhang, P.; Xu, F.; Navrotsky, A.; Lee, J. S.; Kim, S.; Liu, J., Surface Enthalpies of Nanophase ZnO with Different Morphologies. *Chem. Mater.* **2007,** *19* (23), 5687-5693.

46. Park, T.-J.; Levchenko, A. A.; Zhou, H.; Wong, S. S.; Navrotsky, A., Shape-dependent surface energetics of nanocrystalline TiO2. *J. Mater. Chem.* **2010,** *20* (39), 8639-8645.

47. Liu, J.; Aruguete, D. M.; Murayama, M.; Hochella, M. F., Influence of Size and Aggregation on the Reactivity of an Environmentally and Industrially Relevant Nanomaterial (PbS). *Environ. Sci. Technol.* **2009,** *43* (21), 8178-8183.

48. Mihranyan, A.; Strømme, M., Solubility of fractal nanoparticles. *Surf. Sci.* **2007,** *601* (2), 315-319.

49. Schmidt, J.; Vogelsberger, W., Aqueous Long-Term Solubility of Titania Nanoparticles and Titanium(IV) Hydrolysis in a Sodium Chloride System Studied by Adsorptive Stripping Voltammetry. *J. Solution Chem.* **2009,** *38* (10), 1267-1282.

50. Avramescu, M.-L.; Rasmussen, P. E.; Chénier, M.; Gardner, H. D., Influence of pH, particle size and crystal form on dissolution behaviour of engineered nanomaterials. *Environ. Sci. Pollut. Res.* **2017,** *24* (2), 1553-1564.

51. Wolff-Boenisch, D.; Gislason, S. R.; Oelkers, E. H., The effect of crystallinity on dissolution rates and CO2 consumption capacity of silicates. *Geochim. Cosmochim. Acta* **2006,** *70* (4), 858-870.

52. Xue, W.; Liu, X.; Zheng, X.; Ding, C., Effect of hydroxyapatite coating crystallinity on dissolution and osseointegration in vivo. *J. Biomed. Mater. Res., Part A* **2005,** *74A* (4), 553-561.

53. Li, P.; Liu, H.; Lu, B.; Wei, Y., Formation Mechanism of 1D ZnO Nanowhiskers in Aqueous Solution. *J. Phys. Chem. C* **2010,** *114* (49), 21132-21137.

SUPPORTING INFORMATION

Hierarchical surface patterns upon evaporation of a ZnO nanofluid droplet: Effect of particle morphology

Patryk Wąsik[a,b], Christian Redeker[b], Thomas G. Dane[c], Annela M. Seddon[a,d], Hua Wu[b], and Wuge H. Briscoe[b,]*

[a] Bristol Centre for Functional Nanomaterials (BCFN), HH Wills Physics Laboratory, University of Bristol, Tyndall Avenue, Bristol BS8 1TL, UK

[b] School of Chemistry, University of Bristol, Cantock's Close, Bristol BS8 1TS, UK

[c] The European Synchrotron (ESRF) 71, Avenue des Martyrs, Grenoble, France

[d] School of Physics, HH Wills Physics Laboratory, Tyndall Avenue, University of Bristol, Bristol BS8 1TL, UK

Information:

This chapter has been published as a supporting information to the research article: **Wąsik, P**.; Redeker, C.; Dane, T. G.; Seddon, A. M.; Wu, H.; Briscoe, W. H., Hierarchical Surface Patterns upon Evaporation of a ZnO Nanofluid Droplet: Effect of Particle Morphology. *Langmuir* **2018**, *34* (4), 1645-1654. DOI: 10.1021/acs.langmuir.7b03854. This chapter has been authored by the candidate with no more input from co-authors and supervisors that would have been provided in a conventional thesis chapter. Individual contributions as in Chapter 2.

SI1. ZnO nanoparticle synthesis

The in-house ZnO nanoparticles were synthesised according to a modified method described by Sun *et al.* [1]. In the course of synthesis 0.8189 g of zinc acetate dihydrate (Sigma-Aldrich, ACS reagent ≥ 98%) and 250 μL of Mili-Q water (18.2 MΩ·cm at 25 °C) were added to 42 mL of methanol (laboratory grade) in a 250 mL double-neck round bottom flask (RBF). The solution was heated under

reflux to 60 °C under stirring. 0.4865 g of potassium hydroxide (Fisher Scientific, purity 85%) dissolved in 23 mL of methanol was introduced dropwise into the RBF in a period of 10-15 minutes. After the addition of KOH solution, the mixture was heated under reflux to 60 °C for 2 hours and 15 minutes under stirring. Subsequently, the mixture was cooled down and condensed to approximately 1/10 of its initial volume using a rotary evaporator. The condensed solution was heated under reflux at 60 °C for 44 hours and 20 minutes under stirring. The solution containing ZnO nanoparticles was left to cool to the room temperature (RT) and then transferred to a 100 mL RBF. The nanoparticles were then washed using the following procedure. 20 mL of methanol was added to the solution and stirred for 5 minutes. The solution was left for 30 minutes to settle down, and the supernatant of the solution was removed. These steps were repeated three times, using 20 mL of methanol for the first two washes and 40 mL of methanol for the last wash. The excess liquid was evaporated under reduced pressure using a rotary evaporator and the flask was left inside of a vacuum oven dryer at RT for 100 minutes. The sediment was scraped off the wall of the flask using a spatula, giving the yield of 281.1 mg of ZnO powder.

SI2. ZnO particles TEM characterization

For the Transmission Electron Microscopy (TEM) characterization, ZnO particles were weighed and added to a mixture of methanol and water (2:1 volume:volume ratio, respectively) to form suspensions of final concentration 1 mg/mL. The suspensions were sonicated in an ultrasonic bath without heating for 140 minutes to form homogeneous dispersions. After the sonication, 5μL of each solution was pipetted onto the surface of a carbon coated TEM copper grid and left to evaporate. TEM imaging was performed using a JEOL JEM-1400 Transmission Electron Microscope.

SI3. Size distribution of ZnO particles

The sizing of the in-house synthesized ZnO nanoparticles and commercially available ZnO nanopowder and ZnO powder was performed using ImageJ software. The size distribution calculations were based on 1245 measurements of a single particle diameter with the approximation of a spherical shape of the particles for the in-house synthesized ZnO nanoparticles. Maximum diameter (the greatest distance between any two surface points of the particle) distribution for the commercially acquired ZnO nanopowder and ZnO powder were calculated based on 1307 and 686 measurements, respectively.

The size distributions for all ZnO samples were fitted with the lognormal distribution function, eq S1:

$$y = \frac{1}{\ln(\sigma_g)\sqrt{2\pi}} \exp\left[-\frac{(\ln x - \ln M)^2}{2\ln^2(\sigma_g)}\right] \quad \text{(S1)}$$

where y is the probability density function, x is the particle size, σ_g is the geometric standard deviation, and M is the geometric mean particle size by count [2]. The geometric mean particle diameter M for lognormal is the same as the number median diameter, that is essentially the size below or above which half the total number of particles is found [2]. The physical meaning of the geometric standard deviation, σ_g, according to Zender [3], is that 68.3% of all particles in lognormal distribution lie in between M/σ_g and $M\cdot\sigma_g$. The lognormal size distribution fitting parameters (M and σ_g) and their physical interpretations for ZnO particles are shown in **Table S1**. The ZnO nanopowder sample (**Figure 2b**) had particle sizes varying from 10 nm for the smallest spherical particles to up to 530 nm elongated parallelepiped crystals. The size distribution of the ZnO nanopowder sample is shown in **Figure 2e**, with calculated lognormal fit parameters of M = 71.7 nm (the mean maximum dimension) and σ_g = 2.0 nm (the geometric standard deviation). This means that 68.3% of all particles in ZnO nanopowder sample had the maximum dimension between 36.2 nm and 141.8 nm (between M/σ_g and $M\cdot\sigma_g$). The ZnO powder (**Figure 2c**) contained particles with sizes ranging from 15 nm for the smallest spheres to more than 1 μm for elongated crystals, with lognormal fit parameters M = 133.4 nm and σ_g = 2.2 nm. Based on its size distribution analysis (**Figure 2f**), it is concluded that 68.3% of all particles in ZnO powder sample exhibited the maximum dimension between 61.20 nm and 290.86 nm.

Table S1. Lognormal size distribution fit parameters for ZnO particles.

Particles	Geometric mean particle size, M (nm)	Geometric standard deviation, σ_g	M/σ_g (nm)	$M\cdot\sigma_g$ (nm)
ZnO nanoparticles	9.16	1.24	7.39	11.36
ZnO nanopowder	71.73	1.97	36.17	141.79
ZnO powder	133.42	2.18	61.20	290.86

SI4. ZnO particles XRD characterization.

The XRD analysis of ZnO compounds was performed at RT in the Bragg-Brentano geometry using a D8 Advance Bruker-AXS diffractometer with copper Kα radiation (λ = 1.54 Å). Counting time was set to 8 seconds for the in-house synthesized ZnO nanoparticles, and 4 seconds for the commercially acquired ZnO particles (powder and nanopowder) for each 0.05° step in the diffraction angle 2Θ range of 10-90°.

When a crystalline material is illuminated by X-rays, the radiation can be coherently scattered by the crystal lattice as specified by Bragg's law [4]:

$$n\lambda = 2d \sin\theta \tag{S2}$$

where n is the order of diffraction (positive integer), λ is the X-ray wavelength, d is the lattice spacing, and θ is the scattering angle. The shape of the XRD profile is derived from the microstructure of the sample, usually referred to as size and strain broadening due to the finite size of coherently diffracting domains (crystallites) and lattice strains caused by the presence of lattice defects. Information in terms of an average crystallite size and microstrain can be obtained from the width of individual diffraction peaks by line profile analysis methods using the Scherrer formula [5] or the William-Hall plot [6]. In this paper, the crystallinity of the ZnO samples was evaluated on the basis of the coherence length L_a, gives an indication of the lower limit of the crystal domain size [7-8]:

$$L_a = \frac{2\pi K}{\Delta q} \tag{S3}$$

where K is the shape factor from the Scherrer formula [9], and Δq is the width at the half maximum of the diffraction peak expressed in the unites of the wave vector q, where $q = 4\pi \sin\theta / \lambda$. Δq was obtained by fitting peak profiles with a Gaussian function. This was an arbitrary choice of the peak profile function, as a real profile can, in fact, have any shape [10]. The obtained L_a values give an indication of the broadening effects caused by the finite domain size and lattice distortion, which will be referred to as the sample crystallinity in this paper.

Figure 3 presents XRD diffraction profiles of the three types of ZnO particles. All the peaks were characteristic for a Wurtzite structure of ZnO (PDF 01-075-0576) and adequately indexed by Miller indices (*hkl)* as (100), (002), (101), (102), (110), (103), (200), (112), (201), (004), (202), (104), and (203). The XRD line profile of the in-house synthesized ZnO sample (*cf.* **Figure 2a**) exhibits large peak

broadening due to the finite size of coherently diffracting domains (often referred to as crystallite size) and lattice strain effects. The line profiles of commercially acquired ZnO particles, nanopowder and powder (*cf.* **Figure 3b-c**) show sharp peaks, where split peaks due to Cu radiation $K_{\alpha 1}$ and $K_{\alpha 2}$ doublets can be observed, especially for the peaks at higher diffraction angles ($q > 40$ nm^{-1}). The XRD results indicate that the commercial ZnO nanopowder and powder samples possessed higher crystallinity (larger size of coherently scattering domains and less strain caused by crystal defects) compared to the in-house prepared ZnO nanoparticles.

SI5. ZnO particles EDX characterization.

The energy-dispersive X-ray spectroscopy (EDX) characterization of ZnO particles was performed using JSM-IT300 SEM (JEOL) scanning electron microscope (SEM) coupled with the X-Max 80 mm^2 Silicon Drift Detector (Oxford Instruments) and the supplied AZtec 2.3 software (Oxford Instruments). ZnO powders were compressed between two microscope glass slides to form flake-like pellets, which were then placed onto cupped aluminum stubs prior to the measurements. Surfaces of as formed ZnO flake-like pellets were excited with 5 keV electron beam to refine the surface analysis to obtain C peaks as opposed to a bulk with more Zn compared to C. For the in-house synthesized ZnO and commercially acquired ZnO nanopowder, measurements took 5 minutes. For the commercially acquired ZnO powder, a 1 minute pulse measurement was performed. The EDX spectra are presented in **Figure S1**, and the calculated atomic compositions (atomic percentage) of ZnO powders are shown in **Table S2**. The measurements indicated that small amounts of carbon, likely due to airborne contaminants, were present within all the samples: the in-house synthesized ZnO nanoparticles (3.14%), and commercially acquired ZnO nanopowder (5.21%) and ZnO powder (5.96%). In addition, small amounts of potassium (2.38%) was present in the in-house synthesized ZnO, most probably a residue from the synthesis (*cf.* SI1). A background noise coming from aluminum stub is also present in the EDX spectra.

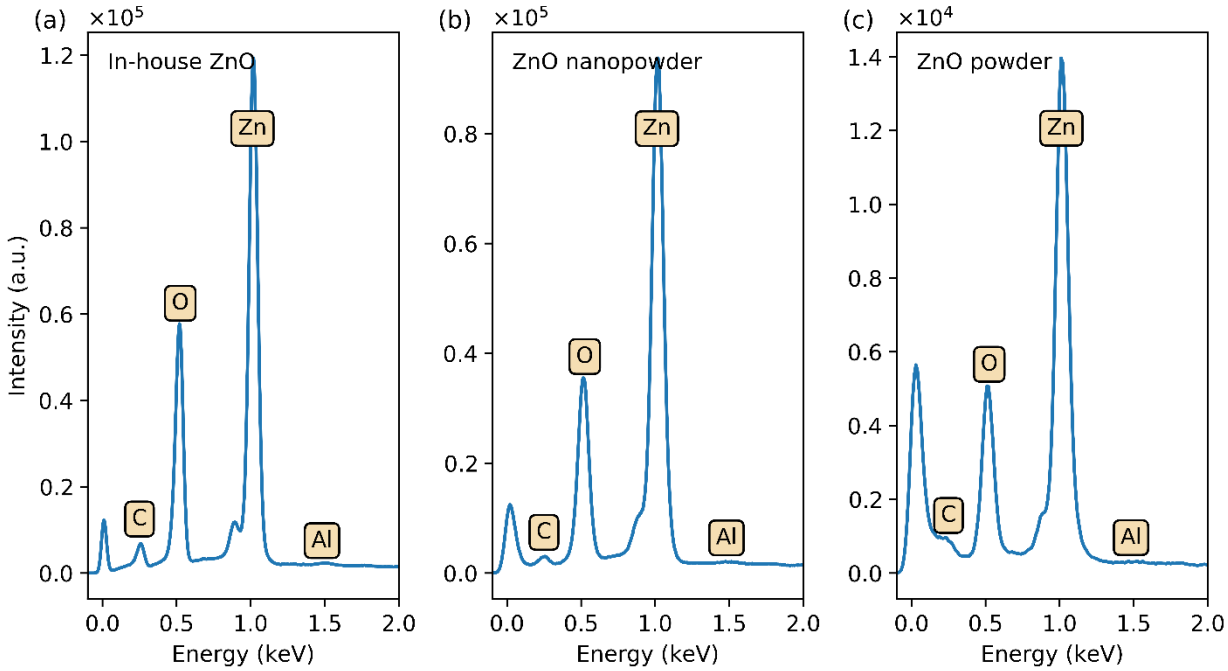

Figure S1. EDX data of different ZnO particles: (a) the in-house synthesized ZnO nanoparticles, and commercially acquired (b) ZnO nanopowder and (c) ZnO powder.

Table S2. Calculated composition (atomic percentage) of the in-house synthesized ZnO nanoparticles, and commercially acquired ZnO nanopowder and ZnO powder, based on the EDX elemental analysis.

Element	Atomic %		
	In-house ZnO	ZnO nanopowder	ZnO powder
C	3.14	5.21	5.96
O	42.68	38.94	37.92
Zn	51.47	55.85	55.80
Al	0.33	-	0.32
K	2.38	-	-

SI6. DLS of ZnO nano/microfluids.

The dynamic light scattering (DLS) analysis of the ZnO nano/microfluids was performed using Zetasizer Nano-ZS (Malvern Instruments) and the software v7.12 supplied by the manufacturer. ZnO nano/microfluid were prepared as described in the „Evaporative drying of ZnO nano/microfluid droplets" section in the main article. In short, ZnO particles (in-house synthesized ZnO nanoparticles, and commercially acquired ZnO nanopowder and ZnO powder) were dispersed in a mixture of cyclohexane and isobutylamine (5:1 volume:volume) to 1 mg/mL concentration by 2 hours sonication. The DLS measurements of each ZnO nano/microfluid were performed immediately after the sonication

(3 sets of 60 seconds measurements at 25 °C per sample). The system parameters in the software were set to the material (ZnO) refractive index (RI) of 2.00 [11] and absorption of 0.01. Properties of the dispersant were calculated based on the weighted contributions proportional to the volume ratio of its components, cyclohexane (RI of 1.4235 at 589 nm and viscosity of 0.894 mPa·s at 25 °C) [11], and isobutylamine (RI of 1.3988 at 589 nm and viscosity of 0.571 mPa·s at 25 °C) [11], and were entered to the software as RI of 1.40 and viscosity of 0.84 mPa·s.

The DLS results are presented in **Table S3**. They indicated cluster formation (1 - 2 μm in size) in all ZnO nano/microfluids, as the suspensions were not inherently stable. As the evaporation process happens rapidly, it is believed that the cluster size has a negligible effect on the final residual surface pattern formation from a sessile drop of a ZnO nano/microfluid.

Table S3. Intensity particle size distribution (PSD) parameters calculated from the DLS measurements of ZnO nano/microfluids.

Intensity PDS parameters	**Nano/microfluids**		
	In-house ZnO	ZnO nanopowder	ZnO powder
Z-Average diameter (μm)	1097	1950	1140
Polydispersity index (PDI)	0.773	0.130	0.209
Peaks (μm)	371	2058	1326

SI7. Optical Microscopy of the residual surface patterns.

Optical microscopy images of residual surface patterns are shown in **Figure S2**.

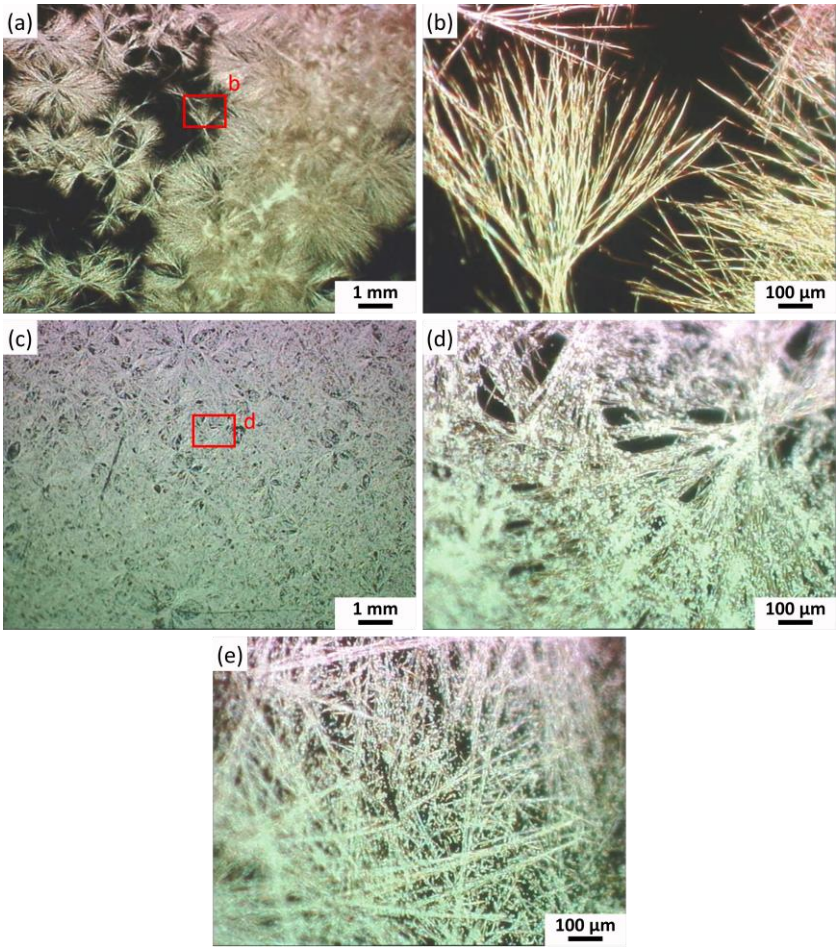

Figure S2. Optical images of the residual surface patterns from evaporative drying of a 30 µL ZnO (nano)fluid sessile droplets on a ~1×1 cm2 silicon wafer at room temperature and relative humidity of ~45%. Nanofluids were prepared from: (a-b) the in-house synthesized ZnO nanoparticles, commercially acquired ZnO (c-d) nanopowder and (e) powder, that were dispersed in a mixture of cyclohexane and isobutylamine (5:1 volume:volume ratio). The rectangular regions in the figures are enlarged, with their labels corresponding to those of the figures.

SI8. µGIXRD analysis of the residual surface patterns.

The micro-focus grazing incidence X-ray diffraction (µGIXRD) analysis of the residual surface patterns was performed at Beamline ID13 at the European Synchrotron Radiation Facility (France). On each sample, a linear, one directional scan was performed over the length of the sample (~1 cm), recording a µGIXD pattern every 2 µm. The beam radiation wavelength was 0.939 Å, the beam size was 2 × 2 μm^2, with the footprint on sample ~ 300 × 2 μm^2, and the incident angle was 0.4°. The

diffraction patterns appeared as isotropic rings, and they were reduced to one-dimensional line profiles using *pygix* [12], based heavily on *pyFAI*, a pythonic library developed the perform 1D azimuthal or 2D radial integrations of diffraction images [13].

Figures 7 and **8** present 2D heat-maps (intensity vs. momentum transfer vector q) from the μGIXRD data by recording an X-ray diffraction pattern at every 2 μm interval across the z-axis (**Figure 1**). To improve the contrast in 2D heat-map plots, intensities were calculated as a percentile (*numpy.percentile* function from *NumPy* (14)) in ranges: 0.05-99.95% (**Figure 7a**), 0.1 - 99.9% (**Figure 8a**), and 0.3 - 99.7% (**Figure 8b**). To provide statistical information for each sample, diffraction profiles were averaged across the scan area of interest and are shown as line plots in **Figure 7b** and **Figure8c**, with diffraction peaks that can be assigned to ZnO, indexed as (100), (002), (101), (102), (110), (103), and (200) according to the ZnO reference standard (PDF 01-075-0576).

SI9. Coherence length analysis of the residual surface patterns

The ZnO (nano)crystal aggregates present within residual surface patterns, were analyzed based upon the averaged micro-focus Grazing Incidence X-ray Diffraction (μGIXRD) profiles (**Figure 7b** and **Figure 8b**). The crystallinity of these aggregates was assessed in terms of their coherence lengths L_a (eq S3), as listed in **Table 1**. However, it should be borne in mind that using the grazing incidence geometry, which is a powerful technique to study thin films, introduces a geometric smearing effect caused by the finite length of the beam footprint on the sample. This is pronounced at large scattering angles (GIXRD and GIWAXS - grazing incident wide angle X-ray scattering), which could limit the coherence length resolution, reaching about 5% of the q value [14]. On the other hand, using a micro-focused X-ray beam of 2×2 μm^2 from a synchrotron light source to perform grazing incident diffraction as in this study reduced the beam footprint to 300 × 2 μm^2, improving the scan resolution. Nevertheless, the values calculated for the ZnO (nano)crystal aggregates are used semi-quantitatively to compare between samples.

Table S4. Correlation length (L_a) calculated for the ZnO residues present in residual surface patterns produced by evaporative drying of ZnO (nano)fluid droplets on a silicon substrate. Calculations are

performed on the parameters obtained by fitting peaks with a Gaussian function. Errors are calculated by the partial derivative method.

	ZnO (nano)fluid:					
	In-house synthesized ZnO NP		ZnO nanopowder		ZnO powder	
Peak (hkl)	L_a (nm)	± δL_a (nm)	L_a (nm)	± δL_a (nm)	L_a (nm)	± δL_a (nm)
(100)	8.9	0.3	53.8	0.5	66.28	0.6
(002)	12.0	0.4	49.4	0.3	67.34	1.1
(101)	9.4	0.2	63.3	0.7	69.50	0.3
(102)	11.8	0.9	43.5	1.2	52.36	1.7
(110)	9.8	0.6	41.6	0.8	56.10	1.0
(103)	12.2	0.7	42.4	0.9	50.43	1.7
average:	10.7	0.5	49.00	0.7	60.34	1.1

Table S4 presents the coherence lengths L_a calculated for peaks indexed as (100), (002), (101), (102), (110) and (103) according to eq 2 in the main text, where the shape constant K was assumed to be unity. The average coherence length of the ZnO residues - left after evaporative drying - composed of in-house synthesized ZnO nanoparticles, is equal to 10.7 nm and the largest value, 12.0 nm, accounts for the (002) reflection along the preferential growth direction of ZnO nanostructures [15-16]. The average values of L_a for the ZnO residues formed from nanofluids of comercially acquired ZnO nanopowder and powder, are 49.0 nm and 60.3 nm respectively. However, contrary to the ZnO residuals from in-house prepared ZnO nanofluid, the L_a values for the (002) reflection are not the largest amongst the first three most pronounced peaks ((100), (002) and (101)). In general, the L_a values for the ZnO residual nano(crystals) follow the same trend as the starting particles used for the preparation of ZnO nanofluids, *i.e.* increasing with the crystal sizes of the particles used for the preparation of ZnO nanofluids (**Figure 2c-d**).

Comparing **Table 1** in the main text and **Table S4**, the relative change in the correlation length varies on the type of ZnO compound used for (nano)fluid preparation, and equals to 19.5%, 20.0% and 35.3 % for the in-house synthesized ZnO, and commercially acquired ZnO nanopowder and ZnO powder, respectively. This change could be attributed to the different instrumental effects, which would have led to the same relative change in the peak broadening for all the samples. This suggests that less

crystalline particles underwent dissolution preferentially, whereas the more crystallinity particles remained.

SI10. Oswald-Freundlich (modified Kelvin) equation

Dissolution of the nanoparticles has been previously considered in terms of the Oswald-Freundlich (modified Kelvin) equation (eq S4), particularly within pharmaceutical nanotechnology. The equation describes the size dependent solubility of solid particles in solutions:

$$\chi_{A(\beta)} = \chi^0_{A(\beta)} \exp\left(\frac{2V^0_{A(\alpha)}\sigma^0_{\alpha/\beta}}{RTr_\alpha}\right) \quad \text{(S4)}$$

where $\chi_{A(\beta)}$ is the solubility of component A in the form of a spherical, pure phase of radius r_α in a given solution β at temperature T and at fixed pressure p; $\chi^0_{A(\beta)}$ is the solubility of an infinitely large phase α; $\sigma^0_{\alpha/\beta}$ is the interfacial energy between the two phases (assumed to be size independent); $V^0_{A(\alpha)}$is the molar volume of the pure phase $A(\alpha)$; and R is the universal gas constant [17]. Accordingly, this equation which predicts that the solubility will increase exponentially with decreasing particle size.

SI11. Aging of ZnO nanofluids.

Figure S3 presents vials with aged ZnO nanofluids.

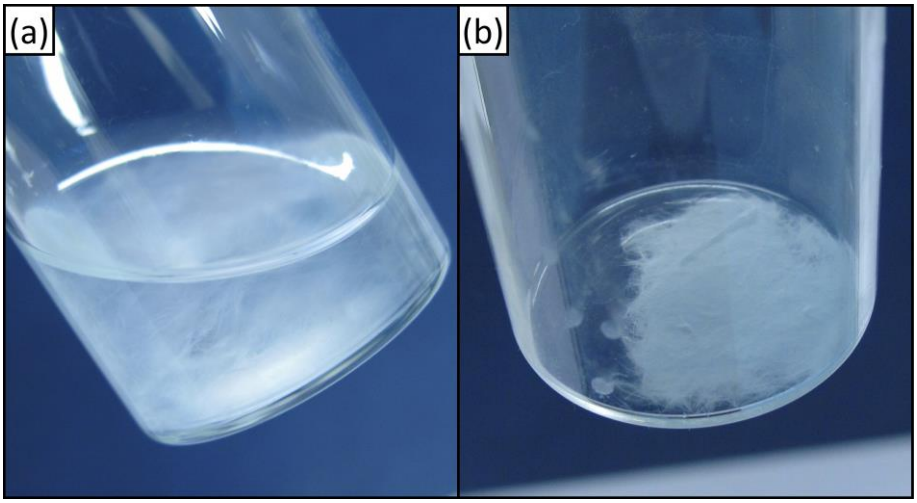

Figure S3. Bottles filled with nanofluids composed of (a) in-house synthesized ZnO and (b) commercially acquired ZnO nanopowder, both dispersed in a mixture of cyclohexane and isobutylamine (5:1 v:v) to the final concentration of 0.1 mg/mL, were left with loosened caps for 7 weeks. White, long fibers dispersed in the solution are observed in (a), where evaporation rate was

much slower, comparing to dried pattern in (b), with faster evaporation rate. Slower evaporation rate increased the length of as formed fibers, which is with an agreement with our previous observations (Hua Wu, in preparation).

SI12. References

1. Sun, B.; Sirringhaus, H., Solution-Processed Zinc Oxide Field-Effect Transistors Based on Self-Assembly of Colloidal Nanorods. *Nano Lett.* **2005,** *5* (12), 2408-2413.

2. Smith, J. E.; Jordan, M. L., Mathematical and graphical interpretation of the log-normal law for particle size distribution analysis. *J. Colloid Sci.* **1964,** *19* (6), 549-559.

3. Zender, C. Particle size distributions: theory and application to aerosols, clouds, and soils. http://dust.ess.uci.edu/facts/psd/psd.pdf (accessed 12th Dec 2017).

4. Bragg, W. H.; Bragg, W. L., The Reflection of X-rays by Crystals. *Proc. R. Soc. London, Ser. A* **1913,** *88* (605), 428-438.

5. Scherrer, P., Estimation of the size and internal structure of colloidal particles by means of röntgen. *Nachr. Ges. Wiss. Göttingen* **1918,** *2*, 96-100.

6. Williamson, G. K.; Hall, W. H., X-ray line broadening from filed aluminium and wolfram. *Acta Metall.* **1953,** *1* (1), 22-31.

7. Dane, T. G.; Bartenstein, J. E.; Sironi, B.; Mills, B. M.; Alexander Bell, O.; Emyr Macdonald, J.; Arnold, T.; Faul, C. F. J.; Briscoe, W. H., Influence of solvent polarity on the structure of drop-cast electroactive tetra(aniline)-surfactant thin films. *Phys. Chem. Chem. Phys.* **2016,** *18* (35), 24498-24505.

8. Sironi, B.; Snow, T.; Redeker, C.; Slastanova, A.; Bikondoa, O.; Arnold, T.; Klein, J.; Briscoe, W. H., Structure of lipid multilayers via drop casting of aqueous liposome dispersions. *Soft Matter* **2016,** *12* (17), 3877-3887.

9. Langford, J. I.; Wilson, A. J. C., Scherrer after sixty years: A survey and some new results in the determination of crystallite size. *J. Appl. Crystallogr.* **1978,** *11* (2), 102-113.

10. Leoni, M.; Di Maggio, R.; Polizzi, S.; Scardi, P., X-ray Diffraction Methodology for the Microstructural Analysis of Nanocrystalline Powders: Application to Cerium Oxide. *J. Am. Ceram. Soc.* **2004,** *87* (6), 1133-1140.

11. Rumble, J. R.; Rumble, J., *CRC Handbook of Chemistry and Physics, 98th Edition (Internet Version 2018)*. CRC Press LLC: 2017.

12. Dane, T. G. pygix - a generic python library for performing reduction of grazing-incidence and fiber X-ray scattering data. https://github.com/tgdane/pygix (accessed 06 Jun 2018).

13. Ashiotis, G.; Deschildre, A.; Nawaz, Z.; Wright, J. P.; Karkoulis, D.; Picca, F. E.; Kieffer, J., The fast azimuthal integration Python library: pyFAI. *J. Appl. Crystallogr.* **2015,** *48* (2), 510-519.

14. Smilgies, D.-M., Scherrer grain-size analysis adapted to grazing-incidence scattering with area detectors. *J. Appl. Crystallogr.* **2009,** *42* (6), 1030-1034.

15. Xu, S.; Wang, Z., One-dimensional ZnO nanostructures: Solution growth and functional properties. *Nano Res.* **2011,** *4* (11), 1013-1098.

16. Pacholski, C.; Kornowski, A.; Weller, H., Self-Assembly of ZnO: From Nanodots to Nanorods. *Angew. Chem. Int. Ed.* **2002,** *41* (7), 1188-1191.

17. Kaptay, G., On the size and shape dependence of the solubility of nano-particles in solutions. *Int. J. Pharm.* **2012,** *430* (1–2), 253-257.

Dendritic surface patterns from Bénard-Marangoni instabilities upon evaporation of a reactive ZnO nanofluid droplet: A fractal dimension analysis

Patryk Wąsik[a,b], Annela M. Seddon[a,c], Hua Wu[b], and Wuge H. Briscoe[b,]*

[a] Bristol Centre for Functional Nanomaterials (BCFN), HH Wills Physics Laboratory, University of Bristol, Tyndall Avenue, Bristol BS8 1TL, UK

[b] School of Chemistry, University of Bristol, Cantock's Close, Bristol BS8 1TS, UK

[c] School of Physics, HH Wills Physics Laboratory, Tyndall Avenue, University of Bristol, Bristol BS8 1TL, UK

Information

This chapter has been published as a communication article: **Wąsik, P.**; Seddon, A. M.; Wu, H.; Briscoe, W. H., Dendritic surface patterns from Bénard-Marangoni instabilities upon evaporation of a reactive ZnO nanofluid droplet: A fractal dimension analysis. *J. Colloid Interface Sci.* **2019**, 536, 493-498. DOI: 10.1016/j.jcis.2018.10.077. This chapter has been authored by the candidate with no more input from co-authors and supervisors that would have been provided in a conventional thesis chapter. PW performed all the experiments and data analysis and wrote the manuscript, PW, HW, and WHB designed the project, WHB co-wrote the manuscript, AMS and WHB supervised the project, and all co-authors commented on the manuscript.

Abstract

We present a box counting fractal dimension (FD) analysis of the dendritic patterns obtained under conditions far from equilibrium *via* rapid evaporation of a sessile drop containing *reactive* ZnO

nanoparticles. These dendrites were manifestations of solidified Bénard-Marangoni (BM) instability convection cells, and we previously noted that their complex hierarchical morphologies were superficially analogous to the foliage of red algae, Spanish dagger, or spider plant. The fractal dimension of the Bénard-Marangoni dendrites was found to vary in the range of 1.77 – 1.89 and also depend on the size of the Bénard-Marangoni cells. These fractal dimension results were correlated with the morphological details of the Bénard-Marangoni cells and ZnO particle characteristics, providing a quantitative description of such complex surface patterns emerging from the dynamic process of the Bénard-Marangoni instability.

Keywords

Evaporation Induced Self-Assembly, zinc oxide, evaporative drying, reactive nanofluids, Bénard-Marangoni instabilities, coffee ring effect, fractal dimension analysis.

Evaporation of a particle laden droplet represents a simple and versatile method to create intricate patterns and particle arrangements on surfaces over different length scales for device fabrication and surface modification – a process termed evaporation induced self-assembly (EISA) [1-2]. Most often, the dispersed particles are *inert*, and the residual pattern formation is determined by inter-particle forces and evaporation-induced solvent flows, which can be controlled by particle size, concentration, solvent composition or evaporation rate.

Our recent study on evaporation of *reactive* ZnO nanofluid sessile droplets [3] has shown that *in situ* generated molecular and particulate species could collude with and modify the solvent flow during evaporation *via* a mechanism different from that observed in the coffee ring effect [4], which would significantly affect the ultimate residual surface pattern. The mechanism is elucidated and described in some detail in Ref. [3] and Chapter 1. In this process, the initial moisture-assisted dissolution of isobutylamine-coated ZnO nanoparticles was identified as a key step [5]. We have also shown that, by varying the morphology, size, and crystallinity of the ZnO particles, it is possible to control the dissolution of the ZnO nanocrystals, which would modify solvent flows and instabilities and in turn the morphology of the residual surface structures [6].

The EISA process based on reactive ZnO nano/microfluids can result in a plethora of hierarchical surface patterns composed of fibres or dendrites [3, 5-6]. For instance, the dendritic patterns triggered by Bénard-Marangoni (BM) instabilities [7-8] were analogous to the foliage of red algae, Spanish dagger, or spider plant [3]. To go beyond such a descriptive account and to seek understanding of the correlation between the surface pattern and the underpinning physical parameters, here we perform fractal dimension (FD) analysis of the surface patterns.

Fractal dimension analysis has evolved since the early work by Mandelbrot in 1982 [9], who described complex geometrical structures that imposed difficulties in representing their form using the classical Euclidean geometry. These irregular structures were called *fractals* and exhibited self-similarities, *i.e.* repetitions of complicated structures at many length scales [10]. Familiar theoretical fractal examples include a Cantor set, von Koch curves, and Sierpiński triangles defined by recursive algorithms that produce self-similar objects at different length scales at each iteration. Examples of natural fractals are also widespread, and fractal dimension analysis can be applied to these structures within a certain length scale range to yield the *fractal dimension* which can be considered a measure of "ruggedness", describing how a fractal structure scales with lengths when compared to classical geometric shapes. For instance, it has been applied to the analysis of the length of a coastline [11], the branching vascular tree in the human retina [12], cell shapes for cancer detection [13], diffusion limited particle aggregation [14], and patterns from chemical dissolutions [15]. The BM cellular pattern with dendritic microstructures we have observed from drying ZnO nano/microfluids exhibits complex hierarchical structures with various quasi-2D spatial arrangements, and thus represents a suitable candidate for the fractal dimension analysis.

Here, the analysis was performed on the residual patterns from evaporation of sessile drops containing three types of ZnO particles differing in size and shape: the in-house synthesised ZnO nanoparticles (*ca* 9 nm in size), and commercially acquired ZnO nanopowder (Sigma-Aldrich, <100 nm particle size, ~80% Zn basis), (*ca* 36-142 nm) and ZnO powder (Sigma-Aldrich, ACS reagent, ≥99.0% (KT)), (*ca* 61-292 nm) dispersed in a mixture of cyclohexane (Fisher Chemicals, 99%) and isobutylamine (Sigma-Aldrich, 99%) [6]. (See section SI.01 in the Supporting Information (SI) for transmission electron microscopy (TEM) analysis of the particles and their size distribution, and SI.02

for ZnO nano/microfluid preparation.) The surface pattern was created by casting a droplet (see SI.04 for details on procedures and conditions) onto a 1 × 1 cm silicon wafer (UV/Ozone treated, water contact angle (CA) = 10.3 ± 2.7°, in-house synthesised ZnO nanofluid CA = 6.5 ± 2.2°, ZnO nanopowder nano/microfluid CA = 5.5 ± 2.0°, and ZnO powder nano/microfluid CA = 4.1 ± 1.9° with the errors quoted as the standard deviation from 56, 28, 35, and 6 separate measurements, respectively). The surface patterns were characterised using scanning electron microscopy (SEM, SI.05). The size distribution of the BM convective cells in the residual surface patterns structure was fitted with the log-normal distribution function (SI.06). Box counting fractal dimension analysis was used to further study images of manifestations of the BM cellular pattern (SI.07) to yield their fractal dimensions as a quantitative measure on these complex cells.

Figure 1 shows examples of the residual surface patterns from evaporation of the droplets of the three types of particle dispersions. The pattern was composed of central cellular structures surrounded by a coffee ring band around the pinned droplet perimeter (**Figure 1a**, **d** and **g**), made of a dense network of intercalating fibres (**Figure 1b-c**, **e-f**, and **h-i**). For the in-house synthesised ZnO nanofluid, the central cells were approximately circular in shape with varying diameters (200 - 800 μm), with their microstructure resembling spoke-like patterns with a bow-tie projection (**Figure 1b**). The BM cell size distributions (**Figure 2**) were fitted with a log-normal function (SI.06) where M is the geometric mean BM cell size by count and σ_g is the geometric standard deviation [16-17]. One of the well-defined cells is shown in **Figure 1c**. These cells, similar to the BM flow pattern observed during the evaporation of polystyrene/toluene solution [14], were identified as solidified manifestations of Bénard-Marangoni (BM) convection cells [3]. The occurrence of the BM instabilities and flows may be gauged by the Marangoni number, B, which considers the counter balancing effects of the surface tension and the viscous force in a liquid film [18], and it also depends on solvent physical parameters such as thermal diffusivity, dynamic viscosity, temperature gradient, thermal conductivity, density, and specific heat capacity (*cf.* equation 2 in Chapter 1). For $B > 80$, spontaneous surface-tension driven flows will result in BM instabilities and the formation of BM flow cells. The BM cell size in the residual pattern, λ_{BM} is related to the Marangoni number by $B = 32(\pi d/\lambda_{BM})^2$, where d is the drop thickness [3]. Wu and

Briscoe calculated that the Marangoni numbers in their evaporating ZnO nanofluid droplet (in a mixture of chloroform, methanol and isobutylamine) were $B \sim 300 - 2000$, much larger than the critical value of 80 [3]. They attributed different BM cell sizes to the fluctuations in the local fluid viscosity induced by the variation in the local particle concentration during the evaporation. Here, the varying BM cell sizes $\lambda_{BM} \sim 200$ - 800 μm suggest that the BM flows were triggered at different droplet thickness d or thinning stages during the evaporation, which may be attributed to the inhomogeneities in the concentration of particle and molecular species *in situ* generated from ZnO dissolution [3, 5].

In contrast, drying of the nano/microfluid droplets from the commercially acquired ZnO nanopowder (**Figure 1d-f)** and ZnO powder (**Figure 1g-i)** left the substrate surface covered with dense, fibrous structures intercalated with ZnO nano/microcrystal residues, as shown in the insets in **Figure 1f** and **i**. This was attributed to ZnO crystals undergoing partial moisture-assisted dissolution over the course of evaporation, described in detail in [6]. These undissolved ZnO nano/microcrystals could have influenced the solvent flows during the evaporation and contributed to the fluid viscosity fluctuations causing the BM instabilities. The BM cells in the residual pattern were less well-defined, with some of the spoke-like radial patterns outlined with yellow circles in the figure, showing dendritic morphologies with fibres radiating from the centre, with the BM cell size distributions shown in **Figure 2b** and **c**.

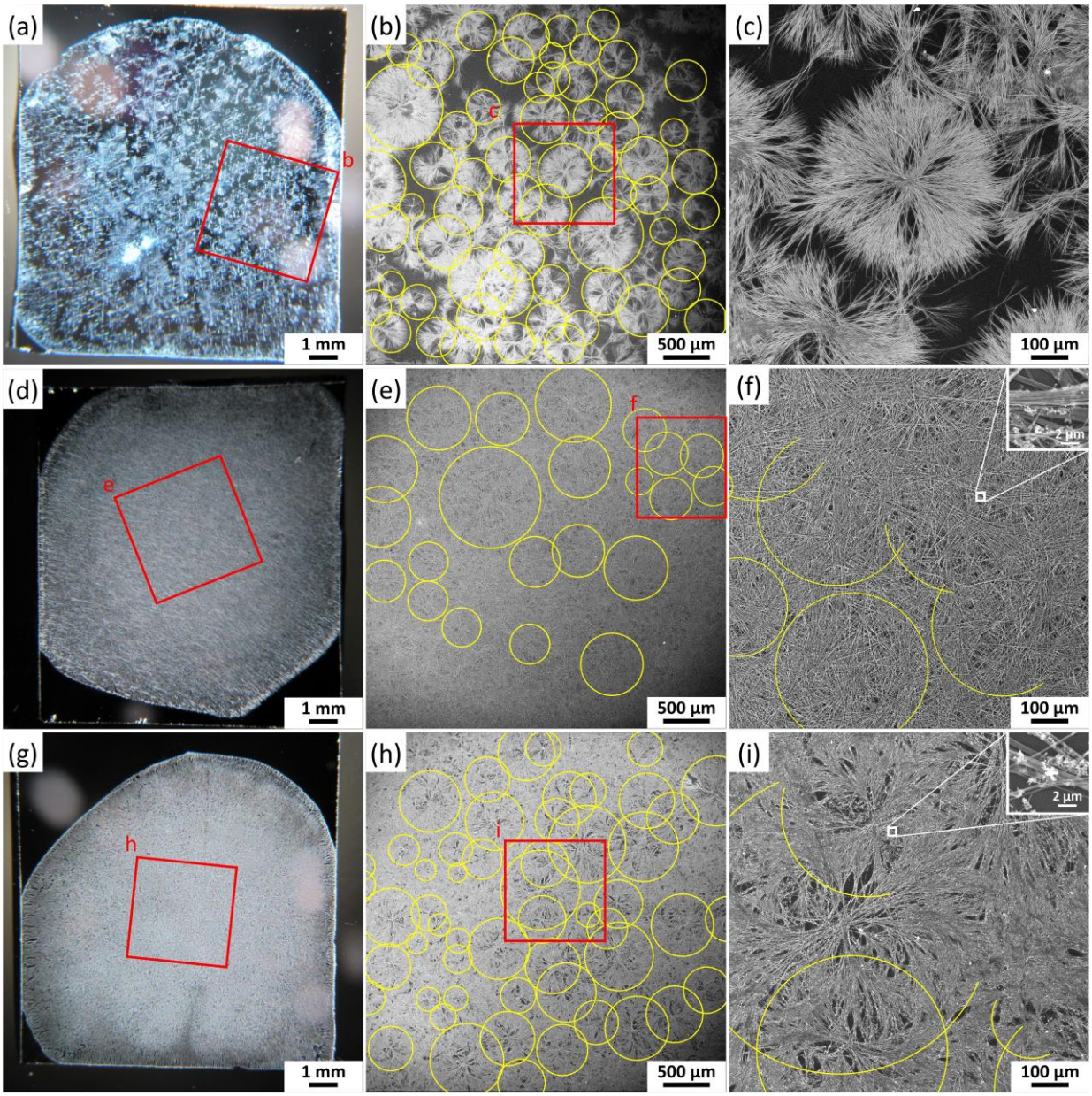

Figure 1. Residual surface pattern formed on the UV/Ozone treated silicon wafer from a 30 µL sessile droplet of the in-house synthesised ZnO nanofluid (**a-c**) and commercially acquired ZnO nanopowder (**d-f**) and ZnO powder (**g-i**) nano/microfluids; optical (**a**, **d** and **g**) and (**b-c**, **e-f** and **h-i**) scanning electron microscopy images. BM cells are marked with yellow circles, shown only for half of the micrographs in (**f**) and (**i**) for clarity. Insets if (**f**) and (**i**) show magnified views of the areas marked with white squares in the images, which reveal ZnO crystalline residues intercalating with fibres.

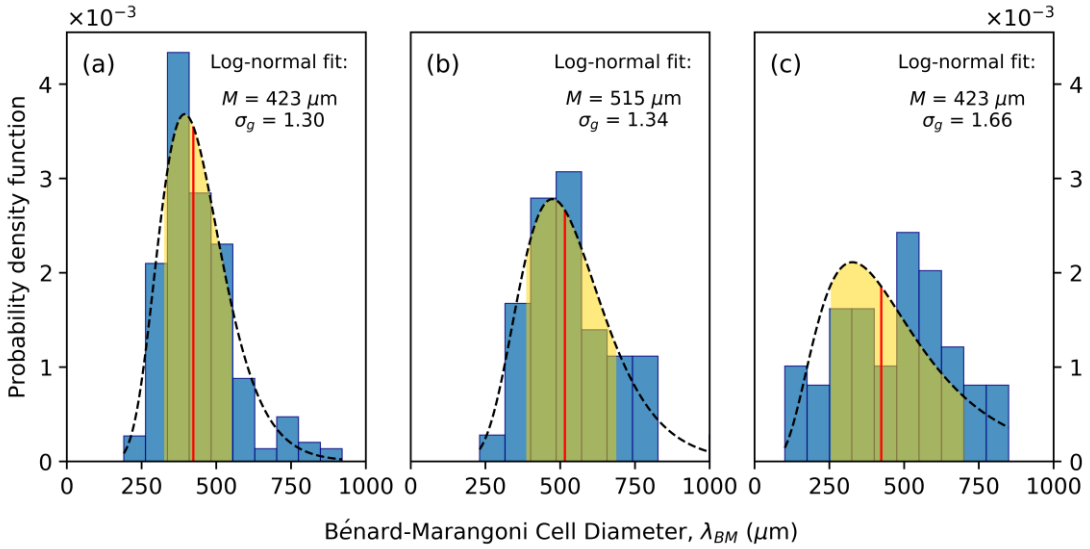

Figure 2. Size distributions as the probability density function (PDF) of BM cells in the central region of the residual surface patterns from (**a**) the in-house synthesised ZnO nanoparticles, and commercially acquired (**b**) ZnO nanopowder and (**c**) ZnO powder on UV/Ozone exposed silicon wafer. BM cell sizes distributions were fitted with a log-normal function (SI.06), shown as dashed lines. Red vertical lines show the geometric mean, M (equal to median size in log-norm distribution). BM cells of sizes contained between M/σ_g and $M \cdot \sigma_g$ (68.3% of all values) are shaded in golden colour under the dashed size distribution curve.

The box counting fractal dimension (FD) analysis was performed for individual BM cells and the process is described in detail in the supplementary information (SI.07). Briefly, BM cells of different diameters λ_{BM} are identified by circles and the FD analysis is performed for each encircled area. The algorithm for the analysis involves laying a grid of square boxes of a side-length ε over an image, and then counting the number of non-empty boxes, $N(\varepsilon)$, which scales with the box size $N(\varepsilon) \sim \varepsilon^{-D}$ (equation S5). The procedure is then repeated for a range of ε to obtain the fractal dimension (FD), D, from the slope of the $\ln(N)$ vs. $\ln(\varepsilon)$ plot (equation S6) [10, 19]. The process is shown in **Figure 3** for the analysis of a single BM cell (cf. **Figure 1c**). As a control, the FD analysis was similarly performed for the whole image instead of individual BM cells.

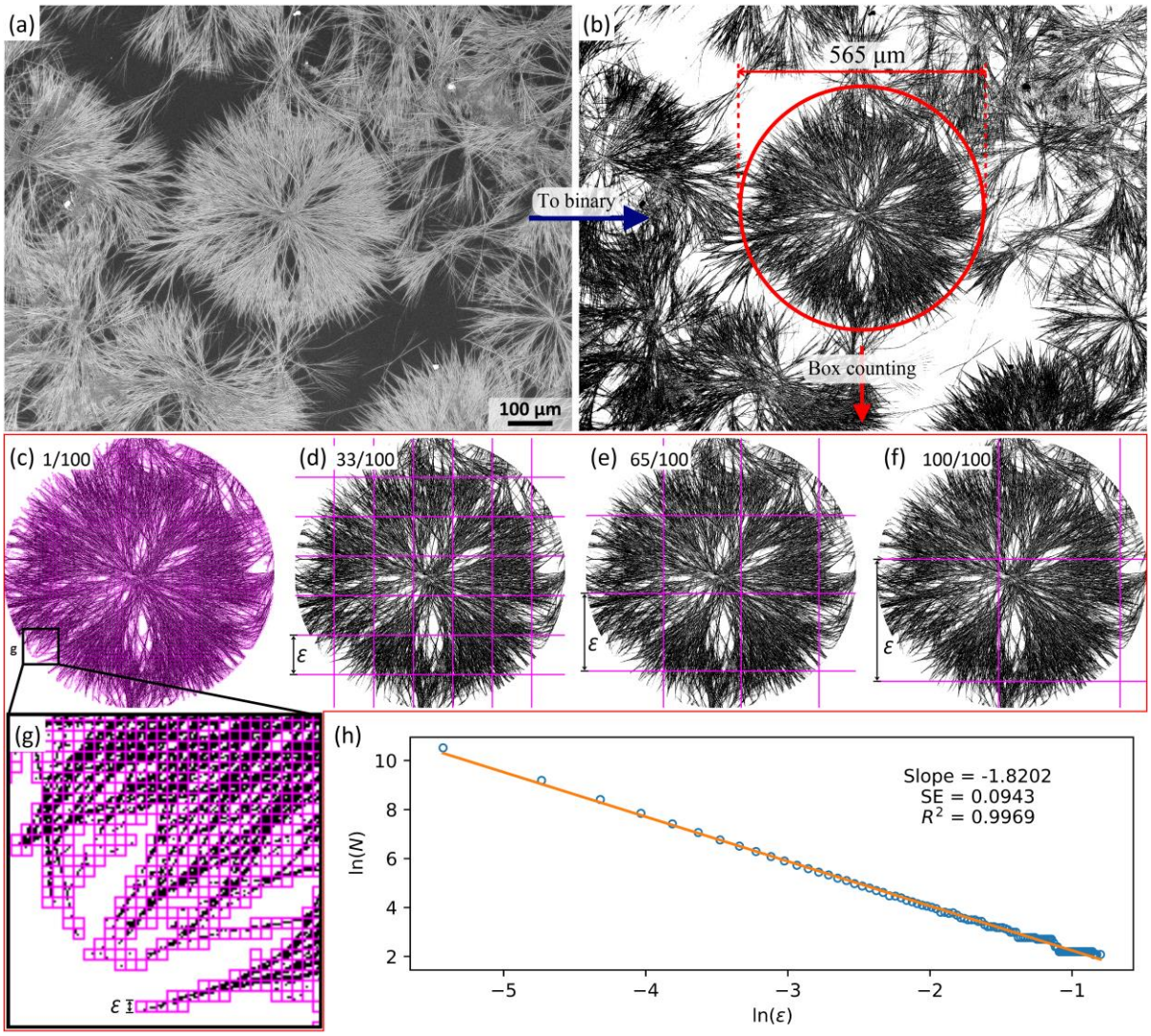

Figure 3. Step-by-step scheme of box counting fractal dimension (FD) analysis. An SEM image (**a**) is converted to binary form (**b**). Then, a circular selection concentric with a Bénard-Marangoni (BM) cell is analysed by superimposing a series of square grids of a box sampling size ε on the image, and the number of boxes containing foreground pixels, N, is counted for each ε (size 5, 165, 325, and 508 pixels for **c-f** respectively). The box counting FD is the negative slope of the best line fit to $\ln(N)$ vs. $\ln(\varepsilon)$ plot (**h**). SE stands for the standard error and R^2 for the correlation.

The results of the box counting FD analysis of the solidified BM cells are presented in **Figure 4**, with the D values in the range 1.76 – 1.89. A fractal dimension can be used to gauge the geometrical properties of a structure, *e.g.* how much space it fills or how pronounced its irregularities are [20]. It can also be used to quantify ruggedness of particle boundaries [21]. The D value distribution calculated as probability density function (PDF) is shown in **Figure 4a**, with the fitted the normal distributions

also shown as black dashed lines and labelled as h_1, h_2, and h_3 for three types of ZnO nano/microfluids. The fitting parameters, μ and σ, stand for the mean D value and its standard deviation, respectively. The BM cells from the in-house ZnO nanofluid had the lowest average D value of $\mu = 1.822$ with a broad distribution ($\sigma = 0.025$). The BM cells from the other two types of ZnO particles (h_2 and h_3) showed a similar, higher average D value of $\mu \sim 1.84$, consistent with a denser structure and a higher surface coverage. Numerically, such values compare to those for the classical fractals, *e.g.* $D \approx 1.8687$ for both monkey trees and snowflake halls, and $D = 1.8928$ for the Sierpiński carpet [9]. For reference, a line gives a value of $D = 1$ and a fully filled area $D = 2$. The scatter in D values is qualitatively consistent with our interpretation on a physical level that the BM cell size variations were due to local inhomogeneities in the viscosity and thermal properties, with the larger BM cells resulting from the instabilities triggered at larger droplet thicknesses. The different flow rates and particulate species participating in the self-assembly process in different BM flow cells would lead to different fractal dimensions D. Furthermore, self-similarity is a measure how the pattern of the entire shape is similar to the pattern of an arbitrary small part of the shape. It can be expressed with the Hurst exponent, $H = 2 - \mathrm{FD}$, for a 2D pattern [22]. The values of the Hurst exponent for all the patterns are $H < 0.5$, which lie in the region of unstable statistical characteristics. For instance, in computer aided cancer diagnosis of magnetic resonance images, this usually suggests that the physiological pattern is related to a pathological condition in contrast to a stable statistical region of $H > 0.5$.

A trend of increasing FD values (D) vs. the BM cell diameter (λ_{BM}) may also be observed (**Figure 4b**) for all the nano/microfluids, initially a rapid increase in D for small BM cell diameters ($\lambda_{BM} < 200$-400 μm), but reaching a plateau for higher λ_{BM} values. A logarithmic function was loosely fitted to the trend, $D = a \ln(\lambda_{BM}) + D_0$, with the intercept value D_0 for the in-house synthesised ZnO nanofluids the smallest *ca* 1.538 compared to those for the other two types ($D_0 = 1.708$ and 1.736 respectively). This could be attributed to the voids (*i.e.* unoccupied areas) towards the centre of the dendritic pattern, giving rise to a smaller D_0 value, characteristic of a fractal pattern with a less densely populated area. The scatter in the data for different particles is enclosed in respective shaded areas bounded also by the logarithmic fits (Section SI.07 in SI). It should be noted (and as discussed in SI.07)

that the choice of the logarithmic function is arbitrary which merely provides a guidance to the eye. It however facilitates an internally consistent comparison between the three sets of FD values.

A benchmark FD analysis was also performed on two known fractal structures, a hexaflake and the Sierpiński carpet (**Figure S3**), using the circles of different diameters (as we did for the different BM cell sizes above). A similar trend of rapid increase in D followed by a plateau was also observed as for the BM cells, again with smaller intercept values D_0 for the patterns with a more open structure in the centre. A series of circular selections of different diameters (in the rage of 8.7% to 62.3% of the largest diameter analysed) that covered a random part of the Sierpiński carpet, instead of being concentrically symmetric with the fractal pattern, were also processed. The D values scattered around the average value ($\mu = 1.75$ and $\sigma = 0.02$; **Figure S3b**), without the depressed D values at smaller circle diameters. This is due to the random placements of the circles which averaged out the less densely packed area close to the centre of the fractal patterns, further confirming the origin of the observed the D vs. λ_{BM} trend in Figure 4b. To appreciate its physical significance, we may draw an analogy between the BM cell dendrites with the polymeric dendrimers smaller (or lower generation) dendrimers possess a more open structure, whilst larger (or higher generation) dendrimers have a much denser packing [23-24].

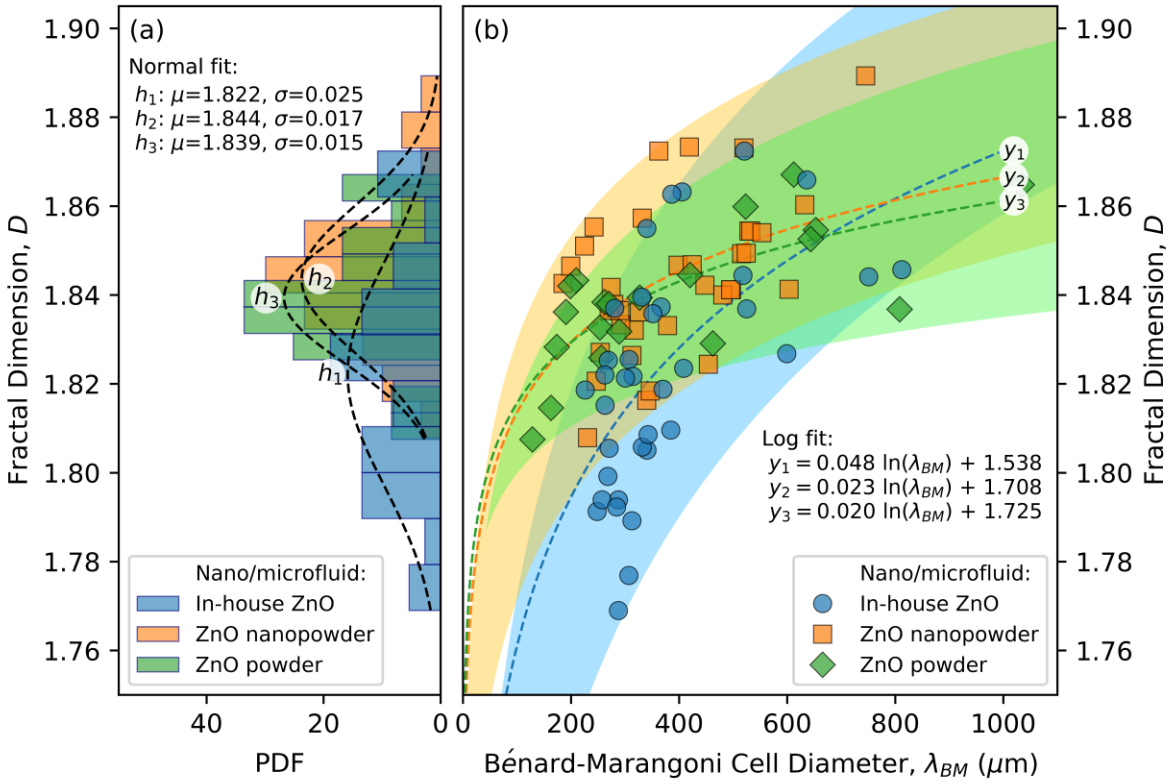

Figure 4. Box counting fractal dimension analysis of the solidified Bénard-Marangoni (BM) cells from drying ZnO nano/microfluids composed the in-house synthesised ZnO nanoparticles, ZnO nanopowder, and ZnO powder on a UV/Ozone exposed silicon wafer. (**a**) FD distribution for all the samples, fitted with normal (Gaussian) distribution function. Data fits are shown as dashed lines and labelled as h_1, h_2, and h_3, respectively for the three particle types. Parameters μ and σ stand for the mean D and its standard deviation. (**b**) The calculated box counting fractal dimension (FD) vs. the diameter of the investigated BM cell λ_{BM}. Dashed lines, labelled y_1, y_2, and y_3, show logarithmic fits. The scatter of the data is enclosed by shaded regions, bounded also by the logarithmic fits (Section SI.07 in SI).

The residual surface patterns formed from ZnO nano/microfluids resembled the structures from diffusion-limited aggregation (DLA) [14, 25-26], and such particle aggregation has been simulated on square lattices (Euclidean dimensions equal to 2). These simulations resulted in branching patterns with a fractal (density correlation) dimension $D \sim 1.70$. However, Bensimon *et al.* [27] modified the approach presented in [14, 26], assuming that the aggregation could be described by ballistic motion of the incoming particles joining the aggregate. The consequent DLA patterns resulted in a fractal dimension $D \sim 1.93 \pm 0.02$. Daccord and Lenormand [15] analysed the patterns obtained from chemical dissolution resembling tree-like structures and obtained a fractal dimension $D \sim 1.6 \pm 0.1$. It is worth mentioning that in addition to analysing circular selection of patterns resembling solidified manifestations of BM cells from ZnO nano/microfluids, the whole SEM images that were used for BM cells analysis were also processed (**Table S3**). The FD values calculated for the whole SEM images follow a similar trend to that observed for the BM cells, with the smallest D value obtained for the in-house ZnO nanofluid (1.896 ± 0.001, for μ and σ, respectively), with the rest of the patterns resulting in $D \sim 1.908 \pm 0.007$ (ZnO powder nano/microfluid) and 1.911 ± 0.006 (ZnO nanopowder nano/microfluid). This is in agreement to the work of Daccord and Lenormand [15], also providing further supporting evidence for the discussion in Ref. [3] that the dendritic patterns are produced in a DLA process. However, one should note different methods for fractal dimension calculation may result in slightly different values of fractal dimensions for the same structure, depending on the dimension definition [20].

In summary, we have presented a fractal dimension analysis of the solidified Bénard-Marangoni cells of complex morphology in the residual surface patterns from evaporation of sessile drops containing different ZnO nano/microfluids. Such an analysis facilitates discussions of the features and properties of the surface patterns beyond the previous descriptive account [3, 5-6]. The fractal dimension D value reflects the ruggedness or how much space the dendritic pattern fills [20-21], whilst the D vs. λ_{BM} (BM cell size) trend and the intercept value D_0 of its logarithmic fit give insights into the spatial variation of the dendrites from the BM cell centre to its periphery. ZnO nanofluids prepared from the commercially acquired ZnO nanopowder and ZnO powder produced patterns of a higher coverage with densely packed BM cells and a higher degree of interpenetration between them, manifesting in higher values of the fractal dimension. Our results demonstrate that fractal dimensional analysis can provide a quantitative description of the properties of these complex surface patterns from evaporative drying of reactive nanofluids, which paves the way for further investigations to seek further correlation between the fractal dimensions and the physical parameters relevant to the evaporation process and solution conditions. For instance, we have applied the fractal dimension analysis developed here to investigate the effect of substrate chemistry on the residue patterns [28]. Our results also point to the feasibility for such an analysis for other similar quasi-2D surface patterns.

Supporting Information

The Supporting Information (SI) associated with this article can be found, in the online version, at https://doi.org/10.1016/j.jcis.2018.10.077. The SI contains: SI.01: ZnO particles; SI.02: Preparation of the nano/microfluids; SI.03: Preparation of the substrates; SI.04: Hierarchal surface pattern formation; SI.05: Characterisation of the hierarchical surface patterns; SI.06: Bénard-Marangoni cell size distribution - log-normal fitting; and SI.07: Fractal dimension analysis of the Bénard-Marangoni cells.

ORCID

Patryk Wąsik - 0000-0002-7447-7472

Annela M. Seddon - 0000-0002-5794-8500

Wuge H. Briscoe - 0000-0001-8025-960X

Acknowledgements

P.W. is supported by the UK Engineering and Physical Sciences Research Council (EPSRC) through the Bristol Centre for Functional Nanomaterials (BCFN) (grant no. 1371498). H.W. is supported by a Marie Skłodowska-Curie Individual Fellowship (Project Number 656830). W.H.B. would like to acknowledge funding from the EPSRC (EP/H034862/1 and Building Global Engagement in Research (BGER)), European Cooperation in Science and Technology (CMST COST) Action CM1101 "Colloidal Aspects of Nanoscience for Innovative Processes and Materials", and Marie Curie Initial Training Network (MCITN) on "Soft, Small, and Smart: Design, Assembly, and Dynamics of Novel Nanoparticles for Novel Industrial Applications" (NanoS3). Mr Jonathan Jones and Dr Sean Davis are thanked for their help with SEM imaging. Ms Anna Slastanova is acknowledged for her help with the contact angle measurements. Mx Kate Oliver is thanked for a discussion about the approach to the fractal dimension analysis of digital images.

References

1. Han, W.; Lin, Z., Learning from "Coffee Rings": Ordered Structures Enabled by Controlled Evaporative Self-Assembly. *Angew. Chem. Int. Ed.* **2012,** *51* (7), 1534-1546.

2. Zhong, X.; Crivoi, A.; Duan, F., Sessile nanofluid droplet drying. *Adv. Colloid Interface Sci.* **2015,** *217*, 13-30.

3. Wu, H.; Briscoe, W. H., Morphogenesis of polycrystalline dendritic patterns from evaporation of a reactive nanofluid sessile drop. *Physical Review Materials* **2018,** *2* (4), 045601.

4. Deegan, R. D.; Bakajin, O.; Dupont, T. F.; Huber, G.; Nagel, S. R.; Witten, T. A., Capillary flow as the cause of ring stains from dried liquid drops. *Nature* **1997,** *389* (6653), 827-829.

5. Wu, H.; Chen, L. X.; Zeng, X. Q.; Ren, T. H.; Briscoe, W. H., Self-assembly in an evaporating nanofluid droplet: rapid transformation of nanorods into 3D fibre network structures. *Soft Matter* **2014,** *10* (29), 5243-5248.

6. Wąsik, P.; Redeker, C.; Dane, T. G.; Seddon, A. M.; Wu, H.; Briscoe, W. H., Hierarchical Surface Patterns upon Evaporation of a ZnO Nanofluid Droplet: Effect of Particle Morphology. *Langmuir* **2018,** *34* (4), 1645-1654.

7. Maroto, J. A.; Pérez-Muñuzuri, V.; Romero-Cano, M. S., Introductory analysis of Bénard–Marangoni convection. *European Journal of Physics* **2007,** *28* (2), 311.

8. Bénard, H., Étude expérimentale des courants de convection dans une nappe liquide. — Régime permanent : tourbillons cellulaires. *J. Phys. Theor. Appl.* **1900,** *9* (1), 513-524.

9. Mandelbrot, B. B., *The Fractal Geometry of Nature*. Freeman and Company: New York, 1982.

10. Alligood, K. T.; Sauer, T. D.; Yorke, J. A., *Chaos: An Introduction to Dynamical Systems*. Springer New York: 2012.

11. Mandelbrot, B., How Long Is the Coast of Britain? Statistical Self-Similarity and Fractional Dimension. *Science* **1967,** *156* (3775), 636-638.

12. Masters, B. R., Fractal Analysis of the Vascular Tree in the Human Retina. *Annual Review of Biomedical Engineering* **2004,** *6* (1), 427-452.

13. Baish, J. W.; Jain, R. K., Fractals and Cancer. *Cancer Research* **2000,** *60* (14), 3683-3688.

14. Witten, T. A.; Sander, L. M., Diffusion-Limited Aggregation, a Kinetic Critical Phenomenon. *Phys. Rev. Lett.* **1981,** *47* (19), 1400-1403.

15. Daccord, G.; Lenormand, R., Fractal patterns from chemical dissolution. *Nature* **1987,** *325*, 41.

16. Smith, J. E.; Jordan, M. L., Mathematical and graphical interpretation of the log-normal law for particle size distribution analysis. *J. Colloid Sci.* **1964,** *19* (6), 549-559.

17. Zender, C. Particle size distributions: theory and application to aerosols, clouds, and soils. http://dust.ess.uci.edu/facts/psd/psd.pdf (accessed 12th Dec 2017).

18. Pearson, J. R. A., On convection cells induced by surface tension. *J. Fluid Mech.* **1958,** *4* (5), 489-500.

19. Napolitano, A.; Ungania, S.; Cannata, V., Fractal Dimension Estimation Methods for Biomedical Images. In *MATLAB - A Fundamental Tool for Scientific Computing and Engineering Applications - Volume 3*, Katsikis, V. N., Ed. InTech: Rijeka, 2012; p Ch. 07.

20. Falconer, K. J., *Fractal geometry: mathematical foundations and applications*. Wiley: Chichester, 1990.

21. Rahman, M. S., Physical meaning and interpretation of fractal dimensions of fine particles measured by different methods. *J. Food Eng.* **1997,** *32* (4), 447-456.

22. Marusina, M. Y.; Mochalina, A. P.; Frolova, E. P.; Satikov, V. I.; Barchuk, A. A.; Kuznetcov, V. I.; Gaidukov, V. S.; Tarakanov, S. A., MRI Image Processing Based on Fractal Analysis. *Asian Pacific Journal of Cancer Prevention : APJCP* **2017,** *18* (1), 51-55.

23. Pilkington, G. A.; Pedersen, J. S.; Briscoe, W. H., Dendrimer Nanofluids in the Concentrated Regime: From Polymer Melts to Soft Spheres. *Langmuir* **2015,** *31* (11), 3333-3342.

24. Fox, L. J.; Richardson, R. M.; Briscoe, W. H., PAMAM dendrimer - cell membrane interactions. *Adv. Colloid Interface Sci.* **2018,** *257*, 1-18.

25. Witten, T. A.; Meakin, P., Diffusion-limited aggregation at multiple growth sites. *Physical Review B* **1983,** *28* (10), 5632-5642.

26. Meakin, P., Diffusion-controlled cluster formation in 2-6-dimensional space. *Physical Review A* **1983,** *27* (3), 1495-1507.

27. Bensimon, D.; Domany, E.; Aharony, A., Crossover of Fractal Dimension in Diffusion-Limited Aggregates. *Phys. Rev. Lett.* **1983,** *51* (15), 1394-1394.

28. Wąsik, P.; Seddon, A. M.; Wu, H.; Briscoe, W. H., Bénard-Marangoni dendrites upon evaporation of a reactive ZnO nanofluid droplet: Effect of substrate chemistry *Langmuir* **2019,** *35* (17), 5830-5840.

SUPPORTING INFORMATION

Dendritic surface patterns from Bénard-Marangoni instabilities upon evaporation of a reactive ZnO nanofluid droplet: A fractal dimension analysis

Patryk Wąsik[a,b], Annela M. Seddon[a,c], Hua Wu[b], and Wuge H. Briscoe[b,]*

[a] Bristol Centre for Functional Nanomaterials (BCFN), HH Wills Physics Laboratory, University of Bristol, Tyndall Avenue, Bristol, BS8 1TL, UK

[b] School of Chemistry, University of Bristol, Cantock's Close, Bristol, BS8 1TS, UK

[c] School of Physics, HH Wills Physics Laboratory, Tyndall Avenue, University of Bristol, Bristol, BS8 1TL, UK

Information

This chapter has been published as Supporting Information to **Wąsik, P.**; Seddon, A. M.; Wu, H.; Briscoe, W. H., Dendritic surface patterns from Bénard-Marangoni instabilities upon evaporation of a reactive ZnO nanofluid droplet: A fractal dimension analysis. *J. Colloid Interface Sci.* **2019**, 536, 493-498. DOI: 10.1016/j.jcis.2018.10.077. This chapter has been authored by the candidate with no more input from co-authors and supervisors that would have been provided in a conventional thesis chapter. Individual contributions as in Chapter 3.

SI.01: ZnO particles

Three types of zinc oxide (ZnO) particles were used in the experiment: in-house synthesized ZnO nanoparticles, and commercially acquired ZnO nanopowder (Sigma-Aldrich, <100 nm particle size, ~80% Zn basis) and ZnO powder (Sigma-Aldrich, ACS reagent). **Figure S1** shows TEM micrographs of ZnO particles taken using a JEOL JEM-1400 Transmission Electron Microscope. The characterisation of all ZnO particles and the synthesis of the in-house synthesised ZnO nanoparticles

are described in detail elsewhere [1]. Briefly, the particle size distributions were modelled with the log-normal distribution function (SI.06), using the particle diameter for the in-house synthesised ZnO nanoparticles, and the maximum dimension (maximum distance between any two surface points) for the commercially acquired ZnO nanopowder and ZnO powder. The in-house synthesised ZnO nanoparticles were monodisperse with the geometric mean particle diameter of 9.2 nm, and 68.3% of all particle diameters between 7.4 and 11.4 nm. The commercially acquired ZnO particles were polydisperse with the geometric mean of 71.7 and 133.4 nm, and 68.3% of all maximum dimensions between 36.2 and 141.8 nm, and 61.2 and 291.9 nm for ZnO nanopowder and ZnO powder, respectively.

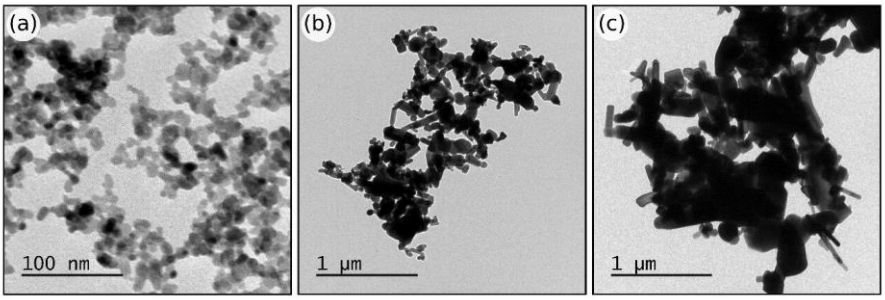

Figure S1. TEM micrographs of ZnO particles used in the experiment: **(a)** the in-house synthesised ZnO nanoparticles, **(b)** ZnO nanopowder, and **(c)** ZnO powder.

SI.02: Preparation of the nano/microfluids

The nano/micro fluids were prepared by dispersing each one of the three ZnO particles in a mixture of cyclohexane (Fisher Chemicals, assay 99%) and isobutylamine (Sigma-Aldrich, assay 99%) in a 5:1 volume ratio. A designated amount of each ZnO powder was transferred into a 7 mL glass vial to which the cyclohexane and isobutylamine mixture was added to give the final concentration of 1 mg/mL (ZnO/mixture). The obtained dispersion was sonicated in an ultrasonic bath for 2 hours to produce homogenous ZnO nano/microfluids.

SI.03: Preparation of the substrates

1×1 cm^2 substrates from silicon wafers (ID 452, 100 mm diameter, P type, B dopant, <100>, 0-100 Ω·cm, 500 µm thick, single-sided polish, test grade, UniversityWafer, Inc.) were prepared by cutting the materials with a pen diamond cutter. The substrates were subsequently sonicated in acetone and ethanol for 10 minutes each, rinsed three times with *Milli-Qwater*, sonicated in *Milli-Q*water for

10 minutes and dried using a stream of nitrogen. Silicon wafer substrates was oxidised in UV/ozone cleaner (42-220 UVO-Cleaner, Jelight Company Inc.) for 10 minutes.

SI.04: Hierarchal surface pattern formation

Hierarchical surface patterns were formed by pipetting a 30 μL drop of a nano/microfluid onto a substrate placed in an uncovered compartment of a petri-dish (25 compartment sterile 100 mm box, Sterilin), which was then left to evaporate at room temperature (~ 23°C) and relative humidity (RH ~45%), both measured with a pen hygrometer (Tracable®). All ZnO nano/microfluid droplets evaporated within several minutes, leaving white residual patterns on the substrates.

SI.05: Characterisation of the hierarchical surface patterns

The hierarchical surface patterns formed by evaporative drying of ZnO nano/microfluids the silicon substrates were imaged using scanning electron microscopy (SEM). Prior to the imaging using JSM-IT300 SEM (JEOL), samples were covered with 15 nm layer of silver. The footprints of the residual surface patterns were calculated using ImageJ software based on their surface area (**Figure 1a**, **d**, and **g**) and are shown in **Table S1**.

Table S1. Residual surface pattern area footprints.

In-house synthesised ZnO	117.3 mm^2
ZnO nanopowder	112.2 mm^2
ZnO powder	107.5 mm^2

SI.06: Bénard-Marangoni (BM) cell size distribution - log-normal fitting

Circles outlining the solidified manifestations of BM cells were drawn on top of SEM images, of which examples are shown in **Figure 1** compiled using Serif DrawPlus X6 software. Subsequently, these circles were manually separated to eliminate overlapping and saved to separate files. This allowed for image analysis using ImageJ software, calculating areas (A) of the BM cell. The BM cell diameters (d) were obtained using equation S1:

$$d = 2\sqrt{\frac{A}{\pi}}, \tag{S1}$$

The size distributions of BM cells were fitted with the lognormal distribution function, equation S2:

$$y = \frac{1}{\ln(\sigma_g)\sqrt{2\pi}} \exp\left[-\frac{(\ln x - \ln M)^2}{2\ln^2(\sigma_g)}\right], \tag{S2}$$

where y is the probability density function, x is the BM cell size, σ_g is the geometric standard deviation, and M is the geometric mean particle size by count [2]. In the log-normal distribution, M is essentially the size below or above which half of the total number of BM cells is found (median size). The skewness and dispersion of the size distribution curve is characterised by the geometric standard deviation σ_g - the larger the value, the more disperse the distribution is [2]. In addition, following the considerations on the physical meaning of the geometric standard deviation σ_g, 68.3% of all BM cells in log-normal distribution is contained in sizes between M/σ_g and $M \cdot \sigma_g$ [3]. This is in analogy to normal distribution, in which 68.3% of all values lie within one standard deviation away from the mean. The log-normal size distribution of solidified manifestation of BM cells are shown in **Figure 2**. The Bénard-Marangoni (BM) cell size distributions were calculated based on 204, 42, and 67 diameter measurements for the in-house synthesised ZnO nanofluid, ZnO nanopowder nano/microfluid, and ZnO powder nano/microfluid, respectively. Marangoni numbers calculated according to [4] for the boundaries of the BM cell size range, in which 68.3% of diameters are located (M/σ_g and $M \cdot \sigma_g$), are presented in **Table S2**.

Table S2. Marangoni numbers calculated accordingly [4] for the boundaries of the BM cell size range in which 68.3% of diameters are located (M/σ_g and $M \cdot \sigma_g$).

Particle Type	M/σ	$M \cdot \sigma_g$
In-house ZnO	195	68
ZnO nanopowder	153	47
ZnO powder	379	50

SI.07: Fractal dimension analysis of the Bénard-Marangoni cells

Mandelbrot used the term “fractal” (*frāctus* in Latin means "broken" or "fractured") when he described structures that were too irregular to be characterised with the traditional geometry framework

[5]. Fractal structures exhibit a fine structure, *i.e.* it does not simplify with magnification. In addition, they have some degree of self-similarity as they are composed of elements resembling the whole to some extent, either geometrically, approximately or statistically [6]. Because methods of the classical Euclidean geometry and calculus are not applicable to studying fractals, a different approach is needed do describe fractal geometry. The main instrument used to provide a quantitative description of fractal structures is fractal dimension in its many forms.

Fractal dimension describes fractal scaling properties and self-similarity. The topological dimensions of familiar structures are simple integers; for example a line is 1-dimentional, a surface is 2-dimensional, and a cube is 3-dimensional object. On the other hand, fractal dimension can take non-integer values, depending qualitatively and quantitatively on how a fractal structure fills its space when compared to classic geometrical objects [7]. This is schematically represented in **Figure S2**, where perfectly self-similar structures are taken as an example, a line (**Figure S2a**), a square (**Figure S2b**), a cube (**Figure S2c**), and the Sierpiński triangle (**Figure S2d**). Each of these structures can be divided into smaller parts, which are the exact copies of the original, only scaled down by ½ or ¼, which is the scaling factor, *r*. The number of the scaled down copies that are necessary to rebuild the original structure, *N*, depends on the scaling factor, and can be expressed as

$$N = \left(\frac{1}{r}\right)^{D}, \tag{S3}$$

where *D* is the similarity dimension, that after solving equation S3 can be calculated as

$$D = -\frac{\ln N}{\ln r}. \tag{S4}$$

The scaling factor and corresponding number of the scale down copies (displayed on the right in **Figure S2**) were used to calculate the similarity dimension, *D*, of the appropriate structures using equation S4. These are equal to 1, 2, 3 and *ca* 1.585 for the line, square, cube, and the Sierpiński triangle, respectively. The similarity dimension can be applied only to a small class of strictly self-similar structures; however, it is possible to define the fractal dimension in a way that can be applied to a wider range of objects.

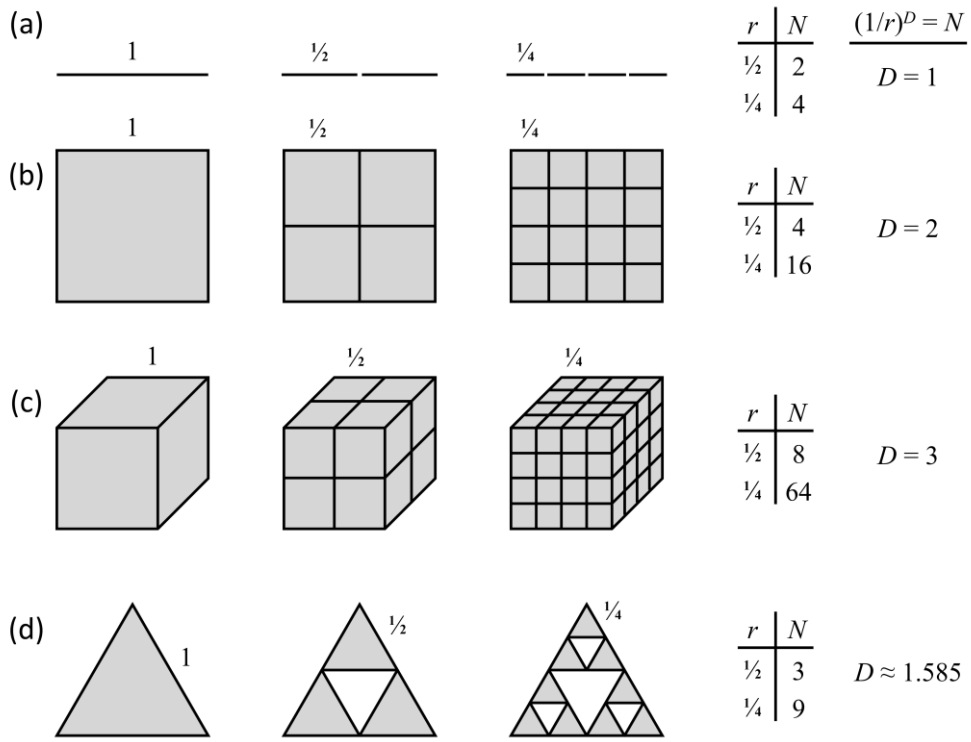

Figure S2. Fractal dimension concept illustrated using perfectly self-similar structures, (**a**) line, (**b**) square, (**c**) cube, and (**d**) the Sierpiński triangle. Each of these structures can be subdivided into N smaller parts that are the exact copies of the original, only scaled down by the scaling factor, r, of ½ or ¼. Using relation $N = (1/r)^D$, the similarity dimension, D, is calculated for each structure using equation S4.

One of the popular methods to investigate the scaling law for fractal structures is the box counting method. The idea behind this approach is to lay a grid of equal spacing over the fractal structure and then count the number of grid boxes required to cover it. The scaling properties are revealed in how this number of grid boxes varies with the decreasing grid size. In general, the number of m-dimensional boxes of side-length ε that are necessary to cover a given object in m-dimensional space can be expressed as:

$$N(\epsilon) = C\epsilon^{-D} \tag{S5}$$

where C is a constant, and D is the dimension of the object. By this definition, the exponent D does not have to be an integer. By solving equation S5 and accounting for the negligible contribution of the term

containing C for small ε, the box-counting dimension, or the box-counting fractal dimension, also referred here as FD of an object, is given by:

$$D = -\lim_{\epsilon \to 0} \frac{\ln(N(\epsilon))}{\ln(\epsilon)}, \tag{S6}$$

when the limit exists [8].

Box counting fractal dimension (FD) analysis of the solidified Bénard-Marangoni (BM) cells formed from ZnO nano/microfluids was performed on SEM images (see SI.05) using ImageJ (version 1.51j8) software [9] with FracLac (version 2015Sep090313a9330) ImageJ plugin [10]. A step-by-step example of undertaken FD analysis is presented in **Figure 3** in the main text. An SEM image of residual surface patterns (here, formed from drying the in-house synthesised ZnO nanofluid droplet on UV/Ozone exposed Si) was loaded to ImageJ (**Figure 3a**) and converted into binary image with a default 'Make Binary' option, setting background (empty) to white and foreground to black colours (**Figure 3b**). A circular outline around a BM cell of interest was selected each time to ensure a consistent selection method throughout the analysis. The diameter of the cell was calculated as an average value of diameters determined from the area and perimeter of the selection. Then, the selected area was analysed using Box Counting and the Lacunarity Analysis scan-mode in FracLac plugin. In this step, a series of square grids containing boxes of a given side length (*i.e.* the sampling size), ε, were laid over the image, and the number of boxes containing foreground pixels, N (*Count* in FracLac) was counted for each box size. This is schematically represented in **Figure 3c-g**, which shows example of 4 out of 100 grids with varying sampling size, ε, demonstrating the different grid calibres and their positions with respect to the image

The box counting fractal dimension of a residual surface pattern in the selected area was calculated according to equation S6, which is the negative slope of the best line fit to ln(N) vs ln(ε) plot, shown in **Figure 3h**. It was accepted to use the FD value calculated only for 1 origin grid position (a position at which a grid is laid on the image during a scan, more positions can be set in FracLac grid design options), as in only 2.6% of the total number of FD measurements for 4 and 12 different grid positions, the obtained FD values differed by more than 1% (a value that is more than the standard error calculated for FD). However, one could use the average FD calculated over multiple grids. In order to produce

consistent FD results, only SEM images that revealed a detailed Bénard-Marangoni structure were used in the FD analysis. This mainly involved images taken at x100 magnification in addition to a few taken at x25, but with adequately resolution. This was in contrast to the Bénard-Marangoni cell size distribution analysis (see SI.06), which involved a range of SEM images that differed in the magnification level. Therefore, some of BM cell sizes that are presented in **Figure 2**, may not be included in the FD analysis due to the lack of an SEM image of that particular pattern with a higher magnification. The histograms in **Figure 4a** are directly produced from the scatter data points in Figure 4b. The number of fractal dimension values, *D*, used to produce the histograms are equal to 36, 36, and 21, for the in-house synthesised ZnO nanofluid, ZnO nanopowder nano/microfluid, and ZnO powder nano/microfluid, respectively. In addition to analysing the selected circles enclosing the BM cells, whole SEM images were also analysed, and the average FD values obtained are presented in **Table S3**.

Table S3. Average box-counting fractal dimension values (*D*) calculated for whole SEM images of residual surface patterns formed from ZnO nano/microfluids.

Nano/microfluid Type	**FD (*D*)**
In-house ZnO	1.896 ± 0.001
ZnO nanopowder	1.911 ± 0.006
ZnO powder	1.908 ± 0.007

As mentioned above, it is possible to define a fractal dimension in many ways, which may result in different values of calculated fractal dimension. In addition, it should be borne in mind that a theoretical fractal dimension does not depend on scale. However, digital images are limited by many factors, especially by resolution, which may in turn affect the output of the fractal dimension analysis. Therefore, it is important to perform benchmark testing based on images of known fractal structures for further comparison with the experimental data, especially in terms of trends presented in **Figure 4** in the main text. The results of the benchmark test analysis performed in this work are presented in **Figure S3**.

Two types of fractal structures were selected for the benchmark analysis, a Sierpiński carpet, 7th iteration rendered at 2187 by 2187 pixels [11] (**Figure S3a)**, and a hexaflake, 6th iteration with centre hexagons rendered at 2000 by 2000 pixels [12] (**Figure S3c**). Both images were analysed utilising the same procedure as it was applied to the experimental data, which is described above and schematically shown in **Figure 3**. The box counting fractal dimensions were calculated for a series of circular areas containing self-similar patterns at different scales (areas are marked with circles and labelled with a type number in **Figure S3a** and **c**), to test how the output FD value depended on the diameter of the circular selection. This was to mimic the analysis of similarly looking but differing in diameters fibrous structures of the BM cells produced from drying ZnO nano/microfluid droplets. In addition, a series of random circular selections with random placement, *i.e.* not concentric with the fractal structure but covering a random section of the whole pattern, were analysed to assess if such placements of the selected area would affect the obtained FD values. These random circular selections are not depicted in the fractal image (**Figure S3a**) for clarity. It can be seen that the FD values calculated for these random circular selections varying in diameter (190 to 1363 pixels, which is 8.7% to 62.3% of the largest diameter in the analysed image) scatter closely around the average FD of 1.75 ± 0.02. This suggest that the average FD value, or even better, the FD value distribution would provide a valuable insight about the intrinsic complexity of the investigated structures.

The box counting fractal dimension values of the above selections plotted with respect to the selections diameters are shown in **Figure S3b** and **d**). The FD values calculated for a series of circular areas containing self-similar patterns, indicated as “Pattern type 1, 2 and 3”, for both fractal images, increase with the value diameter. The increase in FD values is rapid for relatively small diameters, which is an equivalent of 4-7th size iteration, or approximately 0 - 3.7% and 0 - 3.6% of the total image size of both fractals with regards to “Pattern types 1”, the Sierpiński carpet and hexaflake, respectively. Subsequently, the values of the box counting FD reach a plateau, which indicates they would converge to the theoretical fractal dimensions of the appropriate structures with the high enough resolution or size of the image. The initial depression in the FD value is related to the more open structure (*i.e.* less densely populated area towards the centre of the fractal structure). The FD values of the random placement of the circles from the Sierpiński carpet (**Figure S3b**) oscillate around the average value of

1.7495 without the initial depression of the *D* value at the small circle size, as the centre of the circles are no longer coincide with the centre of the fractal structure where the area is more sparsely occupied. All data sets were fitted with a logarithmic function shown in equation S7:

$$y = a\ln(x) + b\,, \tag{S7}$$

where *a* and *b* are constants fitted using the non-linear least squares method. The fitted curves are plotted with dashed lines in colours corresponding to these of the original data points, with labels (as y_1, y_2, and y_3) and calculated equations displayed in each subplot (**Figure S3b** and **d)**. The choice of a logarithmic function to fit the data was arbitrary. As a matter of fact, calculated values of the box counting fractal dimension should lie in the range between 1 and 2 due to the nature of the investigated structures [13]. Here, for a large enough pattern diameter, the logarithmic function would eventually produce a value higher than 2. Therefore, it serves a guide for the eye, and one could use a different function to describe the trend (*i.e.* generalised logistic function [14]).

In addition to calculating the box counting FD values for circular selections in Sierpiński carpet, a FD value for the entire structure was computed for comparison, equal to 1.84 ± 0.12. The FD value calculated for the circular selection of the same diameter as the side-length of the image is equal to 1.77 ± 0.09, smaller by *ca* 4% than for the whole image. However, when calculated areas of the investigated images are compared, the difference is *ca* 21.5%. It is suggested that lower FD values calculated for circular selections are slightly smaller (up to 10% of difference in FD) when compared to the values calculated the whole pattern result from smaller area available for processing as corners of the image are not included.

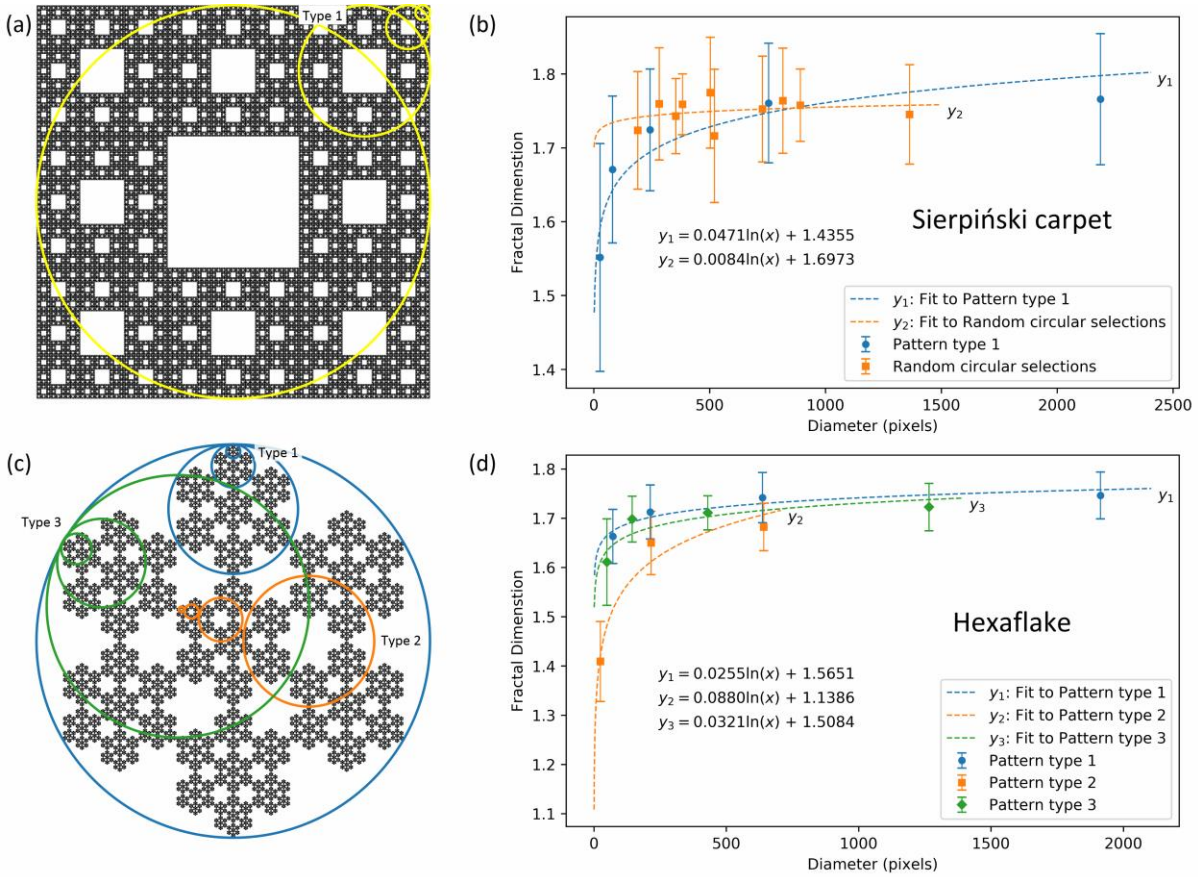

Figure S3. Benchmark testing control fractal samples, Sierpiński carpet **(a)** and hexaflake **(c)**, sourced from [11-12], respectively. Regions indicated by circular selections (marked with type number) were analysed utilising the procedure shown in **Figure 3**), the same as applied to the experimental data. **(b)** and **(d)** show plots of box counting fractal dimensions of the selected areas with respect to their diameters. Data was modelled with a logarithmic function with relevant equations displayed in (**b**) and (**d**).

In order to plot coloured boundaries for each ZnO nano/microflid dataset in **Figure 4b**, the logarithmic function was also fitted to the outermost points of each data sets, both for upper and lower FD values. Equations of the fitted functions are listed in **Table S4**. The shaded area in **Figure 4b** is contained between the lower and upper boundaries, offset by 0.005.

Table S4. Best fit lines ($D = a\ \ln(\lambda_{BM}) + D_0$) calculated for the outermost data points from **Figure 4b** in the main text.

Nano/microfluid Type	**Lower boundary**	**Upper boundary**
In-house ZnO	0.074 $\ln(\lambda_{BM})$ + 1.349	0.067 $\ln(\lambda_{BM})$ + 1.459
ZnO nanopowder	0.034 $\ln(\lambda_{BM})$ + 1.622	0.034 $\ln(\lambda_{BM})$ +1.668
ZnO powder	0.015 $\ln(\lambda_{BM})$ + 1.735	0.034 $\ln(\lambda_{BM})$ + 1.654

SI.08: References

1. Wąsik, P.; Redeker, C.; Dane, T. G.; Seddon, A. M.; Wu, H.; Briscoe, W. H., Hierarchical Surface Patterns upon Evaporation of a ZnO Nanofluid Droplet: Effect of Particle Morphology. *Langmuir* **2018,** *34* (4), 1645-1654.

2. Smith, J. E.; Jordan, M. L., Mathematical and graphical interpretation of the log-normal law for particle size distribution analysis. *J. Colloid Sci.* **1964,** *19* (6), 549-559.

3. Zender, C., Particle size distributions: theory and application to aerosols, clouds, and soils. http://dust.ess.uci.edu/facts/psd/psd.pdf (accessed 12th Dec 2017).

4. Wu, H.; Briscoe, W. H., Morphogenesis of polycrystalline dendritic patterns from evaporation of a reactive nanofluid sessile drop. *Physical Review Materials* **2018,** *2* (4), 045601.

5. Mandelbrot, B. B., *The Fractal Geometry of Nature*. Freeman and Company: New York, 1982.

6. Falconer, K. J., *Fractal geometry: mathematical foundations and applications*. Wiley: Chichester, 1990.

7. Napolitano, A.; Ungania, S.; Cannata, V., Fractal Dimension Estimation Methods for Biomedical Images. In *MATLAB - A Fundamental Tool for Scientific Computing and Engineering Applications - Volume 3*, Katsikis, V. N., Ed. InTech: Rijeka, 2012; p Ch. 07.

8. Alligood, K. T.; Sauer, T. D.; Yorke, J. A., *Chaos: An Introduction to Dynamical Systems*. Springer New York: 2012.

9. Rasband, W. S., ImageJ. https://imagej.nih.gov/ij/ (accessed 4th Jan 2018).

10. Karperien, A., FracLac for ImageJ. http://rsb.info.nih.gov/ij/plugins/fraclac/FLHelp/Introduction.htm (accessed 4th Jun 2018).

11. Greig, J., Sierpinski carpet. https://commons.wikimedia.org/wiki/File:Sierpinski_carpet.png (accessed 30 Mar 2018).

12. 0x0077BE, HexaFlake. https://commons.wikimedia.org/wiki/File:HexaFlake_6th_Iteration_Center.svg (accessed 30 Mar 2018).

13. Walsh, J. J.; Watterson, J., Fractal analysis of fracture patterns using the standard box-counting technique: valid and invalid methodologies. *Journal of Structural Geology* **1993,** *15* (12), 1509-1512.

14. Richards, F. J., A Flexible Growth Function for Empirical Use. *J. Exp. Bot.* **1959,** *10* (2), 290-301.

Bénard-Marangoni dendrites upon evaporation of a reactive ZnO nanofluid droplet: Effect of substrate chemistry

Patryk Wąsik[a,b], Annela M. Seddon[a,c], Hua Wu[b], and Wuge H. Briscoe[b,]*

[a] Bristol Centre for Functional Nanomaterials (BCFN), HH Wills Physics Laboratory, University of Bristol, Tyndall Avenue, Bristol, BS8 1TL, UK

[b] School of Chemistry, University of Bristol, Cantock's Close, Bristol, BS8 1TS, UK

[c] School of Physics, HH Wills Physics Laboratory, Tyndall Avenue, University of Bristol, Bristol, BS8 1TL, UK

INFORMATION

This chapter has been published as a research article: **Wąsik, P.;** Seddon, A. M.; Wu, H.; Briscoe, W. H., Bénard-Marangoni dendrites upon evaporation of a reactive ZnO nanofluid droplet: Effect of substrate chemistry *Langmuir* **2019**, *35* (17), 5830-5840. DOI: 10.1021/acs.langmuir.9b00109. Adopted with permissions from the above. This chapter has been authored by the candidate with no more input from co-authors and supervisors that would have been provided in a conventional thesis chapter. PW performed all the experiments and data analysis and wrote the manuscript, PW, HW, and WHB conceived the project, WHB co-wrote the manuscript, AMS and WHB supervised the project, and all co-authors commented on the manuscript.

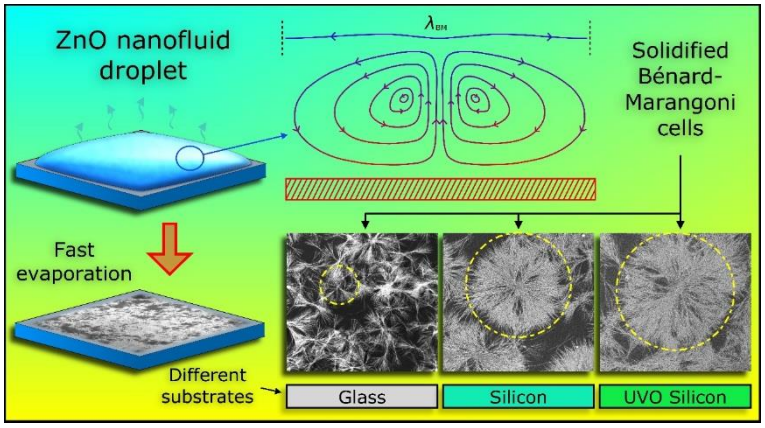

ABSTRACT

Evaporation of a particle laden sessile drop can lead to complex surface patterns with structural hierarchy. Most commonly the dispersed particles are *inert*. We have recently reported that, when the sessile drop contains *reactive* ZnO nanoparticles, solidified Bénard-Marangoni (BM) cells with dendritic micromorphology were formed in the residual surface pattern from *in situ* generated nanoclusters. Here we report the effect of substrate chemistry on the residual pattern from evaporation of nanofluids containing ZnO particles dispersed in a mixture of cyclohexane and isobutylamine, by comparing three different substrates: glass, silicon and hydrophilized silicon. In particular, we performed a quantitative analysis of the BM cell size distribution and the cell morphological characteristics *via* the fractal dimension analysis. We find that the size dimension λ_{BM} of the dendritic Bénard-Marangoni cells varied on the different substrates, attributed to their different hydrophilicity and affinity for water molecules, evident from the different polar components γ^p in their surface free energy from the Owens-Wendt analysis. The average BM cell size was the smallest for the glass substrate (λ_{BM} = 289 μm), and comparable for the unmodified and UVO treated silicon wafers (with λ_{BM} = 466 μm and 423 μm, respectively). The fractal dimension analysis provided a quantitative description of the BM cells with complex structural hierarchy, highlighting the differences in the geometric features of the surface patterns resulting from different substrate chemistry. We also found that the fractal dimensions depended on the BM cell size, attributing it to two different regimes: the growing fractals and the maturing fractals.

KEYWORDS

Evaporation Induced Self-Assembly, nanoparticles, zinc oxide, dissolution, Bénard-Marangoni instabilities, coffee ring effect, fractal dimension analysis

INTRODUCTION

The Bénard convection, also known as the Bénard-Marangoni convection, was first observed by Henri Claude Bénard in 1900 as ordered hexagonal cells formed in a melted paraffin with graphite dusts [1-2]. Intrigued by the observation, he performed comprehensive studies of such cellular vortices in a horizontal layer of different volatile liquids such as ethanol, diethyl ether, and benzene at room temperature, as well as non-volatile wax or spermaceti (whale oil), on a metallic plate heated to 50 – 100 °C [3-4]. In 1916, Lord Rayleigh published first theoretical explanation of Bénard's results based on the stability analysis, which implicated buoyancy as the driving force for the convective motion [5]. However, it has been later shown, both experimentally [6] and theoretically [7], that the convective cells in Bénard's system were induced by variations in the surface tension caused by temperature fluctuations at the free fluid surface. Many studies on Bénard convections have since been reported [8].

Due to localized fluctuations in the droplet surface temperature, multiple Bénard cells can be induced, and dispersed solutes may form corrugated residual patterns of connected polygons templating the convective cells [9]. This has been explored in the evaporation induced self-assembly (EISA) process [10-11] to produce various surface patterns. Some examples include porous films with a knotted-rope structure from zeolite silicalite nanoparticle suspensions dried on silicon [12], and honeycomb patterns from various suspensions, such as silver, cobalt, copper and barium ferrite nanocrystals dispersed in hexane or decane [13-14], polystyrene microspheres in aqueous solutions with added pentadecanoic acid [15-16], toluene solutions of poly(styrene-ran-butadiene) copolymer [17] or calcium carbonate particles [18], and polymethyl(methacrylate) dissolved in chloroform [19]. In addition, the Bénard-Marangoni convection has also been employed to produce other types of structures, such as sol-gel derived titania (TiO_2) films using surface tension changing co-solvents [20], hexagonal and stripe-like

patterns by varying substrate wettability [21], nanoporous TiO_2 films [22], and single-walled carbon nanotubes [23].

In these previous studies [1-2, 5-8, 10-19, 21], the dispersed particles were *inert*, and the residual pattern formation was governed by inter-particle forces and evaporation-induced solvent flows, which in turn could be influenced by particle size, concentration, solvent composition, or evaporation rate. We have recently shown [24-25] that rapid evaporation of a *reactive* ZnO nanofluid sessile drop can lead to the formation of hierarchical residual, and the mechanism was elucidated and described in some detail in Ref. [24] to account for the structural hierarchy on nano-/micro-/maco-scopic levels, combining video microscopy observations of the capillary waves at the droplet surface and time-resolved transmission electron microscopy (TEM) and cryo-TEM observations of the constituent nanostructures inside the droplet at different stages of the evaporation process. Briefly, as a mixed solvent (chloroform/methanol/isobutylamine or cyclohexane/isobutylamine) droplet containing ZnO nanoparticles evaporates on a solid substrate, ZnO particles undergo rapid dissolution. The *in situ* generated molecular and particulate species collude with and modify the solvent flows in the evaporating droplet, which further self-assemble and self-organize into clusters. As the drop thins upon evaporation, Bénard-Marangoni (BM) instabilities are triggered, and the *in situ* self-assembled clusters track the BM convections. Such BM convections manifest as multiple vortices with liquid flowing upward in the center and subsequently outward to the edge of the convection cells. Further removal of solvent upon evaporation leads to solidification and crystallization of the polycrystalline cellular pattern in the drop center with dendritic micromorphology.

The initial moisture-assisted dissolution of isobutylamine-coated ZnO nanoparticles was recognized as a key step in this process. We have shown that different crystallinity of the ZnO nanoparticles led to different dissolution rates, which in turn resulted in different surface patterns [26]. These results may open up new routes for facile fabrication of functional surface patterns with hierarchical structures *via* self-assembly induced by evaporation of *reactive* nanofluids.

The solvent flow in an evaporating droplet is affected by several other factors, which will consequently affect the BM convection and the residual pattern. In this work, we have investigated how the substrate surface chemistry would affect the morphology of the surface patterns produced. Three

different substrates, *i.e.* a glass coverslip, a silicon wafer, and a ultraviolet/ozone (UVO) treated silicon wafer, were compared. Their surface chemistry was assessed with the static contact angle (CA) measurement and their roughness by atomic force microscopy (AFM). In addition, three types of ZnO particles with different sizes and crystallinities [26] were dispersed in a mixture of cyclohexane and isobutylamine, which were used to form the evaporating sessile drops. The resulted hierarchical surface patterns were analyzed by scanning electron microscopy (SEM). We found that the dimensions of the solidified Bénard cells depended on the substrate used due to different BM flows on these substrates. To go beyond a descriptive account of the surface pattern, the quasi-2D BM convection cells were analyzed using the box counting fractal dimension (FD) analysis [27] that provided a quantitative description of the BM cells with complex structural hierarchy, highlighting the differences in the geometric features of the surface patterns resulting from different substrate chemistry. We show that the surface chemistry of the substrate influences the dimension of the solidified BM cells during the ZnO nano/microfluid evaporation, and we discuss this effect in terms of the substrate-water interactions, as water is crucial to the ZnO nanocrystal dissolution in the pattern formation mechanism from such reactive nanofluids.

MATERIALS AND METHODS

ZnO nano/microparticles

Three different types of zinc oxide (ZnO) particles were used: in-house synthesized ZnO nanoparticles, and commercially acquired ZnO nanopowder (Sigma-Aldrich, <100 nm particle size, ~80% Zn basis), and ZnO powder (Sigma-Aldrich, ACS reagent, ≥99.0% (KT)). The in-house ZnO nanoparticles were synthesized using a modified procedure from Sun *et al*. [28]. Transmission electron micrographs of the ZnO particles can be found in Supplementary Information, SI.01, also shown as insets in Figure 5. Detailed characterization of ZnO particles including transmission electron microscopy, particle size distribution, X-ray diffraction, and energy-dispersive X-ray spectroscopy as well as synthesis of the in-house ZnO nanoparticles is reported elsewhere [26].

ZnO nano/microfluid preparation

ZnO nano/microfluids were prepared by dispersing ZnO particles in a mixture of cyclohexane (Fisher Chemicals, assay 99%) and isobutylamine (Sigma-Aldrich, assay 99%), in a 5:1 volume ratio to 1 mg/mL concentration. As prepared suspensions were sonicated for 2 h to form homogeneous dispersions prior to evaporation experiments. Dynamic light scattering data of ZnO nano/microfluid has been reported in [26], which indicated formation of clusters (1 - 2 μm in size) in all ZnO nano/microfluids, as the suspensions were not inherently stable.

Substrates

Evaporation of the ZnO nano/microfluids sessile drops were performed on three different substrates cut into 1×1 cm^2 squares, including standard microscope glass slides (type 7101, 0.8 - 1.0 mm thick), and silicon wafers (UniversityWafer Inc., ID 452, 100 mm diameter, P type, B dopant, <100>, 0-100 Ω·cm, 500 μm thick, single-sided polish, test grade), either unmodified or treated by UV/ozone (UVO) exposure for 10 min. The substrates were cleaned by sonication in acetone and ethanol sequentially for 10 min each, rinsed three times with *Milli-Q* water (18.2 MΩ·cm at 25 °C), then sonicated in *Milli-Q* water for 10 min and dried using a stream of nitrogen prior to the experiment. For the UVO treatment, a 42-220 UVO-Cleaner (Jetlight Company, Inc.) was used to modify the surface chemistry of the Si substrates, making them more hydrophilic by increasing the amount of -OH groups on the surface [29-30] (see SI.02). Both the contact angle measurements and evaporation experiments were performed within 1-2 h of the UVO treatment.

The wettability of the substrates was characterized using sessile droplet static contact angle measurements of probing liquids such as Milli-Q water (18.2 MΩ·cm at 25 °C), diiodomethane (Alfa Aesar, 99%), ethylene glycol (Fluka Analytical, ≥ 99.5%), n-hexadecane (Acros Organics, 99%, pure), n-dodecane (Acros Organics, 99%, pure), cyclohexane (Fisher Chemicals, assay 99%), and a mixture of cyclohexane and isobutylamine (Sigma-Aldrich, assay 99%) in a 5:1 volume ratio, in addition to ZnO nano/microfluids prepared from the in-house synthesized ZnO nanoparticles and commercially acquired ZnO nanopowder and ZnO powder (see SI.01) dispersed in the mixture of cyclohexane and isobutylamine 5:1 volume ratio to 1 mg/mL concentration (see the main text). The measurements were performed at room temperature of 24.5 ± 0.5 °C and relative humidity of ~45% (monitored with

a humidity/temperature pen (Tracable)) using a Drop Shape Analyzer – DSA100 (KRÜSS) operated with the KRÜSS ADVANCE 1.9.0.8 software. In a typical measurement, a 5 μL droplet of the measurement liquid (30 μL for cyclohexane/isobutylamine mixture) was pipetted onto a 1×1 cm^2 substrate, and the image of the drop was recorded for 60 seconds in one second intervals. The value of the contact angle was obtained by tangent fitting method to the drop shape using the software. The errors in mean CA values are quoted as the standard deviations from: 20, 37, and 26 separate measurements for the in-house ZnO nanofluid on glass, unmodified Si, and UVO exposed Si, respectively; 12, 62, and 35 for ZnO nanopowder nano/microfluid on glass, unmodified Si, and UVO exposed Si, respectively; and 8, 25, and 6 for ZnO powder nano/microfluid on glass, unmodified Si, and UVO exposed Si, respectively. Surface free energies were calculated according to the Owens-Wendt method [31], based on the sessile droplet CA measurements of *Milli-Q* water and diiodomethane (see SI.03). Substrate topography was characterized with the atomic force microscopy (AFM) using MultiMode Nanoscope III (Bruker) operated in the tapping mode (see SI.04)

Evaporation of reactive ZnO nanofluid droplets

An air displacement pipet was used to drop-cast 30 μL of ZnO nano/microfluids onto the surface of the substrates, which were placed inside compartments of an uncovered polystyrene Petri dish (Sterilin, 25 compartment sterile 100 mm box). The evaporation took place at room temperature and RH ~45%. The substrates were covered with white deposits within several minutes of evaporation. In the case of UVO-Si, the evaporation experiments were performed within 1-2 h after the UVO treatment.

Residual surface pattern characterization

Residual surface patterns formed from ZnO nano/microfluids were analyzed with scanning electron microscopy (SEM) using a JSM-IT300 SEM, JEOL. Microfocus grazing incidence X-ray diffraction (XRD) characterization has confirmed [26] that the residual surface patterns produced from the in-house ZnO nanofluid were composed almost entirely from layered complexes of zinc hydroxide with anionic interlayer species (interplanar spacing of 1.37 nm and 0.68 nm, indexed as (001) and (002) planes), and brucite-type zinc hydroxide (interplanar spacing of 0.27 nm and 0.52 nm, indexed as (100) and (110) planes) structures. There were also partial contributions (~5% of diffraction signal) of a ZnO phase. For the residual patterns produced from the commercially sources ZnO particles, the diffraction profiles

were dominated by ZnO patterns from undissolved ZnO nano/microcrystals forming aggregates that were deposited across the fibrous network of the residual patterns.

Bénard-Marangoni (BM) cells size distribution analysis

Size distribution analysis of the BM cells was performed using ImageJ (version 1.51j8) software. First, the individual BM cells were outlined on their SEM images using the Serif DrawPlus X6 software, then manually separated to eliminate overlaps for analysis. The size distribution of the BM cells was fitted with the lognormal distribution function (see SI.06).

Fractal dimension analysis

The complex structural hierarchy of BM cells was analyzed using the box counting fractal dimension (FD) analysis, as described in detail in [27]. Briefly, in the box counting algorithm, a grid of equal boxes of a side-length ε is laid over an image, and then the number of non-empty boxes, $N(\varepsilon)$, is counted. This number varies with the box size, $N(\varepsilon) \sim \varepsilon^{-D}$, and the procedure is performed for a range of ε values. The box counting fractal dimension, D, is obtained from the slope of the $\ln(N)$ *vs*. $\ln(\varepsilon)$ plot [32-33]. Specifically for the analysis of the BM cells, the SEM images of the pattern were converted to the binary format in ImageJ, and then circular selections containing BM cells were analyzed using FracLac (version 2015Sep090313a9330) plugin [34]. The analysis process is schematically displayed in **Figure S10**. The analysis is described in the SI section of Ref. [27] and reproduced in the SI section of Chapter 3.

RESULTS AND DISCUSSION

Substrate characterization: Surface energy and roughness

The surface energy of the three different substrates, microscope glass slide, silicon wafer and UVO hydrophilized silicon (UVO-Si) wafer, was assessed with the static contact angle (CA) measurement using different solvents (see SI.03 for details). The results are presented in **Table 1**. The mean CA values measured with a 5 μL droplet of three ZnO nano/microfluids were similar across the substrates, *ca.* $\theta \approx$ 5.5 - 6.5°, with the in-house ZnO nanofluid showing a slightly higher CA on glass (θ = 8.6 ± 2.0°) and ZnO powder nano/microfluid a slightly lower CA on UVO-Si (θ = 4.1 ± 1.9°).

The mean *water* CA was $\theta = 21.7 \pm 3.5°$ on the microscope glass slide, $\theta = 56.5 \pm 1.2°$ on the silicon wafer, and $\theta = 9.8 \pm 1.6°$ on UVO-Si. These broadly agree with the literature values, *i.e.* $\theta \sim 31°$ for glass, $\theta \sim 58°$ for silicon with native SiO_2 [35], and $\theta \sim 10°$ for UVO exposed silicon, respectively [36]. Thus, all the substrates exhibited a certain degree of hydrophilicity, with the UVO-Si most hydrophilic, and untreated Si least.

For the evaporation experiment, the 30 μL droplets would become pinned at the edge with an apparent pinned CA of $\theta \sim 26$ - $27°$ on all the substrates. This is comparable to the pinned CA of the control droplets of cyclohexane/isobutylamine mixtures on the substrates ($\theta \sim 26$ - $27°$) also shown in **Table 1**. The pinned CA values are higher than those for the static CA. As the evaporation took place, the pinned droplet would thin, and the apparent CA at the pinned periphery would decrease to the values of respective nano/microfluids, before the contact line receded upon further evaporation.

The calculated surface free energies (SFE) of the substrates based on the Owens-Wendt method [31] using droplets of *Milli-Q* water and diiodomethane (see SI.03 for details) were $\gamma = 74.4 \pm 1.5$, 50.3 ± 1.6, and 75.5 ± 0.5 mN/m for the microscope glass slide, Si, and UVO-Si, respectively. The UVO-Si had the largest polar SFE contribution ($\gamma^P = 36.4 \pm 0.3$ mN/m), consistent with its smallest water CA. The unmodified Si had the lowest values of disperse and polar components in the surface energy, $\gamma^D = 33.1 \pm 0.8$ and $\gamma^P = 17.2 \pm 0.8$ mN/m, respectively. We note that slightly different surface energy values of diiodomethane exist in the literature, *e.g.* $\gamma^D = 48.5$ (or 49.5) mN/m and $\gamma^P = 2.3$ (or 1.3) mN/m in Ref. [37]. The values of $\gamma^D = 50.8$ mN/m and $\gamma^P = 0$ mN/m have been used in this study as in Refs. [38-40]. Resolving this small controversy is beyond the scope of this study. However, the small differences in the surface energy values (*cf.* **Table S6**) do not affect the discussions presented here, as discussed in SI.03.

In addition, the topography of the substrate surface was characterized with AFM imaging (see SI.04). The surface roughness expressed in both R_a (arithmetic average roughness) and R_{rms} (root mean square average roughness) parameters (**Table S7**) increased slightly in the order from glass ($R_a = 0.09$ nm, $R_{rms} = 0.11$ nm), to unmodified silicon ($R_a = 0.14$ nm, $R_{rms} = 0.17$ nm), and UVO treated silicon

(R_a = 0.17 nm, R_{rms} = 0.22 nm). All the substrates were however all relatively smooth, manifesting in a very low (< 0.2 nm) arithmetic average roughness, R_a.

Table 1. Surface free energies (SFEs) and wettability of the substrates. The mean contact angle (CA) measurements between different substrates and droplets (5 µL) of *Milli-Q* water, diiodomethane, ZnO nano/microfluids (in cyclohexane/isobutylamine 5:1 mixtures), and pinned CA of the control mixture (30 µL droplet, pinned CA). The SFEs were calculated using the Owens-Wendt method [31] (see SI.03 and Chapter 1, in which we note other methods also exist (*e.g.* Neumann, Fowkes, Owens-Wendt-Rabel-Kaelble, van Oss-Chaudhury-Good, and Zisman).

	Microscope glass slide	Silicon wafer (Si)	UVO silicon wafer (UVO-Si)
Testing fluids	Mean contact angle (CA) θ		
In-house ZnO nanofluid	8.6 ± 2.0°	5.7 ± 1.2°	6.5 ± 1.7°
ZnO nanopowder nano/microfluid	5.5 ± 1.0°	6.0 ± 1.9°	5.5 ± 2.0°
ZnO powder nano/microfluid	5.6 ± 1.1°	5.9 ± 1.8°	4.1 ± 1.9°
Milli-Q water	21.7 ± 3.5°	56.5 ± 1.2°	9.8 ± 1.6°
Diiodomethane	29.6 ± 0.5°	52.0 ± 1.3°	41.1 ± 0.9°
Cyclohexane/isobutylamine mixture (pinned)	29.4 ± 4.3°	26.7 ± 1.5°	27.2 ± 2.4°
	Surface free energy (mN/m)		
Total γ	74.4 ± 1.5	50.3 ± 1.6	75.5 ± 0.5
Dispersive component γ^D	44.4 ± 0.2	33.1 ± 0.8	39.0 ± 0.2
Polar component γ^P	30.0 ± 1.3	17.2 + 0.8	36.4 ± 0.3

Descriptive account of the BM cells on three different substrates from ZnO nanofluid sessile drops

An example of the residual surface pattern formed from the in-house synthesized ZnO nanoparticle (diameter ~ 9 nm) dispersion on hydrophilized UVO-Si is shown in **Figure 1**. (Figure 1a, d, and f are

adapted from Ref. [27], which focused on the fractal dimension analysis. These results are included here to compare with the results on two other substrates shown in Figure 2 and Figure 3 below, for clarity and completeness.) It was composed of a central region with packed cellular structures surrounded by a coffee ring around the perimeter of the droplet (**Figure 1b-c**), comprising a dense network of intercalating fibers (**Figure 1c**). The central region of the residual surface pattern consisted of circular patches or cells – identified as solidified Bénard-Marangoni (BM) convection cells, with their diameters corresponding to the BM wavelength (λ_{BM} = 200 - 800 μm). The micromorphology of the cells resembles spoke-like patterns with a bow-tie projection (**Figure 1d**). Their appearance was also similar to the BM flow pattern observed during the evaporation of toluene from polystyrene/toluene solution [14]. One of the well-defined cells is shown in **Figure 1f** (whose fractal dimension analysis has been shown in detail in [27]. The Marangoni number, B, which gauges the balance between the surface tension and the viscous force in a fluid, depends on the parameters such as the temperature gradient across the drop thickness, and the thermal diffusivity, dynamic viscosity, thermal conductivity, density, and specific heat capacity in the drop [7] (see also Chapter 1, equation 2). For the fluid conditions with $B > 80$, spontaneously generated surface-tension driven flows will result in the formation of BM cells. For a drop of thickness d, the ultimate BM cell size or wavelength, λ_{BM}, is related to the Marangoni number by:

$$B = 32\left(\frac{\pi d}{\lambda_{BM}}\right)^2. \quad (1)$$

Wu and Briscoe [24] estimated that, in their ZnO nanofluid (ZnO nanoparticles dispersed in a mixture of chloroform, methanol and isobutylamine), the Marangoni number was much larger ($B \sim 300$ - 2000) than the critical value of 80 [24]. They attributed the formation of the BM cells to the fluctuations in the fluid viscosity due to the variation in the local particle concentration during evaporation. It was also shown [24] that slow evaporation would not lead to the BM cell formation, which could be attributed to the insufficient temperature gradient across the thickness of the drop required to initiated the BM flow. Here we have observed λ_{BM} = 200 - 800 μm, giving a critical thickness range d = 100 – 400 μm at which the BM instabilities were triggered. This variability is consistent with the interpretation that the concentration of the *in situ* generated molecular clusters and particulate species in the reactive ZnO

nanofluid was inhomogeneous inside the drop, leading to BM being triggered at different evaporation stages.

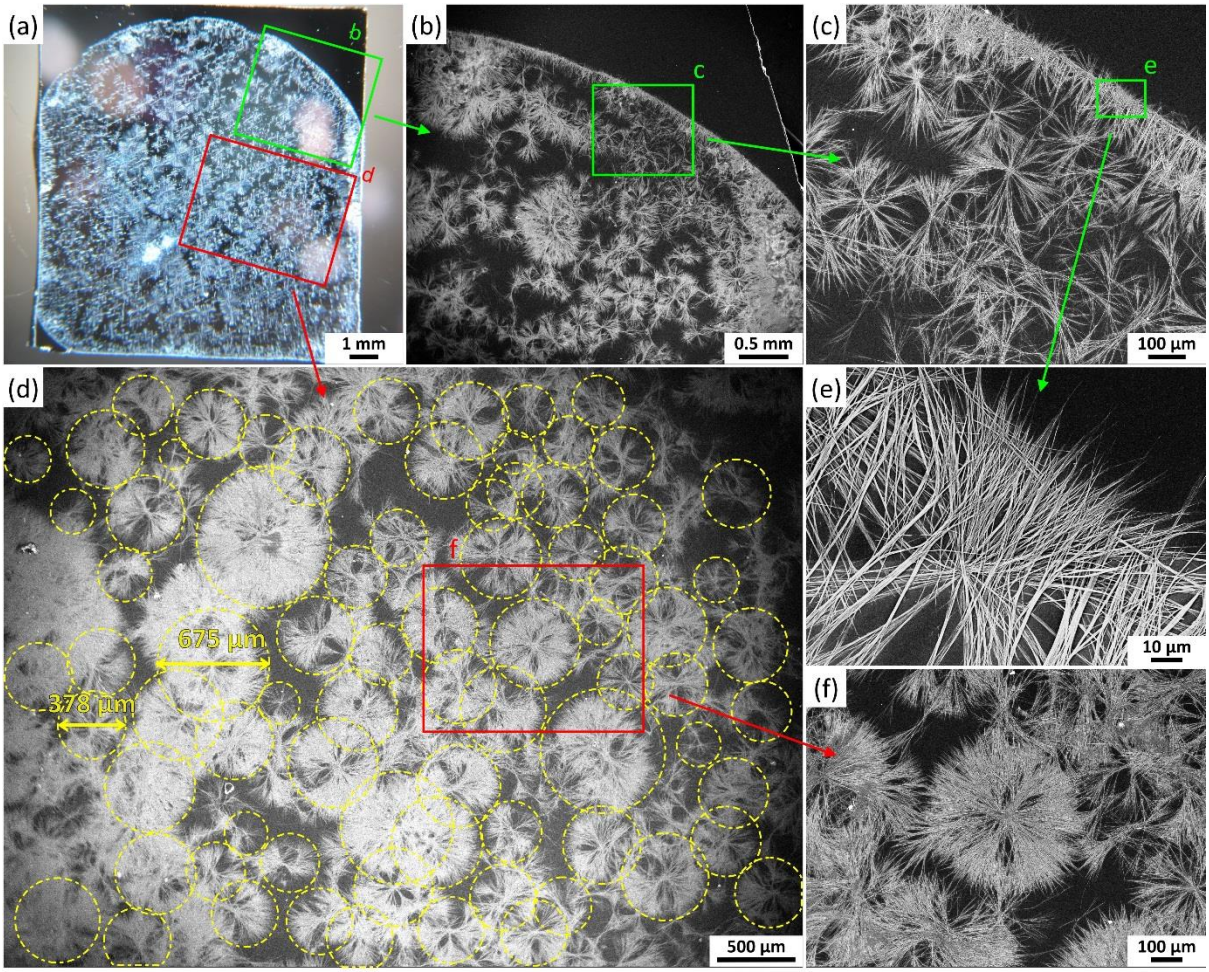

Figure 1. Residual surface pattern formed from a 30 µL sessile drop of the in-house synthesized ZnO nanofluid droplet dried on the UVO treated silicon wafer (UVO-Si): (a) overall optical microscopy image of the pattern; (b-c) enlarged views of an SEM image of a section close to the peripheral coffee ring; (d) a magnified view of a SEM image of the central region that reveals spoke-like patterns with a bow-tie projection, identified as solidified manifestation of Bénard-Marangoni (BM) convection cells; (e) intercalated fibers in the coffee-ring edge; and (f) a magnified view of a BM convective cell. Images in (a), (d), and (f) are adapted from Ref. [27] *J. Colloid Interface Sci.*, 2019, 536, Patryk Wąsik, Annela M. Seddon, Hua Wu, Wuge H. Briscoe, Dendritic surface patterns from Bénard-Marangoni instabilities upon evaporation of a reactive ZnO nanofluid droplet: A fractal dimension analysis, 493-498, Copyright (2019), with permission from Elsevier.

Figure 2 shows that, similar to the residual pattern on UVO-Si, the glass surface was covered with solidified BM convection cells with overall smaller diameters, λ_{BM} = 200 - 500 µm (**Figure 2b-c**). The packing density of the fibers inside BM cells appeared smaller, leading to a higher degree of interpenetration between different BM cells. **Figure 2d** shows the fibers constituting the BM cells, which are re-crystallized from gel-like fibers self-assembled from *in situ* generated clusters, as discussed in detail in Ref [24].

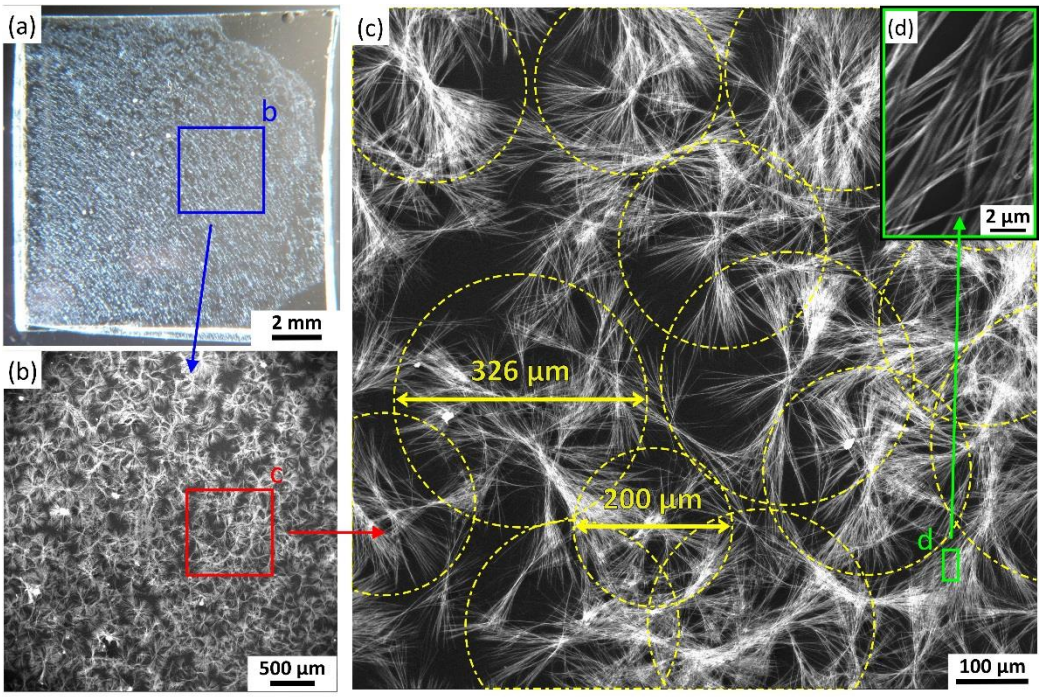

Figure 2. Residual surface pattern formed from a 30 µL sessile drop of the in-house synthesized ZnO nanofluid droplet dried on a microscope glass slip: (**a**) overall optical microscopy image; (**b**) an SEM image of a section in the central region; (**c**) an enlarged view of the central region from (c) showing solidified manifestation of Bénard-Marangoni (BM) convection cells marked by yellow dotted circles; and (**d**) an enlarged view showing the fibrous structure constituting the BM cell.

An example residual surface pattern from the in-house synthesized ZnO nanofluid on an unmodified silicon wafer is presented in **Figure 3**. Similar to the other two substrates, the central region of the substrate was covered with solidified BM cells with a wide range of diameters, *i.e.* λ_{BM} = 250 - 1000 µm, with the fiber-packing denser than those on the glass slide (*cf.* **Figure 2**) and also with significant interpenetrations at the BM cell peripheries.

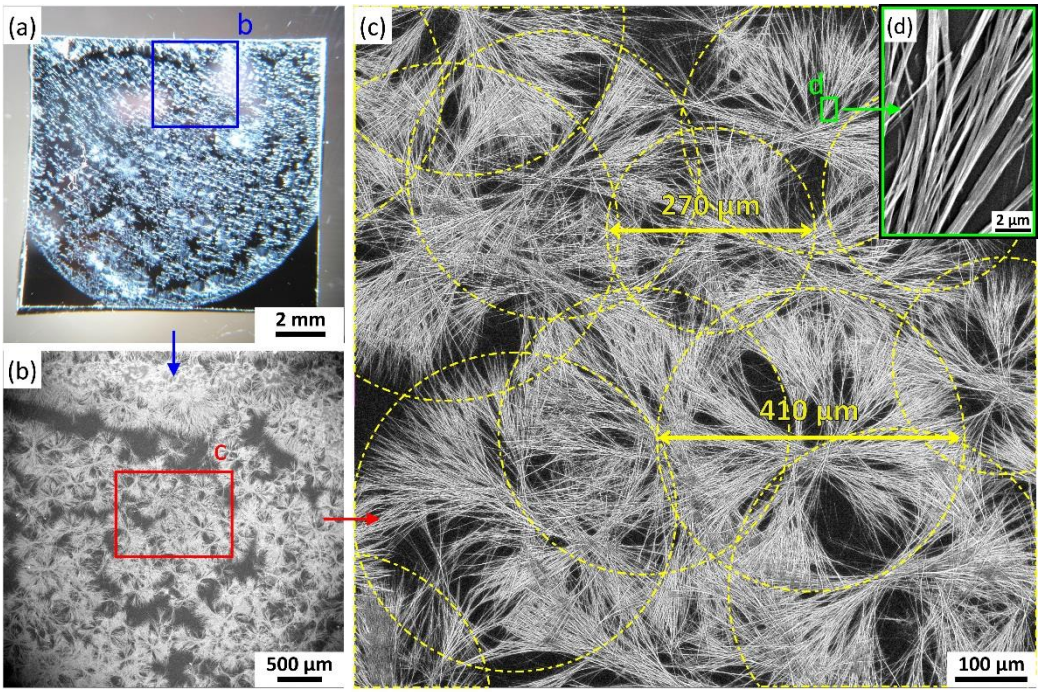

Figure 3. Residual surface pattern formed from a 30 µL sessile drop of the in-house synthesized ZnO nanofluid droplet dried on an unmodified silicon wafer (Si): (**a**) overall optical microscopy image; (**b**) an SEM image of a section in the central region; (**c**) an enlarged view of the central region in (c) showing solidified Bénard-Marangoni (BM) convection cells with borders marked by yellow dotted circles; and (**d**) an enlarged view showing the fibrous structure constituting the BM cell.

Bénard-Marangoni (BM) cell size λ_{BM} distributions on three different substrates

The size distributions of the BM cells in the central region of the residual surface patterns were fitted with the log-normal distribution function (SI.06), with M denoting the geometric mean of the BM cell size λ_{BM} (*i.e.* the median size) by count and σ_g its geometric standard deviation (*i.e.* the skewness and dispersion of the size distribution) [41]. 68.3% of all the BM cells had the size between M/σ_g and $M \cdot \sigma_g$ [42].

The solidified BM cells showed different size distributions on the three different substrates (*i.e.* glass, silicon and UVO exposed silicon), and the results from the in-house synthesized ZnO nanofluid (~ 9 nm nanoparticle diameter) are presented in **Figure 4**. The smallest mean diameters (M = 289 µm, **Figure 4a**) were observed on the glass substrate, with the smallest polydispersity (σ_g = 1.25, *i.e.* 68.3% of λ_{BM} values lying in the range 252-375 µm). The BM cells on Si (**Figure 4b**) showed the largest mean sizes

(M = 466 μm), with a slightly higher diameter dispersion (σ_g = 1.27; 68.3% of λ_{BM} in the range 367-592 μm). By comparison, λ_{BM} on UVO-Si (**Figure 4c**) showed slightly smaller mean size values (M = 423 μm), with the highest dispersion parameter σ_g = 1.30 (*i.e.* 68.3% of λ_{BM} in the range 325-550 μm.

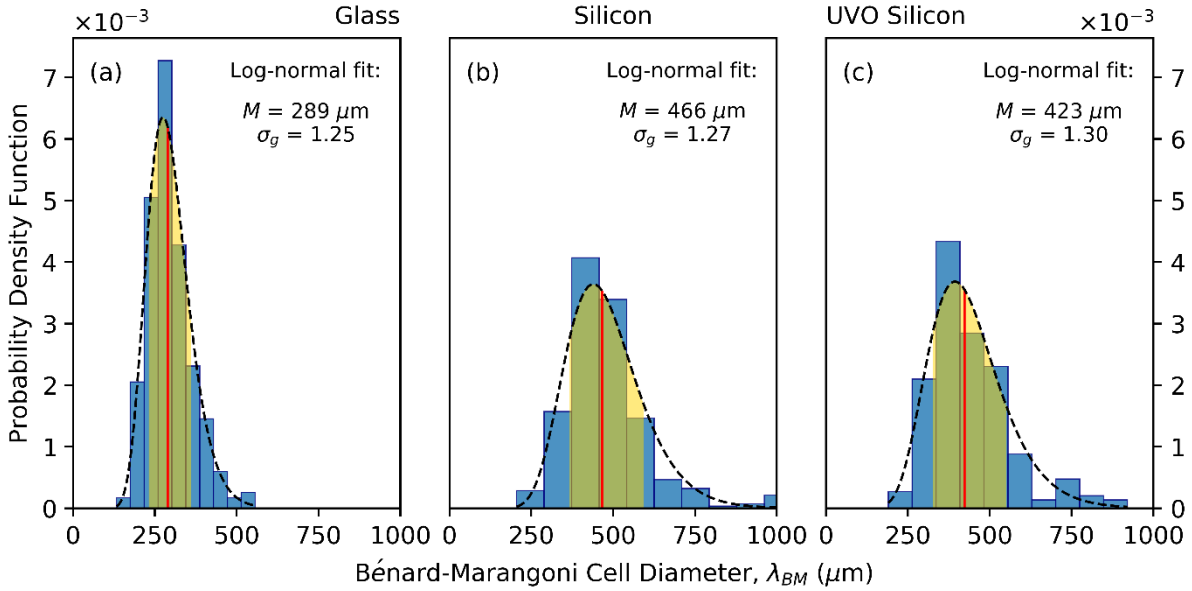

Figure 4. Size distributions of λ_{BM} as the probability density function (PDF) of the BM cells in the central region of the residual surface patterns from the in-house synthesized ZnO nanofluid on the three different substrates: (**a**) microscope glass slide, (**b**) Si, and (**c**) UVO-Si. BM cell sizes distributions were fitted with the log-normal distribution function (dashed lines) (SI.06). Red vertical lines indicate the geometric mean M. BM cell sizes between M/σ_g and $M\cdot\sigma_g$ (68.3% of all values) are shaded in the golden-yellow color under the size distribution curves.

Residual patterns were also studied using the commercially acquired ZnO nanopowder and ZnO powder (*cf.* **Figure S1** in SI.01; at the same particle concentration of 1 mg/mL in the same solvent mixture, cyclohexane and isobutylamine in 5:1 volume ratio), which exhibited a wide range of sizes and morphologies. **Figure S8** shows the SEM images of the central regions of the residual surface patterns from ZnO nanopowder and ZnO powder nano/microfluid droplets on glass, Si, and UVO-Si. The central regions of these patterns were also composed of solidified BM cells, with the dendritic fibers radiating from the cell center. In contrast to the results obtained for the in-house synthesized ZnO

nanofluid (**Figure 1 - Figure 3**), the overall surface coverage and the fiber density in the BM cells were much higher, and there was also more significant inter-cell penetration. The optical microscopy of the overall patterns with the droplet footprints are shown in **Figure S9** and **Table S6**.

A trend in the BM cell size distribution with respect to the substrate was similar to that observed with the in-house ZnO nanofluid. Specifically, the geometric mean BM cell size, *M,* and the geometric standard deviation coefficient, σ_g, increased in the order of glass, unmodified silicon and UVO treated silicon, confirming that the BM cell size depended on the substrate (**Figure 5**). The smallest *M* value was observed for the commercially acquired ZnO powder dried on glass (*M* = 106 μm), and the biggest BM cells were created from the commercially acquired ZnO nanopowder on UVO-Si (*M* = 515 μm).

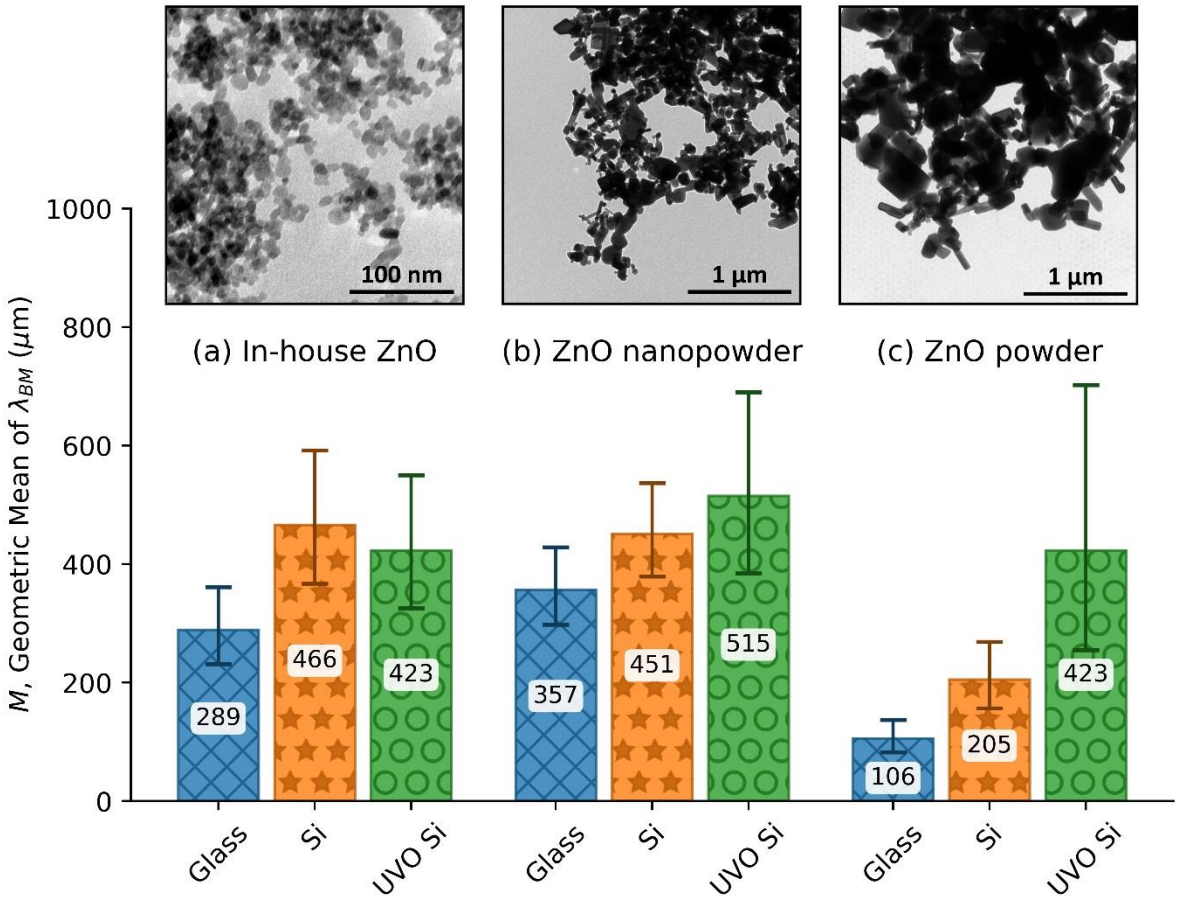

Figure 5. Geometric mean size *M* of Bénard-Marangoni cell size λ_{BM} distribution produced from different nano/microfluids: (**a**) the in-house synthesized ZnO, (**b**) ZnO nanopowder, and (**c**) ZnO powder; formed on different substrates: glass (blue bars with cross "X" pattern), Si (orange bars with star "★″ pattern), and UVO-Si (green bars with circle "O" pattern). The corresponding TEM images of

the ZnO particles in the droplet dispersions are shown at the top. The error bars are calculated as M/σ_g and $M \cdot \sigma_g$ for lower and upper errors, respectively, showing the distribution of λ_{BM}.

Box counting fractal dimension (FD) analysis of Bénard-Marangoni (BM) cell micromorphology

The results of the box counting fractal dimension (FD) analysis of the solidified BM cells on different substrates are presented in **Figure 6**, and all the FD values were in the range $D \approx 1.66$ - 1.89. The fractal dimension of a pattern reflects its geometrical properties, *i.e.* how much space it fills when it is scaled up or down or the prominence of its irregularities [43]. It can also be used to quantify the ruggedness of particle boundaries [44]. Fractal dimensions, in contrast to topological dimensions, can take non-integer values. For reference, a line is 1-dimentional, a surface is 2-dimensional, and a cube is 3-dimensional object. Classical fractals such as the Koch snowflake or the Sierpiński triangle have dimensions of $D \approx 1.262$ and 1.585, respectively [45]. If these structures are scaled up, the Sierpiński triangle would cover more area than the Koch snowflake. However, both of them would cover less area than a scaled up square ($D = 2$), which would fill the entire area; but more than a scaled line ($D = 1$), which would not fill any area at all [43]. The distribution of the D values for the BM cells was calculated as a probability density function (PDF) as shown in **Figure 6a**, **c** and **d** (left hand side). The fitting parameters, μ and σ, the mean value and its standard deviation respectively, are also listed in the figure for the normal distribution fits, shown as dashed lines h_1, h_2 and h_3, respectively for glass, Si and UVO-Si and for different ZnO nano/microfluids. In addition, the apparent trends in the mean value and its standard deviation of fractal dimension distribution are shown in **Figure 7**.

The BM cells formed from the in-house ZnO nanofluid on the glass substrate (h_1 in **Figure 6a**) had the lowest average D value of $\mu = 1.77$ with the highest dispersion of $\sigma = 0.04$, amongst all samples (**Figure 7**). BM cells formed on both unmodified and UVO treated silicon resulted in higher and less dispersed D values, with $\mu = 1.84$ ($\sigma = 0.02$) and 1.82 ($\sigma = 0.03$), respectively (h_2 and h_3 in **Figure 6a**). The scatter in the D values is qualitatively consistent with our interpretation that there were local inhomogeneities in the viscosity and thermal properties in a drying droplet. The various flow rates and solute concentrations involved in the self-assembly process in different BM flow cells would result in a different packing in the dried cell, and in turn different fractal dimension values.

The D values for the BM cells from the other ZnO particles exhibited a smaller scatter ($D \sim 1.82 – 1.84$). For the ZnO nanopowder BM cells, these values were, μ = 1.83 (σ = 0.01), 1.83 ($\sigma = 0.03$), and 1.84 ($\sigma = 0.02$), on glass, Si, and UVO-Si (h_1, h_2, and h_3 in **Figure 6c**, and **Figure 7c**), respectively. Similarly for the BM cells produced from the ZnO powder nano/microfluid, the corresponding values are $\mu = 1.82$ ($\sigma \approx 0.02$), 1.84 ($\sigma = 0.03$), and 1.84 ($\sigma = 0.02$), on the three substrates (h_1, h_2, and h_3 in **Figure 6e**, and **Figure 7b**).

Variation of BM cell fractal dimension with its size: Growing fractals vs. maturing fractals

The fractal dimension values are also plotted against BM cell diameters (D *vs*. λ_{BM}) on the right-hand side of **Figure 6** (**b**, **d** and **f**). There appears a general trend that D increases with λ_{BM} for all the conditions investigated, a trend that has also been observed from a benchmark FD analysis of classic fractals such as a hexaflake and the Sierpiński carpet [27] (also see SI for Chapter 2). The rate of increase is much higher for small BM cell diameters of $\lambda_{BM} < 200$ μm, before a plateau is reached for higher λ_{BM} values. The data for different substrates is enveloped in colored areas for comparison. This trend is consistent with the observation that the BM cells had a more open structure (and thus smaller surface coverage) towards the cell centre, leading to smaller D values for smaller λ_{BM}. As a result, the BM cells with bigger diameters exhibited larger D values, and thus had more rugged structures. This is an interesting result. A fractal is characterized by its constant FD value as it is scaled up or down. Here we show that the solidified BM cells and the classical fractal patterns all display a smaller D value for smaller fractals, and their fractal dimensions then reached a plateau value that is consistent to what has been reported in the literature. We suggest that the FD analysis has revealed two regimes of the fractal growth: an initial stage of growing fractals with a more open structure and a subsequent stage of maturing fractals, and this trend has not been reported previously.

The trend may be fitted to a logarithmic function, $y = a \ln(\lambda_{BM}) + D_0$, shown as the dashed lines in the figure labelled as y_1, y_2 and y_3 for the patterns on glass, Si, and UVO-Si, respectively (**Figure 6b**, **d** and **f**). It should be acknowledged that the choice of the function is arbitrary, mostly as a guide for the eye. We discuss the physical meanings of the fitting parameters in a qualitative manner to compare different conditions. A different fitting function would have equally described the trend (*e.g.* a polynomial), but the discussion below is qualitatively valid and internally consistent.

A smaller D_0 and larger a can be indicative of the presence of more voids (*i.e.* unoccupied areas) towards the center of the dendritic pattern of a BM cell. The BM cells from the ZnO powder resulted in the highest intercept values D_0 (in the range of 1.71 - 1.80), and the lowest a values in the range of 0.01 - 0.02, for all the investigated substrates, indicating the highest fibre density in the BM cells. This is followed by patterns from the ZnO nanopowder on glass and UVO-Si, with D_0 values equal to 1.69 and 1.71, and a values ~ 0.03 and 0.02, respectively. However, the results from the patterns produced from the ZnO nanopowder nano/microfluid on Si (D_0 = 1.51, a = 0.06) are similar to those from the in-house synthesized ZnO nanofluid on all the substrates (D_0 = 1.42 - 1.62, and a = 0.04 - 0.06).

The BM cells from the in-house ZnO nanofluids on glass exhibited the smallest FD values (μ = 1.77) compared to the silicon substrates (h_2 and h_3 *vs*. h_1 in **Figure 6b**). This could be reconciled with the D *vs*. λ_{BM} trend, as the corresponding BM cell size was the smallest (M = 289 μm, **Figure 4**). In addition, the smallest FD value on glass may also be related to the lack of interpenetration between the smaller cells. ZnO nanopowder and ZnO powder nano/microfluids produced residual surface patterns (**Figure S8**) with the highest fiber density and the highest level of inter-cell penetration. Even though the BM cells varied widely in diameters λ_{BM}, from M = 101 μm for the ZnO powder patterns on glass (**Figure S10g**) to M = 558 μm for the ZnO nanopowder patterns on UVO-Si (**Figure S10f**), the fractal dimension analysis revealed that all of them had average D values between $\mu \approx$ 1.82 - 1.84 (**Figure 6c** and **e**) comparable to the BM cells produced from the in-house ZnO nanofluid on Si and UVO-Si (μ = 1.84 and 1.82, respectively), but much larger than the average fractal dimension for the BM cells on glass (μ = 1.77) (**Figure 6a**). This suggests that the smallest FD value on glass was also related to the lack of interpenetration/overlapping between BM cells.

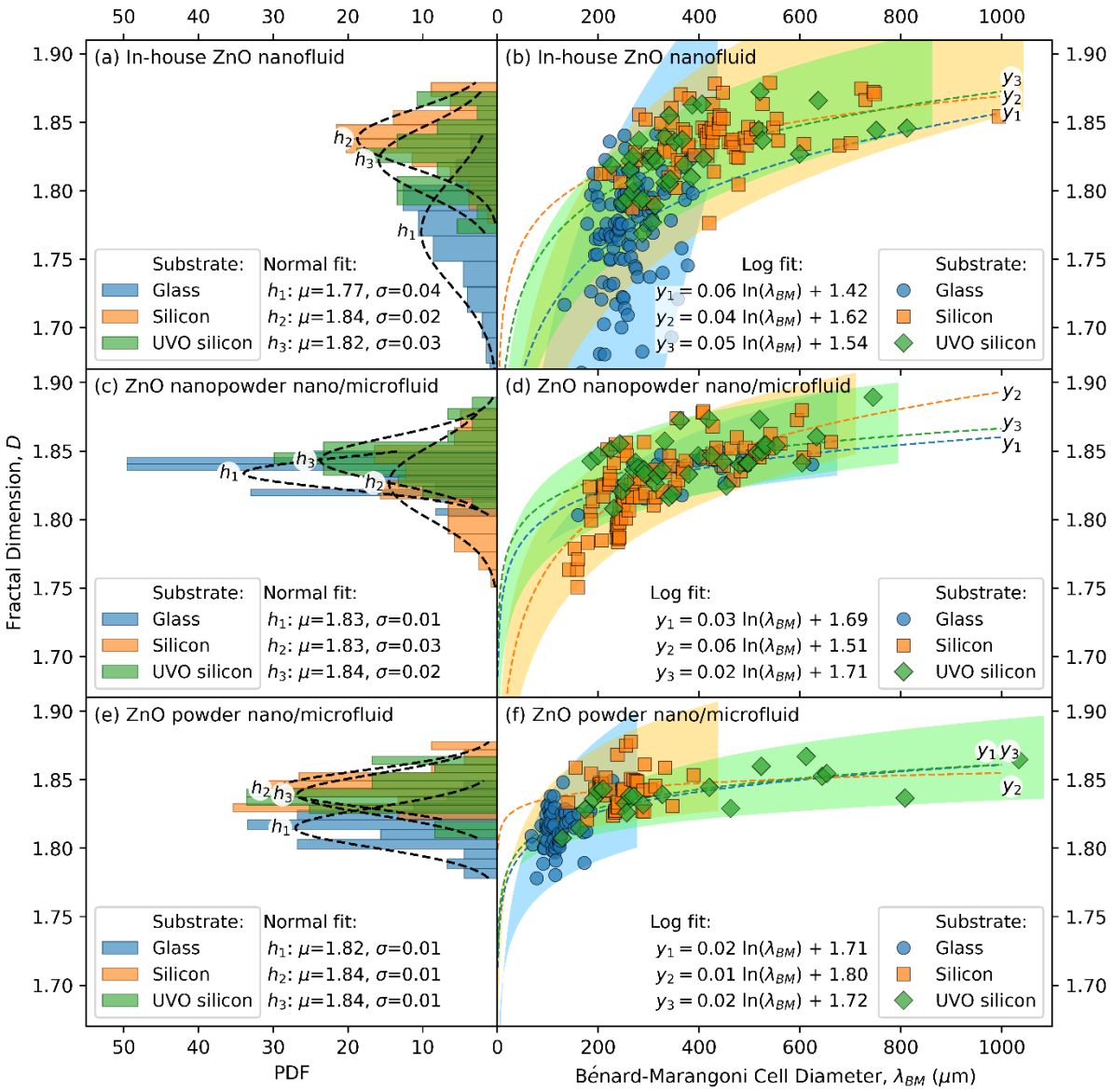

Figure 6. Box counting fractal dimension analysis of the solidified Bénard-Marangoni (BM) cells formed from drying ZnO nano/microfluids composed the in-house synthesized ZnO nanoparticles (**a-b**), ZnO nanopowder (**c-d**), and ZnO powder (**e- f**), on three different substrates, microscope glass slide, Si, and UVO-Si. Left hand side plots (**a**, **c** and **e**) show fractal dimension (FD) distribution for all the samples, fitted with the normal (Gaussian) distribution function. Data fits are shown as dashed lines and labelled as h_1, h_2 and h_3, respectively for glass, Si and UVO-Si for each ZnO nano/microfluid. Parameters μ and σ stand for the mean D and its standard deviation. Right hand side plots (**b**, **d**, **f**) show the calculated box counting fractal dimension, D *vs*. the diameter of the investigated BM cell, λ_{BM}. Dashed lines labelled y_1, y_2, and y_3, show logarithmic fits. The scatter in the data is indicated by the colored regions that enclose the data points.

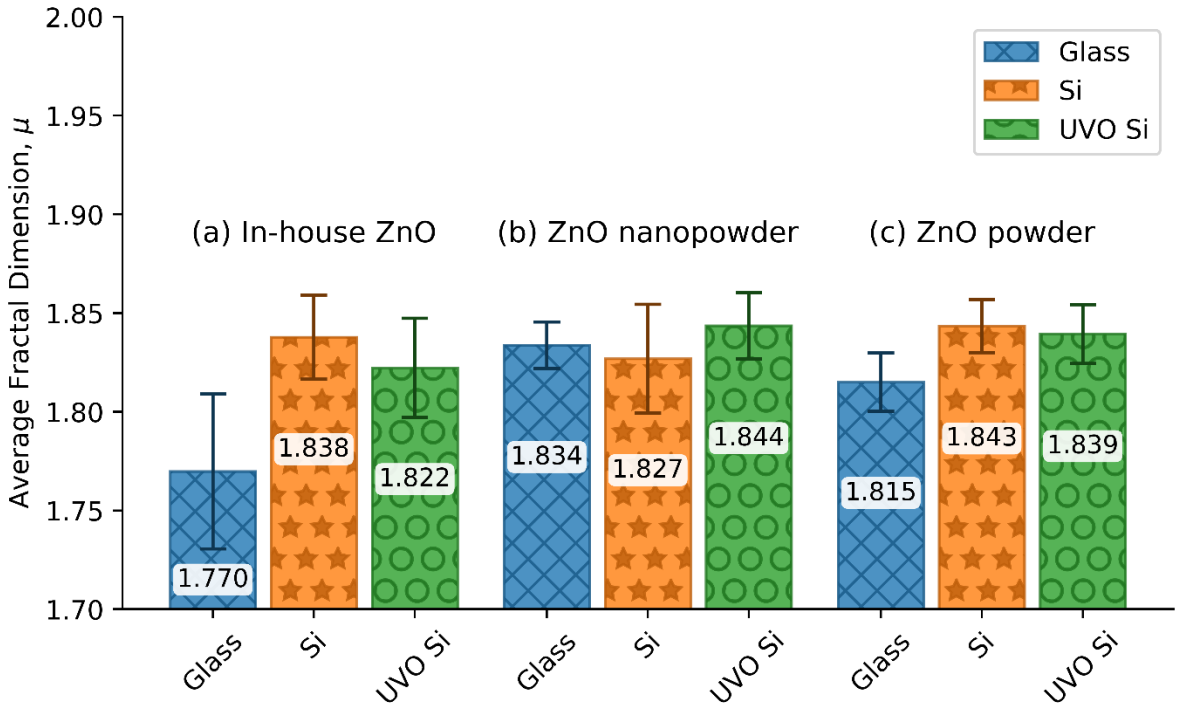

Figure 7. Average fractal dimension, μ, calculated for the Bénard-Marangoni (BM) cells produced from different nano/microfluids: (**a**) the in-house synthesized ZnO, (**b**) ZnO nanopowder, and (**c**) ZnO powder; formed on different substrates: glass (blue bars with "X" pattern), Si (orange bars with star "★" patterns), and UVO-Si (green bars with circle "O" patterns). The error bars are calculated as ± σ, which stand for standard deviation calculated from normal (Gaussian) distribution.

Further discussion on the effect of substrate surface chemistry

As shown in **Table 1**, all the substrates exhibited hydrophilic character, as their water contact angles CA were smaller than 90°. However, the hydrophilicity was in the decreasing of hydrophilized UVO-Si, microscope glass slide and untreated Si, evident both from the water CA and the polar components of the SFE γ^P.

The surface of a silicon wafer is covered with a native layer of silicon oxide or silica (SiO_2), which forms naturally when a silicon surface is exposed to air in ambient conditions [46]. The surface of silicon oxide consists mainly of silanols (Si-OH), siloxanes (Si-O-Si), and their permutations [47]. Silanol groups are responsible for hydrophilic interactions due to their ability to form the hydrogen bond with water. In contrast, siloxanes and other species present on the SiO_2 surface, such as Si-H,

Si-CH_x and Si-F, are responsible for hydrophobic interactions due to their homopolar character [48]. A prolonged UVO exposure of a silicon wafer in air leads to the formation of silanol groups in a reaction of chemical entities produced from bond breaking in the Si-O-Si surface structure and dissociation of water molecules [29]. This in turn greatly increases the hydrophilicity of a UVO treated Si substrate.

The glass surface is composed of the same SiO_2 tetrahedral building block as crystalline silica. However, the arrangement of these tetrahedral units is characterized by the absence of long-range order and the presence of ring-like structures, caused by network modifier ions (Ca^{+2}, Mg^{2+}, Na^{+}, or K^{+}) and non-bridging oxygens [49]. Nevertheless, it is expected that the surface chemistry of the microscope slides, made of silicate glasses, is governed by the relative populations of silanol (Si-OH), siloxide ($Si-O^{-}$), and siloxane (Si-O-Si) surface groups, similar to amorphous silica films [50].

Taking the above into account, the three substrates used in this work, microscope glass slide, silicon wafer and hydrophilized silicon wafer exhibited different levels of hydrophilicity due to different compositions of hydrophilic (silanols, siloxides) and hydrophobic (siloxanes) groups present on their surfaces. The hydrophilized silicon wafer possessed the highest ratio of silanols, generated by the UVO exposure, followed by microscope glass slide, and unmodified silicon wafer.

In general, the solvent evaporation dynamics proximal to the surface and at the dewetting front is affected by the surface wettability by the dispersion, and in turn the substrate surface chemistry. Upon evaporation of a droplet of radius R with a contact angle θ on the substrate at the three-phase contact line, the evaporating flux $J(r)$ at a distance r from droplet center scales as $J(r) \propto (R - r)^{-\lambda}$, where $\lambda = (\pi - 2\theta)/(2\pi - 2\theta)$ [51]. This indicates that the evaporation flux prominent in the coffee ring formation mechanism is similar on all the three substrates, due to the similar initial pinned CA values and those for the nano/microfluids. The significant difference among the three substrates is their hydrophilicity, as indicated by the different water CA values on these substrates and different SFE polar components γ^{P}, which would give rise to different affinities for water molecules and also the amphiphilic molecular clusters generated *in situ* upon evaporation [24].

In the mechanism described in [24], reactive ZnO particles are proposed to alter evaporation induced solvent *via in situ* generated molecular and particulate species. ZnO nanoparticles may undergo rapid

chemical transformation into isobutylamine-ZnOH molecular complexes (iZMCs) of sub-nanometer in size, which further self-assemble into nanoclusters as stimulated by the presence of polar molecules – particularly trace amounts of water. The hydrolysis of isobutylamine by water encourages the formation of iZMCs. These surface active iZMCs and clusters accumulate at the sessile drop surface and the peripheral contact line and would also adsorb to the substrate. As the drop thins, BM instabilities are triggered, and iZMC-cluster coalescence along multiple BM flows leads to the formation of the central cellular patterns. Concurrently, this dendritic cluster growth also occurs at the receding peripheral contact line on the substrate. Further drying drives iZMC organization on the substrate into crystal lattices in the micro-dendrites in the final hierarchical polycrystalline surface structures. Here we show that different surface hydrophilicity of the substrate would affect its interactions with the iZMCs and their self-assembled clusters. This presumably would affect the cluster density, local viscosity, and solvent flows proximal to the substrate during evaporation. It would also influence the final recrystallization on the substrate in which the iZMCs reorganize into the crystal lattices, a process affected by the inter-cluster interactions and the cluster-substrate interactions, both of which would depend on the presence of trace amounts of water.

On the other hand, one could ask whether it is the hydrophilicity of the substrate or the temperature that led to different surface patterns. As discussed in Chapter 1 (equation 2), the Marangoni number depends on the vertical temperature gradient in a thin layer of liquid. The larger the gradient, the higher the Marangoni number, reinforcing the convective flow in a drying drop. **Figure 4** shows that the difference in the BM cell size diameters formed from the in house synthesized ZnO nanofluid on both types of silicon, unmodified and hydrophilised is fairly small (M = 466 μm and M = 423 μm, respectively) when compared to those formed on glass (M = 289 μm). Thermal conductivity in fully amorphous SiO_2 (*i.e.* glass) is primarily due to diffusions in contrast to crystalline Si, where heat is mainly conducted by phonons [52]. Hence, silicon wafers are better heat conductors than silicate glasses.

A drying nanofluid sessile droplet can be considered as heated from below by the substrate. Therefore, the heat conductivity of the substrate could affect the temperature gradient across the height of the drying droplet, influencing the BM instabilities. This would be supported by similar BM cell

diameters produced on both silicon substrates. However, the relation between the Marangoni number and the BM cell size (equation 1 in the text and equation 9 in Chapter 1) shows that the diameter of the convective cell is inversely proportional to the square root of the Marangoni number. This suggests that a higher temperature gradient would result in a smaller BM cell diameter, contrary to the results shown in **Figure 4**. **Figure 5** shows comparison between the size (geometric mean) of BM cells produced from different ZnO nano/microfluids on all substrates, and there is no clear distinction between glass *versus* silicon substrates for the commercially acquired ZnO nanopowder and ZnO powder nano/microfluids.

Based on the equation for the Marangoni number presented in Chapter 1, the thermal properties of the substrates would affect the convection instabilities in the drying ZnO nano/microfluid droplet. The BM convection is affected by a number of different parameters such as the coefficient of thermal volume expansion, the vertical temperature gradient, the thickness of the liquid layer, the kinematic viscosity, the thermal diffusivity, the temperature derivative of the surface tension, and the density of the nano/microfluid at a reference temperature [7]. Therefore, it is challenging to fully deconvolute their contributions to the size of BM cells observed in this work from the chemical and physical properties of the substrates. It nevertheless should remain a challenge for further experimental and theoretical efforts.

CONCLUDING REMARKS

We have observed that the solidified BM dendritic cells formed upon evaporation of sessile drops containing ZnO particulate dispersions in a mixed solvent on three different substrates varying in hydrophilicity. The BM cell size distribution and its fractal dimension both depended on the substrate on which evaporation occurred. The BM cells had the smallest diameters and density on the glass surface when compared to unmodified and hydrophilized silicon substrates for all the ZnO nano/microfluids studied. Meanwhile, the spoke-like radial BM cell structures formed on the UVO hydrophilized silicon had the largest diameters with the widest spread in dimensions.

Fractal dimensional analysis of the BM cells provided a quantitative description of the geometric properties of these structures, to describe their ruggedness or how much space it fills when the structure is scaled up or down [43-44]. It was shown that the in-house ZnO nanofluid produced bigger BM cells

with much higher degree of inter-cell overlapping on both unmodified and UVO treated silicon substrates (D = 1.84 ± 0.02 and 1.82 ± 0.03, respectively) than on glass ($\mu \approx 1.77 \pm 0.04$). On the other hand, ZnO nano/microfluids prepared from the commercially acquired ZnO nanopowder and ZnO powder produced patterns of the highest coverage and level of overlapping of the BM cells, manifested in average D in range 1.82 - 1.84 on all the substrates. The observed trend of the fractal dimension D increasing with the increasing BM diameter λ_{BM} is indicative of a two stage fractal growth, with the smaller BM cells representing growing fractals with a more open structure, and the larger mature BM dendrites possessing a more complicated structure with overlapping boundaries with adjacent BM cells.

As discussed in the previous work, the presence of water molecules is crucial for the moisture-assisted dissolution of ZnO nanocrystals dispersed in a mixture of cyclohexane and isobutylamine [25-26], as well as subsequent cluster formation and recrystallization on the substrate. We attribute the observed different BM cell characteristics (size distributions and FD values) to different surface chemistry of the substrates, particularly their hydrophilicity. Conversely, this provides a mechanism for controlling the morphology of hierarchical surface patterns created after the evaporation of a ZnO nano/microfluid sessile drop.

SUPPORTING INFORMATION

The Supporting Information (SI) associated with this article can be found, in the online version, at https://doi.org/10.1021/acs.langmuir.9b00109. The SI contains: SI.01: ZnO particles; SI.02: UV/Ozone treatment of Si wafer substrates; SI.03: Contact angle (CA) characterization and surface free energy (SFE) calculations; SI.04: Atomic force microscopy (AFM) of the substrates SI.05: Characterization of the residual surface patterns; SI.06: Bénard-Marangoni cell size distribution - log-normal fitting; and SI.07: Fractal dimension analysis of the Bénard-Marangoni cells.

ORC

Patryk Wąsik: 0000-0002-7447-7472

Annela M. Seddon: 0000-0002-5794-8500

Wuge H. Briscoe: 0000-0001-8025-960X

ACKNOWLEDGEMENTS

P.W. is supported by the UK Engineering and Physical Sciences Research Council (EPSRC) through the Bristol Centre for Functional Nanomaterials (BCFN) (grant no. 1371498). H.W. is supported by a Marie Skłodowska-Curie Individual Fellowship (Project Number 656830). W.H.B. would like to acknowledge funding from the EPSRC (EP/H034862/1 and Building Global Engagement in Research (BGER)), European Cooperation in Science and Technology (CMST COST) Action CM1101 "Colloidal Aspects of Nanoscience for Innovative Processes and Materials", and Marie Curie Initial Training Network (MCITN) on "Soft, Small, and Smart: Design, Assembly, and Dynamics of Novel Nanoparticles for Novel Industrial Applications" (NanoS3). Mr Jonathan Jones and Dr Sean Davis are thanked for their help with SEM imaging. Ms Anna Slastanova and Ms Lauren Matthews are acknowledged for their help with the contact angle measurements. Mx Kate Oliver is thanked for a discussion about the approach to the fractal dimension analysis of digital images. Ms Dajana Gubała is thanked for her help with AFM measurements.

REFERENCES

1. Maroto, J. A.; Pérez-Muñuzuri, V.; Romero-Cano, M. S., Introductory analysis of Bénard–Marangoni convection. *European Journal of Physics* **2007,** *28* (2), 311.

2. Bénard, H., Étude expérimentale des courants de convection dans une nappe liquide. — Régime permanent : tourbillons cellulaires. *J. Phys. Theor. Appl.* **1900,** *9* (1), 513-524.

3. Wesfreid, J. E., Scientific Biography of Henri Bénard (1874–1939). In *Dynamics of Spatio-Temporal Cellular Structures: Henri Bénard Centenary Review*, Mutabazi, I.; Wesfreid, J. E.; Guyon, E., Eds. Springer New York: New York, NY, 2006; pp 9-37.

4. Fauve, S., Henri Bénard and pattern-forming instabilities. *Comptes Rendus Physique* **2017,** *18* (9), 531-543.

5. Rayleigh, L., LIX. On convection currents in a horizontal layer of fluid, when the higher temperature is on the under side. *The London, Edinburgh, and Dublin Philosophical Magazine and Journal of Science* **1916,** *32* (192), 529-546.

6. Block, M. J., Surface Tension as the Cause of Bénard Cells and Surface Deformation in a Liquid Film. *Nature* **1956,** *178*, 650.

7. Pearson, J. R. A., On convection cells induced by surface tension. *J. Fluid Mech.* **1958,** *4* (5), 489-500.

8. Mutabazi, I.; Wesfreid, J. E.; Guyon, E., *Dynamics of Spatio-Temporal Cellular Structures: Henri Bénard Centenary Review*. Springer-Verlag New York: 2006; Vol. 207.

9. Getling, A. V.; Brausch, O., Cellular flow patterns and their evolutionary scenarios in three-dimensional Rayleigh-Bénard convection. *Phys. Rev. E* **2003,** *67* (4), 046313.

10. Han, W.; Lin, Z., Learning from "Coffee Rings": Ordered Structures Enabled by Controlled Evaporative Self-Assembly. *Angew. Chem. Int. Ed.* **2012,** *51* (7), 1534-1546.

11. Zhong, X.; Crivoi, A.; Duan, F., Sessile nanofluid droplet drying. *Adv. Colloid Interface Sci.* **2015,** *217*, 13-30.

12. Wang, H.; Wang, Z.; Huang, L.; Mitra, A.; Yan, Y., Surface Patterned Porous Films by Convection-Assisted Dynamic Self-Assembly of Zeolite Nanoparticles. *Langmuir* **2001,** *17* (9), 2572-2574.

13. Maillard, M.; Motte, L.; Ngo, A. T.; Pileni, M. P., Rings and Hexagons Made of Nanocrystals: A Marangoni Effect. *J. Phys. Chem. B* **2000,** *104* (50), 11871-11877.

14. Maillard, M.; Motte, L.; Pileni, M. P., Rings and Hexagons Made of Nanocrystals. *Adv. Mater.* **2001,** *13* (3), 200-204.

15. Nguyen, V. X.; Stebe, K. J., Patterning of Small Particles by a Surfactant-Enhanced Marangoni-Bénard Instability. *Phys. Rev. Lett.* **2002,** *88* (16), 164501.

16. Truskett, V. N.; Stebe, K. J., Influence of Surfactants on an Evaporating Drop: Fluorescence Images and Particle Deposition Patterns. *Langmuir* **2003,** *19* (20), 8271-8279.

17. Sakurai, S.; Furukawa, C.; Okutsu, A.; Miyoshi, A.; Nomura, S., Control of mesh pattern of surface corrugation via rate of solvent evaporation in solution casting of polymer film in the presence of convection. *Polymer* **2002,** *43* (11), 3359-3364.

18. Bassou, N.; Rharbi, Y., Role of Bénard−Marangoni Instabilities during Solvent Evaporation in Polymer Surface Corrugations. *Langmuir* **2009,** *25* (1), 624-632.

19. Bormashenko, E., Surface instabilities and patterning at liquid/vapor interfaces: Exemplifications of the “hairy ball theorem”. *Colloids and Interface Science Communications* **2015,** *5* (Supplement C), 5-7.

20. Uchiyama, H.; Matsui, T.; Kozuka, H., Spontaneous Pattern Formation Induced by Bénard–Marangoni Convection for Sol–Gel-Derived Titania Dip-Coating Films: Effect of Co-solvents with a High Surface Tension and Low Volatility. *Langmuir* **2015,** *31* (45), 12497-12504.

21. Cai, Y.; Zhang Newby, B.-m., Marangoni Flow-Induced Self-Assembly of Hexagonal and Stripelike Nanoparticle Patterns. *J. Am. Chem. Soc.* **2008,** *130* (19), 6076-6077.

22. Suresh Singh, R.; Grimes, C. A.; Dickey, E. C., Fabrication of nanoporous TiO2 films through Benard-Marangoni convection. *Material Research Innovations* **2002,** *5* (3), 178-184.

23. Larouche, F.; Smiljanic, O.; Sun, X.; Stansfield, B. L., Solutal Bénard–Marangoni instability as a growth mechanism for single-walled carbon nanotubes. *Carbon* **2005,** *43* (5), 986-993.

24. Wu, H.; Briscoe, W. H., Morphogenesis of polycrystalline dendritic patterns from evaporation of a reactive nanofluid sessile drop. *Physical Review Materials* **2018,** *2* (4), 045601.

25. Wu, H.; Chen, L. X.; Zeng, X. Q.; Ren, T. H.; Briscoe, W. H., Self-assembly in an evaporating nanofluid droplet: rapid transformation of nanorods into 3D fibre network structures. *Soft Matter* **2014,** *10* (29), 5243-5248.

26. Wąsik, P.; Redeker, C.; Dane, T. G.; Seddon, A. M.; Wu, H.; Briscoe, W. H., Hierarchical Surface Patterns upon Evaporation of a ZnO Nanofluid Droplet: Effect of Particle Morphology. *Langmuir* **2018,** *34* (4), 1645-1654.

27. Wąsik, P.; Seddon, A. M.; Wu, H.; Briscoe, W. H., Dendritic surface patterns from Bénard-Marangoni instabilities upon evaporation of a reactive ZnO nanofluid droplet: A fractal dimension analysis. *J. Colloid Interface Sci.* **2019,** *536*, 493-498.

28. Sun, B.; Sirringhaus, H., Solution-Processed Zinc Oxide Field-Effect Transistors Based on Self-Assembly of Colloidal Nanorods. *Nano Lett.* **2005,** *5* (12), 2408-2413.

29. Lin, X.; Liao, G.; Tang, Z.; Shi, T., UV surface exposure for low temperature hydrophilic silicon direct bonding. *Microsyst. Technol.* **2009,** *15* (2), 317-321.

30. Vig, J. R., UV/ozone cleaning of surfaces. *J. Vac. Sci. Technol., A* **1985,** *3* (3), 1027-1034.

31. Owens, D. K.; Wendt, R. C., Estimation of the surface free energy of polymers. *J. Appl. Polym. Sci.* **1969,** *13* (8), 1741-1747.

32. Napolitano, A.; Ungania, S.; Cannata, V., Fractal Dimension Estimation Methods for Biomedical Images. In *MATLAB - A Fundamental Tool for Scientific Computing and Engineering Applications - Volume 3*, Katsikis, V. N., Ed. InTech: Rijeka, 2012; p Ch. 07.

33. Alligood, K. T.; Sauer, T. D.; Yorke, J. A., *Chaos: An Introduction to Dynamical Systems*. Springer New York: 2012.

34. Karperien, A., FracLac for ImageJ. http://rsb.info.nih.gov/ij/plugins/fraclac/FLHelp/Introduction.htm (accessed 4th Jun 2018).

35. Alam, A. U.; Howlader, M. M. R.; Deen, M. J., The effects of oxygen plasma and humidity on surface roughness, water contact angle and hardness of silicon, silicon dioxide and glass. *J. Micromech. Microeng.* **2014,** *24* (3), 035010.

36. Wang, H.; Yu, B.; Jiang, S.; Jiang, L.; Qian, L., UV/ozone-assisted tribochemistry-induced nanofabrication on Si(100) surfaces. *RSC Advances* **2017,** *7* (63), 39651-39656.

37. Dann, J. R., Forces involved in the adhesive process: I. Critical surface tensions of polymeric solids as determined with polar liquids. *J. Colloid Interface Sci.* **1970,** *32* (2), 302-320.

38. Ström, G.; Fredriksson, M.; Stenius, P., Contact angles, work of adhesion, and interfacial tensions at a dissolving Hydrocarbon surface. *J. Colloid Interface Sci.* **1987,** *119* (2), 352-361.

39. Żenkiewicz, M., Methods for the calculation of surface free energy of solids. *Journal of Achievements in Materials and Manufacturing Engineering* **2007,** *24* (1), 137-145.

40. Wlodek, M.; Kolasinska-Sojka, M.; Wasilewska, M.; Bikondoa, O.; Briscoe, W. H.; Warszynski, P., Interfacial and structural characteristics of polyelectrolyte multilayers used as cushions for supported lipid bilayers. *Soft Matter* **2017,** *13* (43), 7848-7855.

41. Smith, J. E.; Jordan, M. L., Mathematical and graphical interpretation of the log-normal law for particle size distribution analysis. *J. Colloid Sci.* **1964,** *19* (6), 549-559.

42. Zender, C., Particle size distributions: theory and application to aerosols, clouds, and soils. http://dust.ess.uci.edu/facts/psd/psd.pdf (accessed 12th Dec 2017).

43. Falconer, K. J., *Fractal geometry: mathematical foundations and applications*. Wiley: Chichester, 1990.

44. Rahman, M. S., Physical meaning and interpretation of fractal dimensions of fine particles measured by different methods. *J. Food Eng.* **1997,** *32* (4), 447-456.

45. Mandelbrot, B. B., *The Fractal Geometry of Nature*. Freeman and Company: New York, 1982.

46. Morita, M.; Ohmi, T.; Hasegawa, E.; Kawakami, M.; Ohwada, M., Growth of native oxide on a silicon surface. *J. Appl. Phys.* **1990,** *68* (3), 1272-1281.

47. Thomas, R. R.; Kaufman, F. B.; Kirleis, J. T.; Belsky, R. A., Wettability of Polished Silicon Oxide Surfaces. *J. Electrochem. Soc.* **1996,** *143* (2), 643-648.

48. Grundner, M.; Jacob, H., Investigations on hydrophilic and hydrophobic silicon (100) wafer surfaces by X-ray photoelectron and high-resolution electron energy loss-spectroscopy. *Appl. Phys. A* **1986,** *39* (2), 73-82.

49. Melcher, M.; Wiesinger, R.; Schreiner, M., Degradation of Glass Artifacts: Application of Modern Surface Analytical Techniques. *Acc. Chem. Res.* **2010,** *43* (6), 916-926.

50. Warring, S. L.; Beattie, D. A.; McQuillan, A. J., Surficial Siloxane-to-Silanol Interconversion during Room-Temperature Hydration/Dehydration of Amorphous Silica Films Observed by ATR-IR and TIR-Raman Spectroscopy. *Langmuir* **2016,** *32* (6), 1568-1576.

51. Jason, N. N.; Chaudhuri, R. G.; Paria, S., Self-assembly of colloidal sulfur particles influenced by sodium oxalate salt on glass surface from evaporating drops. *Soft Matter* **2012,** *8* (14), 3771-3780.

52. Wingert, M. C.; Zheng, J.; Kwon, S.; Chen, R., Thermal transport in amorphous materials: a review. *Semicond. Sci. Technol.* **2016,** *31* (11), 113003.

Supporting Information

Bénard-Marangoni dendrites upon evaporation of a reactive ZnO nanofluid droplet: Effect of substrate chemistry

Patryk Wąsik[a,b], Annela M. Seddon[a,c], Hua Wu[b], and Wuge H. Briscoe[b,]*

[a] Bristol Centre for Functional Nanomaterials (BCFN), HH Wills Physics Laboratory, University of Bristol, Tyndall Avenue, Bristol, BS8 1TL, UK

[b] School of Chemistry, University of Bristol, Cantock's Close, Bristol, BS8 1TS, UK

[c] School of Physics, HH Wills Physics Laboratory, Tyndall Avenue, University of Bristol, Bristol, BS8 1TL, UK

Information

This chapter has been published as Supporting Information to the research article: **Wąsik, P.**; Seddon, A. M.; Wu, H.; Briscoe, W. H., Bénard-Marangoni dendrites upon evaporation of a reactive ZnO nanofluid droplet: Effect of substrate chemistry, *Langmuir* **2019**, *35* (17), 5830-5840. DOI: 10.1021/acs.langmuir.9b00109. This chapter has been authored by the candidate with no more input from co-authors and supervisors that would have been provided in a conventional thesis chapter. Individual contributions as in Chapter 4.

SI.01: ZnO particles

Three types of zinc oxide (ZnO) particles were used in the experiment: in-house synthesized ZnO nanoparticles, and commercially acquired ZnO nanopowder (Sigma-Aldrich, <100 nm particle size,

~80% Zn basis) and ZnO powder (Sigma-Aldrich, ACS reagent). **Figure S1** shows transmission electron microscopy (TEM) images of ZnO particles taken using a JEOL JEM-1400 transmission electron microscope. Detailed characterization of ZnO particles including particle size distribution, X-ray diffraction, and energy-dispersive X-ray spectroscopy as well as synthesis of the in-house ZnO nanoparticles is reported elsewhere [1]. In summary, the particle size distribution, fitted with the log-normal distribution function (SI.06), showed that the in-house synthesized ZnO nanoparticles were monodisperse with the geometric mean particle diameter of 9.2 nm, and 68.3% of all the particle diameters between 7.4 and 11.4 nm. Commercial ZnO particles were polydisperse with the geometric means of 71.7 and 133.4 nm, and 68.3% of all maximum dimensions between 36.2 and 141.8 nm, and 61.2 and 291.9 nm for ZnO nanopowder and ZnO powder, respectively. The sizes were calculated as a particle diameter for the in-house synthesized ZnO nanoparticles, and a maximum dimension (maximum distance between any two surface points) for the commercially acquired ZnO nanopowder and ZnO powder due to their large shape anisotropy.

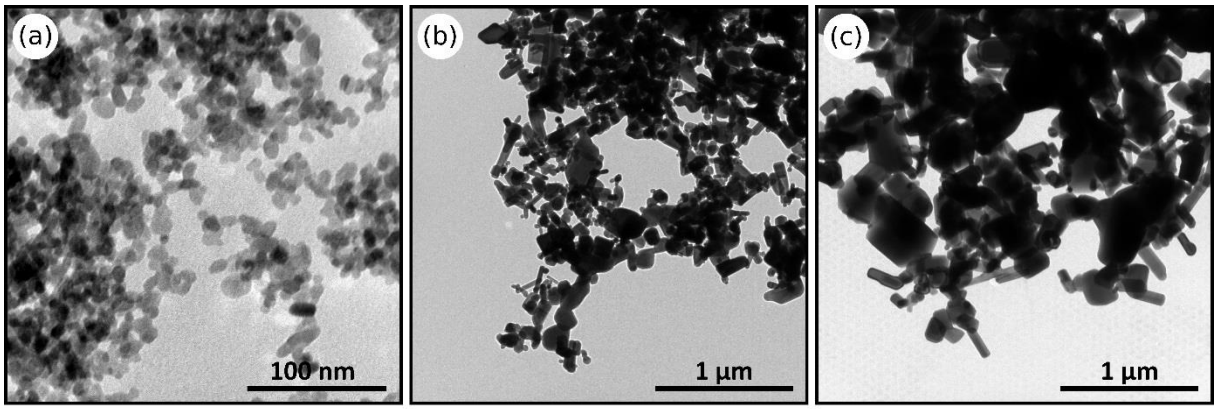

Figure S1. TEM micrographs of ZnO particles used in the experiment: **(a)** the in-house synthesized ZnO nanoparticles, **(b)** ZnO nanopowder, and **(c)** ZnO powder.

SI.02: UV/Ozone treatment of Si wafer substrates

The UV/Ozone exposure is often used as a highly effective method for removal of various contaminants from different types of surfaces. It can produce clean surfaces at room temperature without the use of solvents or controlled atmosphere, or to modify the surface chemistry of a substrate [2-4]. The mechanism of the surface modification using UV/Ozone cleaning technique is based on photosensitization and oxidation effects caused by the ultraviolet radiation [5]. A simple UV/Ozone

cleaner is constructed as a box equipped with a UV source and a platform for a specimen. A schematic model of a UV/Ozone cleaner and a commercial device (42-220 UVO-Cleaner®, Jetlight Company, Inc.) are shown in **Figure S2**.

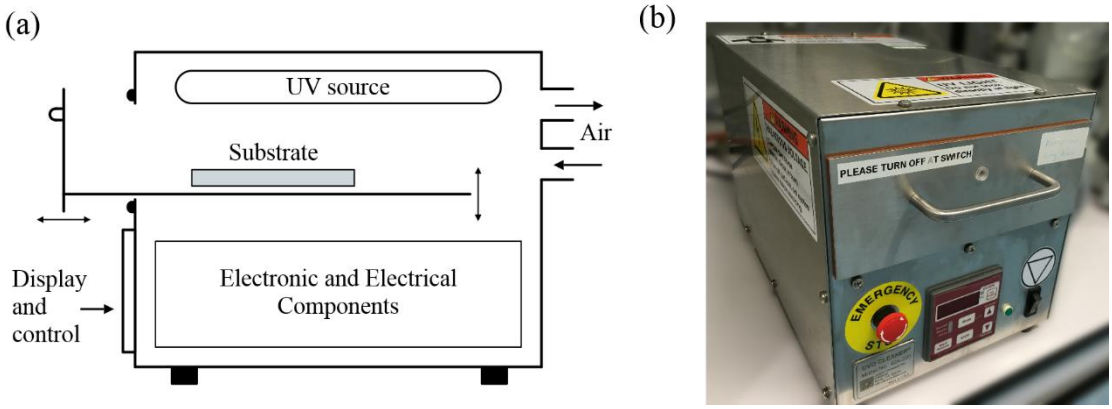

Figure S2. UV/Ozone cleaner: (a) schematic model, (b) 42-220 UVO-Cleaner® (Jetlight Company, Inc.).

According to Vig [5], the 184.9 nm radiation is responsible for the ozone generation due to it being absorbed by oxygen molecules (eq S1), in contrast to the 253.7 nm wavelength, which has low adsorption coefficient for O_2. However, the latter wavelength is readily adsorbed by ozone (eq S2) and most hydrocarbon molecules. The absorption by ozone is directly responsible for ozone destruction. This continuous formation and destruction of ozone molecules in the presence of both wavelengths leads to the production of atomic oxygen, a highly oxidizing specie:

$$\frac{hc}{\lambda_1} + 2O_2 \rightarrow O_3 + O\bullet, \tag{S1}$$

$$\frac{hc}{\lambda_2} + O_3 \rightarrow O_2 + O\bullet, \tag{S2}$$

where h is the Planck constant, c is the speed of light, and λ_1 and λ_2 are wavelengths of the UV radiation corresponding to 184.9 and 253.7 nm, respectively.

In the UV/Ozone cleaning process, presented in **Figure S3**, the contaminant molecules adsorbed on the surface are dissociated or/and excited because of the UV light absorption. As produced ions, free radicals and excited molecules react further with active oxygen atoms to produce volatile by-products such as CO, CO_2, H_2O, N_2, *etc*. that can escape the surface, making it clean.

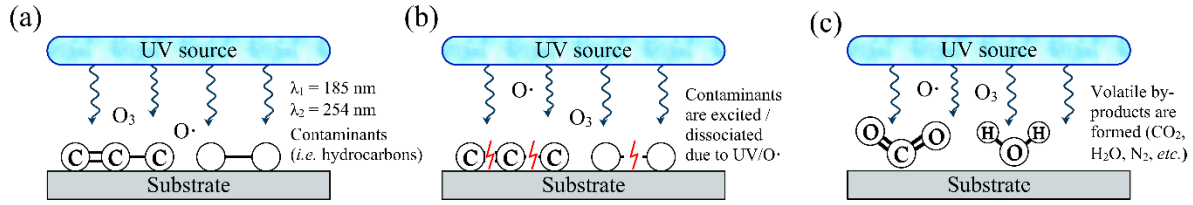

Figure S3. Mechanism of the UV/Ozone cleaning: (**a**) UV radiation causes the formation of atomic oxygen and ozone, (**b**) UV radiation and reactive oxygen decompose contaminant molecules (mostly hydrocarbons) on the surface, (**c**) volatile by-products such as CO, CO_2, H_2O, N_2, *etc*. form and escape the surface.

In addition to cleaning, UV/Ozone can be used to modify the surface chemistry of a substrate (**Figure S4**). As explained by Lin *et al.* [2] with regards to silicon wafers, the UV radiation is capable of breaking Si-O bonds in the Si-O-Si surface structure. At the same time as Si- and Si-O- entities are formed due to the UV/Ozone exposure, water molecules adsorbed on the substrate are dissociated into hydroxyl radicals and hydrogen atoms. More hydroxyls are formed from hydrogen and surrounding oxygen atoms. As the process continues, Si- and Si-O- couple with hydroxyls and hydrogen atoms, respectively, to form Si-OH silanol groups. Silanol groups are responsible for adsorption of water, making it hydrophilic [6].

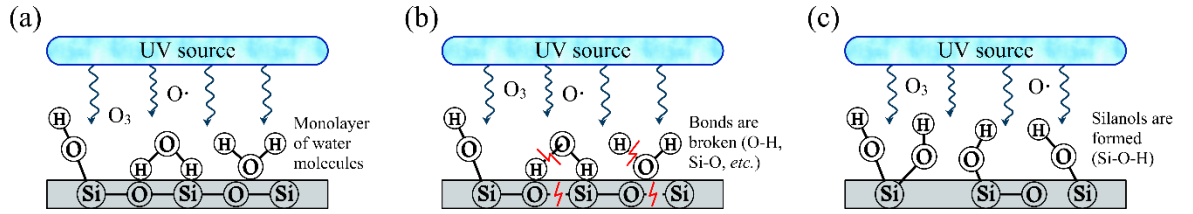

Figure S4. Mechanism of UV/Ozone surface modification: (**a**) a monolayer of water molecules forms on a silicon wafer substrate as a result of pre-cleaning (**Figure S3**), (**b**) UV radiation decompose water molecules into hydroxyl radicals and hydrogen atoms, and Si-O-Si surface structures into Si- and Si-O- entities, (**c**) silanol (Si-OH) groups form on the silicon surface from species described in (**b**).

SI.03: Contact angle (CA) characterization and surface free energy (SFE) calculations

In this work, the wettability of the substrates was characterized using sessile droplet static contact angle measurements of probing liquids such as *Milli-Q* water (18.2 MΩ·cm at 25 °C), diiodomethane

(Alfa Aesar, 99%), ethylene glycol (Fluka Analytical, ≥ 99.5%), n-hexadecane (Acros Organics, 99%, pure), n-dodecane (Acros Organics, 99%, pure), cyclohexane (Fisher Chemicals, assay 99%), and a mixture of cyclohexane and isobutylamine (Sigma-Aldrich, assay 99%) in a 5:1 volume ratio, in addition to ZnO nano/microfluids prepared from the in-house synthesized ZnO nanoparticles and commercially acquired ZnO nanopowder and ZnO powder (see SI.01) dispersed in the mixture of cyclohexane and isobutylamine 5:1 volume ratio to 1 mg/mL concentration (see the main text). The measurements were performed at room temperature of 24.5 ± 0.5 °C and relative humidity of ~45% using a Drop Shape Analyzer – DSA100 (KRÜSS) operated with the KRÜSS ADVANCE 1.9.0.8 software. In a typical measurement, a 5 µL droplet of the measurement liquid (30 µL for cyclohexane/isobutylamine mixture) was pipetted onto a 1×1 cm^2 substrate, and the image of the drop was recorded for 60 seconds in one second intervals. The value of the contact angle was obtained by tangent fitting method to the drop shape using the software. The errors in mean CA values are quoted as the standard deviations from: 20, 37, and 26 separate measurements for the in-house ZnO nanofluid on glass, unmodified Si, and UVO exposed Si, respectively; 12, 62, and 35 for ZnO nanopowder nano/microfluid on glass, unmodified Si, and UVO exposed Si, respectively; and 8, 25, and 6 for ZnO powder nano/microfluid on glass, unmodified Si, and UVO exposed Si, respectively.

As a general trend, it was observed that the CA values for volatile ZnO nano/microfluid drops were decreasing with the increasing time as the evaporation progressed due to the volume liquid loss. Deposition of a pure 30 µL drop of cyclohexane and isobutylamine mixture onto the surface resulted in the droplet being pinned to the edges of the substrate. Mean contact angles calculated for 5 µL drops of ZnO nano/microfluids and mean pinned angles measured for 30 µL drops of cyclohexane and isobutylamine mixture are presented in **Table S1**.

Table S1. Mean contact angle (CA) measurements of ZnO nano/microfluids (5 μL) and mean pinned to the substrate edge angles of a mixture of cyclohexane and isobutylamine (30 μL) on different substrates used in the study.

Substrate	**In-house ZnO nanofluid**	**ZnO nanopowder nano/microfluid**	**ZnO powder nano/microfluid**	**Cyclohexane and isobutylamine (5:1 volume)**
Microscope glass slide	8.6 ± 2.0°	5.5 ± 1.0°	5.6 ± 1.1°	29.4 ± 4.3°
Unmodified silicon (Si)	5.7 ± 1.2°	6.0 ± 1.9°	5.9 ± 1.8°	26.7 ± 1.5°
UVO exposed silicon (UVO-Si)	6.5 ± 1.7°	5.5 ± 2.0°	4.1 ± 1.9°	27.2 ± 2.4°

The surface free energies (SFEs) of the substrates were calculated according to the previously described Owens-Wendt method [7], which separates the SFE into two components, polar and dispersive. Because the calculated SFE value of a solid depends on the liquids chosen for contact angle measurements [8], only measurements for *Milli-Q* water and diiodomethane were used in calculations as their drops produced measurable contact angles on all substrates. It was found that the glass surface was instantly wetted by n-hexadecane and n-dodecane, the unmodified silicon by n-dodecane and cyclohexane, and UVO-Si by ethylene glycol and n-hexadecane. Disperse ($\gamma_{\mathrm{SV}}^{\mathrm{D}}$) and polar ($\gamma_{\mathrm{LV}}^{\mathrm{P}}$) surface tension components of the measuring liquids are listed in **Table S2**. Mean contact angle values recorded for the measuring liquids on glass, unmodified Si, and UVO exposed Si are presented in **Table S3**. The errors in mean CA values on respective substrates, *i.e.* glass, unmodified Si, and UVO exposed Si, are quoted as the standard deviations from 57, 59, and 55 separate measurements for water; 55, 56, and 55 separate measurements for diiodomethane; 2, 56, and 1 separate measurements for ethylene glycol; 1, 56, and 1 separate measurements for n-hexadecane; 1, 1, and 60 separate measurements for n-dodecane; and 5 and 1 separate measurements for cyclohexane. The value of 1 measurement refers to the instant wetting behavior of the probing liquid.

Table S2. Surface free energy (SFE) components of the measuring liquids: water [9], diiodomethane [9], ethylene glycol [10], n-hexadecane [11], n-dodecane [12], cyclohexane [13], and isobutylamine [14].

SFE (mN/m)	Water	Diiodomethane	Ethylene glycol	n-Hexadecane	n-Dodecane	Cyclohexane	Isobutylamine
Total, γ_{LV}	72.8	50.8	48	27.5	25.2	25.1	21.75
Disperse, γ_{LV}^{D}	21.8	50.8	29				
Polar, γ_{LV}^{P}	51	0	19				

Table S3. Mean contact angles measured for probe liquids on glass, unmodified silicon, and UVO exposed silicon substrates. The angle of 0° means that the substrate was instantly wetted by the probe liquid upon the contact.

Substrate	Water	Diiodomethane	Ethylene glycol	n-Hexadecane	n-Dodecane	Cyclohexane
Microscope glass slide	21.7 ± 3.5°	29.6 ± 0.5°	10.4 ± 3.5°	0°	0°	7.5 + 1.7°
Unmodified silicon	56.5 ± 1.2°	52.0 ± 1.3°	19.6 ± 1.8°	10.2 ± 1.7°	0°	0°
UVO exposed silicon	9.8 ± 1.6°	41.1 ± 0.9°	0°	0°	7.8 ± 0.3°	No measurement

The surface free energies (SFEs) of the substrates and the measured mean contact angles of water and diiodomethane are shown in **Table S4**. The SFEs of the substrates were calculated with the KRÜSS ADVANCE 1.9.0.8 software with the selected error weighing option, so liquids with a higher standard error of the mean CA had less influence on the calculated value. The total SFE of glass and UVO exposed silicon wafer were comparable (74.4 ± 1.5 and 75.5 ± 0.5 mN/m for glass and silicon, respectively), and higher than of the unmodified silicon (50.3 ± 1.6 mN/m). The disperse component of the SFE increased in the order from unmodified silicon wafer (33.1 ± 0.8 mN/m), to UVO exposed silicon wafer (39.0 ± 0.2 mN/m), and microscope glass slide (44.4 ± 0.2 mN/m). The polar component of the SFE increased in the order from unmodified silicon wafer (17.2 + 0.8 mN/m), to glass (30.0 ± 1.3 mN/m), and UVO exposed silicon wafer (36.4 ± 0.3 mN/m). The Owens-Wendt plot for the SFE component calculations is shown in **Figure S5**.

Table S4. The total surface free energy (γ_{SV}) with its dispersive (γ_{SV}^{D}) and polar (γ_{SV}^{P}) components and the contact angles of water (Θ_W) and diiodomethane (Θ_D) on different substrates.

Substrate	γ_{SV} (mN/m)	γ_{SV}^{D} (mN/m)	γ_{SV}^{P} (mN/m)	Θ_W	Θ_D
Microscope glass slide	74.4 ± 1.5	44.4 ± 0.2	30.0 ± 1.3	21.7 ± 3.5°	29.6 ± 0.5°
Unmodified silicon (Si)	50.3 ± 1.6	33.1 ± 0.8	17.2 + 0.8	56.5 ± 1.2°	52.0 ± 1.3°
UVO exposed silicon (UVO-Si)	75.5 ± 0.5	39.0 ± 0.2	36.4 ± 0.3	9.8 ± 1.6°	41.1 ± 0.9°

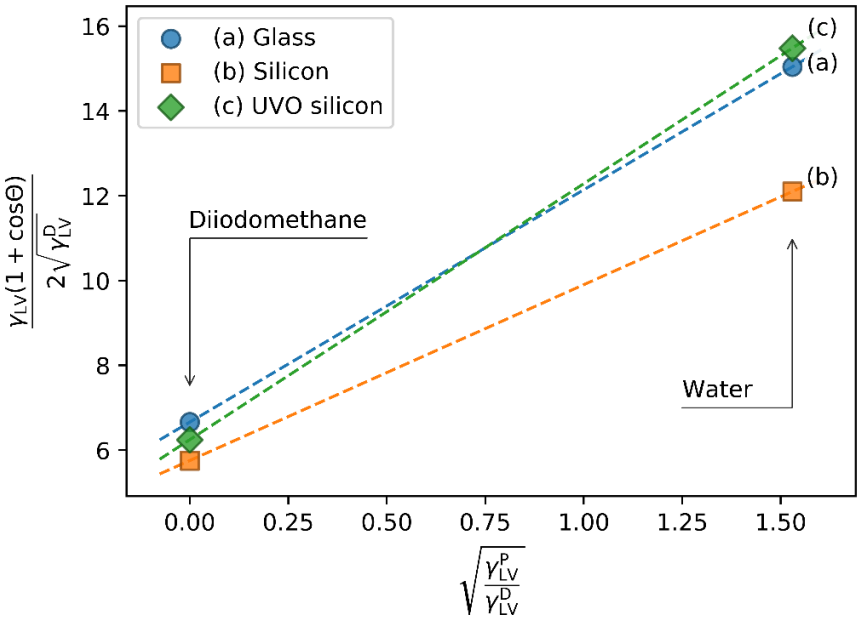

Figure S5. Owens-Wendt plot for the surface free energy components calculations for (**a**) glass, (**b**) unmodified silicon, and (**c**) UV/ozone exposed silicon. Calculated SFE values are shown in **Table S4**.

We would also like to briefly discuss different values of γ_{LV}^{D} and γ_{LV}^{P} for diiodomethane in the literature. That is, values such as γ_{LV}^{D} = 49.5 mN/m and γ_{LV}^{P} = 1.3 mN/m, or γ_{LV}^{D} = 48.5 mN/m and γ_{LV}^{P} = 2.3 mN/m have been reported [15]. The values used in the main text, *i.e.* γ_{LV}^{D} = 50.8 mN/m and γ_{LV}^{P} = 0 mN/m, have been widely used in modern literature, e.g. [16-17]. It is beyond the focus and scope of the current study to delve into the debate. For our purpose, we elect to use the values in the ms for the following considerations. First, the values in the ms are recommended by the manufacturer of the contact angle goniometer (KRÜSS) used in our study [18]. Secondly, we would like to be consistent with the calculations of the surface energy in our previous studies, *e.g.* [9]. Thirdly, we have recalculated the surface energies using the values that one of the anonymous reviewers quoted (see **Table S5** below),

and the differences in the numerical values of the surface energy results would not change our interpretation of the results, *i.e.* the surface chemistry differences among the three substrates in our study are manifested by the polar components of their surface energies.

Table S5. Surface free energies (SFEs) of three different substrates calculated using different γ_{LV}^{D} and γ_{LV}^{P} values for diiodomethane using the Owens-Wendt method.

Substrate	SFE in the ms using γ_{LV} = 50.8 , γ_{LV}^{P} = 0, and γ_{LV}^{D} = 50.8 mN/m			SFE using the values: γ_{LV} = 50.8 , γ_{LV}^{P} = 1.3 and γ_{LV}^{D} = 49.5 mN/m		
	γ_{SV}	γ_{SV}^{P}	γ_{SV}^{D}	γ_{SV}	γ_{SV}^{P}	γ_{SV}^{D}
Glass	74.38	30.00	44.38	70.00	36.75	33.25
Si-wafer	50.32	17.19	33.13	46.89	21.00	25.89
Hydrophilised Si (UVO treated)	75.46	36.43	39.03	72.28	44.78	27.51

SI.04: Atomic force microscopy (AFM) of the substrates

Substrates topography was characterized with the atomic force microscopy (AFM) using MultiMode Nanoscope III (Bruker) operated with NanoScope 6.14R1 (R) software. Areas of 500×500 nm^2 were scanned in the tapping mode with NuSense SCOUT cantilever (uncoated, spring constant: 42 N/m, length: 125 µm, width: 30 µm, thickness: 4 µm, Nu Nano Ltd, UK). AFM height images of the substrates are shown in **Figure S6**.

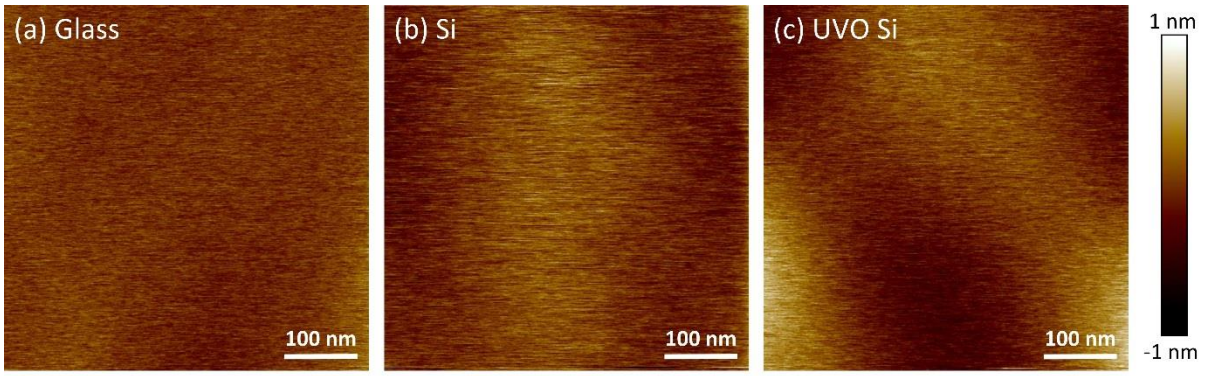

Figure S6. Atomic force microscopy images of different substrates used in the study: (**a**) microscope glass slide, (**b**) unmodified silicon wafer, and (**c**) UV/ozone treated (10 minutes) silicon wafer.

Surface topography of each substrate was characterized with three different parameters: the arithmetic average roughness, R_a, the root mean square average roughness, R_{rms} (often referred as R_q), and the maximum vertical distance between the highest and lowest data points, R_{max}. Following [19-

20], roughness the parameters are determined in relation to the mean plane, $\bar{z}$, which can be calculated according to eq S3:

$$\bar{z} = \frac{1}{N}\sum_{i=1}^{N} z_i \ , \tag{S3}$$

where z is the height value in i-th point in the scanned area, and N is the total number of points measured. The arithmetic average roughness, R_a, is defined as an arithmetic average of the absolute values of the surface height deviations measured from the mean plane, $\bar{z}$. The arithmetic average roughness is expressed in eq S4:

$$R_a = \frac{1}{N}\sum_{i=1}^{N} |z_i - \bar{z}| \ . \tag{S4}$$

The root mean square average roughness, R_{rms}, represents the standard deviation of surface heights, and it is expressed in eq S5:

$$R_{rms} = \sqrt{\frac{1}{N}\sum_{i=1}^{N} (z_i - \bar{z})^2} \ . \tag{S5}$$

The surface topography parameters for each substrate are presented in **Table S**. All substrates were relatively flat, which is manifested in very small (less than 0.2 nm) arithmetic average roughness, R_a. The topography analysis results show that the surface roughness expressed in both, R_a and R_{rms} parameters, increased in the order from glass (R_a = 0.09 nm, R_{rms} = 0.11 nm), to unmodified silicon (R_a = 0.14 nm, R_{rms} = 0.17 nm), and UVO treated silicon (R_a = 0.17 nm, R_{rms} = 0.22 nm). However, the value of the maximum vertical distance between the highest and lowest data points, R_{max}, was the highest for silicon wafer (R_{max} = 3.85 nm), followed by UVO treated silicon (R_{max} = 1.69 nm), and glass (R_{max} = 1.09 nm). It has been reported that after the initial decrease of the surface roughness of silicon wafers due to the exposure of silicon wafers to UVO (time less than 3 - 5minutes), the roughness increased with the exposure time (time longer than 3 - 5minutes) [2-3, 21]. However, the surface roughness values (both R_a and R_{rms}) of UVO-Si exceeded the initial roughness of Si after *ca* 15 minutes of the exposure time [2]. Here, this was observed after 10 minutes of UVO exposure.

Table S6. Surface topography parameters calculated for the substrates used in the study: arithmetic average roughness, R_a, root mean square average roughness, R_{rms} (often referred as R_q), and maximum vertical distance between the highest and lowest data points, R_{max}.

Substrate	R_a **(nm)**	R_{rms} **(or** R_q**) (nm)**	R_{max} **(nm)**
Microscope glass slide	0.09	0.11	1.09
Silicon wafer (Si)	0.14	0.17	3.85
UVO silicon wafer (UVO-Si)	0.17	0.22	1.69

SI.05: Characterization of the residual surface patterns

The residual surface patterns produced by evaporative drying of ZnO nano/microfluids on glass, silicon and UVO exposed silicon substrates were imaged using scanning electron microscopy (SEM). Prior to the imaging using JSM-IT300 SEM (JEOL), samples were covered with 15 nm layer of silver. **Figure S7** shows the SEM micrographs of the central regions of the residual surface patterns from ZnO nanopowder and ZnO powder nano/microfluid droplets on glass, unmodified silicon and UVO exposed silicon. The central part of these patterns was also composed of solidified BM cells, with the dendritic fibers radiating from the cell center. In contrast to the results obtained for the in-house synthesized ZnO nanofluid (**Figures 1-3**), the overall surface coverage and the fiber density in the BM cells were much higher, and there was also more significant inter-cell penetration. In contrast to the residual surface patterns from the in-house synthesized ZnO nanofluids, the fibrous structures produced from the commercially acquired ZnO nanopowder and ZnO powder were intercalated with the ZnO nano/microcrystal residues across the fibers, as shown in insets in **Figure S7**. This was attributed to ZnO nanocrystals undergoing incomplete moisture-assisted dissolution over the course of evaporation, described in detail in [1]. These undissolved ZnO nano/microcrystals could have influenced the solvent flows during the evaporation and contributed to the fluid viscosity fluctuations causing the BM instabilities.

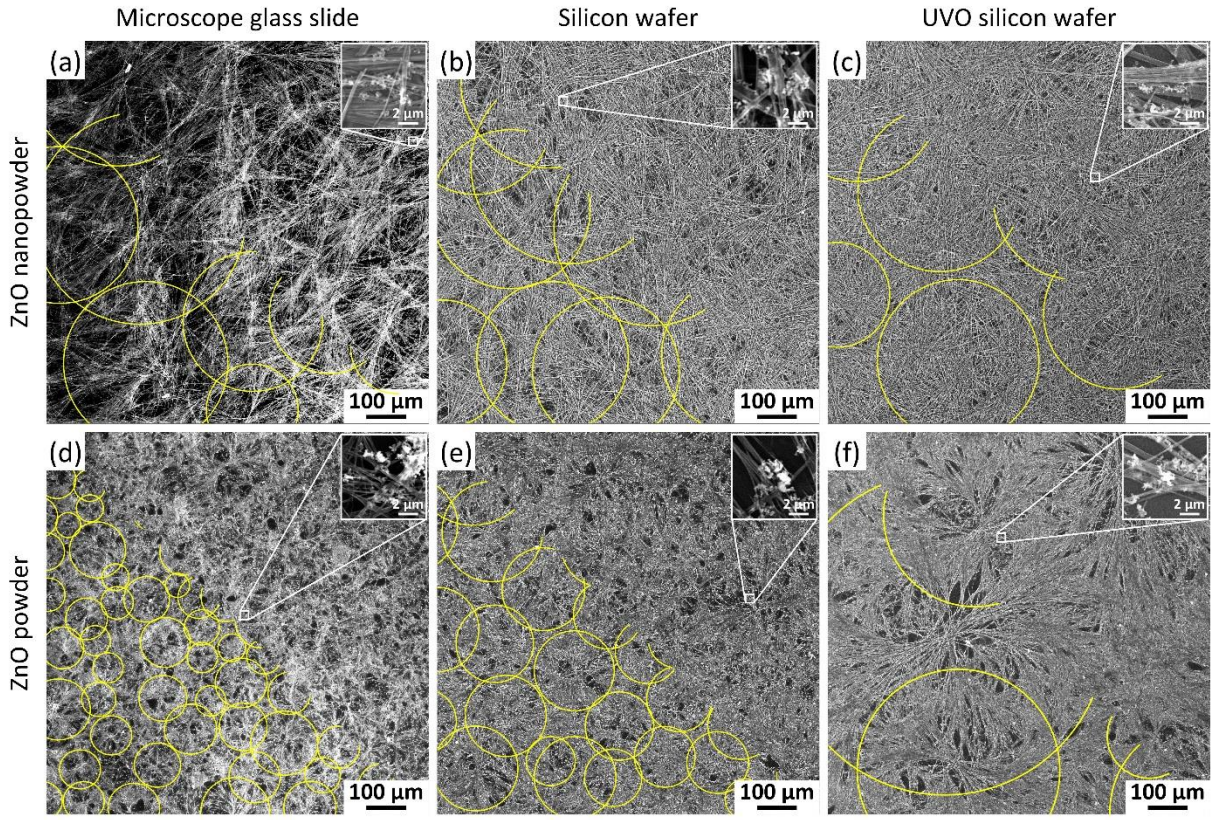

Figure S7. SEM micrographs of the residual surface patterns formed from a 30 µL sessile drop of the commercially acquired ZnO nanopowder (**a-c**) and ZnO powder nano/microfluid drops (**d-e**) dried on different substrates: (**a, d**) microscope glass slide, (**b, e**) unmodified silicon wafer, and (**c, f**) UVO exposed silicon wafer. BM cells are marked with yellow circles in half of the image for clarity. Insets show magnified views of the white squares in the corresponding images, which reveal undissolved ZnO nanocrystal residues that intercalated with the fibers.

The BM cells are outlined in **Figure S7** as yellow circles in only half of the image for clarity. Depending on the ZnO nano/microfluid and substrate used, the BM cells differed in size. In order to quantify the differences, the size distribution of BM cells across the samples was fitted with the log-normal distribution (see SI.06), similarly to the residual surface patterns produced from the in-house ZnO nanofluid (**Figure S9**). The log-normal fit parameters for the size distribution of MB cells formed from the ZnO nanopowder nanofluid are: M = 357, 451, and 515 µm and σ_g = 1.20, 1.19, and 1.34 on glass, silicon and UV/O exposed silicon, respectively. For the structures formed from the ZnO powder nano/microfluid, the corresponding log-normal parameters are: M = 106, 205, and 423 µm, and

σ_g = 1.29, 1.31, and 1.66 respectively. A trend in the BM cell size distribution with respect to the substrate was similar to that observed with the in-house ZnO nanofluid. Specifically, the geometric mean BM cell size, *M,* and the geometric standard deviation coefficient, σ_g, increased for substrate in order: glass, unmodified silicon and UVO treated silicon, confirming that the BM cell size depended on the substrate (**Figure 5**). The smallest *M* value was observed for the commercially acquired ZnO powder dried on glass substrate (*M* = 106 μm), and the biggest BM cells were created from the commercially acquired ZnO nanopowder on UVO treated silicon wafer (*M* = 515 μm).

The optical microscopy images of the residual surface patterns are presented in **Figure S8**. The footprints of the residual surface patterns were calculated using ImageJ software based on their surface area and are shown in **Table S6**.

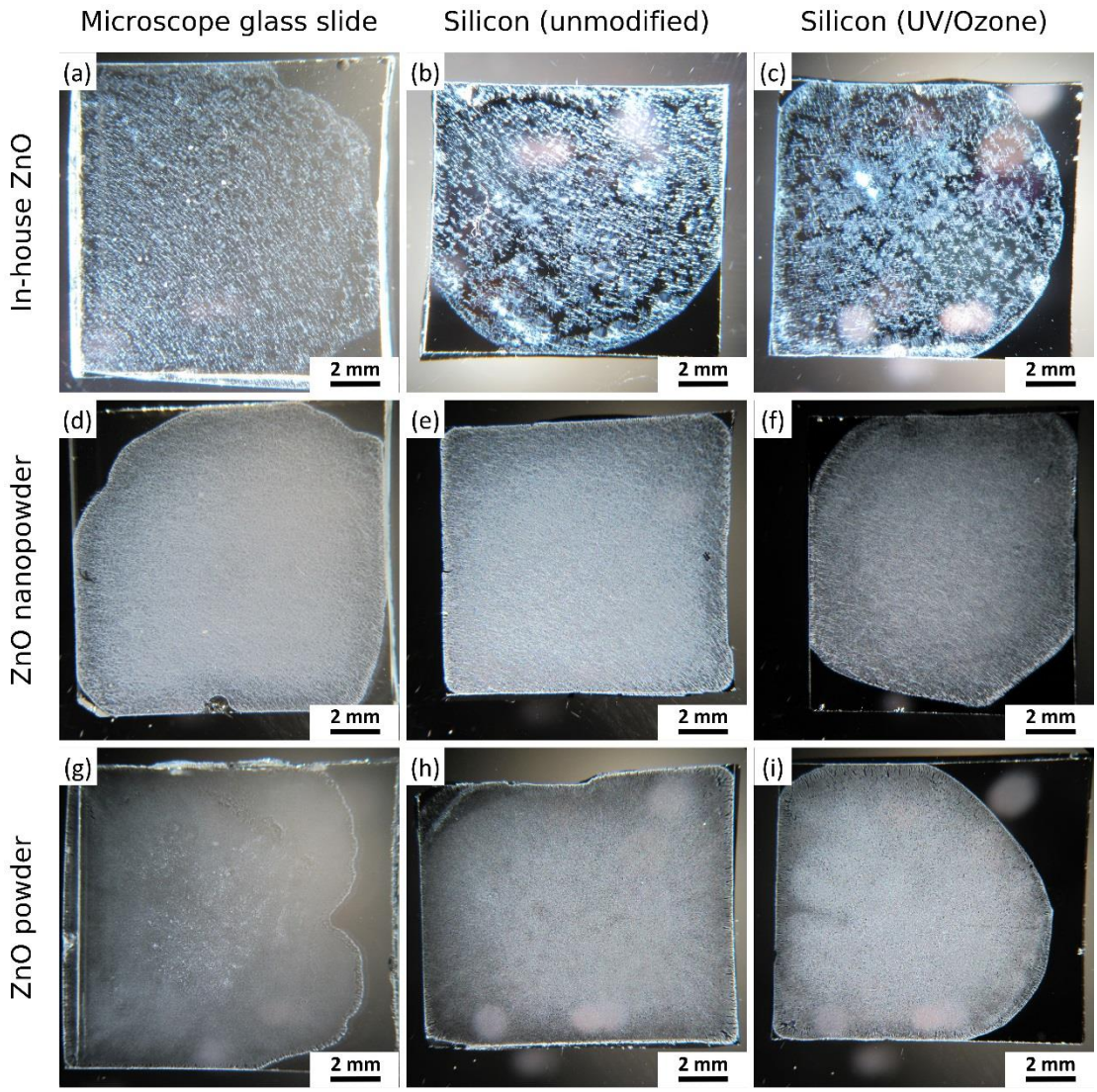

Figure S8. Optical microscopy images of the residual surface patterns formed from ZnO nano/microfluids: (**a-c**) the in-house synthesized ZnO, and commercially available (**d-f**) ZnO nanopowder, and (**g-i**) ZnO powder on different substrates: (**a**, **d**, and **g**) microscope glass slide, (**b**, **e**, and **h**) unmodified silicon wafer, and (**c**, **f**, and **i**) UVO exposed silicon wafer.

Table S6. Residual surface pattern footprints.

	Microscope glass slide	**Unmodified silicon**	**UVO exposed silicon**
In-house synthesized ZnO	141.7 mm^2	115.8 mm^2	117.3 mm^2
ZnO nanopowder	139.4 mm^2	126.2 mm^2	112.2 mm^2
ZnO powder	136.0 mm^2	133.5 mm^2	107.5 mm^2

SI.06: Bénard-Marangoni cell size distribution - log-normal fitting

For completeness, we include this section which has also been presented in the SI section of Ref. [1]. As described in the SI section of [22], circles outlining the solidified manifestation of BM cells were drown on top of SEM images, which examples are shown in **Figures 1-3** and **S8** using Serif DrawPlus X6 software. Subsequently, these circles were manually separated to eliminate overlapping and saved to separate files, which enabled image analysis using ImageJ (version 1.51j8) software. The size distributions of BM cells were fitted with the log-normal distribution function, eq S6:

$$y = \frac{1}{\ln(\sigma_g)\sqrt{2\pi}} \exp\left[-\frac{(\ln x - \ln M)^2}{2\ \ln^2(\sigma_g)}\right], \qquad \text{(S6)}$$

where *y is* the probability density function, *x* is the BM cell size, σ_g is the geometric standard deviation, and *M* is the geometric mean particle size by count [23]. In the log-normal distribution, *M* is the size below or above which half the total number of BM cells is found (median size). The dispersion and skewness of the size distribution curve is represented by the geometric standard deviation σ_g. According to the interpretation of the geometric standard deviation in a physical level, 68.3% of all BM cells in log-normal distribution is contained in sizes between M/σ_g and $M\cdot\sigma_g$ [24]. This is in an analogy to normal distribution, in which 68.3% of all values occur within one standard deviation away from the mean. The lognormal size distribution of BM cells are shown in **Figure S9**. Marangoni numbers calculated accordingly to eq 1 for the boundaries of the BM cell size range in which 68.3% of diameters are located (M/σ_g and $M\cdot\sigma_g$) are presented in **Table S7**.

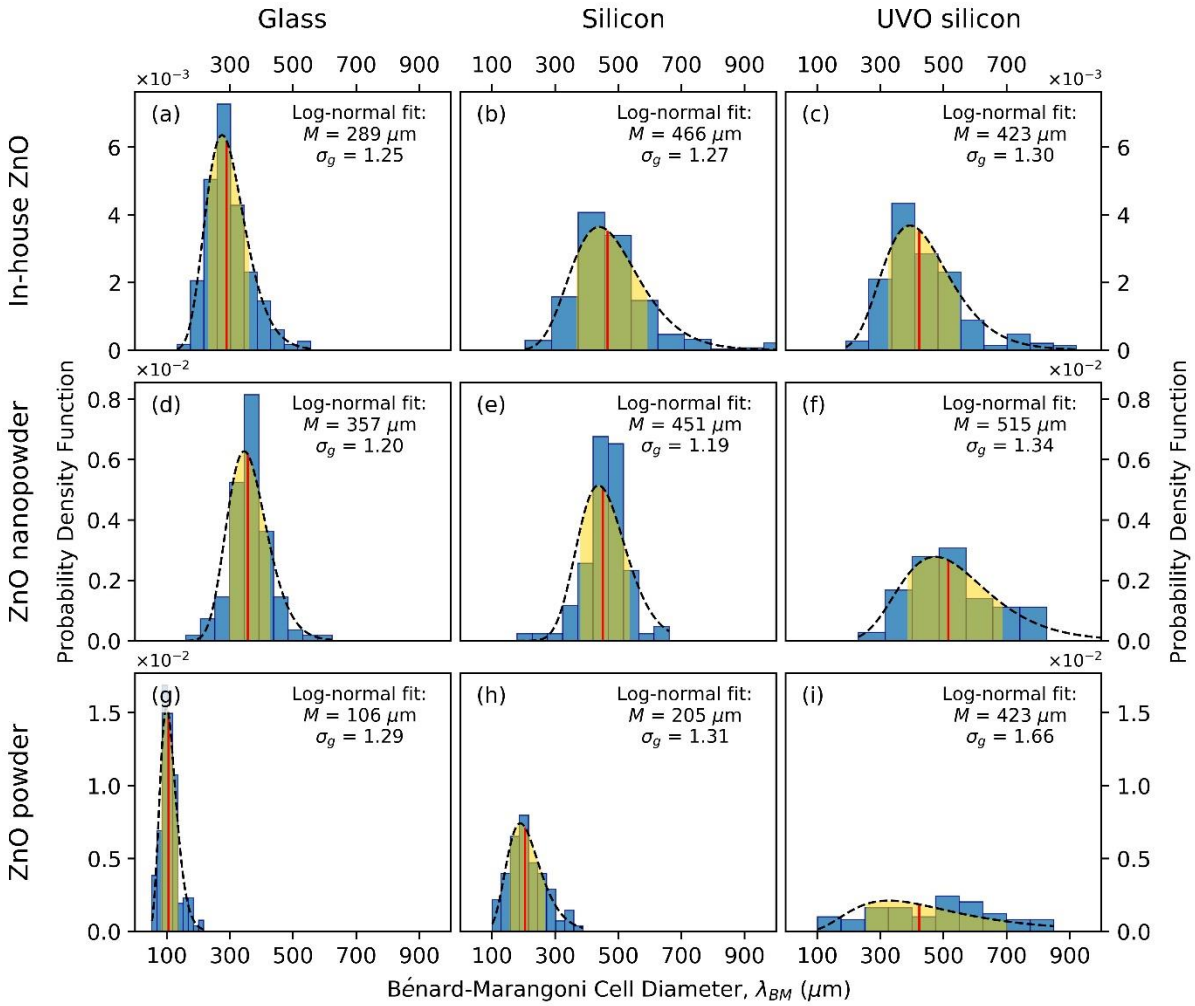

Figure S9. Size distributions as the probability density function (PDF) of BM cells present in the central structure of residual surface patterns formed from ZnO nano/microfluids on different substrates. Top row (**a-c**) in-house ZnO nanofluid; middle row (**d-f**) ZnO nanopowder nanofluid; bottom row (**g-i**) ZnO powder nano/microfluid; left column (**a**, **d**, and **g**) glass; middle column (**b**, **e**, and **h**) unmodified Si; and left column (**d**, **f**, and **i**) UVO exposed Si. The log-normal distribution function is shown as a dashed line. Red vertical lines show the geometric mean, M (equal to median size in log-norm distribution). BM cells of sizes contained between M/σ_g and $M \cdot \sigma_g$ (68.3% of all values) are shaded in golden color under the dashed size distribution curve.

Table S7. Marangoni numbers calculated accordingly to eq 1 for the boundaries of the BM cell size range in which 68.3% of diameters are located (M/σ_g and $M \cdot \sigma_g$).

	Microscope glass slide		**Unmodified silicon**		**Hydrophilised silicon**	
	M/σ	$M \cdot \sigma_g$	M/σ	$M \cdot \sigma_g$	M/σ	$M \cdot \sigma_g$
In-house ZnO	269	110	157	61	195	68
ZnO nanopowder	165	80	124	62	153	47
ZnO powder	2243	810	651	221	379	50

SI.07: Fractal dimension analysis of the Bénard-Marangoni cells

Please see SI sections of Chapter 3 and Refs. [22, 25] for more details. A step-by-step example of undertaken analysis is presented in **Figure S10** based on an SEM image of residual surface patterns formed from drying of the in-house synthesized ZnO nanofluid droplet on UVO exposed Si.

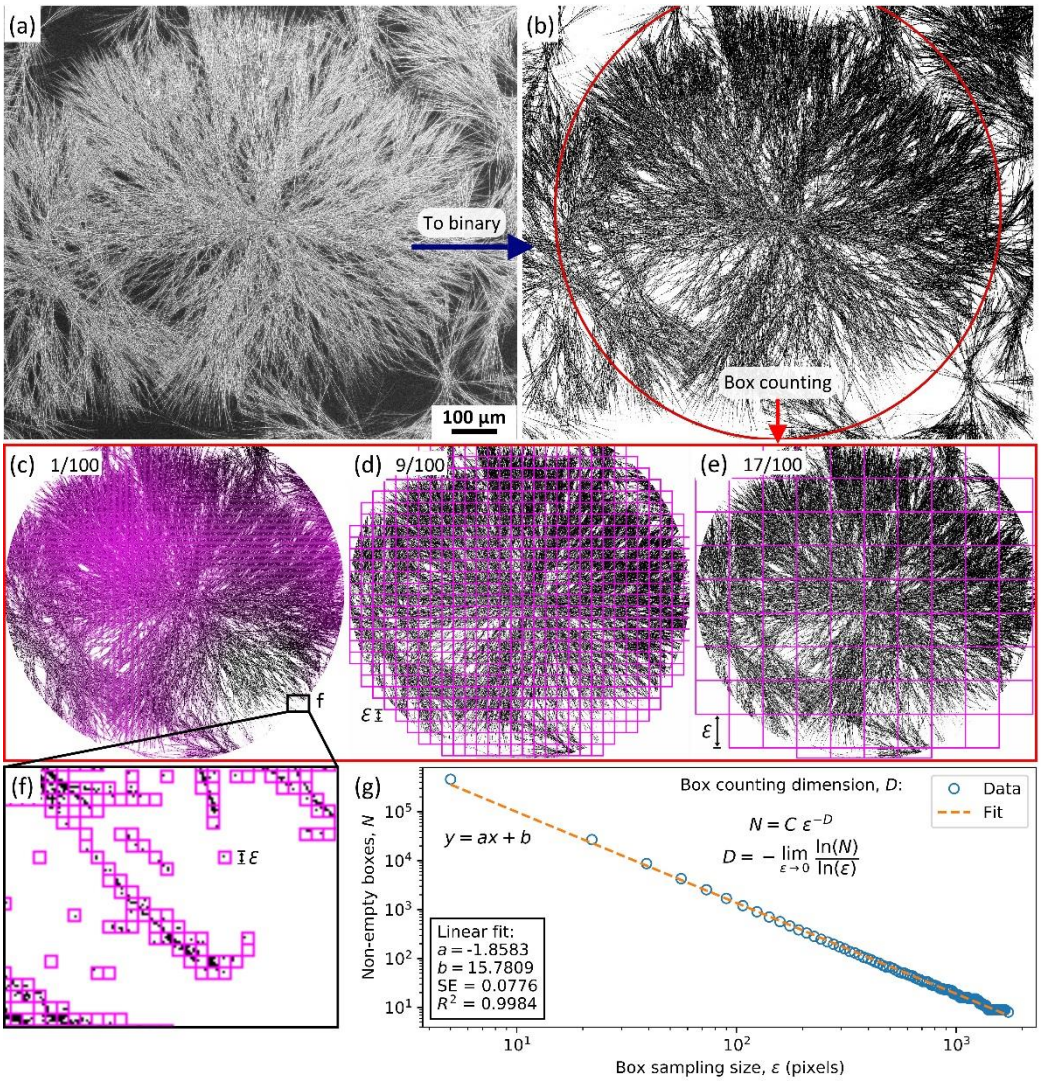

Figure S10. Step-by-step scheme of box counting fractal dimension (FD) analysis undertaken in this work using ImageJ supported with FracLac plugin. An SEM image (**a**) is converted to binary form (**b**). Then, a circular selection containing a Bénard-Marangoni (BM) cell is analyzed by superimposing a series of square grids of a box sampling size ε on the image, and the number of boxes containing foreground pixels, N is counted for each ε (**c-f**). The box counting FD is the negative slope of the best line fit to ln(N) vs. ln(ε) plot (**h**).

SI.08: References

1. Wąsik, P.; Redeker, C.; Dane, T. G.; Seddon, A. M.; Wu, H.; Briscoe, W. H., Hierarchical Surface Patterns upon Evaporation of a ZnO Nanofluid Droplet: Effect of Particle Morphology. *Langmuir* **2018,** *34* (4), 1645-1654.

2. Lin, X.; Liao, G.; Tang, Z.; Shi, T., UV surface exposure for low temperature hydrophilic silicon direct bonding. *Microsyst. Technol.* **2009,** *15* (2), 317-321.

3. Malik, R.; Shi, T.; Tang, Z.; Liu, S., Effect of Ultra Violet Process and Annealing on Reliability in Low Temperature Silicon Wafer Direct Bonding. *Advanced Science Letters* **2011,** *4* (3), 774-780.

4. Fan, J.; Chong, G. Y.; Tan, C. S., Study of Hydrophilic Si Direct Bonding with Ultraviolet Ozone Activation for 3D Integration. *ECS Transactions* **2013,** *50* (7), 17-27.

5. Vig, J. R., UV/ozone cleaning of surfaces. *J. Vac. Sci. Technol., A* **1985,** *3* (3), 1027-1034.

6. Young, G. J., Interaction of water vapor with silica surfaces. *J. Colloid Sci.* **1958,** *13* (1), 67-85.

7. Owens, D. K.; Wendt, R. C., Estimation of the surface free energy of polymers. *J. Appl. Polym. Sci.* **1969,** *13* (8), 1741-1747.

8. Rulison, C., So you want to measure surface energy? In *A tutorial designed to provide basic understanding of the concept solid surface energy, and its many complications, TN306/CR*, 1999; pp 1-16.

9. Wlodek, M.; Kolasinska-Sojka, M.; Wasilewska, M.; Bikondoa, O.; Briscoe, W. H.; Warszynski, P., Interfacial and structural characteristics of polyelectrolyte multilayers used as cushions for supported lipid bilayers. *Soft Matter* **2017,** *13* (43), 7848-7855.

10. Maldas, D. C.; Kamdem, D. P., Surface Tension and Wettability of Cca-treated Red Maple. *Wood and Fiber Science* **1998,** *30* (4), 368-373.

11. Rolo, L. I.; Caço, A. I.; Queimada, A. J.; Marrucho, I. M.; Coutinho, J. A. P., Surface Tension of Heptane, Decane, Hexadecane, Eicosane, and Some of Their Binary Mixtures. *Journal of Chemical & Engineering Data* **2002,** *47* (6), 1442-1445.

12. Kobayashi, H.; Owen, M. J., Surface tension of poly[(3,3,4,4,5,5,6,6,6-nonafluorohexyl)methylsiloxane]. *Macromolecules* **1990,** *23* (23), 4929-4933.

13. Gómez-Díaz, D.; Mejuto, J. C.; Navaza, J. M., Physicochemical Properties of Liquid Mixtures. 1. Viscosity, Density, Surface Tension and Refractive Index of Cyclohexane + 2,2,4-Trimethylpentane Binary Liquid Systems from 25 °C to 50 °C. *Journal of Chemical & Engineering Data* **2001,** *46* (3), 720-724.

14. Jasper, J. J., The Surface Tension of Pure Liquid Compounds. *J. Phys. Chem. Ref. Data* **1972,** *1* (4), 841-1010.

15. Dann, J. R., Forces involved in the adhesive process: I. Critical surface tensions of polymeric solids as determined with polar liquids. *J. Colloid Interface Sci.* **1970,** *32* (2), 302-320.

16. Ström, G.; Fredriksson, M.; Stenius, P., Contact angles, work of adhesion, and interfacial tensions at a dissolving Hydrocarbon surface. *J. Colloid Interface Sci.* **1987,** *119* (2), 352-361.

17. Żenkiewicz, M., Methods for the calculation of surface free energy of solids. *Journal of Achievements in Materials and Manufacturing Engineering* **2007,** *24* (1), 137-145.

18. Skrivanek, T., Determination of the surface free energy of electronic components. https://www.kruss-scientific.com/fileadmin/user_upload/website/literature/kruss-ar234-en.pdf (accessed 16 Mar 2019).

19. Raposo, M.; Ferreira, Q.; Ribeiro, P., *A Guide for Atomic Force Microscopy Analysis of Soft Condensed Matter*. 2007; Vol. 1.

20. Geschwender, T.; Kowalski, C.; Kelley, V., *NanoScope Software 6.13 User Guide*. Veeco Instruments Inc: 2004.

21. Liao, G.; Zhang, X.; Lin, X.; Ma, C.; Nie, L.; Shi, T., Ultraviolet exposure enhanced silicon direct bonding. *Frontiers of Mechanical Engineering in China* **2010,** *5* (1), 87-92.

22. Wąsik, P.; Seddon, A. M.; Wu, H.; Briscoe, W. H., Dendritic surface patterns from Bénard-Marangoni instabilities upon evaporation of a reactive ZnO nanofluid droplet: A fractal dimension analysis. *J. Colloid Interface Sci.* **2019,** *536*, 493-498.

23. Smith, J. E.; Jordan, M. L., Mathematical and graphical interpretation of the log-normal law for particle size distribution analysis. *J. Colloid Sci.* **1964,** *19* (6), 549-559.

24. Zender, C., Particle size distributions: theory and application to aerosols, clouds, and soils. http://dust.ess.uci.edu/facts/psd/psd.pdf (accessed 12th Dec 2017).

25. Wąsik, P.; Seddon, A. M.; Wu, H.; Briscoe, W. H., Bénard-Marangoni dendrites upon evaporation of a reactive ZnO nanofluid droplet: Effect of substrate chemistry *Langmuir* **2019,** *35* (17), 5830-5840.

Structural evolution of the surface pattern in an evaporating nanofluid sessile drop: An *in-situ* synchrotron grazing incident X-ray diffraction study

Patryk Wąsik[a,b] *et al.*

[a] Bristol Centre for Functional Nanomaterials (BCFN), HH Wills Physics Laboratory, University of Bristol, Tyndall Avenue, Bristol, BS8 1TL, UK

[b] School of Chemistry, University of Bristol, Cantock's Close, Bristol, BS8 1TS, UK

Information

This chapter is intended to be published as a research article and has been authored by the candidate with no more input from co-authors and supervisors that would have been provided in a conventional thesis chapter. Individual contributions: Patryk Wąsik conducted the research, analysed the data, and wrote the manuscript, PW, Anna Slastanowa, Jacek M. Wąsik, Tim Snow, Alexander de Bruin, Thomas Arnold (Diamond Light Source), and Wuge H. Briscoe contributed to the synchrotron X-ray scattering measurements, Thomas G. Dane (European Synchrotron Radiation Facility) assisted with analysis of diffraction data, Annela M. Seddon and WHB supervised the project.

Introduction

Drying of a particle laden droplet is widespread in everyday life and industrial processes and can lead to a plethora of residual patterns. The most recognisable is the coffee ring, which formation mechanism was first elucidated around 2 decades ago [1-3]. The vast academic interest it stimulated continues to thrive today, and it is also directly relevant to producing functional devices and nanomaterials [4-6]. However, the dispersed particles are inert in most of the previous studies.

We have recently shown [7-8] that, upon evaporation of a reactive ZnO nanofluid sessile drop, the residual pattern forms in a mechanism very different from that associated with the coffee ring, leading to the hierarchical residual pattern composed of solidified manifestations of Bénard-Marangoni cells. We have also demonstrated [9] that the ultimate residual surface structure can be tuned by the morphology, size, and crystallinity of the ZnO particles. The complex nature of the hierarchical morphologies in the residual surface patterns produced from ZnO nanofluids was descriptively identified as, *e.g.* analogous to the foliage of red algae, Spanish dagger, or spider plant [7]. However, we have recently reported a fractal dimension analysis to provide a more quantitative description of the geometric features of these Bénard-Marangoni cells produced from different ZnO nanofluids [10] that also depended on the substrate used [11]. These findings have opened new routes for fabrication of functional surface patterns *via* self-assembly induced by evaporation of reactive nanofluids.

Our previous studies focused on how the initial conditions of the experimental drying setup would govern the final residual patterns produced from reactive ZnO nano/microfluids. To obtain a better insight into the underlying dissolution-recrystallisation mechanism that leads to the formation of hierarchical network of $Zn(OH)_2$ fibres from ZnO nanocrystals, we utilised the *in-situ* grazing incidence X-ray diffraction to track the temporal evolution of the crystal structures within a sessile nanofluid drop as it dries. Grazing incidence X-ray scattering techniques have been previously employed to study evaporation induced superlattice growth of superparamagnetic Fe_2O_3 nanospheres [12].

High temporal resolution necessary to follow rapidly drying drops was achieved using a high brilliance X-rays beam from a synchrotron light source. This allowed us to resolve intermediate steps in the surface pattern formation as the evaporation ensued rapidly, providing unprecedented mechanistic insights. We used three different types of ZnO nano/microparticles and various substrates, including glass slide, both unmodified and silanised silicon wafers, polytetrafluoroethylene (PTFE), and mica. In addition to ZnO nano/microfluids, we performed evaporation experiments on reactive CuO nanofluids and ZnO nanostructured surfaces. Furthermore, the temperature effect on the phase transition of as-prepared residual surface patterns was studied.

Such an analysis and the unprecedented results will facilitate further studies to seek correlations between the intriguing appearance of the residual surface patterns and the physical parameters relevant

to the novel evaporation process involving reactive nanofluids. Our results also point to the feasibility of grazing incident X-ray diffraction analysis for studying similar systems of other reactive nanofluids such as CuO, CdO, and HgO (Wąsik *et al.*, in preparation) or organic mixtures / reactive ZnO nanostructured surfaces systems (nanorods, nanourchins, nanopallets, *etc*.).

Materials and Methods

Particles

Several different particles were used for nano/microfluids preparation. This includes the in-house synthesised ZnO nanoparticles and commercially acquired ZnO nanopowder (Sigma-Aldrich, <100 nm particle size, ~80% Zn basis), ZnO powder (Sigma-Aldrich, ACS reagent, ≥99.0% (KT)), and CuO nanopowder (Sigma-Aldrich, <50 nm particle size (TEM)). More on the characterisation of ZnO particles and the synthesis of the in-house ZnO nanoparticles can be found in [9] and, while the characterisation of CuO is described in SI.01.

Nano/microfluid preparation

ZnO and CuO particles were added to a mixture of cyclohexane (Fisher Chemicals, assay 99%) and isobutylamine (Sigma-Aldrich, assay 99%), 5:1 volume:volume ratio, in the amount required to produce 1 mg/mL concentrations suspensions. These suspensions were sonicated for 0.5 - 1 hours to form homogenous dispersions just before the *in-situ* drying experiments.

Substrates

The nano/microfluids drops were dried on various 1×1 cm^2 substrates, including standard microscope glass slides (type 7101, 0.8 - 1.0 mm thick), silicon wafers (UniversityWafer Inc., ID 452, 100 mm diameter, P type, B dopant, <100>, 0-100 Ω·cm, 500 μm thick, single-sided polish, test grade), both unmodified and hydrophobised by functionalisation with silane (see SI.02 for the functionalisation procedure), natural muscovite mica with composition $KAl_2(Si_3Al)O_{10}(OH)_2$ (SJ Trading®, A1 special grade), and polytetrafluoroethylene (PTFE) (sourced from the mechanical workshop, School of Chemistry, University of Bristol). All substrates besides mica were cleaned by subsequent sonication in acetone, ethanol, and *Milli-Q* water (18.2 MΩ·cm at 25 °C) for 10 minutes each, then rinsed with *Milli-Q* water and dried using a stream of nitrogen. Mica sheets were cleaved by insertion of a sharp

needle tip into the edge of the sheet prior to the evaporation experiment. In addition, a glass slide with ZnO nanorods grown on the surface (see SI.02 for the synthesis and scanning electron microscopy images) was used as a substrate to dry a droplet of pure cyclohexane and isobutylamine mixture (5:1 v:v) to investigate whether it would produce results similar to these observed for ZnO nano/microfluids. More general information about materials used as substrates, their structures and surface chemistry can be found in SI.05. Water contact angle characterisation of glass and silicon substrates can be found in Chapter 4 and [11].

GIXRD experimental set-up

In situ synchrotron grazing incident X-ray diffraction (GIXRD) experiments were performed at Beamline I07 (Surface and Interface Diffraction) at Diamond Light Source, UK [13]. The experimental set-up is presented in **Figure 1**. The sample chamber was mounted onto a separate stage between the detector (Pilatus P3-2M, Dectris) and the monochromatic X-ray beam source of energy E = 12.5 keV (λ = 0.9919 Å). The chamber had a hole at the bottom that allowed for the sample stage to be inserted from below. In the adopted coordinate system, y-axis was equivalent to the direction of the X-ray beam, with the detector and sample surface planes being parallel to xz- and xy-planes, respectively (see **Figure 1a**). The set-up was calibrated using silver behenate (AgBH). The detector-to-sample distance was equal to 0.396 m. A fixed metal arm was installed inside the sample chamber. This supported tubing which connected with a syringe pump, dispensing a single droplet of nanofluid for the forthcoming experiments (**Figure 1b**). An aluminium block, with a substrate upon it, was placed upon a sample stage, upon a hexapod (**Figure 1c**). The position and temperature of the substrate were controlled with the hexapod and sample stage, respectively.

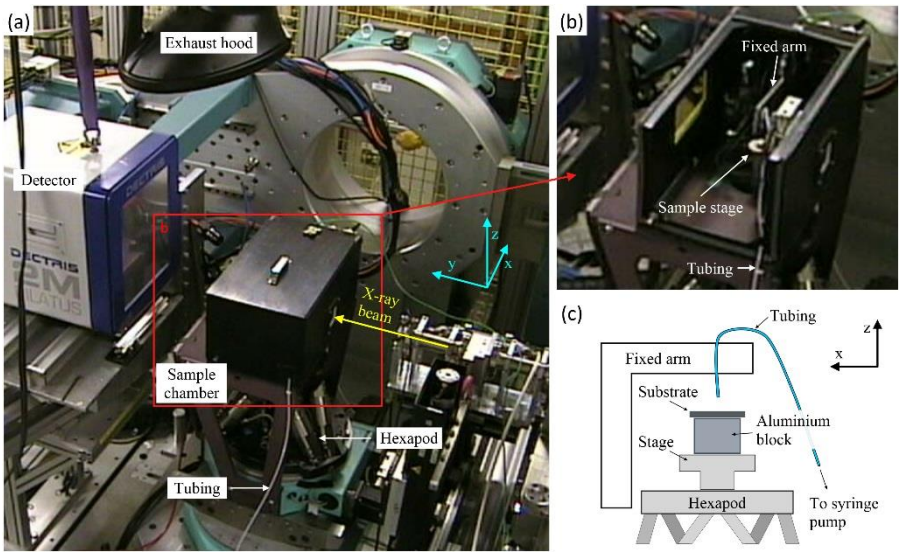

Figure 1. Experimental set-up for *in situ* grazing incident X-ray diffraction at Beamline I07, Diamond Light Source, UK. (**a**) Internal view of experimental hatch; (**b-c**) sample chamber.

Experimental procedures

A typical experimental procedure used to examine individual nanofluid systems consisted of the following steps: initial setup and alignment, main scan of an evaporating nanofluid sessile drop, and series of scans performed at different annealing temperatures of dried patterns. GIXRD measurements, if not specified otherwise in the text, proceeded as described below.

During the initial setup and alignment step, a substrate of choice was placed on top of an aluminium block inside of the sample chamber (**Figure 1c**). The substrate was then aligned by a series of subsequent *height* (along z-axis) and *theta* (rotation around the x-axis) scans. Subsequently, a previously prepared and sonicated (for 0.5 - 1 hours) nano/microfluid was transferred into the experimental setup. This was performed by withdrawing *ca* 400 µL of the nano/microfluid directly from a vial into the tubing connected to a syringe pump. The end of the tubing containing nano/microfluid was then attached above the substrate to the fixed arm (**Figure 1c**). This was followed by re-evaluation of the substrate alignment and prompt execution of the next experimental step in order to minimise the time between the nano/microfluid transfer and drying experiment.

The main part of the experiment investigating the structural evolution of the surface pattern in an evaporating nanofluid sessile drop started immediately after a nano/microfluid was transferred into the system and the substrate alignment was approved. Initially, the substrate was tilted around the x-axis so

the incident X-ray beam hit the sample under a small angle between 0.2 - 0.9° (usually 0.7° if not specified differently) close to the critical angle of total external X-ray reflection. Subsequently, 60 µL of the nano/microfluid was dispensed onto the substrate. This initiated diffraction data collection process by recording diffraction images while the drop was drying on the substrate (referred as *time scan*), which generally lasted for *ca* 200-300 seconds. The dried sample was then laterally scanned along the x-axis (referred as *lateral scan*). The script codes for both, *timescan* and *lateral scan*, are shown in SI.04.

The next step was to investigate how the structure of the residual surface patterns produced from investigated nano/microfluids transitioned with temperature. The substrate with the dried patterns produced in the previous step was annealed and then scanned laterally at a set of different temperatures (referred as *temperature scan*). The annealing temperature ranged from room temperature (RT) to 400 °C, and back to RT, ramped at 50 °C intervals (RT, 50, 100, …, 400, 350, …, 50 °C, RT). The sample was annealed for 10 minutes after reaching 400 °C, prior to returning to RT. The scrip code used to execute *temperature scan* is shown in SI.04.

Data processing and analysis

Raw detector images containing diffraction data were processed using *pygix*, a generic Python library designed for reduction of grazing incidence and fibre X-ray scattering data [14], which relies on *pyFAI*, an another Python library developed to perform 1D azimuthal or 2D radial integrations of diffraction images [15]. The recorded diffraction patterns were reduced to one-dimensional line profiles as they appeared as isotropic rings in two dimensional transformations into the reciprocal space. Baseline correction of the diffraction line profiles was performed accordingly to the penalised asymmetric least-squares algorithm developed by Eilers and Boelens [16]. Selection of the algorithm parameters, comparison with raw data, and the identification of the integration artefacts resulted from the 1D azimuthal integration are discussed in SI.03.

Results

In-house ZnO nanofluid

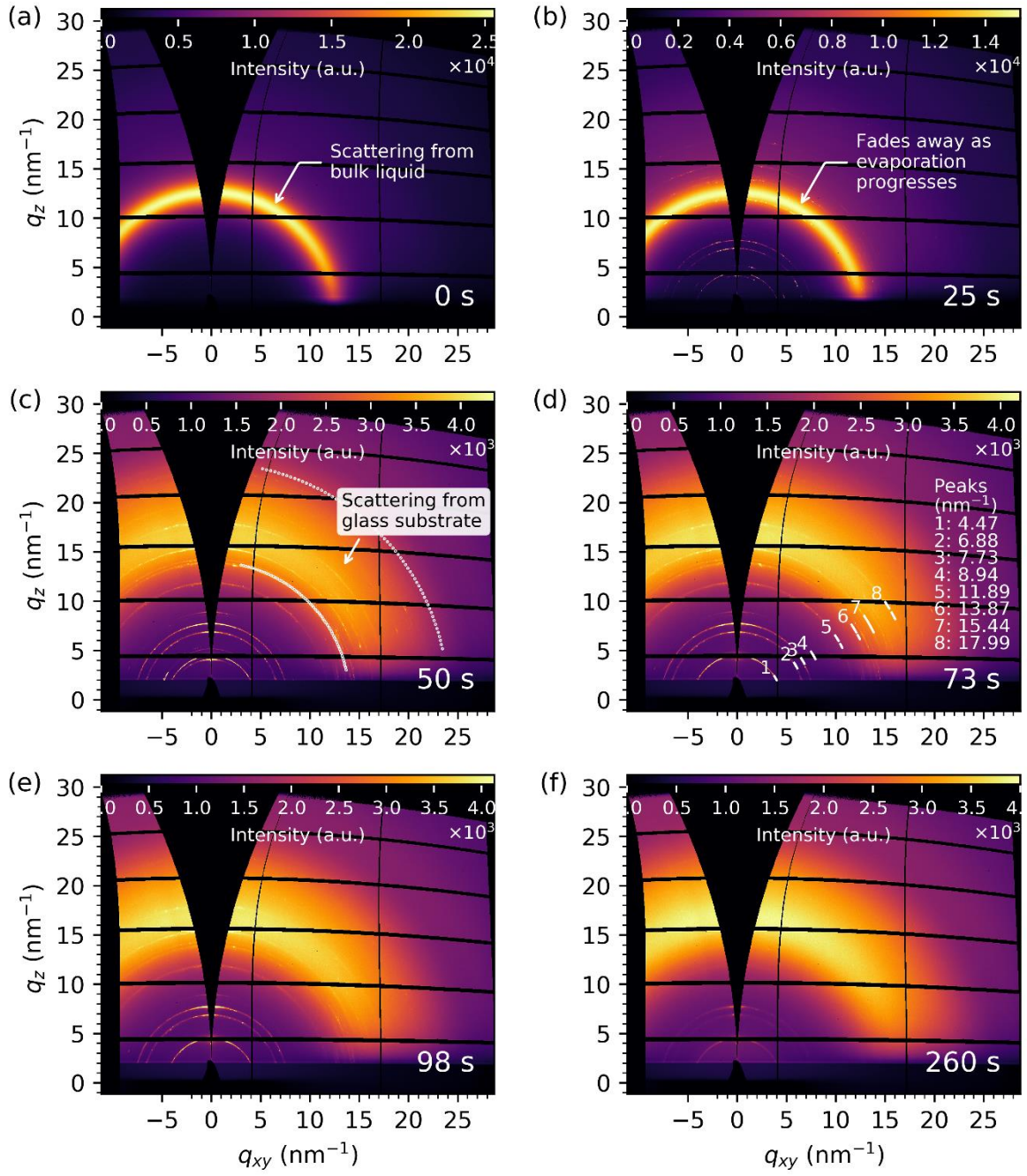

Figure 2. *In situ* grazing incident X-ray diffraction data from an evaporating droplet of the in-house ZnO nanofluid on a glass substrate. (**a-f**) Present detector images taken at different evaporation times projected onto reciprocal space coordinates: q_z (out-of-plane) and q_{xy} (in-plane). Intensity scale colour bars are placed at the top of each diffractogram. (**a-b**) Show the scattering peak coming from the bulk liquid, (**c**) shows diffuse scattering from the glass substrate, (**d**) lists calculated peak positions for

structures formed inside of the drying droplet, and (**e-f**) demonstrate diminishing peak intensities caused likely by the X-ray beam sample damage.

Figure 2 shows an example of the *in situ* grazing incident X-ray diffraction data from drying of a droplet of the in-house ZnO nanofluid on a glass substrate. The diffractograms are produced by projecting real detector images onto the reciprocal space coordinates, q_z (out-of-plane) and q_{xy} (in-plane). Note that the value of the momentum transfer vector is equal to $q = \sqrt{q_z^2 + q_{xy}^2}$. At the initial stage of the evaporation, an intense diffuse peak arising from the short range order interactions in the bulk liquid [17] is observed at $q \approx 12.7 \pm 1.0$ nm^{-1}. The intensity of the liquid peak reduces as the evaporation progress (compare the relative intensities in the colour bars in **Figure 2a-b**), and eventually disappears when the majority of the solvent is lost due to evaporation, which happens around 50 seconds after the droplet was cast on the substrate. (The liquid bulk peak that diminishes after the evaporation is finished has been observed in all experiments that concerned *in situ* GIXRD studies of evaporation nano/microfluid droplets, including CuO and CdO systems, Wąsik *et al.*, in preparation). In addition, the diffraction peaks at positions q = 4.47, 6.99, 7.77, and 8.90 nm^{-1} start to emerge as soon as the evaporation begin, more visible in **Figure 2b** due to the overall lower intensity of the scattering signal. **Figure 2c** shows the broad diffuse scattering ring from the glass substrate (see also the control substrate scan in **Figure S5a-b**) between 14 - 24 nm^{-1}.

Distinct diffraction rings are numbered with their positions listed in **Figure 2d**. The peaks are located at respective q values as follows, 1: 4.47, 2: 6.88, 3: 7.73, 4: 8.94, 5: 11.89, 6: 13.87, 7: 15.44, and 8: 17.99 nm^{-1}. This corresponds to the interplanar spacing ($d = 2\pi/q$) of 1.41, 0.91, 0.81, 0.70, 0.53, 0.45, 0.41, and 0.35 nm, respectively. It is suggested that peaks labelled as 1 (4.47 nm^{-1}), 2 (6.88 nm^{-1}), and 4 (8.94 nm^{-1}) result from stacked (00*l*) planes of the layered structure composed of complex positively charged zinc hydroxide layers and interlayer anionic species with the interplanar *d*-spacing of 2.79 ± 0.02 nm [9, 18-19]. Therefore, peaks 1, 2, and 4 could be indexed as (002), (003), and (004) using Miller indices. The diffraction ring from (001) would appear at $q \approx 2.23$ nm^{-1}, and this q range was partially blocked by the beam stop during the experiment. Peaks labelled as 3 (7.73 nm^{-1}) and 7 (15.44 nm^{-1}) in **Figure 2d** are also equally spaced in the diffractogram and may result from other

stacked crystallographic planes. **Figure 2e-f** shows diffraction patterns at later stages of the drying process with the time elapsed t = 98 and 260 seconds, respectively. The intensity of the diffraction rings, excluding the diffuse scattering from the glass substrate, diminishes over time likely due to beam damage from the prolonged exposure.

Figure 3 presents a detailed analysis of the evaporation process for the in-house ZnO nanofluid droplet dried on a glass substrate. The diffraction images initially shown in **Figure 2** were integrated over the azimuthal angle as they display powder diffraction rings, implying a uniform representation of every possible crystalline orientation in the sample. (The diffraction rings indicated by numbers 2, 3, and 4 have slightly higher intensity in the out-of-plane (q_z) than the in-plane (q_{xy}) direction). The waterfall plot in **Figure 3a** shows how the intensity of the scattering signal varies with respect to the momentum transfer vector, q, over the evaporation time, t. As soon as the drop of the ZnO nanofluid is cast on the substrate, diffraction peaks labelled as 1 (4.47 nm^{-1}), 2 (6.88 nm^{-1}), 3 (7.73 nm^{-1}), 7 (15.44 nm^{-1}), and 8 (17.99 nm^{-1}) emerge, indicating the rapid formation of the layered zinc hydroxide (LZH) structures within $t \approx 0$ - 10 seconds. Interestingly, two additional diffraction peaks labelled as 1a and 1b located at q = 4.11 and 5.21 nm^{-1}, respectively, become very intense between *ca* 15 - 60 seconds and fade as the evaporation time progresses. Thus, they are labelled as "temporary" peaks. The intense scattering signal around $q \approx 12.7 \pm 1.0$ nm^{-1} arising from the bulk liquid [17] diminishes after $t \approx 45$ - 50 seconds, indicating that the droplet evaporates within that time leaving the residual surface pattern on the substrate. The peaks labelled with numbers 8 (17.99 nm^{-1}) and 9 (19.87 nm^{-1}) maintain low intensity through the entire drying process up to 260 seconds in contrast to peaks 1 - 3, and to some extend 4 - 7, and are probably the higher order reflections from (00*l*) planes, *i.e.* (008) and (009) for peaks 8 and 9, respectively [19-20].

Selected diffraction line profiles, marked by horizontal dashed lines in **Figure 3a,** related to different evaporation times of 6, 25, and 98 seconds are plotted in **Figure 3b**. Please note that the relative intensities between the sharp LZH and the bulk liquid peaks are different than in **Figure 2** as the integrated profiles in **Figure 3** have been baseline corrected using the penalised asymmetric least-squares algorithm [16] for better contrast and scattering signal visualisation. This, however, has not caused a negative effect on the data analysis and the relative intensities of the sharp peaks have been

preserved. The correction is discussed in detail in SI.03. **Figure 3c-d** are insets showing magnified views of the area enclosed by black square boxes in **Figure 3b,** also labelled by respective alphabet letters. Sharp and intense LZH peaks numbered 1, 2, and 3, and less intense peaks labelled 4 and 7 - 9, are visible as early as at t = 6 seconds. Other LZH peaks numbered 4, 5, and 6 become more intense after 10 - 15 seconds of evaporation (**Figure 3c**). There are no observed peaks indicating the presence of zinc oxide crystals expected at q values of 22.39, 24.21, 25.45, and 32.94 nm^{-1} for (100), (002), (201), and (102) planes (Powder Diffraction File (PDF) number assigned by the International Centre for Diffraction Data: 01-075-0576).

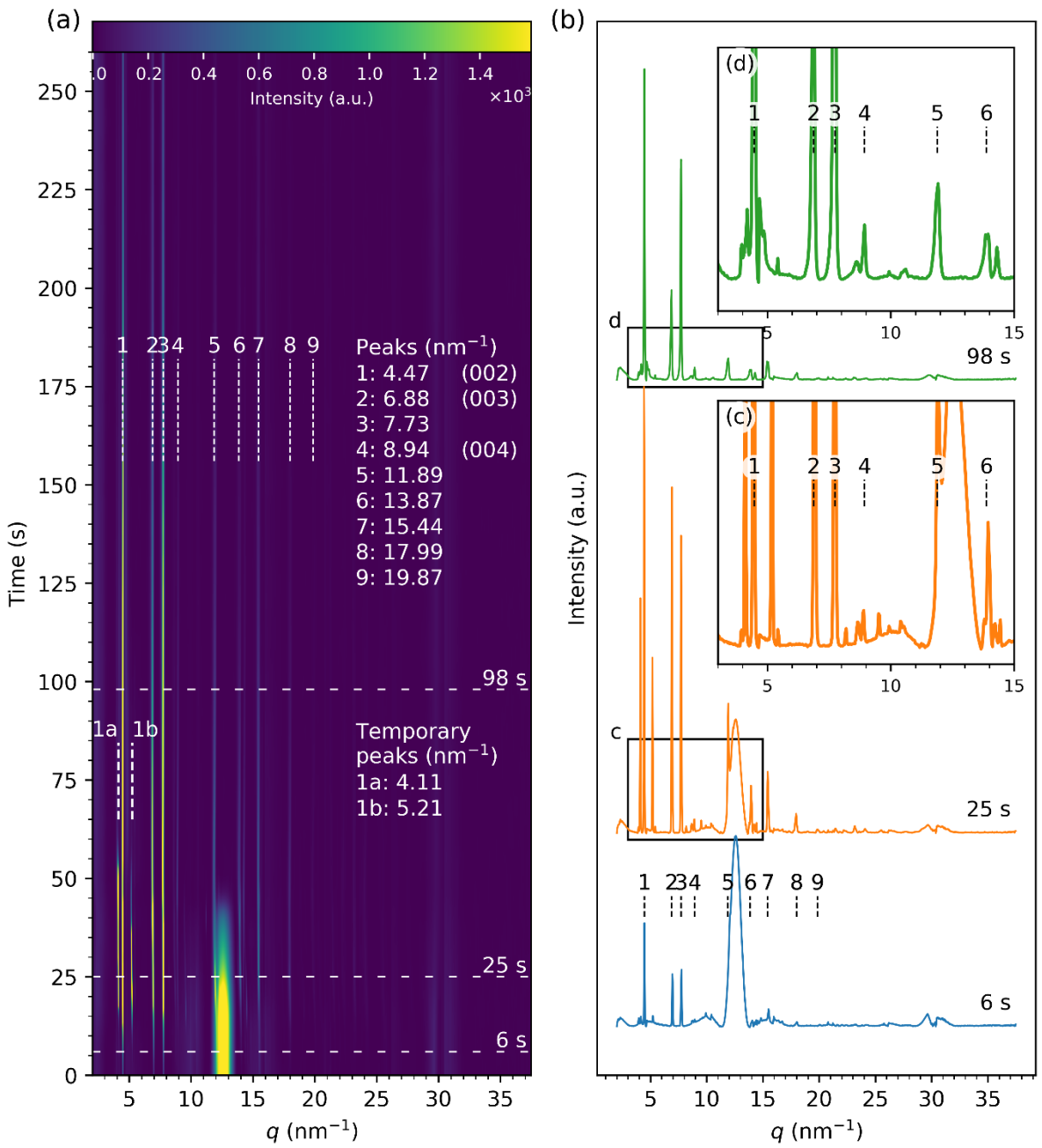

Figure 3. X-ray diffraction data from the evaporating droplet of the in-house ZnO nanofluid on a glass substrate produced by an azimuthal integration of the diffractograms presented in **Figure 2**. (**a**) Waterfall plot showing how the intensity of the scattering signal changes with the evaporation time. Dashed horizontal lines mark positions of line profiles that are shown in (**b**). Vertical lines labelled with numbers 1 - 9 show positions of the peaks fitted to the diffraction data at time $t = 73$ s and the lines labelled 1a and 1b to $t = 25$ s, with positions listed in (**a**). (**b**) Presents selected line profiles with insets (**c-d**) showing the data in the corresponding 25 and 98 s profiles in detail.

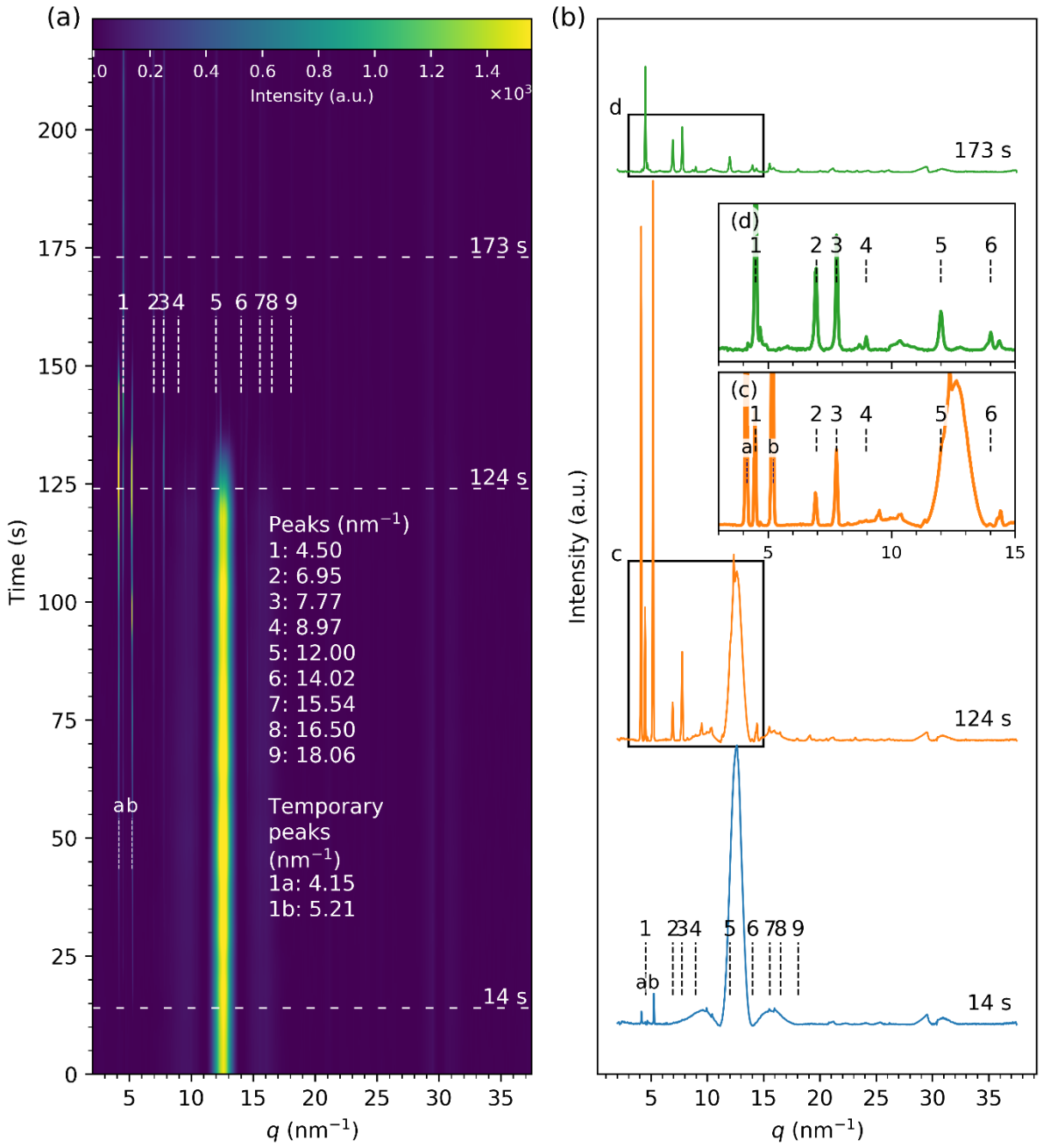

Figure 4. X-ray diffraction data from the evaporating droplet of the in-house ZnO nanofluid on an unmodified silicon substrate: (**a**) Waterfall plot showing how the intensity of the scattering signal changes with the evaporation time. Dashed horizontal lines mark positions of line profiles that are shown in (**b**). Vertical dashed lines labelled with numbers 1 - 9 show positions of peaks fitted to the data; (**c-d**) insets showing lower *q* range of the diffraction profiles at times 124 and 173 seconds.

Figure 4 shows the diffraction data of the in-house ZnO nanofluid dried on an unmodified silicon substrate. As previously, no ZnO diffraction peaks are observed throughout the process, suggesting rapid dissolution of ZnO nanoparticles after the droplet of ZnO nanofluid is cast on the substrate. Intriguingly, the first indication of the structural changes in the evaporating droplet are "temporary" peaks labelled as 1a (4.15 nm^{-1}) and 1b (5.21 nm^{-1}) emerging as early as in 14 seconds after the drop is cast onto the Si substrate. After 6 seconds, the rest of the peaks attributed to the layered zinc hydroxide structures labelled as 1 - 9 appear in the diffractogram; however, their intensities are much smaller than these for the "temporary" peaks, but grow gradually with time (**Figure 4b-c**). After 140 seconds most of the liquid evaporates, marked by the disappearance of the bulk liquid peak at 12.7 ± 1.0 nm^{-1}. At that time, the intensity of the peak labelled as 1 and indexed as (002) at 4.50 nm^{-1} becomes significantly stronger than that of the 1a and 1b peaks. Within the next 33 seconds the "temporary" peaks disappear almost completely, which is visible in the diffraction profile taken at 173 seconds (**Figure 4b**, and **d**). The average interplanar *d*-spacing calculated from position of the 1, 2, and 4 peaks is 2.77 ± 0.02 nm. The overall intensities of the rest of the peaks decrease with time, suggesting sample beam damage.

The diffraction data measured for a drying droplet of the in-house ZnO nanofluid on a silanised (hydrophobic) silicon substrate is shown in **Figure 5**. The diffraction peaks attributed to the LZH structures labelled as 1 - 3 arise within 4 seconds of the drying process at *q* positions equal to 4.47, 6.89, and 7.73 nm^{-1}, respectively. Shortly after, the rest of the LZH peaks labelled as 4 - 7 and 9 at 8.80, 11.89, 13.87, 15.46, and 17.96 nm^{-1}, respectively, emerge and gain in the intensity as the time progresses. Similarly to the evaporation from the two other substrates, glass (**Figure 2** - **Figure 3**) and unmodified silicon (**Figure 5**), additional peaks in the close neighbourhood of the first LZH (4.47 nm^{-1}) peak, labelled as 1a (4.12 nm^{-1}) and 1b (5.20 nm^{-1}) appear in the diffractogram during evaporation. The signal of these peaks gets stronger with time, then suddenly diminishes just after the droplet evaporates, marked by the disappearance of the bulk liquid peak (q = 12.7 ± 1.0 nm^{-1}) after 174 seconds. The intensity of the LZH peak at 4.47 nm^{-1} is much stronger than the intensity of 1a and 1b, similarly to the in-house ZnO nanofluid dried on glass (**Figure 3**), in contrast to the unmodified Si substrate (**Figure 4**), where the "temporary" peaks are dominant until the droplet loses its volume. Based on the presumption that peaks labelled as 1 (4.47 nm^{-1}), 2 (6.89 nm^{-1}), and 4 (8.80 nm^{-1}) result from stacked (00*l*) planes of

the layered zinc hydroxide structures, the average interplanar *d*-spacing is equal to 2.80 ± 0.03 nm. Contrary to the previous data for the in-house ZnO nanofluid (**Figure 2** - **Figure 4**), ZnO diffraction peaks at 22.29, 23.89, 25.34, and 32.76 nm^{-1}, indexed as (110), (002), (101), and (102), respectively, appear in the diffractogram. However, their intensity is relatively low when compared to the main LZH peaks at the low *q* range. The peak broadening is observed for all ZnO peaks, with the full width at half maximum of 0.63 ± 0.04 nm^{-1} calculated for the (110) peak using a Gaussian function fitting.

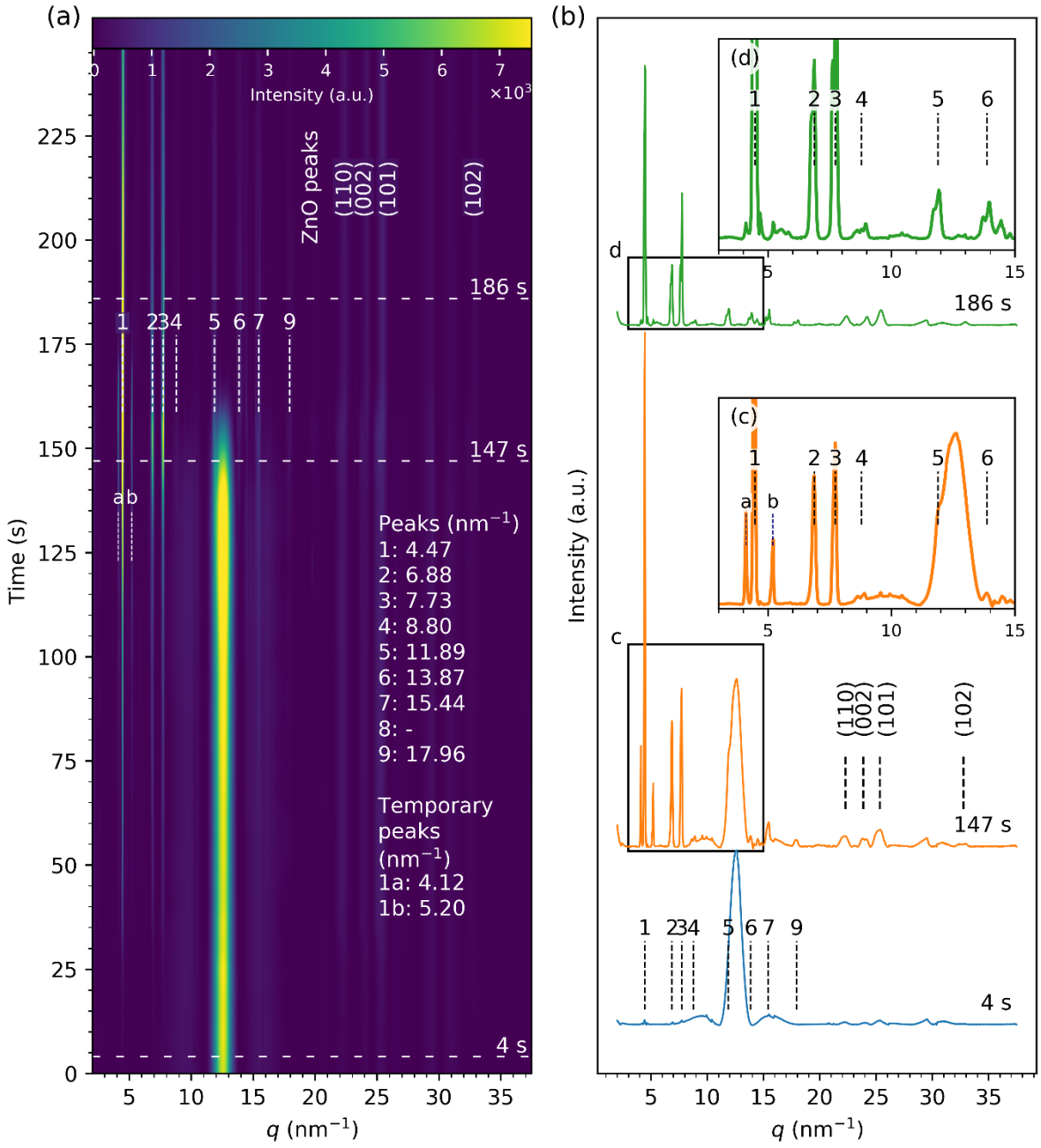

Figure 5. X-ray diffraction data from the evaporating droplet of the in-house ZnO nanofluid on a silanised silicon substrate: (**a**) Waterfall plot showing how the intensity of the scattering signal

changes with the evaporation time. Vertical dashed lines labelled with numbers 1 - 7 and 9 show positions of peaks fitted to the data and horizontal dashed lines mark positions of the selected profiles shown in (**b**). (**c-d**) Insets showing lower q range of the diffraction profiles at times 147 and 186 seconds.

ZnO nanopowder nano/microfluid

This section describes the grazing incident X-ray diffraction data collected for the ZnO nano/microfluid prepared from the commercially acquired ZnO nanopowder (68.3% of crystals between 36 - 142 nm, see SI.01). **Figure 6** presents results of the evaporation experiments from an unmodified silicon substrate. In contrast to the in-house ZnO nanofluid containing particles *ca* 9 nm in diameter, strong ZnO diffraction peaks produced by the wurtzite structure of larger crystals appear at the start of the evaporation at $t = 0$ seconds. These ZnO peaks located at 22.43, 24.24, 25.48, and 32.97 nm^{-1}, indexed as (110), (002), (101), and (102), respectively, become more intense when the droplet starts thinning around $t = 44$ seconds, and remain present at the full length of the drying process. In addition, the peaks indicating the presence of the LZH structures numbered as 1 at 4.50 nm^{-1} and 2 at 6.99 nm^{-1} start emerging after 30 seconds of the evaporation. This time difference with respect to the in-house ZnO nanofluid can be related to the longer dissolution times of crystals in the commercially acquired ZnO nanopowder due to their size, morphology, and crystallinity [9].

The gain in the intensity of the LZH peaks becomes significant around 44 seconds, with the overall intensities comparable with the ZnO peaks, suggesting the abundance of both LZH structures and undissolved ZnO nano/microcrystals in the drying droplet and then resulting residue. The bulk liquid peak at $q = 12.7 \pm 1.0$ nm^{-1} disappears after 80 seconds, which indicates the time at which most of the solvent is lost due to evaporation, leaving a fibrous residual pattern on the surface. Also, the rest of the peaks labelled as 3 (7.80 nm^{-1}), 4 (8.98 nm^{-1}), 5 (12.00 nm^{-1}), 6 (14.02 nm^{-1}), and 9 (18.06 nm^{-1}) also become clearly visible after that time. The average interplanar d-spacing calculated from positions of peaks 1, 2, and 4 is equal to 2.76 ± 0.03 nm. In contrast to the in-house ZnO nanofluid dried on glass (**Figure 3**), there are no distinguishable peaks in the diffractogram that could be attributed to the positions of 7 and 8. (The peak numbering is preserved amongst different data sets to be consistent).

The peaks observed at q values around 15.8, 21.0, 28.0 - 32.0 nm^{-1} maintain the same shape and intensity throughout the entire time of the evaporation process, thus they are believed to result from the data processing. Interestingly, the peaks around the (002) LZH peak labelled as 1, termed as "temporary" for the in-house synthesised ZnO nanofluid (**Figure 2** and **Figure 3**), appear at 4.18, 4.69, 4.89, and 5.11 nm^{-1} (labelled with a-d letters, respectively) as early as t = 0 seconds. In addition, these peaks maintain constant shapes and intensities throughout the measurement, with intensities negligible when compared to the first LZH peak at 4.50 nm^{-1}. The changes in the diffraction signal are shown using profiles taken at different evaporation times, 22, 125, and 172 seconds, with insets showing magnified views of the area enclosed by black square boxes in detail (**Figure 6**b-d).

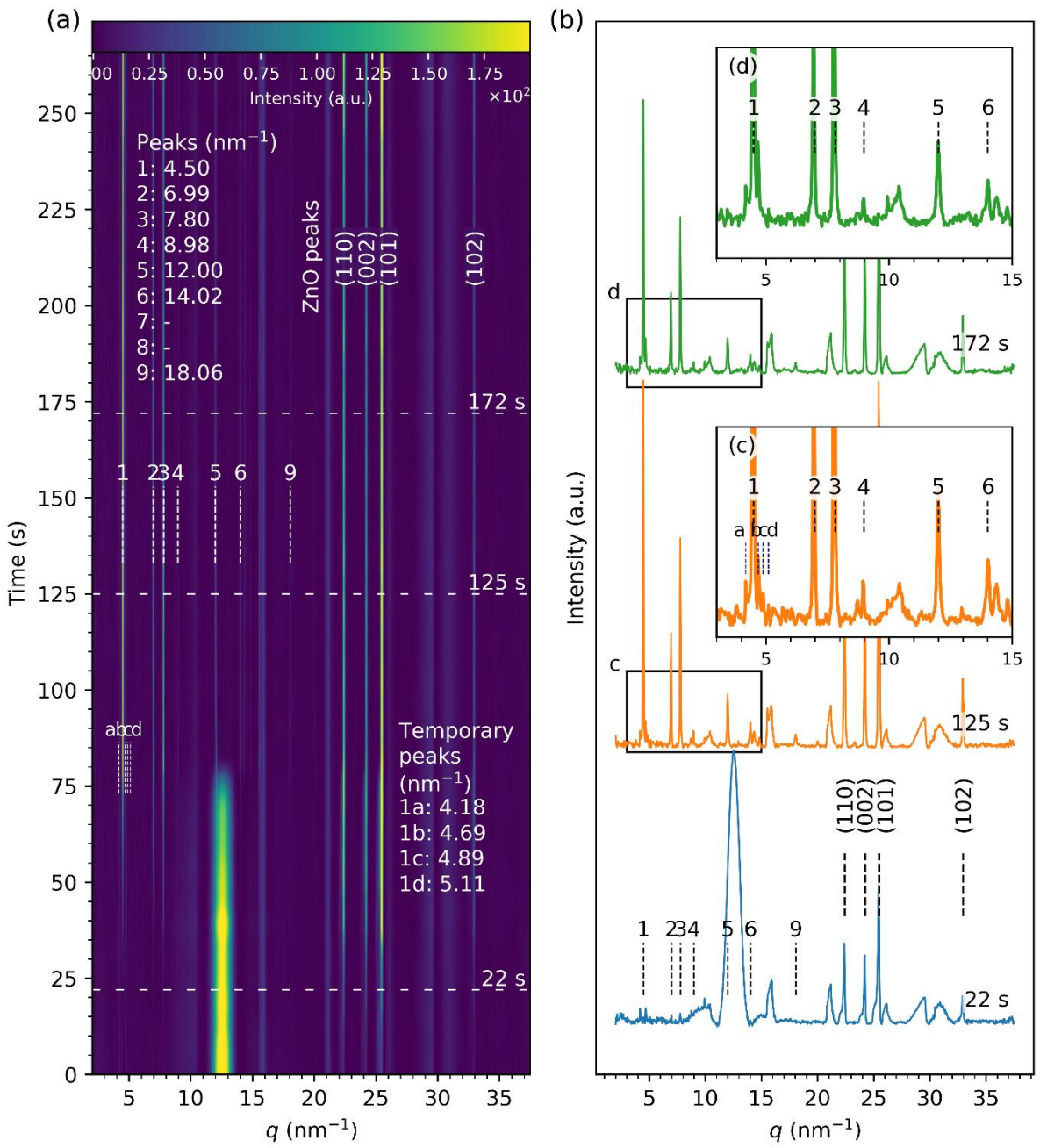

Figure 6. X-ray diffraction data from the ZnO nanopowder nano/microfluid droplet dried on an unmodified silicon substrate: (**a**) Waterfall plot of diffraction line profiles with peaks annotated; (**b**) selected diffraction profiles for different times of the evaporation process; (**c-d**) insets of the data enveloped with black squares and annotated with respective letters.

Figure 7 - **Figure 10** show diffractograms collected for the ZnO nanopowder nano/microfluid evaporated on various substrates, glass, silanised Si, muscovite mica and PTFE. It is visible that diffraction peaks at q = 22.38, 24.21, and 25.45 nm^{-1} appeared in every diffractogram since the start of the evaporation. They are related to (100), (002), and (101) of the crystallographic planes of ZnO (PDF 01-075-0576), and come from the undissolved ZnO nano/microparticles inside of the drying droplet, similarly for the ZnO powder nano/microfluid (**Figure 11** - **Figure 14**). In all of them, besides PTFE, the low q range peaks can be observed, indicating the formation of LZH structures, similar as in **Figure 6**.

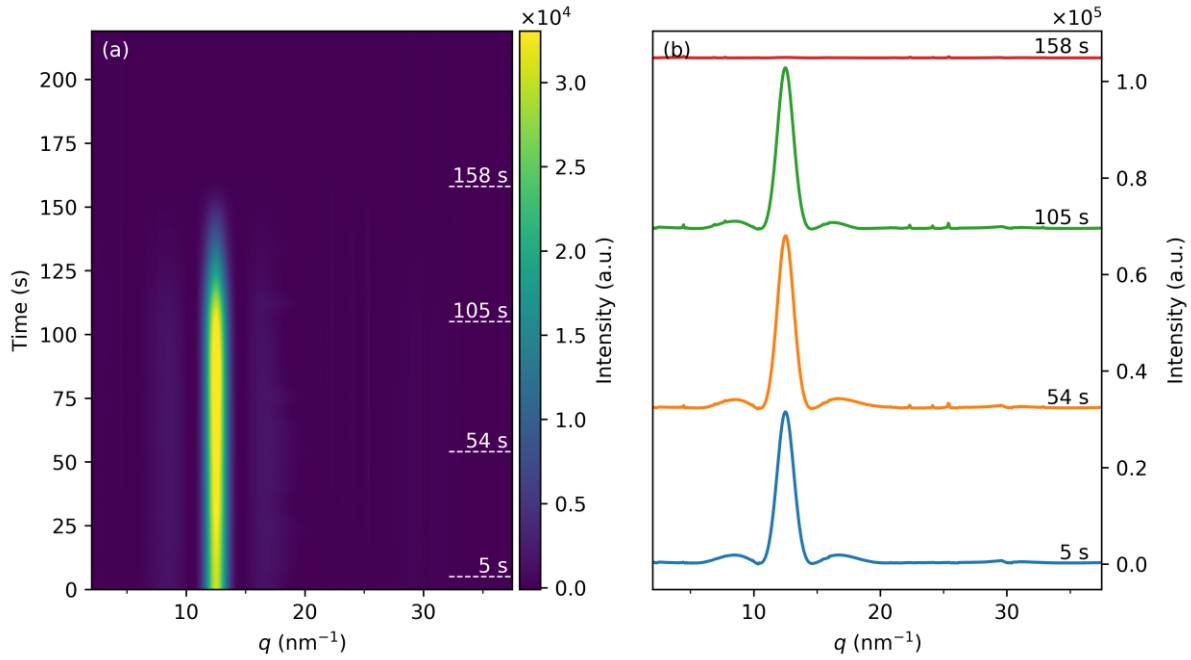

Figure 7. ZnO nanopowder nano/microfluid dried on glass substrate.

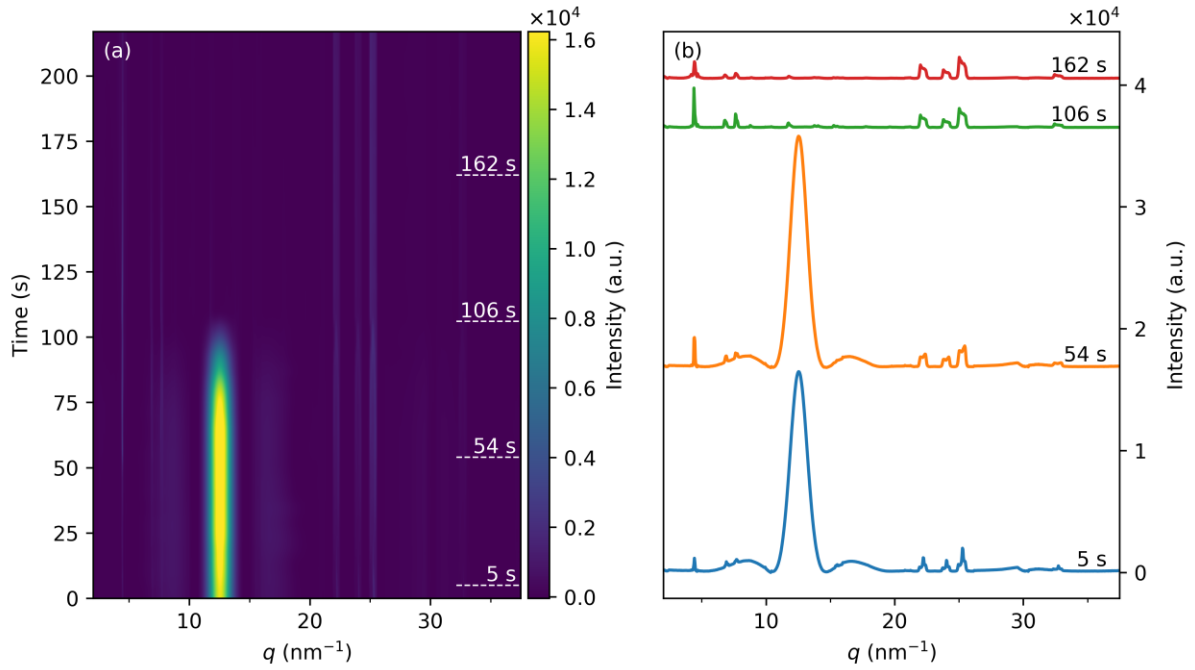

Figure 8. ZnO nanopowder nano/microfluid dried on silanised silicon substrate.

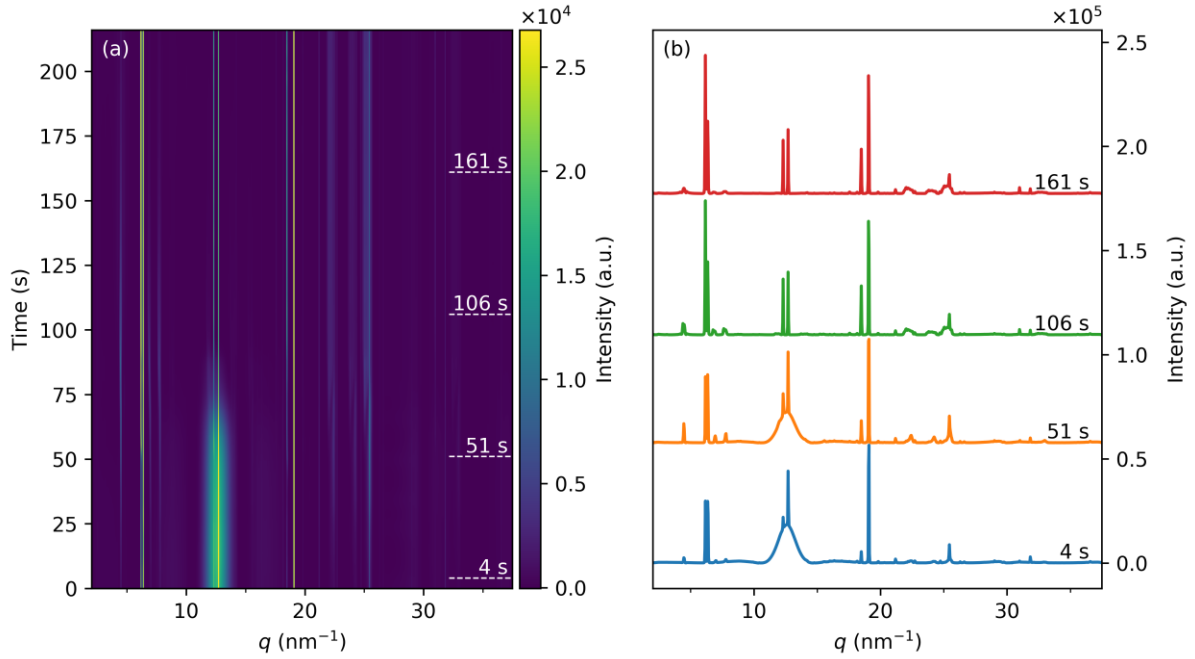

Figure 9. ZnO nanopowder nano/microfluid dried on mica substrate.

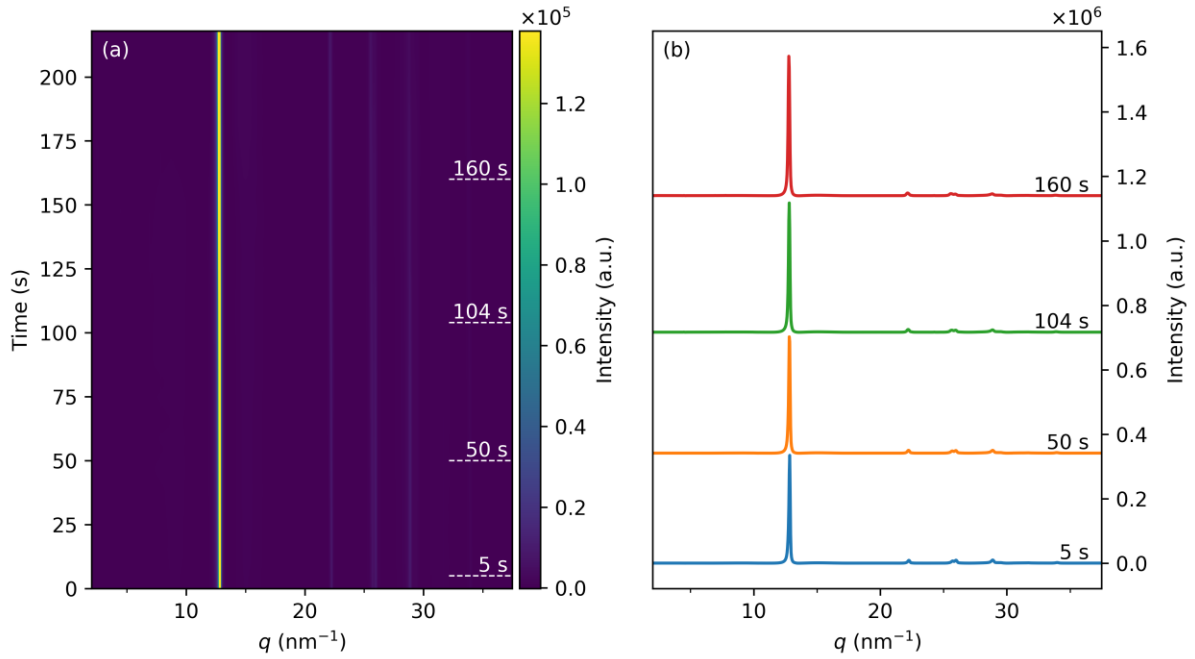

Figure 10. ZnO nanopowder nano/microfluid dried on PTFE substrate.

ZnO powder nano/microfluid

This part describes the *in situ* X-ray diffraction data collected for an evaporating droplets of the ZnO nano/microfluid composed of the commercially acquired ZnO powder (68.3% of crystals between 61 - 291, see SI.01). **Figure 11** shows result collected for the ZnO powder nano/microfluid dried on a glass substrate. Similarly to the ZnO nanopowder nano/microfluid, strong diffraction peaks resulting from ZnO crystals appear at 22.36, 24.21, 25.45, and 32.94 nm^{-1}, indexed respectively as (110), (002), (101), and (102), and are present right at the start of the evaporation process at $t = 0$ seconds. Their intensity becomes stronger after *ca* 25 seconds and fully intensifies after 75 seconds, which coincides with the droplet thinning due to evaporation. The bulk liquid peak at $q = 12.7 \pm 1.0$ nm^{-1} is visible for first 125 seconds. A set of three low intensity peaks attributed to LZH structures labelled as 1 (4.50 nm^{-1}), 2 (6.88 nm^{-1}), and 3 (7.77 nm^{-1}) with the first two indexed as (002) and (003) start emerging at $t = 27$ seconds, however their intensity is a fraction of that for ZnO peaks (**Figure 11**b). This agrees with the slower dissolution rate of the commercially acquired ZnO powder particles due to their size, morphology, and crystallinity [9].

As the drying progresses, other peaks labelled as 4 (8.98 nm^{-1}), 5 (11.89 nm^{-1}), 6 (13.95 nm^{-1}), 7 (15.51 nm^{-1}), and 9 (18.06 nm^{-1}) become more visible in the diffractogram and the intensity of the

peaks labelled as 1 - 3 becomes comparable to that of ZnO (**Figure 11c**), indicating strong presence of both type of structures: layered for zinc hydroxides and wurtzite for ZnO. The average interplanar *d*-spacing calculated from positions of the peaks labelled as 1 (4.50 nm^{-1}), 2 (6.88 nm^{-1}), and 4 (8.98 nm^{-1}) is equal to 2.78 ± 0.02 nm.

The "temporary" peaks around the position 1, labelled with letters a - d, show at 4.11, 4.68, 5.21, and 5.44 nm^{-1}, respectively. The intensity of these peaks varies throughout the process, apart from the 1a peak, which stays relatively unchanged. Peaks 1c-d gradually increase in the intensity until the droplet dries at around 125 seconds (**Figure 11c**), then shortly become negligible when compared to the rest of the diffraction signal (**Figure 11d**). In addition, the 1b peak becomes slightly stronger than the 1 peak (4.50 nm^{-1}) after 175 seconds of the measurement, which loses a significant amount of the intensity at that point, especially when compared to the ZnO peaks, most likely due to the sample beam damage. It is later shown by a lateral scan of the substrate (octagonal to the beam direction), that the LZH peaks were on average comparable with these of ZnO (**Figure 17**).

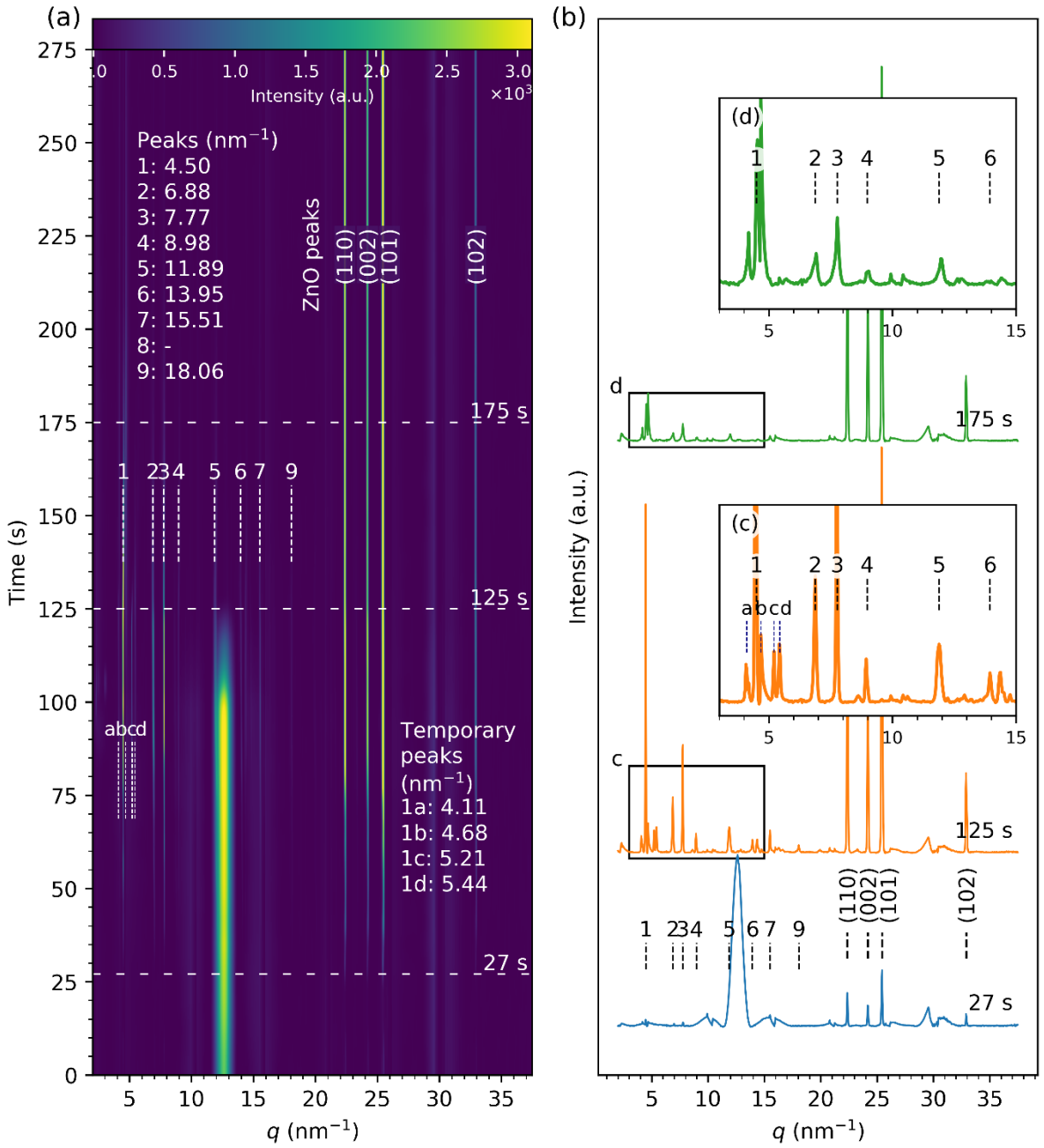

Figure 11. X-ray diffraction data for the ZnO powder nano/microfluid dried on a glass substrate: (**a**) Waterfall plot of integrated diffraction line profiles with fitted peaks annotated; (**b**) selected diffraction profiles measured at different times of the evaporation process; (**c-d**) insets of the data enveloped with black squares and annotated with respective letters.

Figure 12 - Figure 14 show diffractograms collected for the ZnO powder nano/microfluid evaporated on an unmodified silicon, silanised silicon, and mica. The diffraction peaks at q = 22.38, 24.21, and 25.45 nm^{-1} appear in every diffractogram since the start of the evaporation and are attributed

to the (100), (002), and (101) of the crystallographic planes of ZnO (PDF 01-075-0576). The low *q* range peaks can be observed in all the diffractograms, indicating the formation of LZH structures, similarly to **Figure 11**.

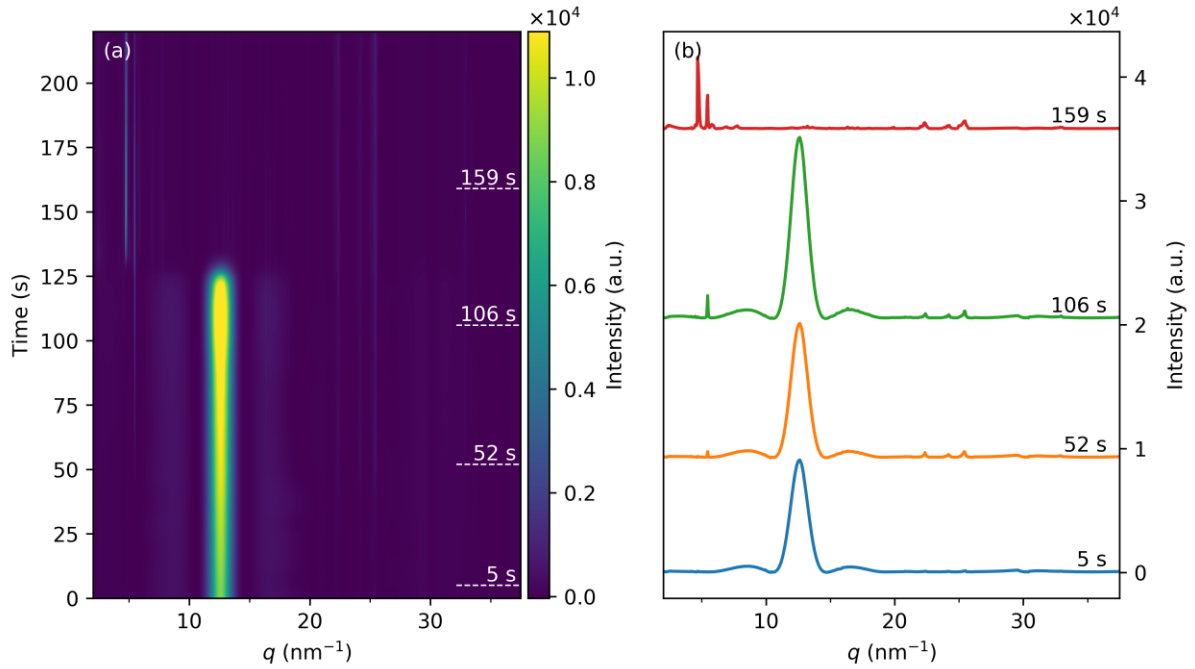

Figure 12. ZnO powder nano/microfluid dried on an unmodified silicon substrate.

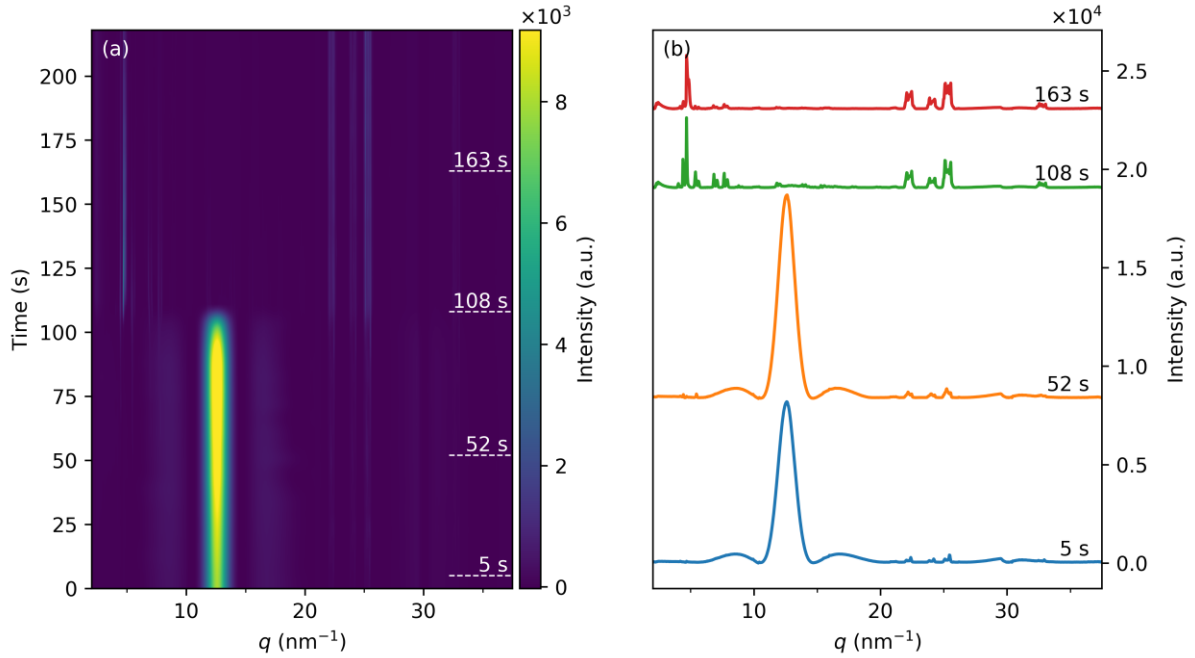

Figure 13. ZnO powder nano/microfluid dried on silanised silicon substrate.

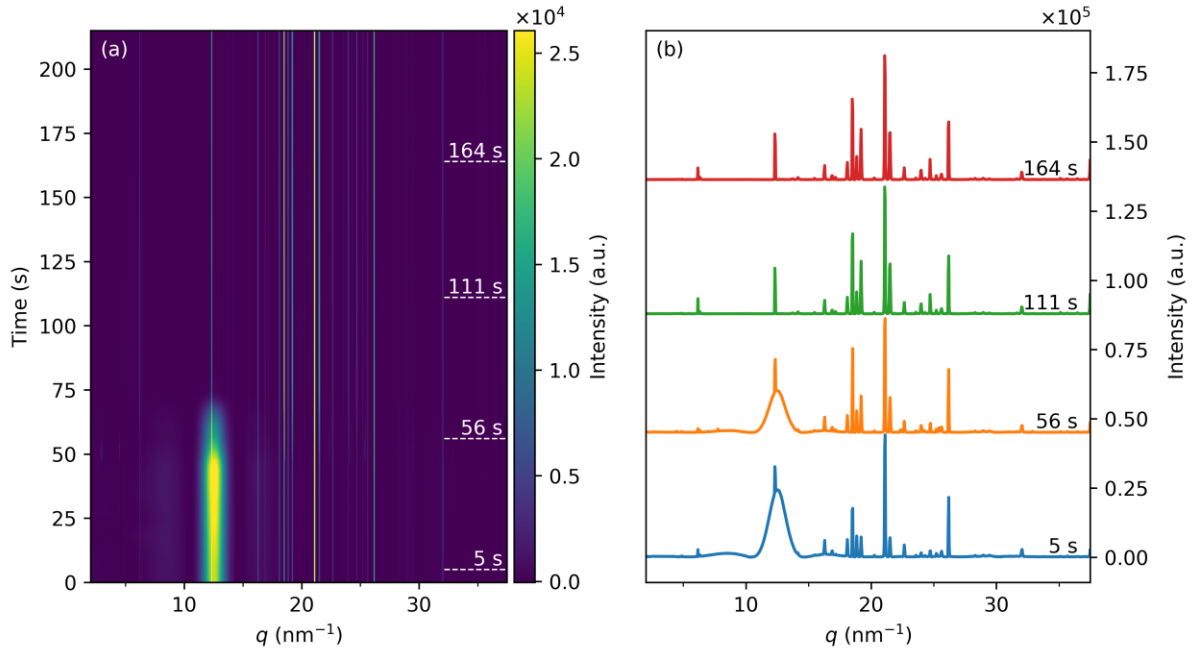

Figure 14. ZnO powder nano/microfluid fried on mica substrate.

CuO nanotubes nanofluid

The structure and morphology of the fibrous residual surface patterns produced from evaporation of reactive ZnO nanofluids are very similar to those of zinc hydroxide nanostrands synthesised from aqueous solution of zinc salts [21-22]. Intriguingly, other types of nanostrands formed from various hydroxides, including copper, have been reported in the course of similar synthesis methods [23-25]. This provided a solid ground for a presumption that it would be possible to produce fibrous residuals from a reactive CuO nanofluid. To investigate this possibility, *in situ* grazing incidence X-ray diffraction measurements were performed on a nanofluid droplet produced from a commercially acquired CuO nanopowder (*cf.* SI.01) dried on an unmodified silicon substrate, especially that the formation of fibrous residues from a CuO nanofluid was later confirmed by scanning electron microscopy studies (*cf.* **Figure 2f** in Chapter 6).

Figure 15 presents the X-ray diffraction data collected during the evaporation of a CuO nanofluid droplet from a silicon substrate. As in the evaporation of ZnO nano/microfluids, weak diffraction peaks emerge in the low q region at the early stage of the drying process (within 11 seconds), suggesting a rapid formation of layered hydroxide structures in the drying CuO nanofluid droplet. These peaks,

labelled as 1 - 3, are located at q equal to 4.42, 6.88, and 7.73 nm^{-1}, respectively. With the elapsing time, peaks labelled as 4 - 7 (q = 8.92, 11.83, 13.86, and 15.40 nm^{-1}, respectively) start appearing in the diffractogram, which is particularly visible after 133 seconds when the bulk liquid peak ($q = 12.7 \pm 1.0$ nm^{-1}) disappears completely, marking the time when the most of the liquid is lost due to evaporation.

It is suggested that the peaks labelled as 1, 2, and 4 (q = 4.42, 6.88, and 8.92 nm^{-1}, respectively) could be attributed to the respective (00*l*) planes of the layered structure, *i.e.* (002), (003), and (004), indicating the average interplanar d-spacing of 2.80 ± 0.02 nm [26]. It is also likely that the peaks labelled as 3 (7.73 nm^{-1}) and 7 (15.40 nm^{-1}) could relate to different orders of the same set of planes due to the equal distance between their positions. The "temporary" peaks labelled as 1a (4.11 nm^{-1}) and 1b (5.19 nm^{-1}) start to emerge at the later stage of the drying process (t = 94 seconds) and disappear after 133 seconds, together with the bulk liquid peak.

Strong diffraction peaks, which positions and relative intensities match well with the X-ray diffraction standard for copper(II) oxide (PDF number: 01-073-6023 45-937), appear immediately in the scattering signal confirming the presence of CuO nanoparticles in the drying droplet and remain there for long after the evaporation is completed, suggesting that a large number of CuO nanocrystals persists undissolved within the residual surface patterns. This has also been reported for the ZnO nano/microfluids prepared from the commercially acquired ZnO nanopowder and ZnO powder (**Figure 6** - **Figure 11**) [9]. The CuO diffraction peak at 22.71 nm^{-1} corresponds to (110) and (1-10) planes, 24.77 nm^{-1} (position of two very close peaks) to (002), (11-1), and (1-1-1) planes, 26.94 nm^{-1} (again, position of two very close peaks) to (1-11), (111), and (200) planes, 31.84 nm^{-1} to (11-2) and (1-1-2) planes, 33.54 nm^{-1} to (20-2) plane, and 36.50 nm^{-1} to (112) and (1-12) planes.

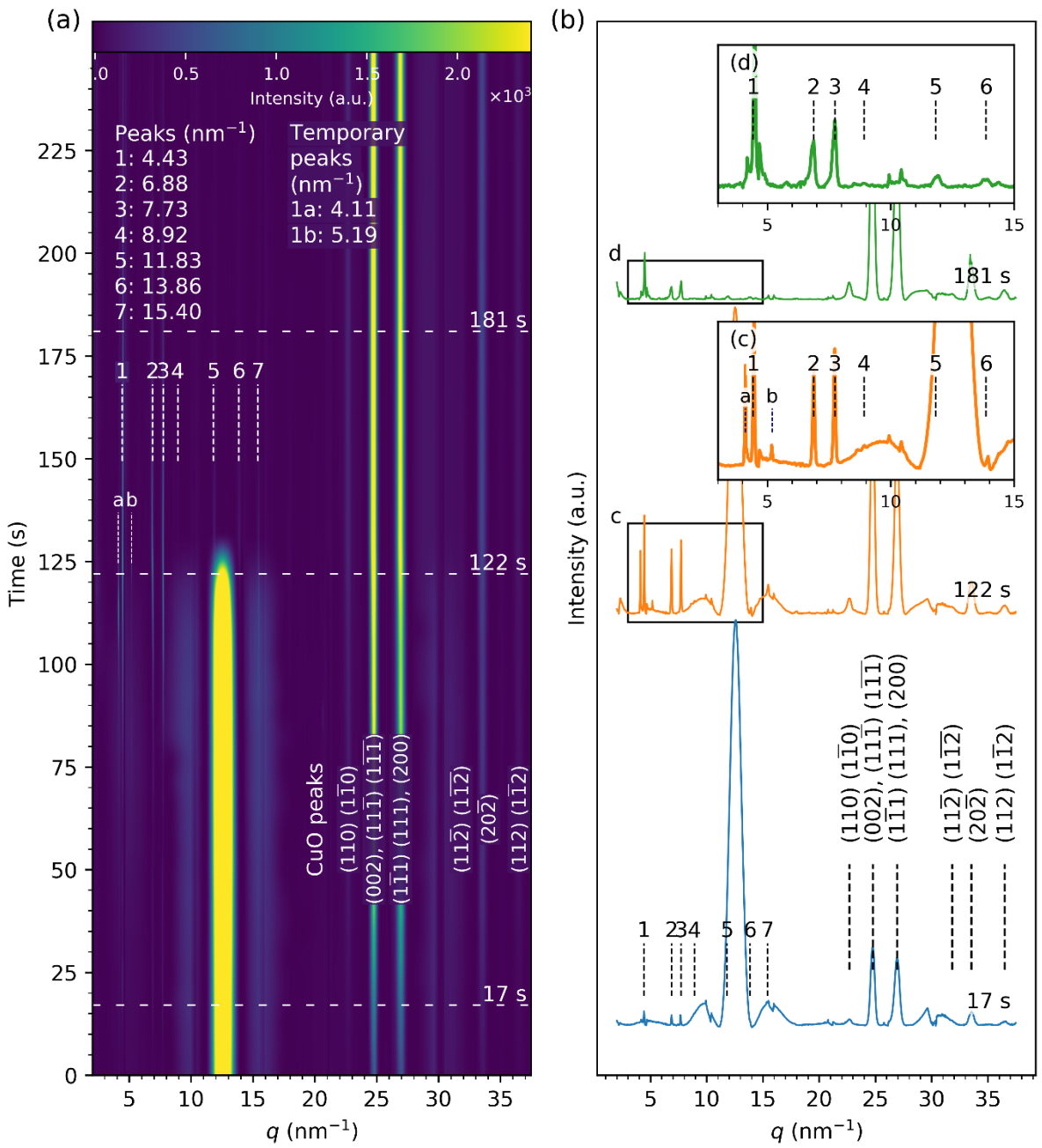

Figure 15. X-ray diffraction data for the CuO nanofluid dried on a silicon substrate: (**a**) Stacked diffraction profiles showing the changes in the scattering pattern with time, (**b**) selected profiles taken at different times of the evaporation (17, 122, and 181 seconds), and (**c-d**) insets showing two profiles in detail at the low *q* range.

ZnO nanostructured glass surface

A droplet of the cyclohexane and isobutylamine mixture was dried from the top of a glass substrate covered with randomly oriented ZnO nanorods grown on it previously. Unfortunately, the

transformation of the ZnO nanorods fixed to the substrate into the layered zinc hydroxide structures during the evaporation, similar to that observed for reactive ZnO nanofluids discussed above, cannot be observed in the grazing incident X-ray diffraction data taken for that system during the experiment performed at Diamond Light Source (**Figure 16**). This is unexpected, as the formation of fibrous structures composed of zinc hydroxides from reactive ZnO surfaces has been previously observed (Wąsik *et al.*, in preparation) and is supported by the scanning electron microscopy results shown in **Figure 1** in Chapter 6. The only visible diffraction patterns in **Figure 16** are ZnO peaks located at 22.11, 23.74, 24.99, and 32.26 nm^{-1}, confirming the presence of the ZnO nanorods on the substrate.

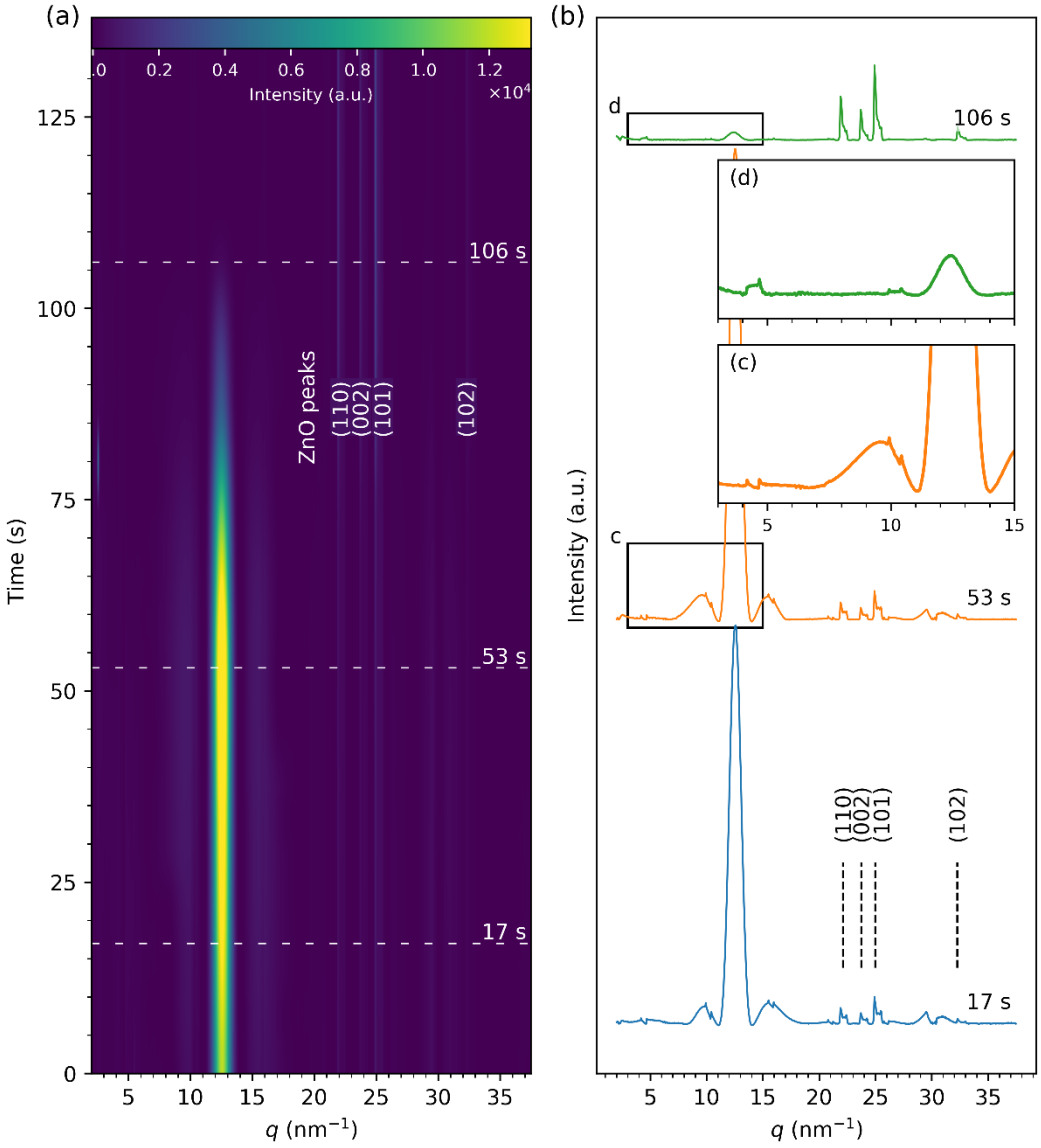

Figure 16. Droplet of a cyclohexane and isobutylamine mixture evaporated from a glass substrate with randomly oriented ZnO nanorods grown on top: (**a**) stacked grazing incidence X-ray diffraction profiles

showing the changes in the scattering intensity with time, (**b**) selected profiles at times 17, 53, and 106 seconds of the evaporation, and (**c**-**d**) insets showing two profiles in detail at the low *q* range.

Thermal annealing

Annealing is a heat treatment process in which the material is heated to a desired temperature for a specific time, followed by a controlled cooling. It is often used as a conventional and effective way to modify intrinsic defects and improve crystallinity of ZnO thin films for structural defect studies [27] or in a ZnO nanostructure-based device optimisation [28]. In addition, it has been widely employed in the synthesis of ZnO nanostructures where the thermal decomposition of zinc salts is used to form seeds for further crystal growth [29-31].

Wu *et al.* have previously reported that it is possible to transform the fibrous residual pattern composed of zinc hydroxide crystals, formed from evaporation of a ZnO nanofluid droplet, into a three-dimensional porous network made of zinc oxide nanocrystals by thermal treatment [8] (see also Chapter 1, pages 21 -22). They have also shown that the pore size depends on temperature, as samples annealed at 100 and 250 °C consisted of ZnO nanocrystals of 4 - 7 nm in size whereas those annealed at 550 °C consisted of ZnO nanocrystals of 20 - 70 nm in size. The authors have suggested that elevated temperature causes creation of pores between the nanocrystals by the evaporation of isobutylamine and water molecules and then rearrangement and realignment of the nanocrystals, with smaller ZnO nanocrystals being sintered into larger ones.

To observe the structural changes in the residual surface patterns formed from evaporation of reactive ZnO and CuO nano/microfluids during a thermal treatment, a series of *in situ* grazing incidence X-ray diffraction measurements were performed on the residues at different temperatures. After a droplet of nano/microfluid dried, leaving a residual pattern behind, the sample was scanned laterally to collect diffraction signal at different points across the residue. The lateral scan was repeated at every temperature step that the sample was heated to and annealed at, with the results for the ZnO powder and CuO nanoparticles nano/microfluids described below.

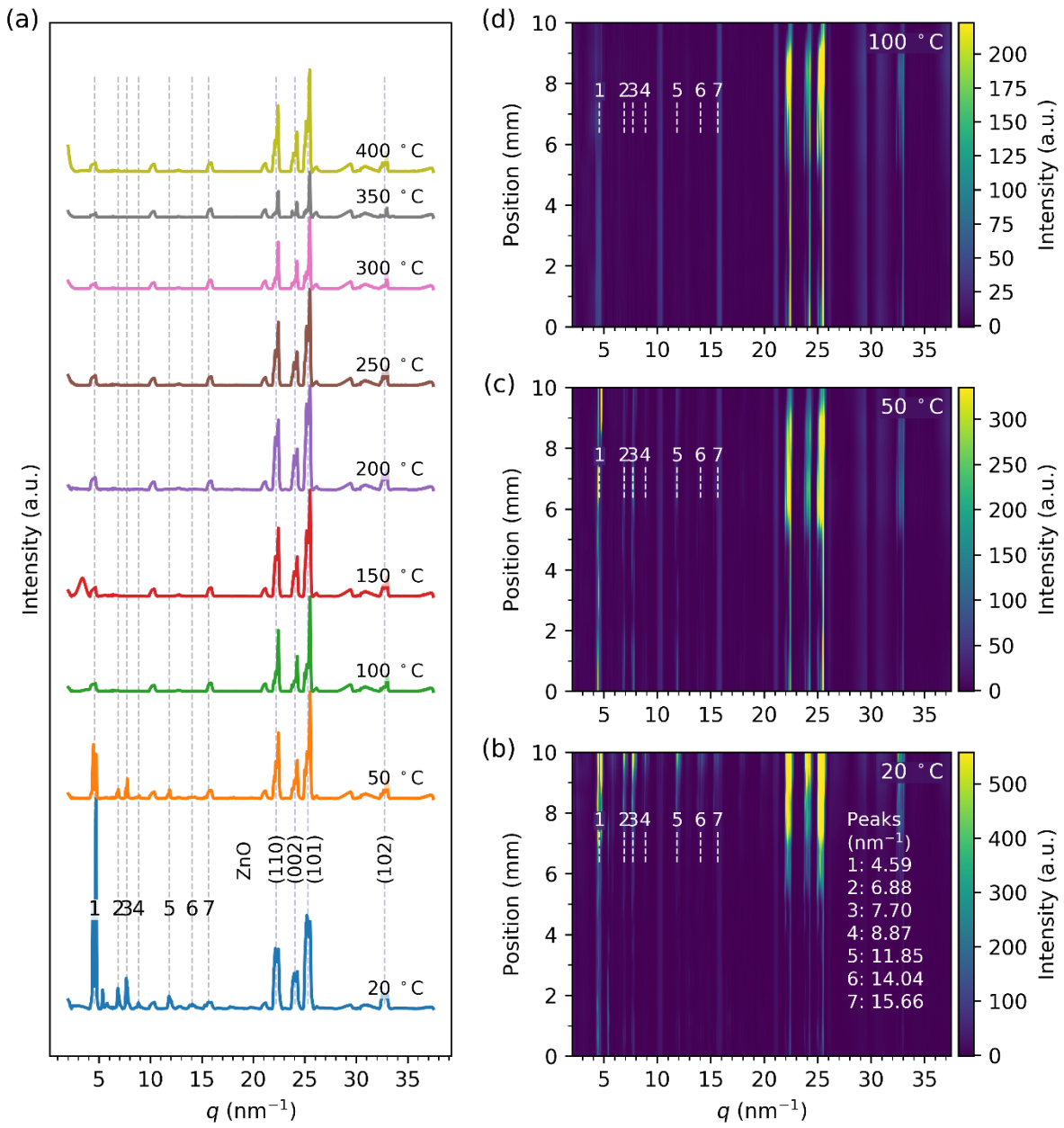

Figure 17. The effect of the annealing temperature on the residual surface pattern produced from the ZnO powder nano/microfluid on a silanised silicon substrate: (**a**) Diffraction profiles averaged over different positions measured during lateral scans across the substrate at different temperatures; (**b-c**) diffraction profiles taken at different sample positions (lateral scan) at a specific temperature. Dashed vertical lines mark peak positions calculated for the averaged diffraction profile taken at room temperature (20 °C) related to the layered zinc hydroxide structures (1 - 7) and zinc oxide crystals (plane indices).

Figure 17 presents the grazing incidence X-ray diffraction results on the effect of the annealing temperature on the residual surface pattern produced from the ZnO powder nano/microfluid on a silanised silicon substrate. The diffraction profiles for different temperatures shown in **Figure 17a** are produced by averaging the diffraction data collected across the substrate. The diffraction signal, recorded at different temperatures: 20 (room temperature), 50, and 100 °C, with respect to the position across the sample is presented in **Figure 17b-d**. Vertical dashed lines mark peak positions calculated for the averaged diffraction profile taken at 20 °C. The peaks labelled as 1 - 7 and located at q equal to 4.59, 6.88, 7.70, 8.87, 11.85, 14.03, and 15.66 nm^{-1}, respectively, are thought to be related to the layered zinc hydroxide structures. The peaks labelled as 1, 2, and 4 are likely to be attributed to (002), (003), and (004) LZH basal planes and give the average d-spacing of 2.77 ± 0.03 nm. The peaks resulting from the ZnO wurtzite structure related to (110), (002), (101), and (102) planes are located around 22.18, 24.03, 25.31, and 32.75 nm^{-1}, respectively.

The intensity of the 1 - 7 peaks reduces between 20 and 50 °C and then completely diminishes between 50 and 100 °C temperature steps. This indicates that the temperature transition between the layered zinc hydroxide and wurtzite zinc oxide structures happens between 20 - 50 °C and can be completed below 100 °C, at least to the point where there are no ordered LZH structures to diffract X-rays (**Figure 17d**). The ZnO peaks appear as the only diffraction signal throughout the entire temperature range of 20 - 400 °C. This is not counting the integration artefacts due to the conversation of detector pixels into the reciprocal space, seen as peaks of the same shape and intensity in **Figure 17a**, or uniform lines along the same sample position in **Figure 17b-d**, around q values of 4.4, 10.2, 15.8, 21.0, 26.0, 29.0, and 31.0 nm^{-1}, discussed to some extend SI.03. However, it should be noted that in some instances the artefact peaks can coincide with real diffraction peaks. Based on the lateral scans presented in **Figure 17b-d**, some areas of the sample (5 - 10 mm) scatter more strongly than others (0 - 5 mm). This could be related to a nonuniform deposition of the material across the substrate, slight misalignment between the two ends of the sample, or both. However, both diffraction signals related to the LZH and ZnO structures are present somewhat homogeneously across the substrate when considering the diffractograms at 20 and 50 °C.

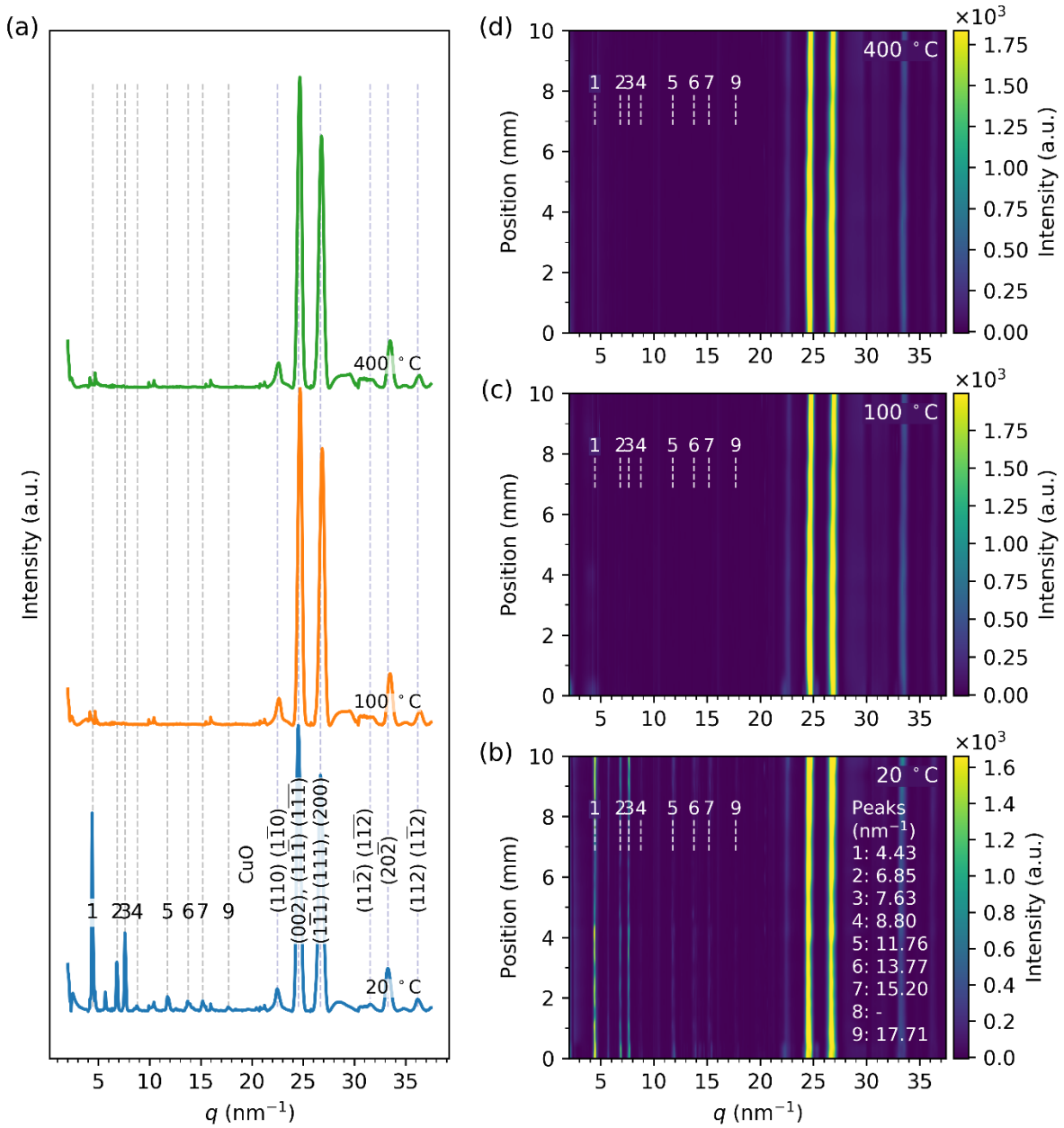

Figure 18. The effect of the annealing temperature on the residual surface pattern produced from the CuO nanopowder nanofluid on a silicon substrate: (**a**) Diffraction profiles averaged over different positions measured during a lateral scans across the substrate at different temperatures; (**b-c**) diffraction profiles taken at different sample positions (lateral scan) at a specific temperature. Dashed vertical lines mark peak positions calculated for the averaged diffraction profile taken at room temperature (20 °C) related to the layered copper hydroxide structures (1 - 9) and copper(II) oxide crystals (plane indices). The drying process leading to the formation of the residual examined here is shown in **Figure 15**.

The effect of the thermal annealing was also investigated on the residual surface pattern produced from the CuO nanopowder dispersion on a silicon substrate, formed as a result of the evaporation process shown in **Figure 15**. However, in contrast to the previous residual pattern prepared from the ZnO powder nano/microfluid, the sample was measured only at three different temperatures, *i.e.* 20, 100, and 400 °C. The grazing incidence X-ray diffraction results for the residual pattern on a silicon substrate are presented in **Figure 18**. The diffraction profile taken at 20 °C is characterised by a series of peaks, postulated to be associated with the layered copper hydroxide (LCH) structures, with positions at 4.43, 6.85, 7.63, 8.80, 11.76, 13.77, 15.20, and 17.71 nm^{-1}, and labelled as 1 - 7, and 9, respectively. It is likely that peaks 1, 2, and 4 can be attributed to different diffraction orders of the (00*l*) planes, that is (002), (003), and (004), respectively, yielding the average *d*-spacing of 2.82 ± 0.03 nm [26]. This agrees with the interplanar *d*-spacing of 2.80 ± 0.03 nm calculated from the evaporation scan on non-position averaged diffraction profile (**Figure 15**).

The 1 - 9 peaks disappear completely from the diffractogram produced by the sample heated to 100 °C, suggesting that the postulated thermal conversion of layered copper hydroxide into copper(II) oxide structures can occur completely between room temperature and 100 °C. This is also supported by the fact that there are no other diffraction peaks than those related to CuO at 100 and 400 °C. The copper(II) oxide diffraction peaks, based on the position averaged diffractogram taken at 20 °C, at *q* values equal to 22.50, 24.56 (two closely positioned peaks), 26.69 (again, two very close peaks), 31.55, 33.29, and 36.17 nm^{-1} are well matched with the CuO powder diffraction standards (PDF number: 01-073-6023 45-937) and [32]. A uniform distribution of diffraction signal across the substrate for both the layered copper hydroxide (**Figure 18b)** and CuO structures (**Figure 18b-d** can be observed, suggesting an even coverage of the substrate by the residual pattern.

Discussion

In this work we have used the *in-situ* grazing incidence X-ray diffraction measurements to follow the temporal structural changes during a novel evaporation-induced self-assembly process, in which *reactive* ZnO nanofluids are used to produce hierarchical surface patterns in a mechanism very different from that associated with the coffee ring effect [7-9]. When a reactive ZnO nanofluid sessile drop dries

on a solid substrate, the ZnO nanocrystals undergo spontaneous chemical and morphological transformation leading to the formation of fibrous and dendric networks made of zinc hydroxide structures covering the surface. The goal of this investigation was to probe the structural evolution of the surface pattern as it is formed when the droplet of a reactive nanofluid is drying, in contrast to the previous work which focused on the analysis of the residues performed after the evaporation process was completed [9-11].

The evaporative drying experiments were performed using reactive nano/microfluids prepared from the in-house synthesised ZnO nanoparticles and commercially acquired particles such as ZnO nanopowder, ZnO powder, and CuO nanoparticles. The *in-situ* grazing incidence X-ray diffraction data was collected for each nano/microfluid evaporated on various substrates including glass, silicon, silanised silicon, mica, and polytetrafluoroethylene. In addition, a droplet of a pure solvent mixture without the addition of any reactive particles was evaporated from a ZnO nanostructured surface, which had ZnO nanorods grown on top of it prior to the experiment.

In every ZnO nano/microfluid investigated (**Figure 2** - **Figure 14**), a series of peaks emerge in the diffraction signal in due course of the evaporation process. Not considering the diffraction peaks coming from the respective particles used in the ZnO nano/microfluid preparation, the strongest peaks appear in the lower q region below 10 nm^{-1} and other, less intense peaks between q of 10 - 20 nm^{-1}. These peaks preserve the similar position, shape, and relative intensity across investigated diffractograms, and therefore are considered as resulting from the same type of a structure present within the drying droplet or formed residue (and are labelled with respective numbers). Thus, the preserved peak labelling is consistent amongst different data sets for easier referral or comparison.

For the ZnO nano/microfluids related diffractograms (**Figure 2** - **Figure 6**, and **Figure 11**), the distinct peaks labelled with numbers are located on average as follows: 1 (4.49 nm^{-1}), 2 (6.92 nm^{-1}), 3 (7.76 nm^{-1}), 4 (8.93 nm^{-1}), 5 (11.91 nm^{-1}), 6 (13.94 nm^{-1}), 7 (15.48 nm^{-1}), 8 (16.50 nm^{-1}), and 9 (18.03 nm^{-1}). There are likely more peaks in the scattering signal, and some peaks may be in fact a convolution of more. Therefore, any further analysis of the data does not have to be limited to the peaks selected for the analysis in this work. It is postulated that this series of nine peaks is associated with the layered zinc hydroxide (LZH) structures forming inside of a drying ZnO nano/microfluid

droplet. Based on the previous works, it is suggested that peaks labelled as 1, 2, and 4 result from stacked (00*l*) planes of the layered structure composed of complex positively charged zinc hydroxide layers and interlayer anionic species, indexed as (002), (003), and (004), respectively [9, 18-20, 33]. The average interplanar *d*-spacing calculated for the in-house ZnO nanofluid, based on the positions of the peaks labelled as 1, 2, and 4, dried on glass (**Figure 3**) is $d = 2.79 \pm 0.02$ nm^{-1}, silicon (**Figure 4**) is $d = 2.77 \pm 0.02$ nm^{-1}, and silanised silicon (**Figure 5**) is $d = 2.80 \pm 0.03$ nm^{-1}. In addition, the values of the interplanar *d*-spacing calculated for the ZnO nanofluids made of commercially acquired powders are very similar, $d = 2.76 \pm 0.03$ nm^{-1} for the ZnO nanopowder nano/microfluid dried on silicon (**Figure 6**) and 2.78 ± 0.02 nm^{-1} for the ZnO powder nano/microfluid dried on glass substrate (**Figure 11**). This suggest that similar structures of layered zinc hydroxides are formed regardless of the ZnO particles type used for the preparation ZnO nano/microfluids.

Interestingly, the time when these low *q* peaks labelled as 1 - 4 emerge during the evaporation process, suggesting the immediate formation of LZH structures, is different with respect to the type of particles the ZnO nano/microfluids are prepared from. For the in-house ZnO nanofluids, these peaks emerge as early as a droplet is cast on the substrate (**Figure 2** - **Figure 3**, and **Figure 5**). However, for the ZnO nanopowder and ZnO powder dispersions it takes much longer, which is around 30 seconds for both the ZnO nanopowder dispersion dried on an unmodified silicon substrate (**Figure 6**) and the ZnO powder dispersion dried on glass (**Figure 11**). This is in agreement with the slower dissolution rates attributed to the commercially acquired ZnO nanopowder and ZnO powder, discussed in detail in Ref. [9] and Chapter 2.

It is possible that the peaks labelled as 3 and 7, positioned around averaged positions of 7.76 and 15.48 nm^{-1}, respectively, may result from other stacked crystallographic planes due to their equal spacing in the diffractogram. In addition, the averaged position of the peak labelled as 9 (18.03 nm^{-1}) suggests that it may result from the higher order diffraction from the (00*l*) planes, *i.e.* (008). On the other hand, one can argue that the relative peak spacing suggests the following pairs as suitable candidates for the different order diffraction patterns from stacked sets of planes: 1 (4.49 nm^{-1}) and 4 (8.93 nm^{-1}), and then 2 (6.92 nm^{-1}) and 6 (13.94 nm^{-1}). Nevertheless, it is noted that the peak indexing

needs further and more in-depth crystallographic analysis, which should be a scope of any future work in this area.

Surprisingly, a series of additional diffraction peaks located in the proximity of the main LZH (002) peak, labelled as 1, can be observed throughout the evaporation process of the ZnO nano/microfluid investigated. These peaks are labelled as 1a - 1d, depending on how many of them emerge in the diffractogram; however, the most common are those located at q = 4.11 and 5.21 nm^{-1}. They display a very interesting behaviour during the drying process, as they gradually become more intense with the evaporation progressing. However, they fade away almost immediately after the drying process is finished, marked by the disappearance of the broad bulk liquid peak (12.7 ± 1.0 nm^{-1}), discussed later. These peaks are termed as "temporary", as they appear only during a limited time of the drying process. When these temporary peaks do not change in shape nor intensity throughout the process, they may be related to the data integration artefacts (computational conversation of the real detector pixels into the reciprocal space), as two artefacts can be observed at q values of 4.18 and 4.68 nm^{-1} in a diffractogram of a sample after the heat treatment, where no LZH data is expected (**Figure 17**a). On the other hand, the temporary peaks, 1a (4.15 nm^{-1}) and 1b (5.21 nm^{-1}) become even stronger than the main peak (labelled as 1) for the in-house ZnO nanofluid dried on an unmodified silicon (**Figure 4**), or comparable to it as the temporary 1a (4.12 nm^{-1}) and 1b (5.20 nm^{-1}) peaks for the in-house ZnO nanofluid evaporated from a silanised silicon. For the ZnO powder nano/microfuid dried on glass (**Figure 11**), temporary peaks 1a - d at 4.11, 4.68, 5.21, and 5.44 nm^{-1}, respectively, emerge later in the process and then diminish, with only the 1b peak at 4.68 nm^{-1} contributing significantly to the diffraction data. The origin of the temporary peaks observed during the evaporation of the reactive ZnO nano/microfluids remains uncertain. It is proposed that an intermediate phase formation occurs during the evaporation process, perhaps bilamellar with different distances attributed to the differences in the overlap and/or tilt angles of the organic molecules between the inorganic layers [34-35]. Then, at the end of the drying process, the lubrication provided by the solvent molecules in the residual pattern together with the final solvent removal, proposed earlier by Wu and Briscoe [7], may drive the rearrangement of the layered structures, resulting in the disappearance of the temporary peaks. However, it is noted that further experimental efforts should be directed to explain this phenomenon.

In addition to the sharp peaks in the scattering signal, associated with the layered hydroxide structures or oxide particles used in the nano/microfluid preparation, an intense diffuse peak at $q \approx 12.7 \pm 1.0$ nm^{-1} is observed at the initial stage of every evaporation experiment. This peak is attributed to the short range order interactions in the bulk liquid [17]. Its disappearance from the diffractogram is related to the end of the drying process, when most of the liquid is removed due to evaporation. This peak disappears at different times across the investigated drying conditions, *e.g.* as early as within 50 seconds for the in-house ZnO nanofluid dried on glass (**Figure 3**) , or as late as within 174 seconds for the for the in-house ZnO nanofluid dried on silanised silicon (**Figure 5**). However, it is believed that this time difference is likely to be related to the amount of a nano/microfluid being cast successfully on the substrate. The previous experiments were performed with 30 μL drops on 10×10 mm^2 substrates using a Gilson pipette to carefully dispense a ZnO nano/microfluid droplet [9-11]. Here, however, the casting step had to be automated and performed from a height of a few centimetres due to the constrains of the synchrotron radiation source experiment. A volume of 60 μL was used, therefore the amount of the ZnO nano/microfluid deposited on the substrate may have slightly varied.

The previous studies performed on the hierarchical surface patterns produced from reactive ZnO nanofluids revealed that the micromorphology of the residue was dependent on the substrate used. This was manifested in the shape of the dendritic structures [7-8] and the size distribution together with the fractal properties of the solidified Bénard-Marangoni cells formed on the substrate [10-11]. In this work, we investigated the following substrates including glass, silicon, silanised silicon, muscovite mica, and polytetrafluoroethylene. The detailed analysis of the diffractograms obtained for the in-house ZnO nanofluid dried on glass (**Figure 3**), unmodified silicon (**Figure 4**), and silanised silicon (**Figure 5**), the ZnO nanopowder nano/microfluid on an unmodified silicon substrate (**Figure 6**), and ZnO powder on glass (**Figure 11**), shows that the resulting residual surface patterns are composed of zinc hydroxide layers with the mostly uniform crystal structure, especially that the values of the interplanar *d*-spacing calculated for these structures do not vary significantly (variance = 2.07×10^{-4}, standard deviation $\sigma = 1.44 \times 10^{-2}$, which is ≈ 0.5% of the average *d* value of 2.78 ± 0.01 nm). The qualitative examination of the diffraction data presented for the ZnO nano/microfluids prepared from the commercially acquired

ZnO nanopowder and ZnO powder evaporated from the remaining substrates (**Figure 7 - Figure 9**, **Figure 12 - Figure 14**) besides the polytetrafluoroethylene (**Figure 10**), suggest that the observed peaks in the low *q* region would produce similar values of the interplanar *d*-spacing to these quoted above. (The measurements for PTFE would need to be repeated in the future as there is no indication that the droplet of the ZnO nanopowder dispersion remained on the substrate, manifested by the absence of the bulk liquid peak at 12.7 ± 1.0 nm^{-1}.) It is suggested that the choice of the substrate does not affect the nanoscale properties such as the crystal structure of the residual patterns formed from reactive ZnO nano/microfluids as it does to their macroscopic morphologies specified in the previous work [7-8, 10-11]. However, it is noted that the rest of the diffraction data would need to be fully analysed to further support this claim.

To investigate the promising possibility of using copper(II) oxide nanoparticles in the production of hierarchal residual surface patterns in a process similar to this observed for ZnO nanofluids, the *in situ* grazing incidence X-ray diffraction measurements were performed on a CuO nanopowder nanofluid droplet dried on an unmodified silicon substrate (**Figure 15**). A series of peaks positioned similarly to those in the ZnO nano/microfluid diffractograms are observed: 1 (4.42 nm^{-1}), 2 (6.88 nm^{-1}), 3 (7.73 nm^{-1}), 4 (8.92 nm^{-1}), 5 (11.83 nm^{-1}), 6 (13.86 nm^{-1}), and 7 (15.40 nm^{-1}). It is suggested that the peaks 1, 2 and 4 can be attributed to the respective (00*l*) planes of the copper layered structure, *i.e.* (002), (003), and (004) [26]. The average interplanar *d*-spacing calculated from these peaks is equal to 2.80 ± 0.02 nm, which is very similar to those calculated for the layered zinc oxide structures of the average $d = 2.78 \pm 0.01$ nm. This striking observation suggests that the CuO nanocrystals undergo the same chemical and morphological transformation into the layered hydroxide structures that was previously thought to be reserved only to ZnO crystals. In addition, the formation of fibrous residues from a CuO nanofluid was later confirmed by scanning electron microscopy studies (*cf.* **Figure 2f** in Chapter 6).

A drying droplet of a cyclohexane and isobutylamine mixture (without the addition of any reactive particles) was evaporated from a glass surface with the previously grown ZnO nanorods on top of the substrate. Even though the fibrous residuals have been produced from various reactive ZnO nanostructured surfaces and observed in the scanning electron microscopy studies (Wąsik *et al.*, in

preparation, also see **Figure 1** in Chapter 6), we are not able to observe the process in detail (**Figure 16**) as in the *in situ* grazing incident X-ray diffraction data taken for other ZnO and CuO nano/microfluid systems. We believe that it is likely related to the experimental set-up at that time and would like to point out that similar experiments would be worth performing in the future.

The effect of a thermal treatment on the structure of the residual surface patterns produced from the evaporation of reactive ZnO and CuO nano/microfluids droplets was also investigated using the *in situ* grazing incidence X-ray diffraction measurements. The diffractograms related to the ZnO powder nano/microfuid evaporated on a silanised silicon substrate (**Figure 17**) reveal that the temperature transition between the layered zinc hydroxide and wurtzite zinc oxide structures starts to occur between 20 - 50 °C and is completed between 50 - 100 °C, manifested by the disappearance of all low q region peaks related to the LZH structures. Between 100 - 400 °C only the ZnO phase is present. The residual pattern produced from the CuO nanopowder nanofluid on a silicon substrate was investigated only at 20, 100, and 400 °C. When the sample is heated to 100 °C, all peaks related to the layered copper hydroxide structures disappear, leaving only the CuO peaks present in the diffractogram. This also suggest that the structures formed from the CuO nanofluids are similar to those from the ZnO nano/microfluids. To fully investigate the effect of a thermal treatment on the structure of the residual surface pattern, measurements with much lower temperature steps are suggested, however the constant sample realignment to account for the thermal expansion poses additional experimental challenges.

Conclusions

Using the *in situ* grazing incident X-ray diffraction measurements, we were able to track the structural changes occurring in the drying reactive nano/microfluid droplets leading to the formation of hierarchical surface structures. The formation of the layered zinc hydroxide structures characterised by the average interplanar d-spacing of 2.78 ± 0.02 nm was confirmed for the ZnO nano/microfluids prepared from the in-house synthesised ZnO nanoparticles and commercially acquired ZnO nanopowder and ZnO power. In addition, a formation of an intermediate layered phase, perhaps bilamellar with different distances attributed to different overlapping and angles between the organic molecules and inorganic layers, was proposed based on the observation of “temporary” peaks that

appeared only during a limited time of the evaporation process. Strikingly, we also observed the formation of the layered copper hydroxide structures inside of a drying CuO nanofluid droplet, which was previously thought to be reserved only for ZnO nano/microfluids. The averaged interlayer *d*-spacing calculated for the layered zinc oxide structures was 2.80 ± 0.02 nm. In addition, the effect of the thermal treatment on the structure of the residual patterns formed from the ZnO and CuO nano/microfluids was investigated, suggesting that the decomposition of the layered hydroxide structures happens between 50 - 100 °C. We believe that the insights revealed by the *in situ* grazing incident X-ray diffraction studies are unprecedented and may facilitate further discussion relevant to the novel evaporation induced self-assembly process involving reactive nanofluids.

Supporting Information

The Supporting Information (SI) associated with this article can be found, in the online version, at https://doi.org/XXX.

Orc

Patryk Wąsik: 0000-0002-7447-7472

Annela M. Seddon: 0000-0002-5794-8500

Wuge H. Briscoe: 0000-0001-8025-960X

Acknowledgements

P.W. is supported by the UK Engineering and Physical Sciences Research Council (EPSRC) through the Bristol Centre for Functional Nanomaterials (BCFN) (grant no. 1371498). H.W. is supported by a Marie Skłodowska-Curie Individual Fellowship (Project Number 656830). W.H.B. would like to acknowledge funding from the EPSRC (EP/H034862/1 and Building Global Engagement in Research (BGER)), European Cooperation in Science and Technology (CMST COST) Action CM1101 “Colloidal Aspects of Nanoscience for Innovative Processes and Materials”, and Marie Curie Initial Training Network (MCITN) on “Soft, Small, and Smart: Design, Assembly, and Dynamics of Novel Nanoparticles for Novel Industrial Applications” (NanoS3). We acknowledge the Diamond Light Source for provision of synchrotron radiation facilities (Beamline I07).

References

1. Deegan, R. D., Pattern formation in drying drops. *Phys. Rev. E* **2000,** *61* (1), 475-485.

2. Deegan, R. D.; Bakajin, O.; Dupont, T. F.; Huber, G.; Nagel, S. R.; Witten, T. A., Capillary flow as the cause of ring stains from dried liquid drops. *Nature* **1997,** *389* (6653), 827-829.

3. Deegan, R. D.; Bakajin, O.; Dupont, T. F.; Huber, G.; Nagel, S. R.; Witten, T. A., Contact line deposits in an evaporating drop. *Phys. Rev. E* **2000,** *62* (1), 756-765.

4. Lin, Z., *Evaporative Self-assembly of Ordered Complex Structures*. World Scientific: Singapore, 2012.

5. Zhong, X.; Crivoi, A.; Duan, F., Sessile nanofluid droplet drying. *Adv. Colloid Interface Sci.* **2015,** *217*, 13-30.

6. Xu, Z.; Wang, L.; Fang, F.; Fu, Y.; Yin, Z., A Review on Colloidal Self-Assembly and their Applications. *Current Nanoscience* **2016,** *12* (6), 725-746.

7. Wu, H.; Briscoe, W. H., Morphogenesis of polycrystalline dendritic patterns from evaporation of a reactive nanofluid sessile drop. *Physical Review Materials* **2018,** *2* (4), 045601.

8. Wu, H.; Chen, L. X.; Zeng, X. Q.; Ren, T. H.; Briscoe, W. H., Self-assembly in an evaporating nanofluid droplet: rapid transformation of nanorods into 3D fibre network structures. *Soft Matter* **2014,** *10* (29), 5243-5248.

9. Wąsik, P.; Redeker, C.; Dane, T. G.; Seddon, A. M.; Wu, H.; Briscoe, W. H., Hierarchical Surface Patterns upon Evaporation of a ZnO Nanofluid Droplet: Effect of Particle Morphology. *Langmuir* **2018,** *34* (4), 1645-1654.

10. Wąsik, P.; Seddon, A. M.; Wu, H.; Briscoe, W. H., Dendritic surface patterns from Bénard-Marangoni instabilities upon evaporation of a reactive ZnO nanofluid droplet: A fractal dimension analysis. *J. Colloid Interface Sci.* **2019,** *536*, 493-498.

11. Wąsik, P.; Seddon, A. M.; Wu, H.; Briscoe, W. H., Bénard-Marangoni dendrites upon evaporation of a reactive ZnO nanofluid droplet: Effect of substrate chemistry *Langmuir* **2019,** *35* (17), 5830-5840.

12. Josten, E.; Wetterskog, E.; Glavic, A.; Boesecke, P.; Feoktystov, A.; Brauweiler-Reuters, E.; Rücker, U.; Salazar-Alvarez, G.; Brückel, T.; Bergström, L., Superlattice growth and rearrangement during evaporation-induced nanoparticle self-assembly. *Scientific Reports* **2017,** *7* (1), 2802-.

13. Nicklin, C.; Arnold, T.; Rawle, J.; Warne, A., Diamond beamline I07: a beamline for surface and interface diffraction. *Journal of Synchrotron Radiation* **2016,** *23* (Pt 5), 1245-1253.

14. Dane, T. G., pygix - a generic python library for performing reduction of grazing-incidence and fiber X-ray scattering data., https://github.com/tgdane/pygix (accessed 06 Jun 2018).

15. Ashiotis, G.; Deschildre, A.; Nawaz, Z.; Wright, J. P.; Karkoulis, D.; Picca, F. E.; Kieffer, J., The fast azimuthal integration Python library: pyFAI. *J. Appl. Crystallogr.* **2015,** *48* (2), 510-519.

16. Eilers, P. H. C.; Boelens, H. F. M., Baseline Correction with Asymmetric Least Squares Smoothing.
https://zanran_storage.s3.amazonaws.com/www.science.uva.nl/ContentPages/443199618.pdf
(accessed 7 Sep 2018).

17. Shpyrko, O. G.; Streitel, R.; Balagurusamy, V. S. K.; Grigoriev, A. Y.; Deutsch, M.; Ocko, B. M.; Meron, M.; Lin, B.; Pershan, P. S., Crystalline surface phases of the liquid Au-Si eutectic alloy. *Physical Review B* **2007,** *76* (24), 245436.

18. Song, B.; Wang, Y.; Cui, X.; Kou, Z.; Si, L.; Tian, W.; Yi, C.; Wei, T.; Sun, Y., A Series of Unique Architecture Building of Layered Zinc Hydroxides: Self-Assembling Stepwise Growth of Layered Zinc Hydroxide Carbonate and Conversion into Three-Dimensional ZnO. *Cryst. Growth Des.* **2016,** *16* (2), 887-894.

19. Leung, A. H. M.; Pike, S. D.; Clancy, A. J.; Yau, H. C.; Lee, W. J.; Orchard, K. L.; Shaffer, M. S. P.; Williams, C. K., Layered zinc hydroxide monolayers by hydrolysis of organozincs. *Chemical Science* **2018,** *9* (8), 2135-2146.

20. Song, R. Q.; Xu, A. W.; Deng, B.; Li, Q.; Chen, G. Y., From Layered Basic Zinc Acetate Nanobelts to Hierarchical Zinc Oxide Nanostructures and Porous Zinc Oxide Nanobelts. *Adv. Funct. Mater.* **2007,** *17* (2), 296-306.

21. Peng, X.; Jin, J.; Kobayashi, N.; Schmitt, W.; Ichinose, I., Time-dependent growth of zinc hydroxide nanostrands and their crystal structure. *Chem. Commun.* **2008,** (16), 1904-1906.

22. Li, J.; Cao, W.; Mao, Y.; Ying, Y.; Sun, L.; Peng, X., Zinc hydroxide nanostrands: unique precursors for synthesis of ZIF-8 thin membranes exhibiting high size-sieving ability for gas separation. *CrystEngComm* **2014,** *16* (42), 9788-9791.

23. Wang, Z. L.; Kong, X. Y.; Wen, X.; Yang, S., In Situ Structure Evolution from Cu(OH)2 Nanobelts to Copper Nanowires. *J. Phys. Chem. B* **2003,** *107* (33), 8275-8280.

24. Lu, C.; Qi, L.; Yang, J.; Zhang, D.; Wu, N.; Ma, J., Simple Template-Free Solution Route for the Controlled Synthesis of Cu(OH)2 and CuO Nanostructures. *J. Phys. Chem. B* **2004,** *108* (46), 17825-17831.

25. Yu, Q.; Huang, H.; Chen, R.; Wang, P.; Yang, H.; Gao, M.; Peng, X.; Ye, Z., Synthesis of CuO nanowalnuts and nanoribbons from aqueous solution and their catalytic and electrochemical properties. *Nanoscale* **2012,** *4* (8), 2613-2620.

26. Park, S.-H.; Lee, C. E., Layered Copper Hydroxide n-Alkylsulfonate Salts: Synthesis, Characterization, and Magnetic Behaviors in Relation to the Basal Spacing. *J. Phys. Chem. B* **2005,** *109* (3), 1118-1124.

27. Jian-Ping, X.; Shao-Bo, S.; Lan, L.; Xiao-Song, Z.; Ya-Xin, W.; Xi-Ming, C., Effects of Annealing Temperature on Structural and Optical Properties of ZnO Thin Films. *Chinese Physics Letters* **2010,** *27* (4), 047803.

28. Barnett, C. J.; Mourgelas, V.; McGettrick, J. D.; Maffeis, T. G. G.; Barron, A. R.; Cobley, R. J., The effects of vacuum annealing on the conduction characteristics of ZnO nanorods. *Mater. Lett.* **2019,** *243*, 144-147.

29. Greene, L. E.; Law, M.; Tan, D. H.; Montano, M.; Goldberger, J.; Somorjai, G.; Yang, P., General Route to Vertical ZnO Nanowire Arrays Using Textured ZnO Seeds. *Nano Lett.* **2005,** *5* (7), 1231-1236.

30. Greene, L. E.; Yuhas, B. D.; Law, M.; Zitoun, D.; Yang, P., Solution-Grown Zinc Oxide Nanowires. *Inorg. Chem.* **2006,** *45* (19), 7535-7543.

31. Tripathy, A.; Wąsik, P.; Sreedharan, S.; Nandi, D.; Bikondoa, O.; Su, B.; Sen, P.; Briscoe, W. H., Facile Fabrication of Multifunctional ZnO Urchins on Surfaces. *Colloids Interfaces* **2018,** *2* (4), 74.

32. Asbrink, S.; Norrby, L.-J., A refinement of the crystal structure of copper(II) oxide with a discussion of some exceptional e.s.d.'s. *Acta Crystallographica Section B* **1970,** *26* (1), 8-15.

33. Demel, J.; Hynek, J.; Kovář, P.; Dai, Y.; Taviot-Guého, C.; Demel, O.; Pospíšil, M.; Lang, K., Insight into the Structure of Layered Zinc Hydroxide Salts Intercalated with Dodecyl Sulfate Anions. *J. Phys. Chem. C* **2014,** *118* (46), 27131-27141.

34. Kandare, E.; Chigwada, G.; Wang, D.; Wilkie, C. A.; Hossenlopp, J. M., Nanostructured layered copper hydroxy dodecyl sulfate: A potential fire retardant for poly(vinyl ester) (PVE). *Polym. Degrad. Stab.* **2006,** *91* (8), 1781-1790.

35. Deng, B.; Wang, C.-C.; Li, Q.-G.; Xu, A.-W., Highly Ordered Lamellar Mesostructure of Nanocrystalline PbSO4 Prepared by Hydrothermal Treatment. *J. Phys. Chem. C* **2009,** *113* (43), 18473-18479.

Supplementary Information

Structural evolution of the surface pattern in an evaporating nanofluid sessile drop: An *in-situ* synchrotron grazing incident X-ray diffraction study

Patryk Wąsik[a,b] *et al.*

[a] Bristol Centre for Functional Nanomaterials (BCFN), HH Wills Physics Laboratory, University of Bristol, Tyndall Avenue, Bristol, BS8 1TL, UK

[b] School of Chemistry, University of Bristol, Cantock's Close, Bristol, BS8 1TS, UK

Information

This chapter is intended to be published as a research article and has been authored by the candidate with no more input from co-authors and supervisors that would have been provided in a conventional thesis chapter. Individual contributions as in Chapter 5.

SI.01: Particles

Several different particles were used to prepare nano/microfluids: the in-house synthesised ZnO nanoparticles and commercially acquired ZnO nanopowder (Sigma-Aldrich, <100 nm particle size, ~80% Zn basis), ZnO powder (Sigma-Aldrich, ACS reagent, ≥99.0% (KT)), and CuO nanopowder (Sigma-Aldrich, <50 nm particle size (TEM)). Transmission electron microscopy (TEM) images of these particles, taken using JEOL JEM-1400 Transmission Electron Microscope, are shown in **Figure S1**. Particle size distribution and energy-dispersive X-ray spectroscopy analysis of ZnO particles in addition to the synthesis of the in-house ZnO nanoparticles is reported elsewhere [1]. Summarising, particle size distribution was fitted with the log-normal distribution function, thus can be interpreted that *ca* 68.3% of all particles is contained between M/σ_g and $M \cdot \sigma_g$, where M is the geometric

mean particle diameter and σ_g is the geometric standard deviation [2-3]. The analysis revealed the in-house synthesised ZnO nanoparticles were monodisperse (68.3% diameters between 7.4 and 11.4 nm). Contrary, commercially acquired ZnO nanopowder and ZnO power were polydisperse, with ~68.3% of their maximum size dimension contained in between 36 - 142 nm and 61 - 291 nm, respectively.

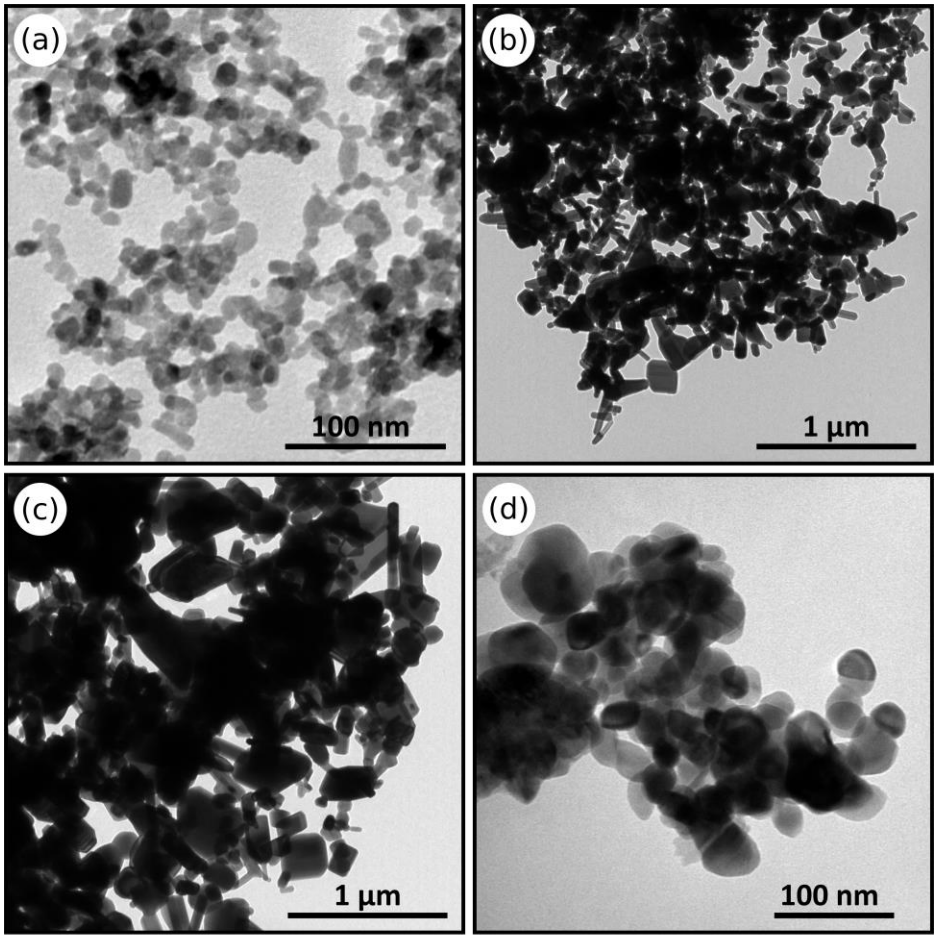

Figure S1. Transmission electron microscopy of different particles used in the study: (**a**) in-house synthesised ZnO nanoparticles, (**b**) ZnO nanopowder, (**c**) ZnO powder, and (**d**) CuO nanoparticles.

X-ray diffraction (XRD) patterns of the particles were taken using the experimental setup described in the main text. A thin layer of each powder was manually deposited onto a bare silicon substrate so that the diffraction image could be recorded. **Figure S2** presents XRD results of the ZnO and CuO particles as projections of raw diffraction images into reciprocal space and integrated line profiles. The numbers in parentheses are the Miller indices of the crystallographic planes identified accordingly to ZnO (PDF 01-075-0576) and CuO (PDF 01-073-6023 45-937) reference standards.

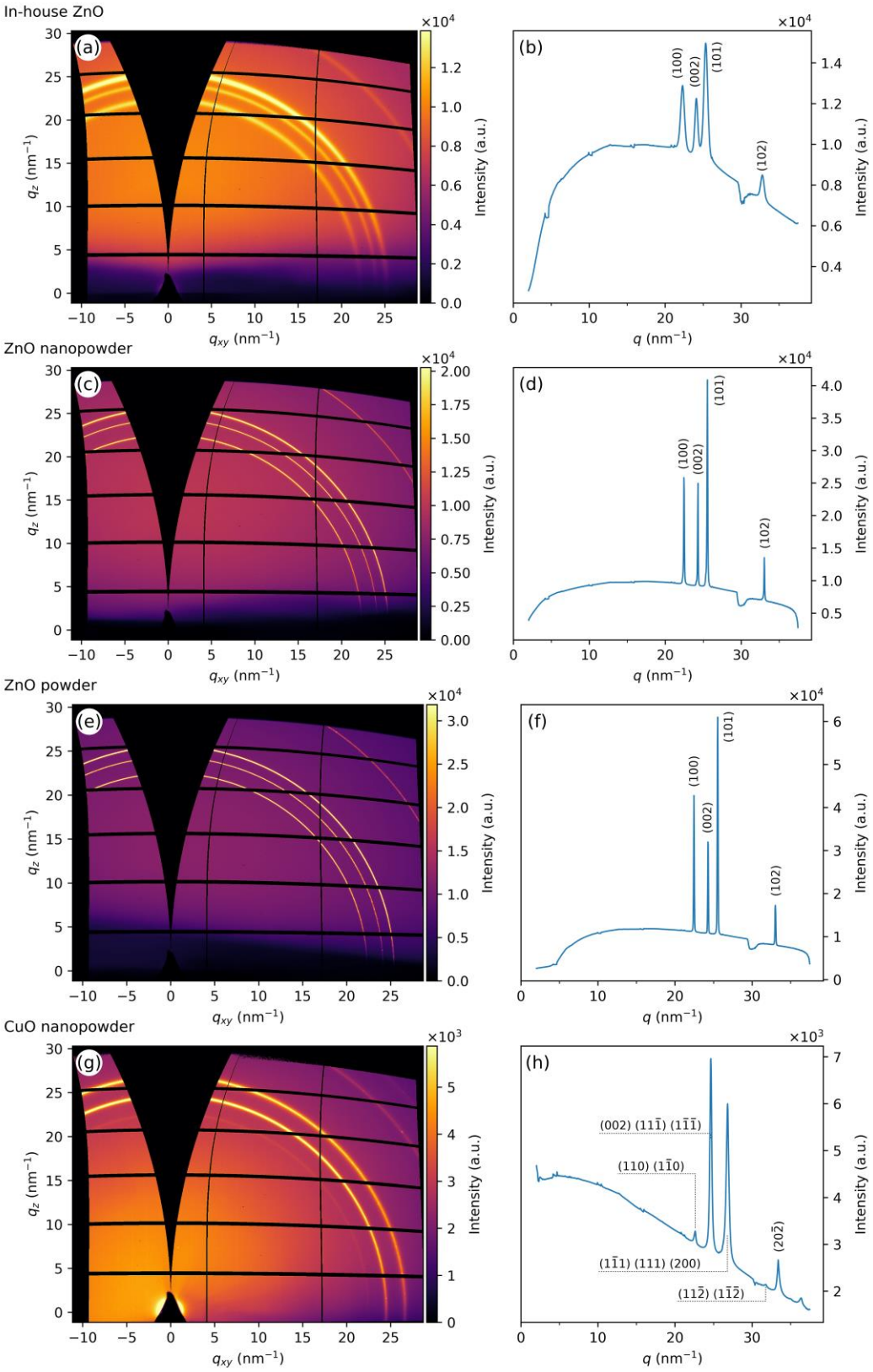

Figure S2. X-ray diffraction data of the particles used in the study: (**a-b**) in-house synthesised ZnO nanoparticles, (**c-d**) ZnO nanopowder, (**e-f**) ZnO powder, and (**g-h**) CuO nanoparticles. Left-hand side

(**a**, **c**, **e**, **g**) shows projections of diffraction images into reciprocal space and right-hand side (**b**, **d**, **f**, **h**) shows integrated line profiles.

SI.02: Substrates

Various different substrates cut to 1×1 cm^2 pieces were used: standard microscope glass slides (type 7101, 0.8 - 1.0 mm thick), silicon wafers (UniversityWafer Inc., ID 452, 100 mm diameter, P type, B dopant, <100>, 0-100 Ω·cm, 500 μm thick, single-sided polish, test grade), both unmodified and hydrophobised by silane functionalisation (see "Silanation of Si wafer procedure" paragraph below), natural muscovite mica with composition $KAl_2(Si_3Al)O_{10}(OH)_2$ (SJ Trading®, A1 special grade), polytetrafluoroethylene (PTFE) sourced from the Mechanical Workshop (School of Chemistry, University of Bristol), and glass substrates with randomly oriented ZnO nanorods grown on the surface (see "ZnO nanorods on glass synthesis" below). Theoretical information on these substrates is presented in SI.05. All these substrates were scanned using the grazing incidence set-up described in the experimental section in the main text to produce control diffraction data shown below (**Figure S5** and **Figure S6**).

Silanation of Si wafer procedure

Silanation (silanisation) is a process in which long aliphatic chains, such as alkylchlorosilanes, alkylalkoxysilanes and alkylaminosilanes, are grafted on hydroxylated surfaces (*i.e.* silica) *via* trichlorosilane group (-Si-Cl_3). As a result, a self-assembled monolayer composed of these aliphatic chains, driven by the *in-situ* formation of polysiloxane, is anchored to surface silanol groups (Si-OH) *via* Si-O-Si bonds [4-5]. This is a popular technique used to create (super)hydrophobic surfaces, which is caused by aliphatic chains grafted onto the surface [6-8]. A schematic representation of this process is shown in **Figure S3**. Initially, the aliphatic chains are attracted to the silica surface *via* the trichlorosilane groups that behave like polar head of amphiphilic molecules. Subsequently, they become hydrolysed when in contact with a water layer adsorbed to the surface. As a result, the aliphatic chains are bonded to the surface silanol groups and to their adjacent neighbours *via* hydrogen bonds. This is followed by a condensation reaction, resulting in a stable and well-oriented network of chains linked to

the surface and their neighbours. However, it is suggested that the layer is not linked to the surface by all the individual molecules in as formed network, but by a part of them [4].

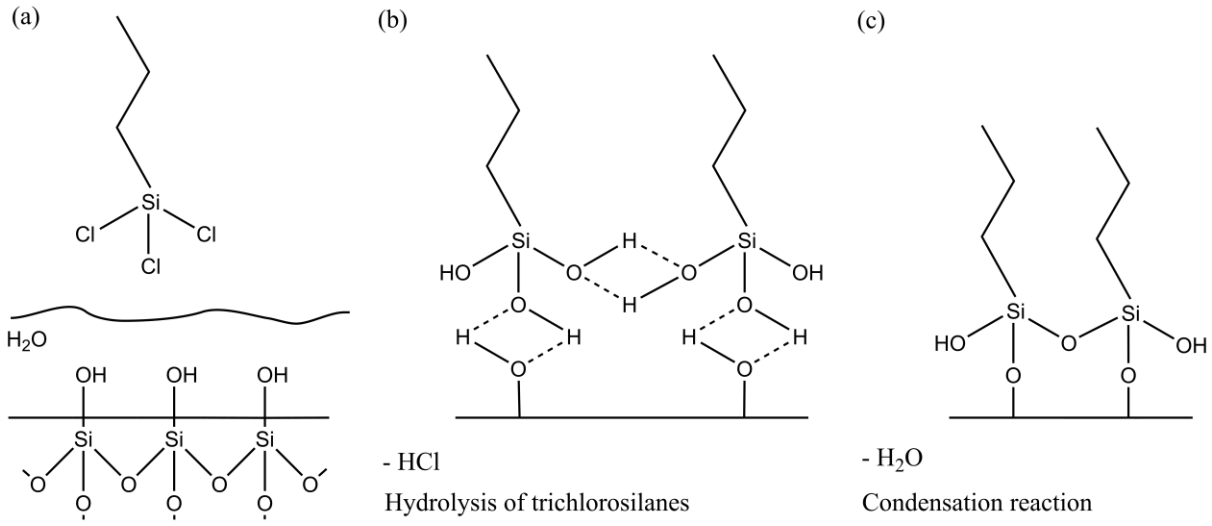

Figure S3. Schematic representation of the silanation process: (**a**) physisorption of trichlorosilane molecule, (**b**) hydrolysis and hydrogen bond formation, and (**c**) water elimination resulting in a chemically bonded monolayer.

In this work, freshly cleaned Si wafer was exposed to UV/ozone for 10 minutes in 42-220 UVO-Cleaner®, Jetlight Company, Inc. Subsequently, the wafer was submerged overnight in a solution of 1*H*,1*H*,2*H*,2*H*-perfluorooctyltriethoxysilane (Sigma-Aldrich, 98%) and dried with a stream of N_2. The wettability of the silanised Si wafer was tested with sessile droplet contact angle (Drop Shape Analyzer – DSA100, KRÜSS), using *Milli-Q* water at room temperature (~24.5 °C) and relative humidity ~45%. The measured mean water contact angle was equal to 93.7 ± 0.8°.

ZnO nanorods on glass synthesis

Randomly oriented ZnO nanorods on a glass surface were synthesised in a two-step procedure including seeding glass substrates with ZnO nanocrystals [9] and hydrothermal growth of ZnO nanowires [9-10]. In the first step, 5 mM zinc acetate dihydrate (Sigma-Aldrich, ACS reagent, ≥ 98%) solution in ethanol was prepared by mixing 90.9 ± 0.1 mg of zinc acetate dihydrate and 83.0 ± 0.5 mL with ethanol using magnetic stirrer for *ca* 1 hour at room temperature. Microscope glass slide substrates were cut and cleaned accordingly to the procedure described in the main text. Then, each substrate was submerged into the seeding solution for ~10 seconds, followed by rinsing with clean ethanol. This step

was repeated 5 times per single substrate. Subsequently, all substrates were annealed on a preheated hot plate at 300 °C for 20 minutes and then placed inside of a glass Petri dish.

In the second step of the synthesis, an equimolar 25 mM aqueous solution of zinc nitrate hexahydrate (Sigma-Aldrich, reagent grade, 98%) and hexamethylenetetramine (Sigma-Aldrich, ACS reagent, ≥ 99.0%) was prepared by mixing 1.8686 ± 0.0001 g of zinc nitrate hexahydrate and 0.8771 ± 0.0001 g of hexamethylenetetramine with 250 mL of *Milli-Q* water (18.2 MΩ·cm at 25 °C) in a round bottom flask. The Petri dish containing substrates was placed inside of a vacuum oven (Heraeus Vacutherm VT 6025, Thermo Fisher Scientific) and preheated to 90 °C under atmospheric pressure (vacuum pump turned off). In the meantime, the growth solution inside of the round bottom flask, sealed with a rubber stopper, was preheated to 90 °C with the help of magnetic stirring. During the preheating step, which took about 30 minutes, the colour of the growth solution became milky. Subsequently, the growth solution was poured into the Petri dish fully covering all the substrates. The dish was kept inside of the oven at 90 °C for 2 hours and 20 minutes. After that time, substrates were removed from the growth solution, rinsed in *Milli-Q* water, and baked on the hotplate at 300 °C for 15 minutes.

Figure S4 presents scanning electron microscopy (SEM) images of as synthesised randomly oriented ZnO nanorods on glass substrates, taken with JSM-IT300 SEM, JEOL microscope. Prior to the imaging, a ~15 nm layer of silver film was deposited onto the substrates. The entire glass surface was uniformly covered with ZnO nanorods (**Figure S4a**), which were bundled into aggregates (**Figure S4b**) composed of *ca* 1 - 5 μm ZnO rods (**Figure S4c-d**).

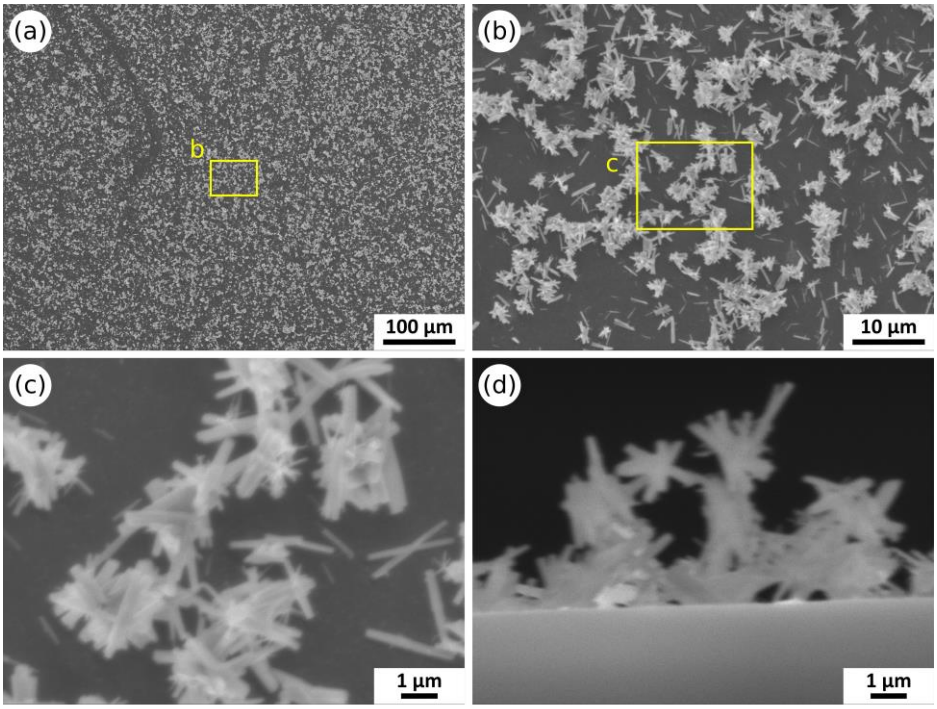

Figure S4. Scanning electron microscopy images of glass substrates with randomly oriented ZnO nanorods. (**a-c**) show the top view of the substrate and (**d**) shows the side view of ZnO nanorods, obtained by breaking the substrate into two parts. The rectangular regions in the figures are enlarged, with their labels corresponding to those of the figures.

GIXRD control scans of substrates

Control grazing incidence X-ray diffraction patterns of the substrates taken using the experimental setup described in the main text are shown in **Figure S5** for microscope glass slide, unmodified Si, and silanised Si, and in **Figure S6** for polytetrafluoroethylene, muscovite mica, and ZnO nanorods grown on glass surface. Artefacts which are present in the same positions in all 1D profiles at q equal to ~2.9, 5.3 - 5.9, 12.6 - 13.4, 19.6 - 20.3, 26.0 - 26.7, 31.9 - 32.5, and 36.2 - 37.3 nm^{-1} are produced during the profile integration of 2D diffraction images in reciprocal space likely due to experimental geometry set-up, multimodule detector used (Pilatus 2M, Dectris), and processing pipeline (pyFAI [11] and pyGIX [12]). These integration artefacts are marked with dashed circles in **Figure S5f**. Polytetrafluoroethylene (PTFE) diffraction peaks in **Figure S6b** were identified accordingly to [13] and ZnO diffraction peaks in **Figure S6b** accordingly to ZnO reference standard (PDF 01-075-0576). An example of the baseline correction in the integrated diffraction profile accordingly to the penalized asymmetric least-squares

algorithm by Eilers and Boelens [14] is shown in **Figure S6f** (notice the integration artefacts visible in the corrected profile). Baseline correction is discussed in detail in SI.03.

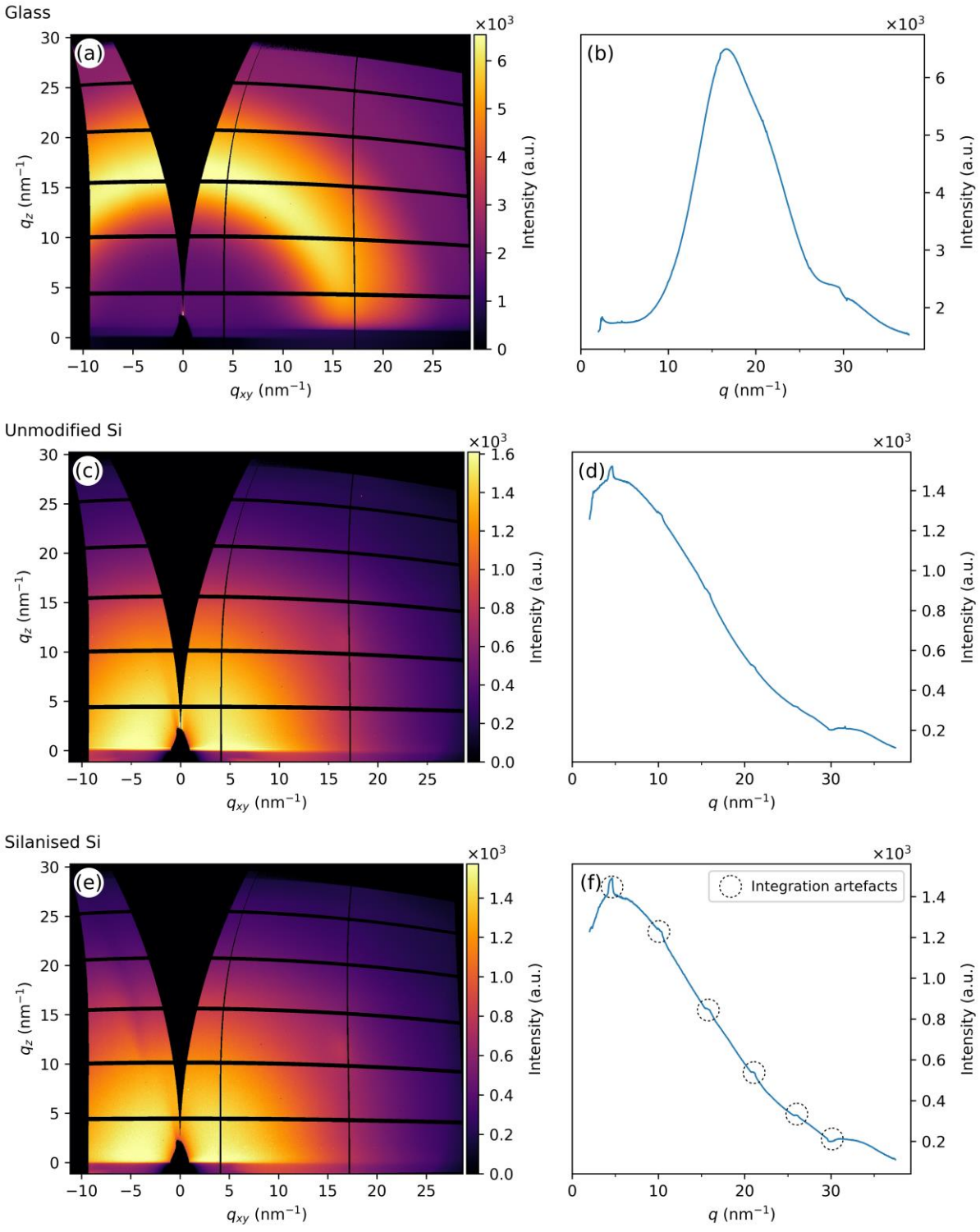

Figure S5. Control grazing incidence X-ray diffraction scans of selected substrates: (**a-b**) microscope glass slide, (**c-d**) unmodified silicon, and (**e-f**) silanised silicon wafer. Integration artefacts in the intensity signal produced during the profile integration are marked as circles in (**f**).

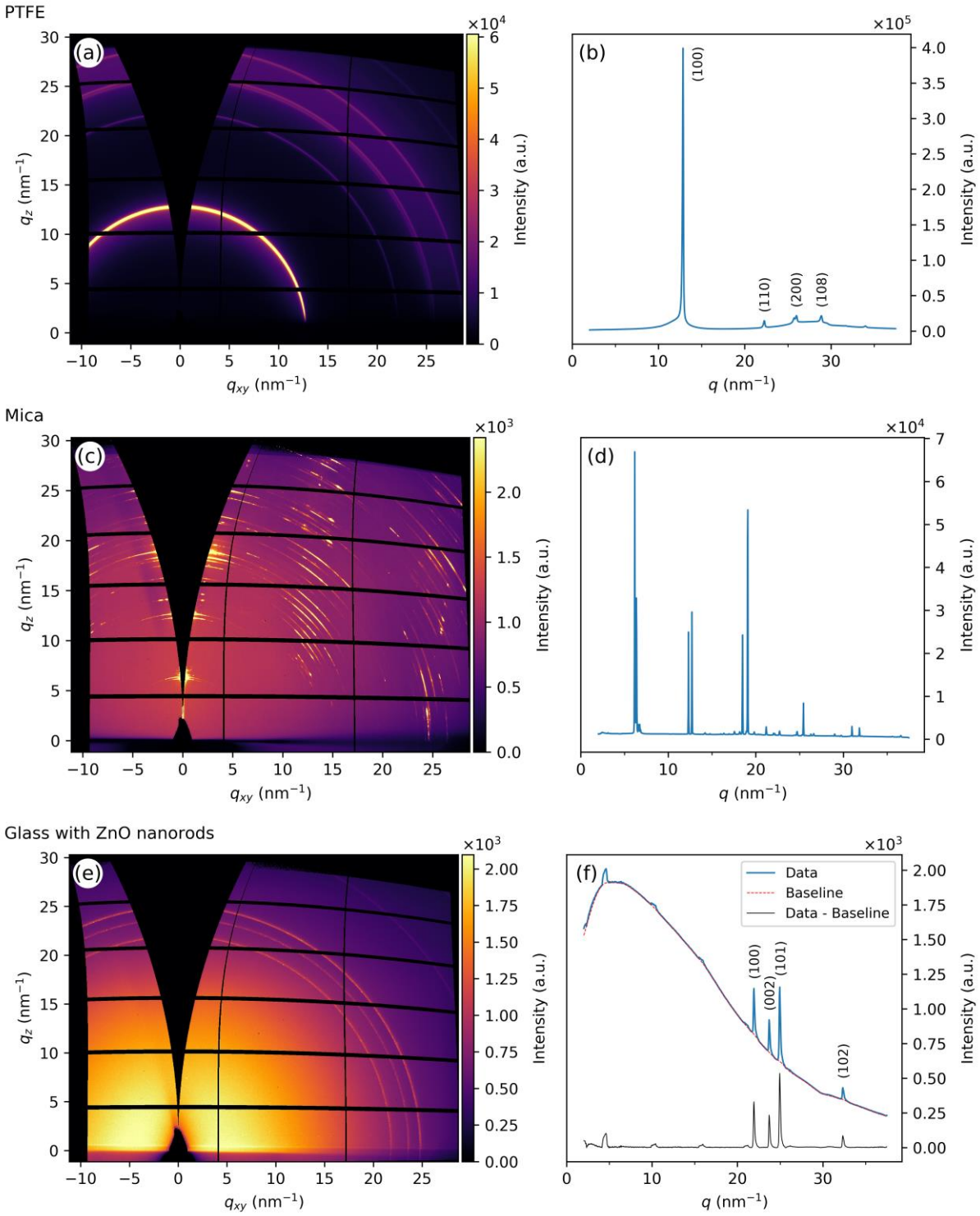

Figure S6. Control grazing incidence X-ray diffraction scans of selected substrates: (**a-b**) polytetrafluoroethylene (PTFE), (**c-d**) muscovite mica, and (**e-f**) glass with grown ZnO nanorods on the surface. Baseline fitting and baseline data correction (see SI.03) are shown in (**f**).

SI.03: Baseline correction of diffraction profiles

Baseline correction has been implemented into the data processing pipeline as a baseline trend has been observed in all of the integrated X-ray diffraction profiles (see **Figure S2**, **Figure S5**, and **Figure S6**). This was aimed to increase the contrast and readability of the figures that show the time or temperature evolution of the studied processes. We include the details of the baseline correction applied to the GIXRD data in this work for completeness and to familiarise the reader with its outcomes on the data visualisation.

The implemented baseline correction was based on the penalised asymmetric least-squares algorithm (ALS) developed by Eilers and Boelens [14]. In short, a Whittaker smoother is employed to calculate a slowly varying estimate of the baseline. However, positive deviations from the estimated baseline are weighted (much) less than negative ones, which contrasts with ordinary least squares smoothing. This baseline estimation algorithm requires two pre-set parameters that must be tuned to the data at hand. This includes the asymmetry parameter, p, used to calculate asymmetric weights of the residuals (p for positive residual and 1 - p for negative residual) and the smoothness parameter, λ. The authors suggested setting the value of p in a range from 0.001 to 0.1 for a signal with positive peaks, and the value of λ between 10^2 and 10^9, subject to exceptions that may occur [14].

Python code implementation of the penalised asymmetric least-squares algorithm was adopted from [15]. We found that a set of parameters $p = 0.001$ and $\lambda = 10^2$ resulted in a relatively good baseline estimation for a range of diffraction profiles exhibiting sharp peaks. **Figure S7** illustrates results of the baseline calculation algorithm for different values of p (0.001, 0.01, 0.1, and 1) and λ (1, 10^2, 10^4, 10^6, and 10^8) coefficients for an example X-ray diffraction profile data of a glass substrate with grown ZnO nanorods on top of it (*cf.* **Figure S4** and **Figure S6e-f**). Baseline correction performed for the optimal set of p (0.001) and λ (10^2) is shown in **Figure S7e** and highlighted with light green colour.

The baseline correction was intended to increase the contrast in the 2D heatmap (waterfall) plots, which show the intensity of the scattered X-rays with respect to the momentum transfer vector, q, and the time of the evaporation process (alternatively, annealing temperature in the temperature effect study). **Figure S8** visualises the differences between the unprocessed raw data (**Figure S8a-b**), baseline corrected data using the ALS algorithm ($p = 10^{-3}$ and $\lambda = 10^3$) (**Figure S8c-d**), and the data corrected

by subtraction of a GIXRD line profile of a blank sample scan, *i.e.* bare substrate, measured just before a drop of ZnO nanopowder nano/microfluid was cast on the Si substrate (**Figure S8e-f**), used in this example. The highest contrast in the 2D heatmap was obtained using the ALS algorithm for the base line estimation. However, the relative height of the broad peak related to the droplet on the surface (q ~ 11 - 14 nm^{-1}) is significantly reduced when compared to its height in the raw and the blank sample correction data, by a factor of 4 and 2, respectively. This could be improved by increasing the smoothness parameter, λ, however it would reduce the quality of the baseline estimation in the other parts of the line profile. We found the value of $\lambda = 10^3$ was a good compromise to the previously established parameters of $p = 0.001$ and $\lambda = 10^2$, which performed well for line profiles with sharp peaks.

The baseline correction based on the background subtraction is an attractive alternative as it preserves the relative ratio of the broad peak (q ~ 11 - 14 nm^{-1}) to other sharp peaks present in the diffractogram (*e.g.* 22.4, 24.2, and 25.5 nm^{-1} for ZnO) and removes the positive peaks coming from the integration artefacts. However, it amplifies the negative integration artefact peaks, but most importantly, a blank sample scan is not always available for the baseline calculation.

We acknowledge that baseline correction based on the blank sample would be a suitable choice for the example data shown in **Figure S8** in terms of the clarity and readability of the diffraction signal as it reduces the integration artefacts and preserves the relative height of the broad peak to some extent. However, this approach was not always applicable as it required a blank scan taken in the same geometry prior to the measurement the correction is intended for. Therefore, to remain consistent with the processing approach to all data sets, we decided to use the penalised asymmetric least-squares algorithm for the baseline correction as it can be implemented independently and reliably to all diffraction line profiles.

The exact positions of the integration artefacts were determined based on the comparison between the ALS and blank sample corrected diffraction profiles of ZnO nanopowder nano/microfluid dried on a silicon substrate taken as an example, shown in **Figure S9**. It was assumed that the contributions of the integration artefacts due to the detector image processing were the same in the blank sample scans and evaporation data profiles. Therefore, the peaks that only appeared in the raw or ALS corrected data

but were not present after the subtraction of the blank sample profile, can be considered as artefacts. **Figure S9a** shows diffraction profiles taken 108 seconds after the start of the drying process (*cf.* **Figure S8**), the top one baseline corrected using the ALS algorithm with parameters $p = 10^{-3}$ and $\lambda = 10^{3}$, and the bottom one with the blank sample scan subtraction. The scattered X-ray intensity 2D heatmaps (q *vs.* time) in **Figure S9b-k**, and sections of diffraction line profiles in **Figure S9l-p** are detailed magnifications of corresponding q ranges marked as blue squares in **Figure S9a**. By comparison of these magnified regions depicted regions in **Figure S9b-p** between the ALS and blank sample corrected profile, it was established that the positive peaks in positions of *ca.* 4.18, 4.68, 15.7 - 16, 20.8 - 21.3, 25.7 - 26.2, 29.3, and 30.9 nm^{-1} and negative peaks in *ca.* 2.7, 5.1, and 29.5 - 30.9, are related to azimuthal integration of the detector images (transformation of detector pixels into the reciprocal space coordinates) and considered as the integration artefacts.

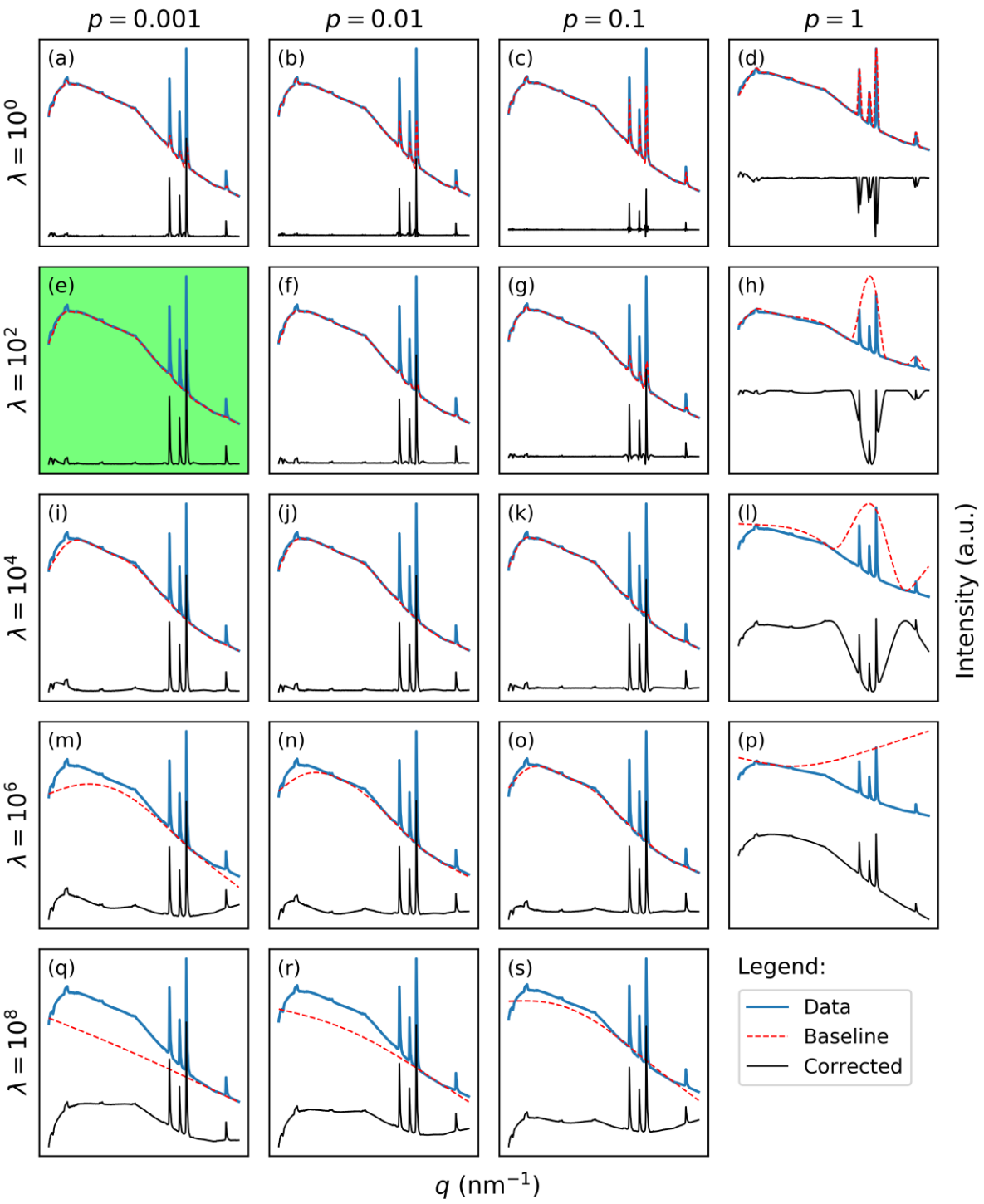

Figure S7. Baseline correction performed for the grazing incidence X-ray diffraction profile of the glass surface with ZnO nanorods grown on top of it (*cf.* **Figure S4** and **Figure S6e-f**). Baselines were calculated using the penalised asymmetric least-squares algorithm [14] with a different values of asymmetry, p, and smoothness, λ, parameters. The set of p and λ parameters equal to 0.001 and 100 was

found to produce a relatively good baseline estimations for a range of different diffraction profiles. Here, the correction based on this set of p and λ is shown in (**e**) and highlighted with light green colour.

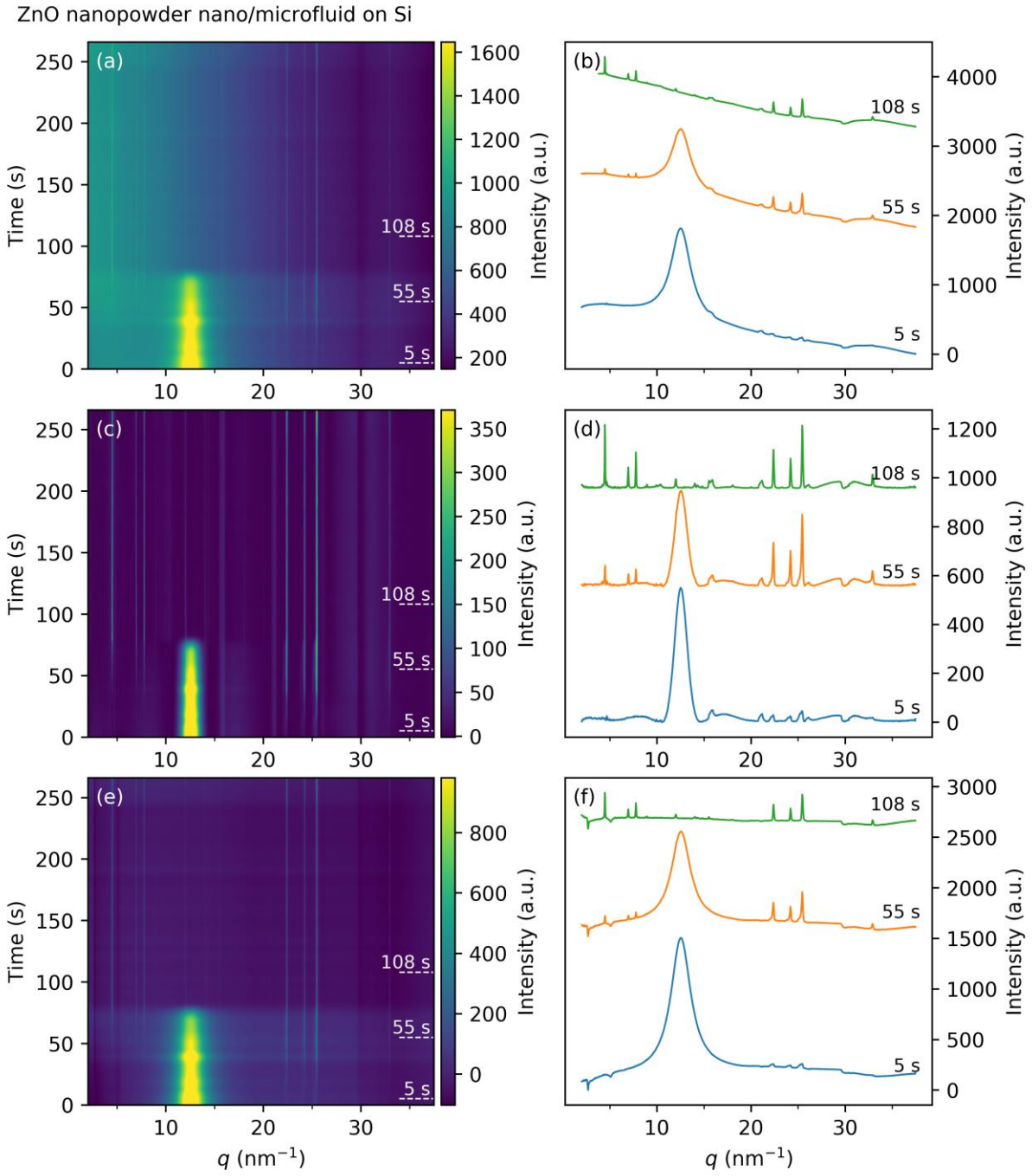

Figure S8. Visualisation of the differences in the 2D heatmaps and 1D line profiles plots with respect to the baseline correction on data produced by a drop of ZnO nanopowder nano/microfluid dried on a silicon substrate. Subplots (**a-b**) show raw data, (**c-d**) data corrected with the penalised asymmetric least-squares algorithm (p = 10^{-3} and λ = 10^{3}), and (**e-f**) data corrected by subtracting a line profile

calculated for a blank scan, *i.e.* bare substrate, taken prior to the deposition of the drop of ZnO nano/microfluid. Dotted lines in 2D heatmaps and lines in 1D profile subplots are labelled with corresponding times counted from the start of the evaporation.

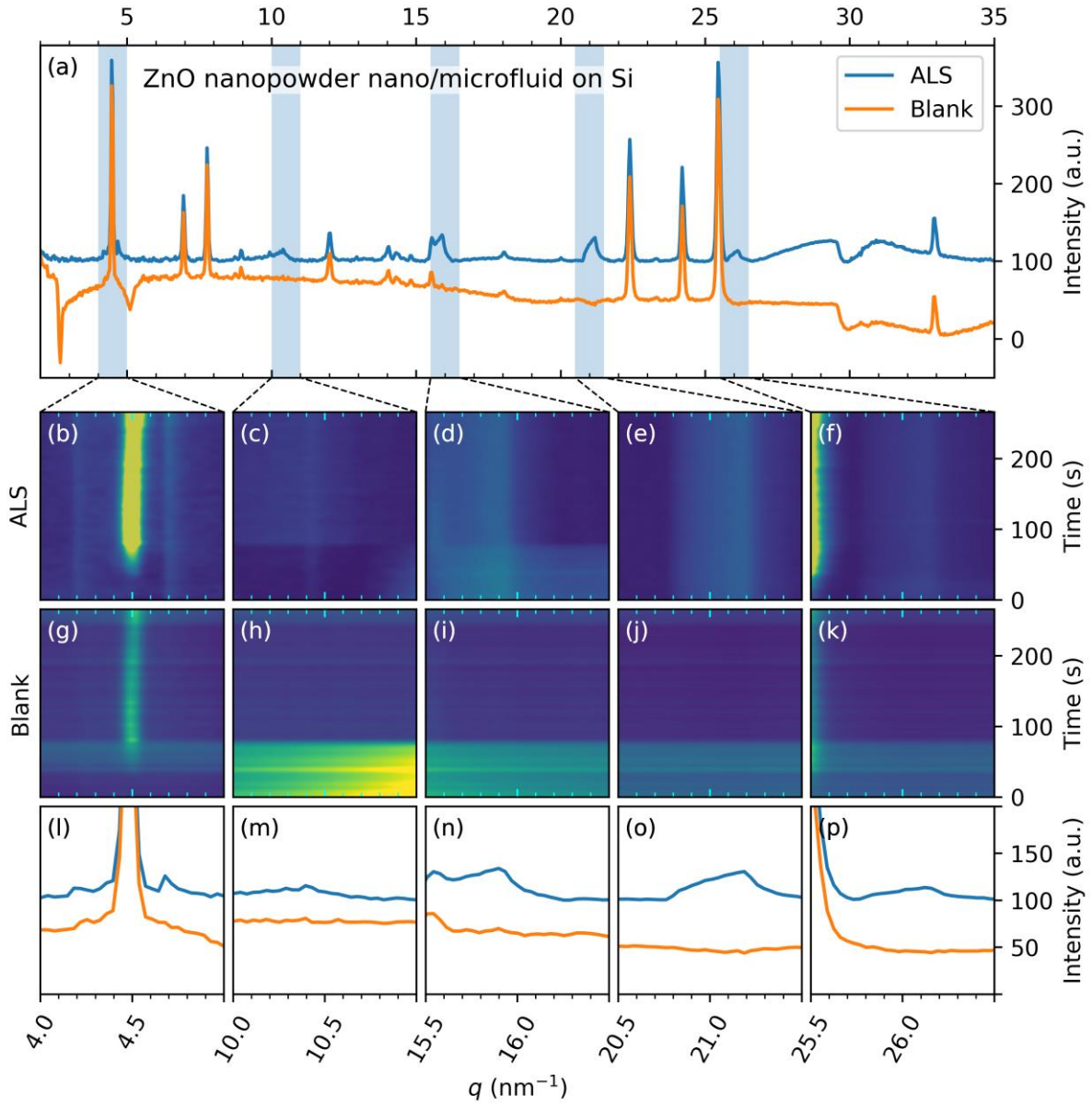

Figure S9. Detailed comparison of two baseline correction methods applied to X-ray diffraction data produced from ZnO nanopowder nano/microfluid dried on Si substrate. (**a**) shows diffraction profiles taken 108 seconds after the start of the drying process, the top one baseline corrected using the penalised asymmetric least-squares algorithm (ALS) with parameters $p = 10^{-3}$ and $\lambda = 10^{3}$, and the bottom one with the blank sample scan subtraction. (**b-f**) and (**g-k**) show the scattered intensity during the evaporation process for corresponding q ranges marked as blue squares in (a) for the ALS and blank

sample methods, respectively. (**l-p**) show diffraction profiles from (a), *i.e.* upper blue for the ALS and lower orange for the blank sample corrections in q ranges corresponding to the marked regions in (a).

SI.04: Scripts

This section contains examples of scripts used to execute experimental procedures at I07 beamline (Surface and Interface Diffraction) at Diamond Light Source, UK.

time scan

```
pos filterset 0
pos gw_bsy 14

pos hex1rx
pos hex1z
pos temp21
pos syringe_right

# Tilt sample for GI geometry, change value for different theta
inc hex1rx 0.7

# Dispense nano/microfluid
inc syringe_right - 60

# Scan
cscan testMotor1 0 300 3 pil2roi 0.5 clock temp21 ionc1 1 qbpm3 1

pos filterset 150
```

lateral scan

```
pos filterset 10
pos gw_bsy 14

pos hex1rx
pos hex1z
pos temp21

# Scan 5 mm either side with 0.5 mm step for 2 seconds per step
cscan hex1x 5 0.5 pil2roi 2 clock temp21 ionc1 1 qbpm3 1

pos filterset 150
```

temperature scan

```
# ---Temperature scan that aligns z at each step---

# Define parameters, these can be changed as needed
startTemperature = 50
endTemperature = 400
temperatureStep = 50
annealingTimeInSeconds = 600

# Make sure the full beam intensity is recorded and that the beamstop is in place
pos gw_bsy 14
pos filterset 0

# Make sure to wait for the right temperature
temp21.setAccuracy(1)
```

```
15.
16. # Surface scan along x-axis (2s exposure)
17. cscan hex1x 5 0.5 pil2roi 2 clock temp 21 ionc1 qbpm3 1
18.
19. # Temperature loop up
20. for temperature in range(startTemperature, endTemperature+1, temperatureStep):
21.         # Set temperature
22.         pos temp21 temperature
23.         # z scan to account for thermal expansion
24.         cscan hex1z 0.3 0.05 pil2roi 1
25.         # Move to new z value
26.         cen "roi2_maxval"
27.         # Do lateral scan across sample at 1 mm increments (1s exposure)
28.         cscan hex1x 5 1 pil2roi 1 clock temp 21 ionc1 qbpm3 1
29.
30. # Anneal sample
31. sleep(annealingTimeInSeconds)
32. # Do z-scan again, in case of change
33. cscan hex1z 0.3 0.05 pil2roi 1
34. # Move to new z vale
35. cen "roi2_maxval"
36. # Do lateral scan across sample at 1 mm increments (1s exposure)
37. cscan hex1x 5 1 pil2roi 1 clock temp 21 ionc1 qbpm3 1
38.
39. # Temperature loop down
40. for temperature in range(startTemperature, endTemperature, temperatureStep):
41.         # Calculate temperature as ranges only goes up...
42.         temperature = endTemperature - temperature
43.         # Set temperature
44.         pos temp21 temperature
45.         # z scan to account for thermal expansion
46.         cscan hex1z 0.3 0.05 pil2roi 1
47.         # Move to new z value
48.         cen "roi2_maxval"
49.         # Do lateral scan across sample at 1 mm increments (1s exposure)
50.         cscan hex1x 5 1 pil2roi 1 clock temp 21 ionc1 qbpm3 1
51.
52. # Close shutter
    and return sample to room temperature and some default beamline settings
53. pos filterset 150
54. shclose
55. temp21.setAccuracy(10)
56. pos temp21 23
```

SI.05: Theoretical information about substrates

Microscope Glass Slides

Microscope glass slides are thin flat pieces of glass commonly used for sample preparation, so that the specimen can be hold and viewed under a microscope. Due to their low cost, practicable dimensions and relative ease to cut into appropriate fragments, microscope glass slides can be used as a solid substrate in a variety of experimental set-ups outside the scope of the optical microscopy. They are usually made of optically transparent glass, such as soda-lime glass (SiO_2 + Na_2O + CaO + Al_2O_3 + fining agents) or borosilicate glass (SiO_2 + B_2O_3 + Na_2O + Al_2O_3 + fining agents) [16].

Tetrahedral SiO_4 units, connected to each other through their corners, are the basic structural elements of silicate glasses and exhibit well-defined geometry. However, the arrangement of these tetrahedral units is characterised by the absence of long-range order in contrast to crystalline silica. Nonetheless, the tetrahedra form a network of ring-like structures that results in ordering on intermediate length scales. The addition of network modifiers such as CaO, Na_2O leads to the generation of non-bridging oxygens. The non-bridging oxygens are connected to the glass network with a single covalent bound and have a negative charge to compensate for the network modifier ions [17]. Schematic silicate glass structure is shown in **Figure S10**.

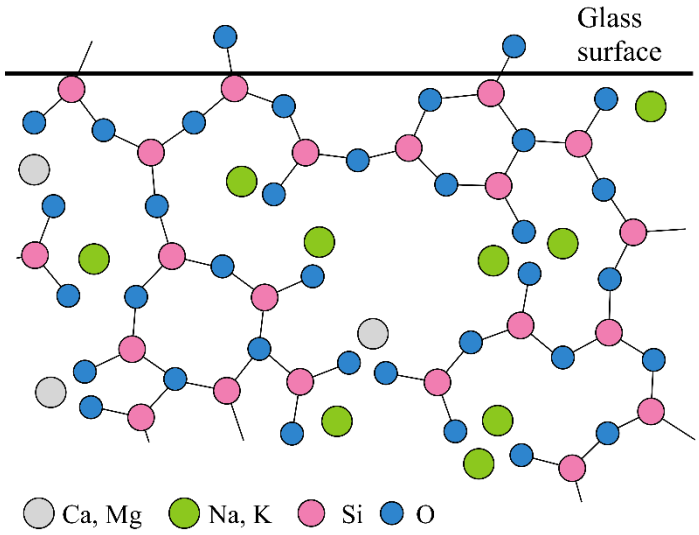

Figure S10. Silicate glass structure. Introduction of network modifier ions such as Ca^{+2}, Mg^{2+}, Na^+, or K^+ leads to creation of non-bridging oxygens. Adapted with permission from Ref. [18]. Copyright (2019) American Chemical Society.

The surface chemistry of the glass is dominated by the hydrous species (Si-OH and H_2O) and surface network structure composed of bridging (Si-O-Si) and non-bridging ($Si-O^-$) oxygens, that have a direct effect on the mechanical strength and chemical reactivity of glass [19]. The interaction with an aqueous medium often leads to the weathering process and corrosion of the glass surface. The process involves the initial ion exchange of alkaline ions (Na^+, K^+, Ca^{2+}, Mg^{2+}) from the surface for H^+ from hydrogen-bearing species of the medium. This can be followed by the reaction of hydroxyl ions (OH^-) released in the aqueous medium with siloxanes (Si-O-Si) to generate silanol groups (Si-OH) and non-bridging oxygen groups ($Si-O^-$). The whole process results in a gradual destruction of the surface glass network

by appearance of cracks and crystalline corrosion products due to the long term exposure to unfavourable conditions such as gaseous acid pollutants (*i.e.* SO_2 or NO_x) and humidity [18].

Nevertheless, it is expected that the surface chemistry of the microscope slides, made of silicate glasses, is governed by the relative populations of silanol (Si-OH), siloxide ($Si-O^-$), and siloxane (Si-O-Si) surface groups, similarly to the amorphous silica films [20]. This should be manifested in the water contact angle measurements of microscope glass slides surfaces [21].

Silicon Wafer Substrates

A silicon wafer surface is covered with a native layer of silicon oxide (SiO_2), with a thickness of approximately 0.4 - 2.0 nm, which forms naturally when a silicon surface is exposed to air in ambient conditions [22]. The spontaneous formation of a native oxide at the surface and the ability to grow it further in a control manner make silicon the most commonly used material in the semiconductor industry. A thin layer of SiO_2 acts as a chemically stable protective layer with high quality electrical insulator properties, mainly applicable as a dielectric in numerous devices or a masking layer during device fabrication [23]. The surface of silicon oxide consists of many different chemical species, however the basic chemical moieties present in the structure are silanols (**Figure S11a-c**), siloxanes (**Figure S11d**) and their permutations (**Figure S11e**).

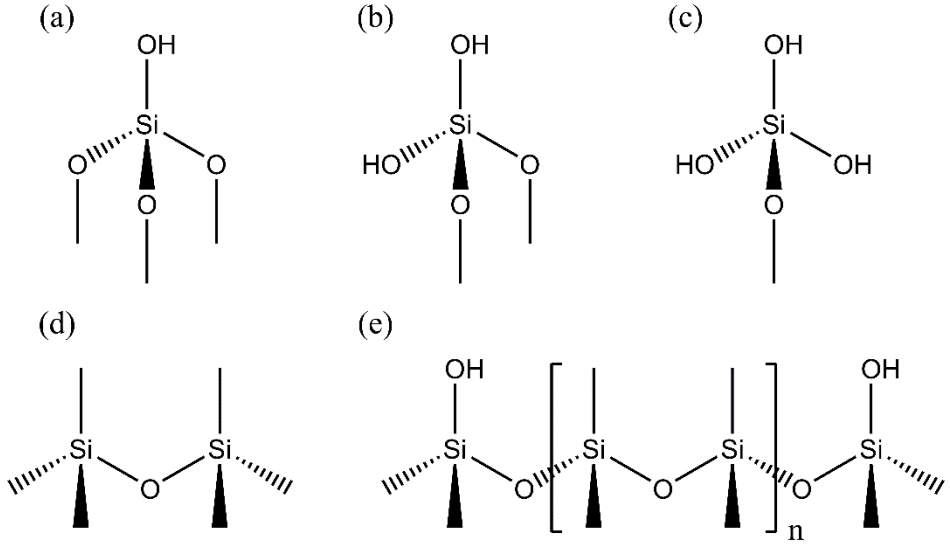

Figure S11. Examples of (**a-c**) silanols, (**d**) siloxanes and (**e**) their permutations present on the surface of a silicon oxide layer. Adopted with permission from Ref. [24]; permission conveyed through Copyright Clearance Center, Inc.

The chemical behaviour of the siloxane bridges is determined by the method of the surface preparation, humidity, and thermal and ambient history, particularly for the formation of silanols through hydrolysis. Each chemical moiety existing on the surface will exhibit different properties. This is especially highlighted in their hydrophilicity (water-like nature), susceptible in the water contact angle studies [24]. Silanol groups (Si-OH) present on the SiO_2 surface are responsible for adsorption of water, making it hydrophilic. As shown by Young [25], physical adsorption of water vapour is confined only to the neighbourhood areas of silanol sites on the silica surface, even at high relative pressures. On the other hand, homopolar character of the silicon-oxygen surface bonds (Si-O-Si) prevents water molecules from adsorption on the silica surface, making it hydrophobic. What is more, in addition to siloxanes, researchers have identified other chemical moieties that give the silica surface hydrophobic properties. They can be created as a result of an appropriate silicon wafer (pre)cleaning procedure, *i.e.* with the use of hydrofluoric acid (HF). Amongst these moieties are Si-H, Si-CH_x, and to a lesser extend Si-F [26].

Using different (pre)cleaning/surface modification techniques, it is possible to increase hydrophilic properties of silica by creating more silanol groups (S-OH) on the surface. These include treating silicon wafers in $HNO_3/H_2O/HF$, HNO_3/HF, or $H_2SO_4/H_2O_2/HF$ solutions followed by rinsing in de-ionized water [27-29], or exposing wafers to UV/Ozone [30]. Hydrophobicity of silica can be induced by the removal of surface silanol groups by annealing [31] or by grafting of long aliphatic chains on silica surface *via* trichlorosilane group (silanation reaction) [4]. UV/Ozone, thermal annealing and silanation methods are discussed in detail in the following sections.

Mica Substrates

Mica is a group of sheet silicate (phyllosilicate) minerals that exhibit nearly perfect basal cleavage. Muscovite, a representative mineral of the mica family, with formula $KAl_2(Si_3Al)O_{10}(OH)_2$ is often selected as a solid substrate in a range of scientific experiments due to the aforementioned cleavage property. Muscovite mica is built of alternated structures composed of aluminosilicate and K^+ ion layers, parallel to the (001) plane (**Figure S12**) [32]. In the crystal structure, Si^{4+} ions are replaced by Al^{3+} ions at the ratio of 3:1, respectively, making the aluminosilicate layer negatively charged. This negative charge is balanced by the K^+ ion layer that electrostatically binds the two adjacent

aluminosilicate layers together. The crystal can be easily cleaved along the K^+ layer between the two $(Si,Al)O_2$ tetrahedron sheets, with K^+ ions usually equally distributed between this two freshly formed surfaces [32].

The aforementioned property is often used to produce an atomically flat, negatively charged and flexible substrate. A freshly cleaved mica displays a hydrophilic nature with a water contact angle equal to zero, and 11% of Si surface atoms constituting silanol groups (Si-OH) [33]. Therefore, when cleaving is performed in air, water molecules adsorb on the surface forming a thin film [32]. Molecular dynamic simulation studies revealed that the adsorbed water molecules form hydrogen bonds with O atoms on the surface, with K^+ ions surrounded by hydrogen bonded water cages [34]. With respect to the ion exchange reaction on the mica surface, two types of adsorption sites were identified concerning permanent and pH dependant charge. The permanent charge type is related to the unbalance structural charge of K^+ ions, and the pH dependant type to protonation or deprotonation of hydroxyl (aluminol and silanol) groups on the tetrahedral or octahedral layers [35].

It is possible to modify the surface of mica by argon/water vapour plasma activation. This results in loss of Al atoms (20-40%) and generation of Si-OH groups (from 11% to 30-32%). Substrates can be further modified by heat treatment that results in the loss of Si-OH and Al-OH groups, and polar Al ions, increasing the hydrophobic character of the surface [33].

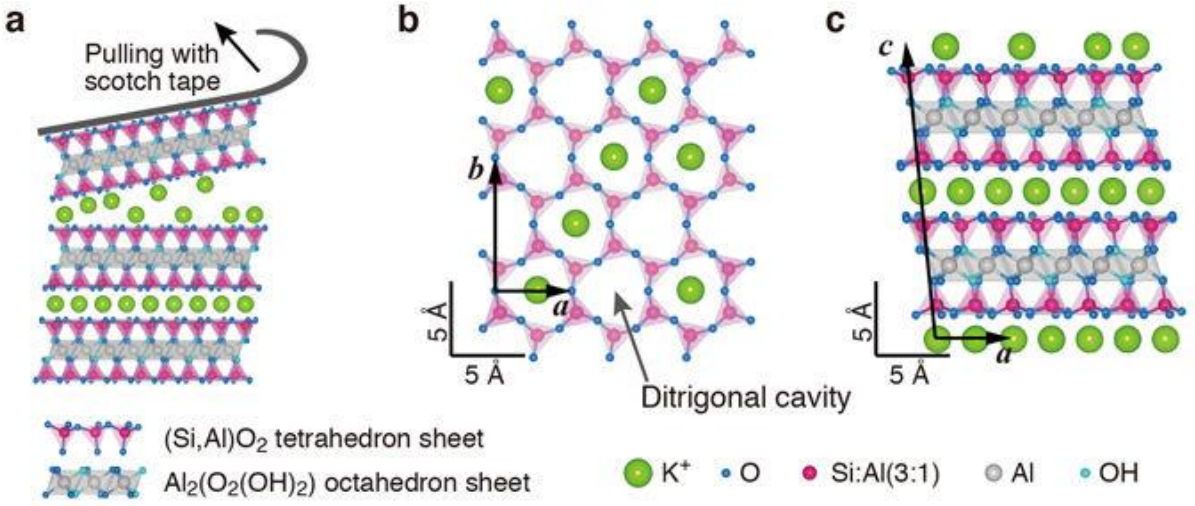

Figure S12. Crystal structure of muscovite mica. (**a**) Cleavage along the K^+ layer between two SiO_2 tetrahedron sheets (along the (001) plane). (**b**) Model of the cleaved (001) surface composed of

hexagonal network of $(Si,Al)O_2$ and K^+ ions occupying the ditrigonal cavities of the network. (**c**) Side view of the [010]-directional projection. Si atoms are replaced by Al atoms at the ratio of 3:1, respectively. ***a***, ***b*** and ***c*** are muscovite mica unit cell vectors. Reprinted from [32] under a Creative Commons Attribution 4.0 International License.

Polytetrafluoroethylene (PTFE) Substrates

Polytetrafluoroethylene (PTFE) is a synthetic fluoropolymer of tetrafluoroethylene (**Figure S13**), widely associated with its trade name - Teflon, even though the trade mark is used for PTFE and other fluoropolymers. It has been used in numerous applications due to its extraordinary properties such as chemical resistance, temperature stability, low coefficient of friction, low dielectric constant and, high breakdown voltage. However, it exhibits poor wear and abrasion resistance and creep (deformation, often referred as cold-flow) under load [36-38]. In addition, PTFE is a typical low surface energy material, intrinsically hydrophobic and oleophilic. Therefore, it is possible to produce smooth PTFE films that exhibit water and diesel oil contact angles of 120 - 150°, and 0 - 12°, respectively [39]. In addition, hydrophobicity can be further increased with surface roughness, which extend the surface area that has to be wetted by water (low surface roughness values). For high roughness values, the water drop is in contact only with a small fraction of the surface, with air trapped in between. This can be used to produce PTFE substrates with water contact angle up to 170°.

Even though PTFE can be challenging to process, it is relatively easily cut into small pieces, which combined with high chemical resistance and temperature stability, makes it an accessible substrate to use in various experimental designs.

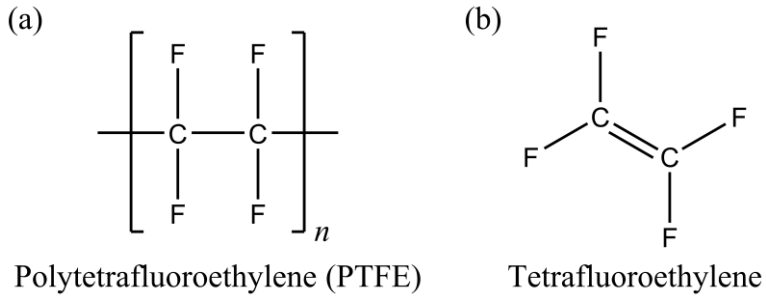

Figure S13. Structures of (**a**) polytetrafluoroethylene and its precursor monomer, (**b**) tetrafluoroethylene.

SI.06: References

1. Wąsik, P.; Redeker, C.; Dane, T. G.; Seddon, A. M.; Wu, H.; Briscoe, W. H., Hierarchical Surface Patterns upon Evaporation of a ZnO Nanofluid Droplet: Effect of Particle Morphology. *Langmuir* **2018,** *34* (4), 1645-1654.

2. Smith, J. E.; Jordan, M. L., Mathematical and graphical interpretation of the log-normal law for particle size distribution analysis. *J. Colloid Sci.* **1964,** *19* (6), 549-559.

3. Zender, C., Particle size distributions: theory and application to aerosols, clouds, and soils. http://dust.ess.uci.edu/facts/psd/psd.pdf (accessed 12th Dec 2017).

4. Silberzan, P.; Leger, L.; Ausserre, D.; Benattar, J. J., Silanation of silica surfaces. A new method of constructing pure or mixed monolayers. *Langmuir* **1991,** *7* (8), 1647-1651.

5. Ulman, A., Formation and Structure of Self-Assembled Monolayers. *Chem. Rev.* **1996,** *96* (4), 1533-1554.

6. Sriramulu, D.; Reed, E. L.; Annamalai, M.; Venkatesan, T. V.; Valiyaveettil, S., Synthesis and Characterization of Superhydrophobic, Self-cleaning NIR-reflective Silica Nanoparticles. *Scientific Reports* **2016,** *6*, 35993.

7. Sun, Z.; Liao, T.; Li, W.; Dou, Y.; Liu, K.; Jiang, L.; Kim, S.-W.; Ho Kim, J.; Xue Dou, S., Fish-scale bio-inspired multifunctional ZnO nanostructures. *Npg Asia Materials* **2015,** *7*, e232.

8. Lee, E.; Lee, K.-H., Facile fabrication of superhydrophobic surfaces with hierarchical structures. *Scientific Reports* **2018,** *8* (1), 4101.

9. Greene, L. E.; Law, M.; Tan, D. H.; Montano, M.; Goldberger, J.; Somorjai, G.; Yang, P., General Route to Vertical ZnO Nanowire Arrays Using Textured ZnO Seeds. *Nano Lett.* **2005,** *5* (7), 1231-1236.

10. Law, M.; Greene, L. E.; Johnson, J. C.; Saykally, R.; Yang, P., Nanowire dye-sensitized solar cells. *Nat Mater* **2005,** *4* (6), 455-459.

11. Ashiotis, G.; Deschildre, A.; Nawaz, Z.; Wright, J. P.; Karkoulis, D.; Picca, F. E.; Kieffer, J., The fast azimuthal integration Python library: pyFAI. *J. Appl. Crystallogr.* **2015,** *48* (2), 510-519.

12. Dane, T. G., pygix - a generic python library for performing reduction of grazing-incidence and fiber X-ray scattering data., https://github.com/tgdane/pygix (accessed 06 Jun 2018).

13. Tieyuan, F. U.; Zhishen, M. O.; Ping, H.; Yuchen, Q.; Shuyun, W.; Donglin, C., Study on factors affecting room temperature transition of polytetrafluoroethylene. *Chin. J. Polym Sci.* **1986,** *2*, 170-179.

14. Eilers, P. H. C.; Boelens, H. F. M., Baseline Correction with Asymmetric Least Squares Smoothing.
https://zanran_storage.s3.amazonaws.com/www.science.uva.nl/ContentPages/443199618.pdf (accessed 7 Sep 2018).

15. @Sparrowcide, Python baseline correction library. https://stackoverflow.com/questions/29156532/ (accessed 28 Aug 2018).

16. Khatib, J. M., *Sustainability of construction materials / edited by Jamal M. Khatib*. Cambridge : Woodhead ; Boca Raton, Fla. : CRC Press: Cambridge : Boca Raton, Fla., 2009.

17. S. Henderson, G.; Calas, G.; F. Stebbins, J., The structure of silicate glasses and melts. *Elements* **2006,** *2*, 269-273.

18. Melcher, M.; Wiesinger, R.; Schreiner, M., Degradation of Glass Artifacts: Application of Modern Surface Analytical Techniques. *Acc. Chem. Res.* **2010,** *43* (6), 916-926.

19. Amma, S.-i.; Luo, J.; Pantano, C. G.; Kim, S. H., Specular reflectance (SR) and attenuated total reflectance (ATR) infrared (IR) spectroscopy of transparent flat glass surfaces: A case study for soda lime float glass. *J. Non-Cryst. Solids* **2015,** *428*, 189-196.

20. Warring, S. L.; Beattie, D. A.; McQuillan, A. J., Surficial Siloxane-to-Silanol Interconversion during Room-Temperature Hydration/Dehydration of Amorphous Silica Films Observed by ATR-IR and TIR-Raman Spectroscopy. *Langmuir* **2016,** *32* (6), 1568-1576.

21. Engländer, T.; Wiegel, D.; Naji, L.; Arnold, K., Dehydration of Glass Surfaces Studied by Contact Angle Measurements. *J. Colloid Interface Sci.* **1996,** *179* (2), 635-636.

22. Morita, M.; Ohmi, T.; Hasegawa, E.; Kawakami, M.; Ohwada, M., Growth of native oxide on a silicon surface. *J. Appl. Phys.* **1990,** *68* (3), 1272-1281.

23. Ghita, R.; Logofatu, C.; Negrila, C.-C.; Ungureanu, F.; Cotirlan, C.; Manea, A.-S.; Lazarescu, M.-F.; Ghica, C., Study of SiO2/Si Interface by Surface Techniques. In *Crystalline Silicon - Properties and Uses*, Basu, S., Ed. InTech: Rijeka, 2011; p Ch. 02.

24. Thomas, R. R.; Kaufman, F. B.; Kirleis, J. T.; Belsky, R. A., Wettability of Polished Silicon Oxide Surfaces. *J. Electrochem. Soc.* **1996,** *143* (2), 643-648.

25. Young, G. J., Interaction of water vapor with silica surfaces. *J. Colloid Sci.* **1958,** *13* (1), 67-85.

26. Grundner, M.; Jacob, H., Investigations on hydrophilic and hydrophobic silicon (100) wafer surfaces by X-ray photoelectron and high-resolution electron energy loss-spectroscopy. *Appl. Phys. A* **1986,** *39* (2), 73-82.

27. Tong, Q. Y.; Gan, Q.; Fountain, G.; Enquist, P.; Scholz, R.; Gösele, U., Fluorine-enhanced low-temperature wafer bonding of native-oxide covered Si wafers. *Appl. Phys. Lett.* **2004,** *85* (17), 3731-3733.

28. Gondek, C.; Lippold, M.; Röver, I.; Bohmhammel, K.; Kroke, E., Etching Silicon with HF-H2O2-Based Mixtures: Reactivity Studies and Surface Investigations. *J. Phys. Chem. C* **2014,** *118* (4), 2044-2051.

29. Ljungberg, K.; Söderbärg, A., Improved direct bonding of Si and SiO2 surfaces by cleaning in H2SO4:H2O2:HF. *Appl. Phys. Lett.* **1995,** *67* (5), 650-652.

30. Lin, X.; Liao, G.; Tang, Z.; Shi, T., UV surface exposure for low temperature hydrophilic silicon direct bonding. *Microsyst. Technol.* **2009,** *15* (2), 317-321.

31. Lamb, R. N.; Furlong, D. N., Controlled wettability of quartz surfaces. *Journal of the Chemical Society, Faraday Transactions 1: Physical Chemistry in Condensed Phases* **1982,** *78* (1), 61-73.

32. Arai, T.; Sato, K.; Iida, A.; Tomitori, M., Quasi-stabilized hydration layers on muscovite mica under a thin water film grown from humid air. *Scientific Reports* **2017,** *7* (1), 4054.

33. Liberelle, B.; Banquy, X.; Giasson, S., Stability of Silanols and Grafted Alkylsilane Monolayers on Plasma-Activated Mica Surfaces. *Langmuir* **2008,** *24* (7), 3280-3288.

34. Odelius, M.; Bernasconi, M.; Parrinello, M., Two Dimensional Ice Adsorbed on Mica Surface. *Phys. Rev. Lett.* **1997,** *78* (14), 2855-2858.

35. Maslova, M. V.; Gerasimova, L. G.; Forsling, W., Surface Properties of Cleaved Mica. *Colloid J.* **2004,** *66* (3), 322-328.

36. Unal, H.; Mimaroglu, A.; Kadıoglu, U.; Ekiz, H., Sliding friction and wear behaviour of polytetrafluoroethylene and its composites under dry conditions. *Materials & Design* **2004,** *25* (3), 239-245.

37. Yoshida, A.; Matsumoto, E.; Yamada, H.; Okada, H.; Wakahara, A., Microfabrication of high quality polytetrafluoroethylene films by synchrotron radiation. *Nuclear Instruments and Methods in Physics Research Section B: Beam Interactions with Materials and Atoms* **2003,** *199*, 370-374.

38. Li, F.; Hu, K.-a.; Li, J.-l.; Zhao, B.-y., The friction and wear characteristics of nanometer ZnO filled polytetrafluoroethylene. *Wear* **2001,** *249* (10), 877-882.

39. Feng, L.; Zhang, Z.; Mai, Z.; Ma, Y.; Liu, B.; Jiang, L.; Zhu, D., A Super-Hydrophobic and Super-Oleophilic Coating Mesh Film for the Separation of Oil and Water. *Angew. Chem.* **2004,** *116* (15), 2046-2048.

Chapter 6

During my doctorate research project, I worked on the formation of complicated surface structures under conditions far from equilibrium *via* rapid evaporation of a sessile drop containing reactive ZnO nanoparticles. The underlying mechanism of the formation of these structures is very different from the one observed in the coffee ring effect. In a drying sessile drop of ZnO nanofluid, the dispersed ZnO nanocrystals undergo spontaneous chemical and morphological transformation into a fibrous surface network composed of layered $Zn(OH)_2$ nanocrystals [1-2].

I investigated the influence of the starting ZnO particles used for nano/microfluid preparation on the final residual surface pattern. Our analysis described in detail in Chapter 2 and Ref. [3] shows that the residual patterns produced from ZnO nanofluids are linked to the morphology, size, and crystallinity of ZnO particles through its influence on the initial moisture-assisted rapid dissolution of isobutylamine-coated ZnO nanocrystals, and that the shape anisotropy of the commercial ZnO particles can influence the Marangoni flows and the occurrence of the Bénard-Marangoni instabilities in the drying drop. This underlined the importance of the moisture assisted dissolution process and how the final residual pattern could be controlled by affecting it.

During the elucidation of the effect of starting ZnO particles and the surface chemistry of the substrate on the residual patterns, it was concluded that the dendritic structures formed within the residues can be identified as solidified manifestations of Bénard-Marangoni (BM) instability convection cells. As the recent work used a superficial description of these structures, identified as analogous to the foliage of red algae, Spanish dagger, or spider plant [2], I developed a methodology to provide a quantitative description of the geometric features of these BM cells produced from three different ZnO nanofluids using the fractal dimension analysis, which is discussed in detail in Chapter 3 and Ref. [4].

The already established methodology involving the fractal dimension analysis was employed in the investigation of the effect of substrate chemistry on the residual pattern where three different substrates including glass, silicon, and hydrophilised silicon were compared. In our findings discussed in

Chapter 4 and Ref. [5], we found that the morphological details of the solidified dendritic BM cells varied depending on the different substrates, attributed to different evaporation induced flows due to different substrate surface chemistry, which in turn reflected in their calculated fractal dimension values.

To provide mechanistic insights into this novel system involving rapid evaporation of a sessile drop of a ZnO nanofluid under conditions far from equilibrium, I performed an *in situ* grazing incident X-ray diffraction experiments to investigate the evolution of crystal structure of the constituents inside of a drying drop as the evaporation progressed. Thanks to the high temporal and spatial resolution provided by the synchrotron radiation, it was possible to observe the initial ZnO dissolution and recrystallisation and to identify the diffraction patterns from layered zinc hydroxide and zinc oxide at different evaporation times. In addition, the effect of the annealing temperature on the phase transition of $Zn(OH)_2$ into ZnO in the residual patterns was investigated. The initial results from the grazing incident XRD studies are partially reported in Chapter 5.

During my research, several interesting avenues were explored, and I would like to report the preliminary results here. To further study the possibility of creating different residual surface patterns from ZnO nanocrystals, a series of experiments based upon the evaporation of a droplet of a pure solvent (cyclohexane mixed with isobutylamine without the addition of ZnO particles) from various ZnO nanostructured surfaces was performed. The synthesis of ZnO nanorods on glass coverslips was performed according to the methods described in Refs [6-7] (**Figure 1a**), the synthesis of ZnO nanoplates on glass (**Figure 1c**), ZnO nanourchins on zinc (**Figure 1e**, **i**), and ZnO nanourchins on vertically aligned ZnO nanorods (**Figure 1g**, **k**) was based on the method reported in Ref. [8]. The residual patterns from ZnO nanostructured surfaces were produced by drop casting a drop of cyclohexane and isobutylamine mixture (5:1 volume ration) onto each substrate and leaving this to evaporate. The grown ZnO nanostructures remained largely undissolved and intercalated with the zinc hydroxide fibres of different dimensions. This shows that the reactive evaporation induced self-assembly is not restricted only to the ZnO nanocrystals dispersed in a solution but can be successfully applied to various ZnO nanostructured surfaces.

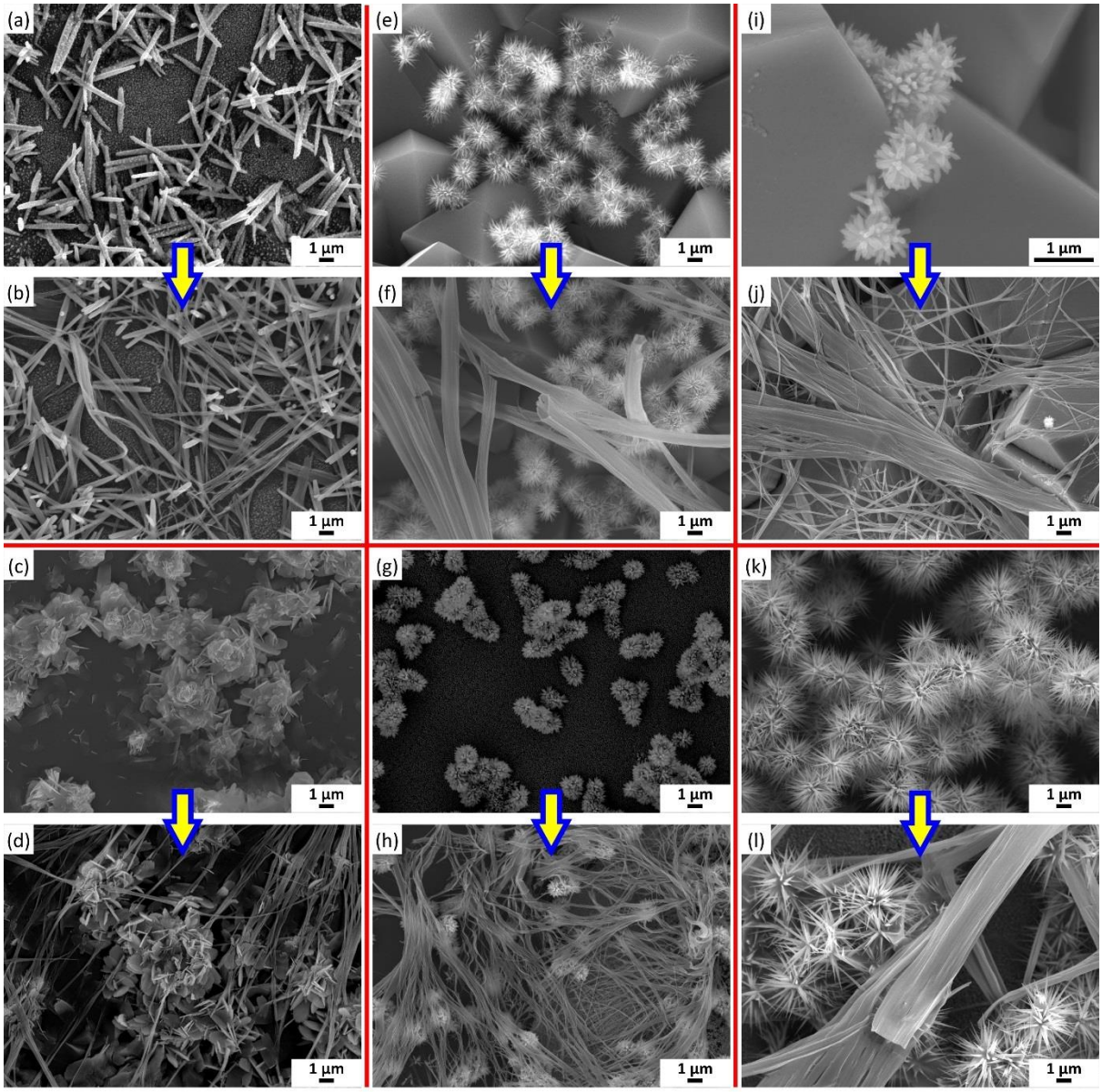

Figure 1. Evaporation induced self-assembly from different ZnO nanostructured surfaces: (**a**) ZnO nanorods on glass, (**c**) ZnO nanoplates on glass, and ZnO nanourchins on different substrates such as (**e**, **i**) zinc foil and (**g**, **k**) silicon wafer. The residual patterns from ZnO nanostructured surfaces were produced by drop casting a drop of cyclohexane and isobutylamine mixture (5:1 volume ratio) onto each substrate and leaving it to evaporate. Residual fibres composed of zinc hydroxide nanocrystals are marked by arrows for corresponding surfaces (**b**, **d**, **f**, **h**, **j**, and **l**).

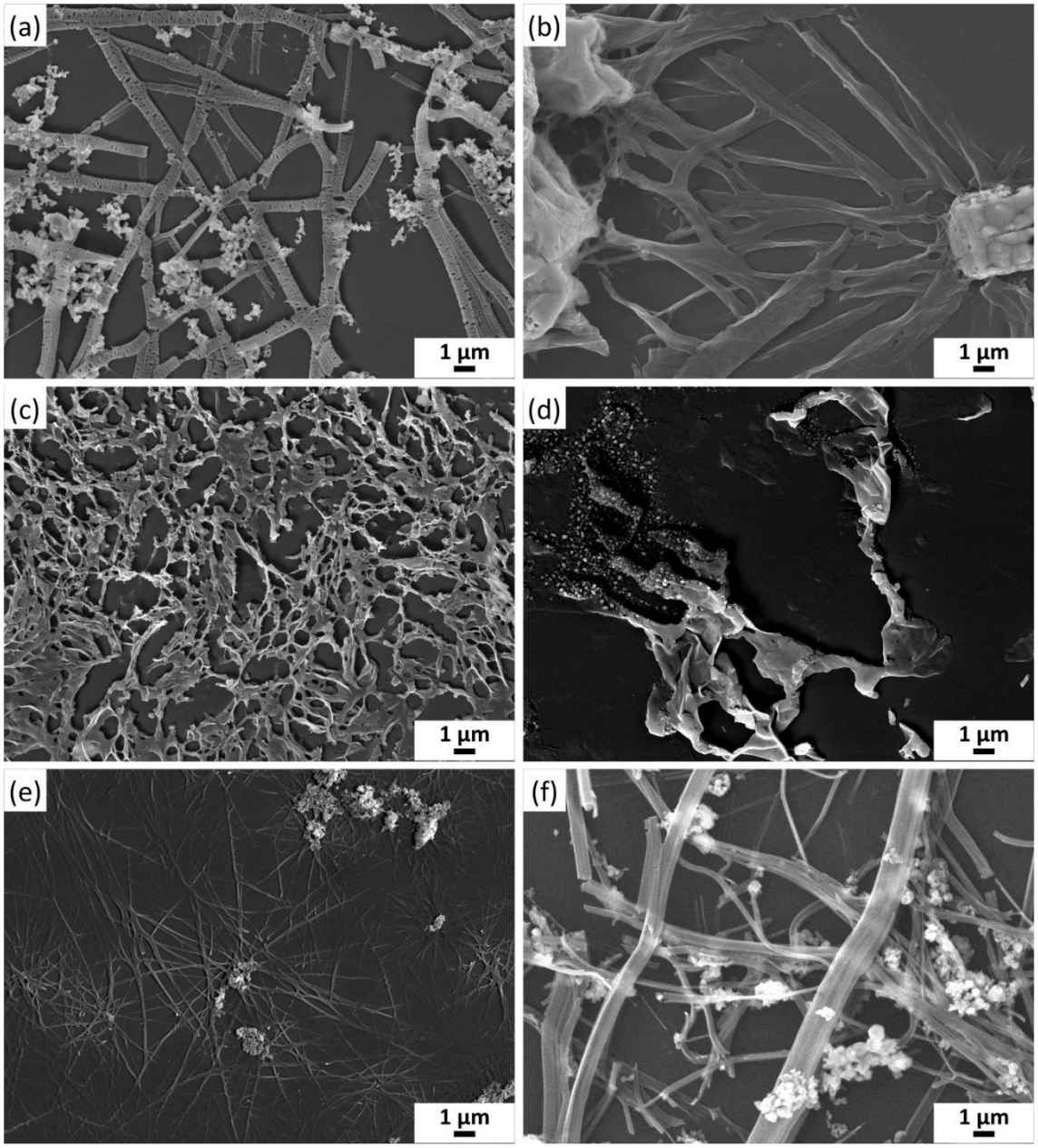

Figure 2. Scanning electron microscopy images of the residual surface pattern formed as a result of evaporating a droplet of a reactive nano/microfluid composed of (**a**) CdO, (**b**) HgO, (**c**) SrO, (**d**) MnO, (**e**) CuO nanotubes, and (**f**) CuO nanoparticles in a mixture of cyclohexane and isobutylamine (5:1 v:v) on a silicon substrate.

Another study involved investigating whether other materials can undergo this unexpected morphological and chemical transformation triggered by the evaporation of a reactive nanofluid. Oxides of Cd and Hg were selected as they are in the same group in the periodic table as Zn. In addition, nanostrands composed of hydroxides of metals such as Cd, Cu, Mn, in addition to Zn, reported in the

literature resembled similar morphologies to the residual patterns produced from ZnO nanofluids [9-19]. The full list of oxides in the form of powders that were investigated included CuO, Cu_2O, HgO, NbO, NbO_2, Nb_2O_5, SrO, and TiO_2. All powders were dispersed in the mixture of cyclohexane and isobutylamine (5:1 volume ratio) to the concentration of 1 mg / mL (the same as ZnO nanofluids). A droplet of each fluid was then drop cast onto a silicon substrate and left to evaporate. As prepared residual surface structures were characterised by scanning electron microscopy and X-ray diffraction (XRD). In addition, CuO and CdO nano/microfluid drops were also studied using the *in situ* grazing incidence XRD during evaporation at the European Synchrotron Radiation Facility (France). The results showed that the evaporation of the nano/microfluids prepared from CdO, HgO, SrO, MnO and CuO (**Figure 2**) led to the formation of hierarchical fibrous structures, similar to these observed for ZnO [1-5], emphasising that this evaporation induced self-assembly method from reactive nano/microfluids is not limited to ZnO crystals only.

Our results point to a new route for generating surface patterns of ZnO and $Zn(OH)_2$ in addition to nano/microfluids of various oxides such as CdO, HgO, SrO, MnO and CuO, and ZnO nanostructured surfaces, with morphological sophistication and structural hierarchy, whose functionality is of relevance to bioanalytical, optoelectronic, friction control, and antimicrobial materials applications. What is more, we believe the proposed fractal dimension analysis and the unprecedented results will facilitate further studies to seek correlations between the intriguing appearance of the residual patterns and the physical parameters relevant to the novel evaporation process involving reactive nanofluids.

In summary, Chapter 1 elaborated in detail on the proposed mechanism for the generation of zinc hydroxides residual structures from evaporation of a reactive ZnO nanofluid droplet on a solid substrate and their possible thermal conversion back to zinc oxide crystals. In addition, the theoretical basis of the Bénard-Marangoni convection with relevant equations including thermal and concentrational causes of the instabilities were explained. That chapter also covers the principles of the main techniques used in the thesis, *i.e.* X-ray diffraction, electron microscopy, and contact angle measurements, including assumptions and limitations relevant to the work presented in subsequent chapters.

Chapter 2, based on a research article published in *Langmuir* [3], discussed in detail how different morphologies and crystal structures of ZnO particles impact on the mechanism discussed in Chapter 1.

The residual patterns from three different ZnO particles, in-house synthesized ZnO nanoparticles, and commercially acquired ZnO nanopowder and ZnO powder have been investigated. The microscopic and nanoscopic structures of the residual patterns are associated with that of the starting particles, *via* detailed electron microscopy and X-ray diffraction analyses. It has been shown that the morphology, size, and crystallinity of starting ZnO particles affect the final patter formation through their influence on the initial moisture-assisted rapid dissolution of isobutylamine-coated ZnO nanocrystals. The shape anisotropy of the particles might also play a role in modifying the Marangoni flows and the occurrence of the Bénard-Marangoni instability, which is the subject of the following chapters.

Chapter 3 is based on a communication article published in the *Journal of Colloid and Interface Science* [4] and focuses on a fractal dimension analysis of the solidified Bénard-Marangoni cells. These cells were formed in the central part of the residual surface patterns created from evaporation of sessile drops containing different ZnO nano/microfluids and resembled a complex morphology. Such an approach was used to facilitate the discussion of the properties and features of the surface patterns beyond the descriptive account presented previously [1-3]. The fractal dimension value reflects the ruggedness of the dendritic pattern or how much space the dendritic pattern fills when it scaled up or down, whilst the fractal dimension value *versus* the size of the BM cell trend and its logarithmic fit give insights into the spatial distribution of the dendritic structures from the BM cell centre to its edge. ZnO nano/microfluids prepared from the commercially acquired ZnO nanopowder and ZnO powder formed patterns of a higher coverage with densely packed BM cells and a higher degree of interpenetration between them, displayed in higher values of the fractal dimension values. The results demonstrated that the fractal dimension analysis can be employed to provide a quantitative description of the geometric features of these complex surface structures from evaporative drying of reactive nanofluids.

Chapter 4, based on a recent publication in *Langmuir* [5], investigated the effect of substrate chemistry on the residue patterns, also applying the fractal dimension analysis presented in Chapter 3 and Ref. [4]. The solidified BM dendritic cells were produced upon evaporation of sessile drops comprising ZnO particulate dispersions in a mixed solvent (cyclohexane and isobutylamine) on substrates differing in hydrophilicity. The distribution of BM cell size and its fractal dimension both reflected on the substrate on which evaporation was performed. The smallest diameters and density

exhibited BM cells formed on the glass surface when compared to unmodified and hydrophilised silicon substrates for all the ZnO nano/microfluids studied. The BM cells resembling the spoke-like radial structures formed on the hydrophilised silicon had the largest diameters with the widest spread in dimensions. The in-house ZnO nanofluid resulted in larger BM cells with much higher degree of inter-cell penetration on both unmodified and ultraviolet/ozone (UVO) treated silicon substrates than on glass. However, ZnO nano/microfluids composed of the commercially acquired ZnO nanopowder and ZnO powder formed residual patterns of the highest coverage and level of interpenetration of the BM cells, manifested in the highest average fractal dimension on all the substrates. The trend of the fractal dimension increasing with the increasing BM diameter could indicate a two-stage fractal growth, with the smaller BM cells representing growing fractals with a more open structure, and the larger mature BM dendrites possessing a more intricate structure with overlapping boundaries with neighboring BM cells. The varying BM cell characteristics in terms of size distributions and fractal dimension values were attributed to different surface chemistry of the substrates, particularly their hydrophilicity, based on the fact that the presence of water molecules is crucial for the moisture-assisted dissolution of ZnO nanocrystals dispersed in a mixture of cyclohexane and isobutylamine [1, 3]. However, the effect of the thermal conductivity of the used substrate should be further investigated.

Chapter 5 is based on the *in situ* grazing incident X-ray diffraction experiments performed at I07, Diamond Light Source (United Kingdom). The crystal structure evolution of the constituents inside of reactive ZnO nano/microfluid drops on various substrates was investigated during evaporation. The initial ZnO dissolution and recrystallisation into zinc hydroxide fibres were identified at different evaporation times. Even though the substrate dependency of the residual pattern morphology was shown in the previous chapter, the crystal structure of the residual surface pattern was substrate independent. In addition, the effect of the annealing temperature on the phase transition of zinc hydroxide structures, which caused it to revert to ZnO in the residual patterns was investigated and the transition occurred between 50 - 100 °C. The results paved the way for further *in situ* investigations of different reactive nano/microfluids and nanostructured surfaces performed at the European Synchrotron Radiation Facility (France), yet to be published. The initial results have shown the dissolution of CdO and CuO

particles and transformation into their hydroxide structures, composing the residual surface patterns left due to solvent evaporation.

In Chapter 6, in addition to summarising the insights from the thesis work, some unpublished results were also presented, including those from evaporation from ZnO nanostructured surfaces and using nano/microfluids containing different metal oxides. A series of experiments based on drying a drop of cyclohexane and isobutylamine mixture without any dispersed particles from substrates covered with various ZnO nano/microstructures showed interesting results. The results have demonstrated that it is not necessary to use a reactive ZnO nano/microfluid droplet to facilitate the mechanism of the transformation of ZnO crystals into fibrous zinc hydroxide residual structures; evaporation of an appropriate solvent from a *reactive* ZnO nanostructured surface can also be used. The observations also further demonstrate that the dissolution of ZnO crystals plays a crucial role in this process as many undissolved ZnO nano/microstructures intercalated with the fibrous network were still present on the substrates, similar to the commercially acquired ZnO nanopowder and ZnO powder in Chapter 2 and Ref. [3]. The experiments with different metal oxides revealed that zinc oxide may not be the only compound susceptible to undergoing the chemical (oxide to hydroxide) and morphological (nano/microcrystals to long fibres) transformations in the process of drying reactive nano/microfluids composed of these compounds in a carefully designed solvent mixture. The initial candidates for these materials besides ZnO are CdO, CuO, HgO, MnO, and SrO.

A more general reaction scheme for the generation of hydroxides from drying reactive mixtures, based on reactions 10 - 12 from Chapter 1 is proposed. Similarly to ZnO nanofluids [1], when a droplet containing oxide crystals in a form of MxO, where Mx is a suitable transition metal (*e.g.* Zn, Cd, Cu, Hg, Mn, or SrO) in a mixture of isobutylamine (initial results have shown that other amines could be viable) and cyclohexane is placed on a solid substrate, water molecules are rapidly adsorbed from air and incorporated onto the surface of isobutylamine-coated MxO crystals, where reaction 1 is initiated:

$$\text{i-}C_4H_{11}N + H_2O \leftrightarrow \text{i-}C_4H_{12}N^+ + OH^- \quad (1)$$

The moisture assisted dissolution of MxO crystals continues afterwards as follows

$$MxO_{(s)} + i\text{-}C_4H_{12}N^+ + OH^- + H_2O \leftrightarrow Mx(OH)_3^{-\cdot+}Ni\text{-}C_4H_{12(aq)} \quad (2)$$

Convective flows transport liquid $Mx(OH)_3^{-\cdot+}Ni\text{-}C_4H_{12(aq)}$ away from the crystals, permitting their further dissolution. As the evaporation advances, the solution reaches its saturation point at the liquid-air interference towards the edge of the droplet, where crystallisation of $Mx(OH)_2$ is initiated according to reaction 3:

$$Mx(OH)_3^{-\cdot+}Ni\text{-}C_4H_{12(aq)} \leftrightarrow Mx(OH)_{2(s)} + i\text{-}C_4H_{11}N + H_2O \quad (3)$$

Even though this dissertation shows a comprehensive analysis of the formation of hierarchical surface patterns from evaporation of a reactive ZnO nanofluid droplets through a range of experimental techniques including electron microscopy, *in situ* X-ray scattering, contact angle, energy dispersive spectroscopy, dynamic light scattering, atomic force microscopy, applying quantitative approaches such as fractal dimension analysis or size distribution calculations, to investigating various experimental systems *i.e.* ZnO nanostructured surfaces, other transition metal oxides, or range of solvent mixtures, there are still questions that should be further investigated.

With respect to the Bénard-Marangoni instabilities observed in drying droplets, it would be worth to provide further experimental evidence for the instabilities implementing particle tracing, probing the temperature gradient across the droplet thickens, establishing solutal and thermal contributions to the flow, and supporting calculating Marangoni numbers with computer simulations. It is challenging to explain solidified cells overlapping or bow-tie projections of some observed structures using only the BM convection. Further investigation should focus on *in situ* experiments as it remains little understood what the complete structure of primary clusters formed from amphiphilic isobutylamine-ZnOH complexes during evaporation is. This should also include studies of different systems, *i.e.* using reactive nano/microfluids with alternative crystals or solvent composition to provide more insights into the mechanism. Different techniques of depositions should be explored as new routes to control the deposition patterns. This list is far from being exhausted but can be thought as a good starting point for any future experiments.

Taking everything into consideration, the thesis covers different aspects of creating hierarchical surface structures from reactive ZnO nanofluids, built upon the initial paper by Wu *et al.* [1] and

Master's thesis by Redeker [20]. It was demonstrated how to control the morphology of the residual surface patterns using ZnO particles with different crystallinities and morphologies, varying surface chemistry of a substrate, performing evaporation from nanostructured ZnO surfaces, and drying nano/microfluids composed of other metal oxides. A routine for the fractal dimension analysis to provide a quantitative description of the properties of these complex surface structures was established and discussed, paving the way for further investigations to seek correlation between the fractal dimensions and the physical parameters relevant to the evaporation process and solution conditions. The results also point to the feasibility for using *in situ* synchrotron generated X-ray scattering techniques for further elucidation of the processes involved into the chemical and morphological transformation of crystals inside a reactive drying drop.

References

1. Wu, H.; Chen, L. X.; Zeng, X. Q.; Ren, T. H.; Briscoe, W. H., Self-assembly in an evaporating nanofluid droplet: rapid transformation of nanorods into 3D fibre network structures. *Soft Matter* **2014,** *10* (29), 5243-5248.

2. Wu, H.; Briscoe, W. H., Morphogenesis of polycrystalline dendritic patterns from evaporation of a reactive nanofluid sessile drop. *Physical Review Materials* **2018,** *2* (4), 045601.

3. Wąsik, P.; Redeker, C.; Dane, T. G.; Seddon, A. M.; Wu, H.; Briscoe, W. H., Hierarchical Surface Patterns upon Evaporation of a ZnO Nanofluid Droplet: Effect of Particle Morphology. *Langmuir* **2018,** *34* (4), 1645-1654.

4. Wąsik, P.; Seddon, A. M.; Wu, H.; Briscoe, W. H., Dendritic surface patterns from Bénard-Marangoni instabilities upon evaporation of a reactive ZnO nanofluid droplet: A fractal dimension analysis. *J. Colloid Interface Sci.* **2019,** *536*, 493-498.

5. Wąsik, P.; Seddon, A. M.; Wu, H.; Briscoe, W. H., Bénard-Marangoni dendrites upon evaporation of a reactive ZnO nanofluid droplet: Effect of substrate chemistry *Langmuir* **2019,** *35* (17), 5830-5840.

6. Greene, L. E.; Law, M.; Tan, D. H.; Montano, M.; Goldberger, J.; Somorjai, G.; Yang, P., General Route to Vertical ZnO Nanowire Arrays Using Textured ZnO Seeds. *Nano Lett.* **2005,** *5* (7), 1231-1236.

7. Law, M.; Greene, L. E.; Johnson, J. C.; Saykally, R.; Yang, P., Nanowire dye-sensitized solar cells. *Nat Mater* **2005,** *4* (6), 455-459.

8. Wu, X.; Bai, H.; Li, C.; Lu, G.; Shi, G., Controlled one-step fabrication of highly oriented ZnO nanoneedle/nanorods arrays at near room temperature. *Chem. Commun.* **2006,** (15), 1655-1657.

9. Yu, Q.; Huang, H.; Chen, R.; Wang, P.; Yang, H.; Gao, M.; Peng, X.; Ye, Z., Synthesis of CuO nanowalnuts and nanoribbons from aqueous solution and their catalytic and electrochemical properties. *Nanoscale* **2012,** *4* (8), 2613-2620.

10. Wang, Z. L.; Kong, X. Y.; Wen, X.; Yang, S., In Situ Structure Evolution from Cu(OH)2 Nanobelts to Copper Nanowires. *J. Phys. Chem. B* **2003,** *107* (33), 8275-8280.

11. Tang, Z.; Kotov, N. A.; Giersig, M., Spontaneous Organization of Single CdTe Nanoparticles into Luminescent Nanowires. *Science* **2002,** *297* (5579), 237-240.

12. Peng, X.; Jin, J.; Kobayashi, N.; Schmitt, W.; Ichinose, I., Time-dependent growth of zinc hydroxide nanostrands and their crystal structure. *Chem. Commun.* **2008,** (16), 1904-1906.

13. Peng, X.; Ichinose, I., Green-Chemical Synthesis of Ultrathin β-MnOOH Nanofibers for Separation Membranes. *Adv. Funct. Mater.* **2011,** *21* (11), 2080-2087.

14. Luo, Y.-H.; Huang, J.; Jin, J.; Peng, X.; Schmitt, W.; Ichinose, I., Formation of Positively Charged Copper Hydroxide Nanostrands and Their Structural Characterization. *Chem. Mater.* **2006,** *18* (7), 1795-1802.

15. Luo, Y.-H.; Huang, J.; Ichinose, I., Bundle-like Assemblies of Cadmium Hydroxide Nanostrands and Anionic Dyes. *J. Am. Chem. Soc.* **2005,** *127* (23), 8296-8297.

16. Lu, C.; Qi, L.; Yang, J.; Zhang, D.; Wu, N.; Ma, J., Simple Template-Free Solution Route for the Controlled Synthesis of Cu(OH)2 and CuO Nanostructures. *J. Phys. Chem. B* **2004,** *108* (46), 17825-17831.

17. Li, J.; Cao, W.; Mao, Y.; Ying, Y.; Sun, L.; Peng, X., Zinc hydroxide nanostrands: unique precursors for synthesis of ZIF-8 thin membranes exhibiting high size-sieving ability for gas separation. *CrystEngComm* **2014,** *16* (42), 9788-9791.

18. Ichinose, I.; Kurashima, K.; Kunitake, T., Spontaneous Formation of Cadmium Hydroxide Nanostrands in Water. *J. Am. Chem. Soc.* **2004,** *126* (23), 7162-7163.

19. Ichinose, I.; Huang, J.; Luo, Y.-H., Electrostatic Trapping of Double-Stranded DNA by Using Cadmium Hydroxide Nanostrands. *Nano Lett.* **2005,** *5* (1), 97-100.

20. Redeker, C.; Briscoe, W. H. Evaporative Self-Assembly of ZnO Nanorods. University of Bristol, 2013.